UNIVERSITY
OF TRENTO - Italy
DEPARTMENT OF INDUSTRIAL ENGINEERING

XXX cycle

Doctoral School in Materials, Mechatronics and Systems Engineering

Surface Treatments to Protect Conventional and Rheo-High Pressure Die Cast Al-Si Alloys from Corrosion

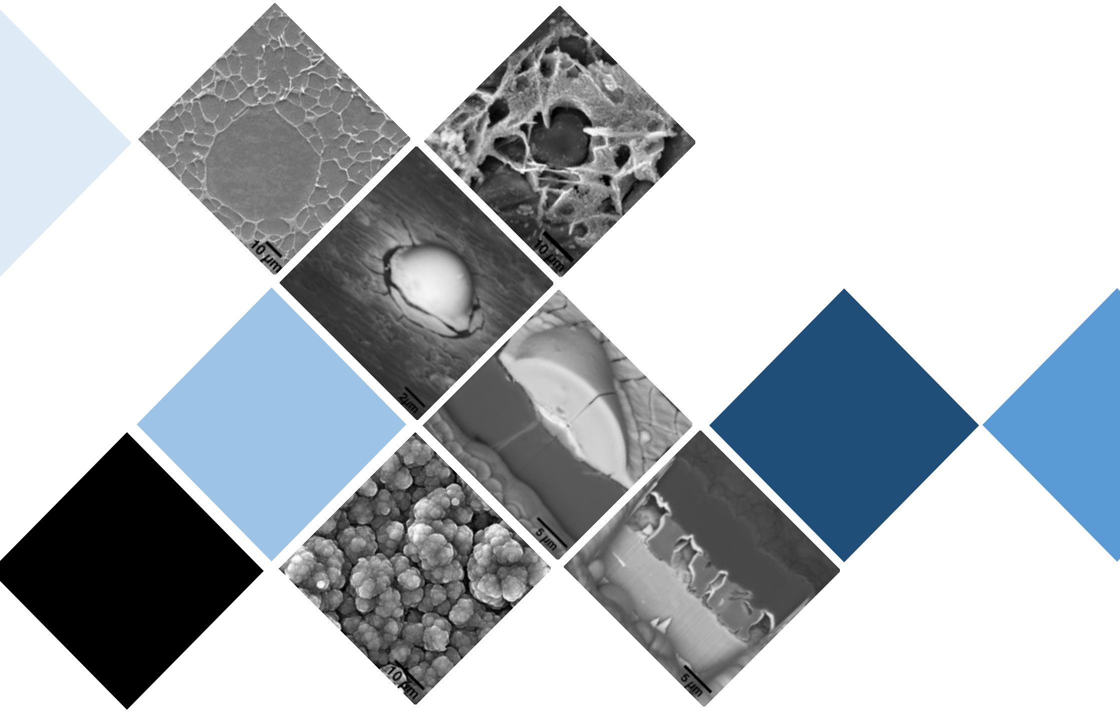

Maryam Eslami
January 2019

THESIS FOR THE DEGREE OF DOCTOR OF PHILOSOPHY

Surface Treatments to Protect Conventional and Rheo-High Pressure Die Cast Al-Si Alloys from Corrosion

Maryam Eslami

Approved by

Prof. Flavio Deflorian
Department of Industrial Engineering
University of Trento, Italy

Dr. Caterina Zanella
Department of Materials and Manufacturing
Jönköping University, Sweden

PhD commission

Prof. Jinshan Pan
School of Chemical Science and Engineering
KTH Royal Institute of Technology, Sweden

Dr. Cecilia Monticelli
Department of Engineering
University of Ferrara, Italy

Dr. Massimo Pellizzari
Department of Industrial Engineering
University of Trento, Italy

University of Trento
Department of Industrial Engineering
Trento, Italy 2019

Surface Treatments to Protect Conventional and Rheo-High Pressure Die Cast Al-Si Alloys from Corrosion

Cover Photo:

From the top left: the microstructure of Rheo-HPDC Al-Si alloy, localized corrosion (trenching) around the eutectic silicon, a cerium-based nucleus, a cross-sectional view of the same nucleus showing the selective deposition site (an intermetallic particle), the surface morphology of polypyrrole coating and the cross-sectional view of oxidation occurring at the polypyrrole/Al interface.

Doctoral Thesis

Published in Trento (Italy) – by University of Trento
ISBN: - - - - - - - - -

Will is character in action.

William McDougall

Abstract

Surface Treatments to Protect Conventional and Rheo-High Pressure Die Cast Al-Si Alloys from Corrosion

Rheocasting process integrated with the high pressure die casting method (Rheo-HPDC) has established itself as a new promising technology to produce high-quality components. However, different types of microstructural segregation induced by the semi-solid process influence the properties of the final component.
The semi-solid microstructural features and the new compositions require detailed corrosion studies and verification.

The first part of this thesis deals with microstructural and corrosion studies of the conventional and Rheo-HPDC Al-Si alloys.
In this part, corrosion properties of two Al–Si alloys containing 2.5 and 4.5 wt % silicon cast by Rheo-HPDC method were examined in the diluted Harrison solution using polarization and electrochemical impedance spectroscopy (EIS) techniques on as-cast and ground surfaces.
The microstructural studies revealed that samples taken from different positions (with respect to the feeding gate) contain different fractions of solid and liquid parts of the initial slurry.
It was shown that the Rheo-HPDC Al-Si alloys are prone to the localized form of corrosion inside the eutectic region at the interface of aluminum with silicon phase and intermetallic particles.
Electrochemical behavior of as-cast, ground surface, and bulk material was shown to be different due to the presence of a segregated skin layer and the surface quality.
Corrosion properties of the two Al-Si alloys cast by the conventional and Rheo-HPDC process were also evaluated and compared in 0.01, 0.05, 0.1 and 0.6 M NaCl solutions.
The conventional HPDC and semi-solid alloys presented similar EIS responses. However, the semi-solid samples with a lower fraction of the eutectic phase showed slightly higher impedance values in the more diluted sodium chloride solutions. Corrosion morphological

features, including localized corrosion, trenching and co-operative corrosion rings were comparable for both types of alloys. However, in the anodic polarization test, the semi-solid alloys presented a higher resistance to pitting corrosion.

To protect aluminum alloys from corrosion, chromium-based conversion coating has been successfully used for decades, due to its extensive protection. However, rising concerns and new restrictions on the environmental hazards of Cr (VI) compounds have led to intensive efforts to develop alternative coatings. The second and third parts of this thesis address the effort to investigate two alternatives in this field.

Cerium-based conversion coatings were deposited on the conventional and Rheo-HPDC Al-Si alloys by immersion in cerium nitrate aqueous solutions. Different parameters were studied to optimize the conversion coating, and NaCl or H_2O_2 were also added to the solution to modify or accelerate the deposition process.

The results revealed that applying cerium-based conversion coating on Al-Si alloys, is possible and a selective deposition is obtained due to the presence of iron-rich intermetallic particles inside the eutectic region.

Under the accelerated conditions, the deposition mechanism includes dissolution of the aluminum matrix, selective dissolution of aluminum from the noble intermetallic particles, oxidation of iron from these particles, and the deposition of cerium hydroxide/oxide layer.

The results revealed that the improvement in corrosion resistance in the presence of selectively deposited cerium-based conversion coating is more significant compared to the homogenous coating obtained from the conversion solution containing H_2O_2.

The aluminum alloy with a higher amount of silicon showed more active surface during the conversion process which reduces the required concentration of $Ce(NO_3)_3$ but also makes it difficult to work with more aggressive solutions.

In the third part of this thesis, the possible protective effect of polypyrrole coating on pure aluminum and Rheo-HPDC Al-Si alloys was investigated.

Different electropolymerization solutions containing the Py monomer, SDS, DHBDS (Tiron), $C_6H_8O_7$ and $NaNO_3$ were used.

The presence of nitrate anions led to the passivation of the aluminum electrode (both pure and alloy) during the electropolymerization and to the deposition of a thicker/more conductive coating.

These facts resulted in longer and more efficient corrosion protection in NaCl solutions. This polypyrrole coating was able to keep the alloys' surface potential noble for at least 168 hours. Which can be attributed to the anodic protection provided by the reduction of the polymer.

It was shown that the presence of silicon phase or intermetallic particles has a positive effect on the electropolymerization of polypyrrole film. Therefore, the coatings deposited on the alloys possess higher thicknesses compared to those deposited on the pure aluminum.

In the presence of chloride ions, all coatings suffered from the formation of blisters as a result of severe (localized) galvanic interaction of polypyrrole with aluminum. This may question the application of polypyrrole coating in concentrated NaCl solutions. However, it is shown that the protection efficiency can be improved by altering the solution chemistry which affects the polymer/metal interface and the conductivity and the barrier properties of the coating. Therefore, the application of polypyrrole in corrosion protection is not totally ruled out but needs specific considerations.

Acknowledgments

I would like to express my sincere gratitude to my supervisors Prof. Flavio Deflorian and Dr. Caterina Zanella (Jönköping University, Sweden) for their scientific guidance and support during my PhD. They truly supported me through many tough times and never gave up on me.

I would also like to acknowledge Dr. Michele Fedel for many fruitful discussions and his helpful comments and suggestions.

Many sincere thanks go to Mr. Luca Benedetti for his unconditional and kind assistance to my experiments.

I gratefully acknowledge Dr. Giorgio Speranza (FBK-CMM) for his great help with the XPS measurements and analysis.

I would also like to thank Prof. Sasha Omanovic (McGill University, Canada) for his hospitality, guidance and support during my internship in Montreal. In addition, I would like to express my gratitude to the colleagues and staff at Electrochemistry/Corrosion lab and Chemical Engineering department at McGill University.

I am also grateful to the members of the Material and Manufacturing group at Jönköping University for their collaboration and hospitality during my stay in Jönköping. I would like to especially thank Dr. Anders E. W. Jarfors and Dr. Mostafa Payandeh for their prestigious help with the first part of my research. I would also like to acknowledge Dr. Nils-Eric Andersson and Dr. Ehsan Ghassemali for their assistance with the SEM-FIB analysis.

I would like to thank COMPtech AB (Sweden) for the production of alloy components and the technical support. I would also like to appreciate the European Cooperation in Science and Technology for partially funding this project.

Last but not least, I would like to acknowledge the unconditional love and support from my family and friends, especially my mom and my cousin Roya and her lovely family. I would also like to thank my friend Hamid Hassani for being a kind brother to me in Trento.

A special appreciation goes to my dearest friend Rajeev Piyare who has been always there for me.

List of Publications

This thesis is primarily based on the work presented in the following papers. In the text they are referred by roman numerals.

Journal publications:

Paper I

M. Eslami, M. Fedel, G. Speranza, F. Deflorian, N-E. Andersson, C. Zanella, *Study of selective deposition mechanism of cerium-based conversion coating on Rheo-HPDC aluminum-silicon alloys*, Electrochimica Acta 255 (2017) 449-462.

Paper II

M. Eslami, M. Fedel, G. Speranza, F. Deflorian, C. Zanella, *Deposition and characterization of cerium-based conversion coating on HPDC low Si content aluminum alloy*, Journal of the Electrochemical Society 164 (9) (2017) C581-C590.

Paper III

M. Eslami, M. Payandeh, F. Deflorian, A. E. W. Jarfors, C. Zanella, *Effect of segregation and surface condition on corrosion of Rheo-HPDC Al-Si alloys*, Metals 8(4) 209 (2018).

Proceedings:

Paper IV

M. Eslami, F. Deflorian, S. Omanovic, N-E. Andersson, M. Fedel, C. Zanella, *Studying electropolymerization and corrosion protection mechanism of polypyrrole coating on aluminum*, 69th annual meeting of the international society of electrochemistry, Bologna, Italy, September 2018.

Paper V

M. Eslami, F. Deflorian, M. Fedel, C. Zanella, *Ce-based conversion coatings on Rheo-HPDC low Si content aluminum alloy*, EUROCORR 2017, Prague, Czech Republic, September 2017.

Paper VI

M. Eslami, F. Deflorian, M. Fedel, C. Zanella, *Characterization of Ce-based conversion coatings on HPDC low Si content aluminum alloy*, SMT 31, Mons, Belgium, July 2017.

Paper VII

M. Eslami, F. Deflorian, M. Payandeh, A. E. W. Jarfors, C. Zanella, *Investigation of corrosion behavior of SSM-HPDC aluminum-silicon alloys*, EUROCORR 2016, Montpellier, France, September 2016.

Manuscript journal papers:

Paper VIII

M. Eslami, G. Speranza, M. Fedel, N-E. Andersson, F. Deflorian, S. Omanovic, C. Zanella, *Electropolymerization and possible corrosion protection effect of polypyrrole coatings on AA1050 in NaCl solutions*, submitted to CORROSION, the Journal of Science and Engineering.

Paper IX

M. Eslami, M. Fedel, F. Deflorian, S. Omanovic, C. Zanella, *Electrochemical interaction of polypyrrole coating with aluminum-silicon alloys*, In preparation.

Paper X

M. Eslami, M. Fedel, F. Deflorian, C. Zanella, *Effect of electrodeposition conditions on the properties of polypyrrole coating on aluminum-silicon alloy*, In preparation.

Paper XI

M. Eslami, G. Speranza, F. Deflorian, C. Zanella, *XPS study of electrodeposition of polypyrrole coating on pure aluminum and aluminum-silicon alloy*, In preparation.

Paper XII

M. Eslami, F. Deflorian, C. Zanella, *Corrosion behavior of conventional and rheo-high pressure die cast Al-Si alloys in NaCl solutions*, In preparation.

Contents

Chapter 1 **Introduction**

This chapter describes the motivations, the main subjects, the methodology and the structure of this thesis.

1.1. Motivation and aim

This thesis is based on the study of the electrochemical properties of aluminum- (low content) silicon alloy components which were produced by the conventional and semi-solid (rheo)-high pressure die cast (HPDC) processes.

There are four main motivations:

(i) The semi-solid casting technology (Rheo-HPDC) is new and promising, while its influence on the corrosion properties of aluminum alloys and the corrosion protection strategies have not been studied yet.

The specific semi-solid microstructure and its differences with the conventional casting microstructure make the study of corrosion behavior and surface treatment essential.

(ii) The effect of silicon content on the corrosion properties and the corrosion protection treatments in the low silicon content aluminum alloys has not been studied before.

(iii) The component used for this study is a prototype of the real component used in telecom base stations. These components are subjected to corrosion due to the different environmental conditions. The knowledge investigated in this thesis can be transferred to manufactures and designer for future research and development.

(iv) The growing industrial demand for environmental friendly corrosion protection treatments for aluminum alloys has led many researchers to devote effort in this field. In this thesis two different types of alternative coatings have been investigated.

1.2. Research design

1.2.1. Research perspectives

Based on the motivations described earlier a series of investigations on the corrosion properties of the alloys and on the corrosion protection treatments were designed:

(i) For the corrosion investigations, firstly behavior of the semi-solid alloys was investigated in a diluted Harrison solution. The focus of this study was to correlate the effect of semi-solid casting process and the semi-solid microstructure to the corrosion properties, with an especial emphasize on the effect of the surface liquid segregation.

Moreover, corrosion properties of the conventional and Rheo-HPDC aluminum-silicon alloys were studied and compared in sodium chloride solutions with different concentrations.

(ii) The first surface treatment studied in this thesis was cerium-based conversion coatings (CeCCs). The initial aim was the optimization of the treatment parameters to achieve the highest level of protection. Moreover, the deposition mechanism of the conversion coating was studied and compared for the conventional and semi-solid cast alloys.

(iii) The second surface treatment (coating) studied in this thesis was polypyrrole coating. Due to the complexity of the electrodeposition process and the corrosion protection mechanism, the study was first performed and optimized on the pure aluminum. Subsequently, the conductive polymer coating was applied on Rheo-HPDC aluminum-silicon alloys and the results were compared.

The initial subject of this study was investigation of the effect of solution chemistry, voltage range and the substrate nature on the electropolymerization. While the main focus was to understand the possible corrosion protection mechanism of polypyrrole coating and the influence of substrate composition and microstructure on this protection effect.

1.2.2. Research questions

The following main questions are answered in this thesis:

Corrosion investigations

How do the semi-solid microstructure and the segregation due to rheo-casting process affect the corrosion properties?

What are the differences between the corrosion properties of the conventional and Rheo-HPDC Al-Si alloys?

How does the silicon content influence the corrosion properties?

Cerium-based conversion coating

What are the effects of semi-solid microstructure and the silicon content on the deposition and the corrosion properties of CeCCs?

What is the deposition mechanism of CeCC on the conventional and Rheo-HPDC Al-Si alloys?

Is there any difference in the deposition and the corrosion properties of CeCCs on the conventional and Rheo-HPDC Al-Si alloys?

Polypyrrole coatings

What are the effect of nitrate and citrate anions on the electrodeposition and the properties of polypyrrole coatings on aluminum and Rheo-HPDC Al-Si alloys?

How do the semi-solid microstructure and the silicon content influence the electrodeposition and the properties of polypyrrole coating?

What is the corrosion protection mechanism of polypyrrole coating on aluminum and Rheo-HPDC Al-Si alloys?

1.3. Thesis structure

Chapter 2 provides a short literature review on the main subjects of this thesis.
Chapter 3 describes the principles of main characterization techniques used in this study.
Chapter 4 presents and compares microstructural features and corrosion properties of the conventional and Rheo-HPDC Al-Si alloys in diluted Harrison solution and sodium chloride solutions with different concentrations.
Chapter 5 addresses the study on deposition and electrochemical properties of CeCC on the conventional and Rheo-HPDC Al-Si alloys.
Chapter 6 presents the experimental work and the related results and discussion on electropolymerization and electrochemical characterization of polypyrrole coatings on pure aluminum (AA1050) and Rheo-HPDC Al-Si alloys for corrosion protection purpose.
To avoid any confusion, at the beginning of chapters 4-6, separate "materials and methods" sections describe the detailed experimental procedures for each part.

Chapter 2 **Literature review**

This chapter addresses a short literature review on the main subjects of this thesis.

2.1. Aluminum-silicon (Al-Si) alloys

2.1.1. Generalities and research backgrounds

Binary system of Al-Si is the base for 90% of casting aluminum alloys [1]. These alloys provide excellent castability, low melting point, low shrinkage, low coefficient of thermal expansion, low specific gravity, proper wear and good corrosion resistance [2]. Application of these alloys is not limited to those in military, automotive, aerospace, and general engineering industries.

Depending on the silicon percentage, Al-Si alloys are categorized into hypoeutectic alloys with 5 to 10% silicon, eutectic alloys containing 11–13% silicon, and hypereutectic alloys with a silicon content commonly between 14 and 20% [3]. In the semi-solid casting processes, the lower limit of silicon can be reduced to 2-3%.

Typical microstructure of these alloys mainly consists of α-aluminum solid solution, the eutectic phase and silicon crystals [3]. Inevitable presence of iron in the alloy composition either in the form of impurity or alloying element results in the formation of AlFeSi intermetallic (IM) particles [4, 5]. Different forms of AlFeSi compounds, based on the silicon content have been reported, including β-AlFeSi in hypoeutectic alloys and α-AlFeSi and δ-AlFeSi in hypereutectic alloys [4, 5]. These brittle intermetallic compounds with a relatively low bond strength with the aluminum matrix lead to inferior mechanical properties [5]. Besides this disadvantage, in high pressure die cast alloys, which are the subject of this thesis, the presence of iron in the composition prevents the soldering of molten alloy to the die.

The morphological features and subsequently the properties (mechanical, electrical, thermal, etc.) of Al-Si alloys are dependent on the alloy composition, the casting technology and the heat treatment procedure. Specifically, the morphology and the fraction of main phases (α-Al, eutectic silicon and silicon crystals) and intermetallic compounds govern the mechanical properties of alloys.

From almost 100 years ago [6], until present research on Al-Si alloys includes those on the modification of eutectic silicon morphology (from coarse plate-like to fine fibrous networks) by chemical modifiers such as strontium (Sr), sodium (Na) and Antimony (Sb) [7-10]. Due to the tribological applications of Al-Si alloys, the subsequent researches mostly focus on the relationship between the microstructure and the mechanical and specifically wear properties [7, 11, 12].

The development of low silicon content aluminum alloys (especially for using in high pressure die cast process) to increase the thermal conductivity is the subject of some other studies [13, 14].

2.1.2. Corrosion of Al-Si alloys

Despite its reactive nature, pure aluminum is resistant to most environments and chemicals thanks to the formation of a protective oxide (passive) layer. The corrosion of aluminum only occurs once the oxide film has been dissolved or damaged. This film is stable in neutral conditions, but soluble in acidic and alkaline environments and is sensitive to the presence of halide ions such as chloride. The growth of oxide film is affected by the alloying elements and impurities [15].

Aluminum is anodic to many metals. When it is coupled with them in an electrolyte, the resultant potential difference causes a galvanic couple and considerable corrosion can result. Similarly, the galvanic potential difference between the aluminum matrix and the secondary phases can result in severe corrosion [16].

Different microstructural components in Al-Si alloys, including the eutectic silicon phase and the IM particles, exhibit various electrochemical potentials with respect to the aluminum matrix, rendering the alloy susceptible to localized forms of corrosion such as pitting [4, 16-18].

The so-called "pitting corrosion" is a localized breakdown of the passive layer on an open surface. The presence of aggressive anionic species, usually chloride ions, is essential for the pitting to occur [19]. Adsorption of chloride ions on the oxide film and the subsequent chemical reaction between these anions and $Al(OH)_2^+$ cations result in the formation of the soluble aluminum chloride salt leading to the localized oxide dissolution and pit initiation [20, 21]. The preferential sites for pitting corrosion are the locations where the oxide film is, presumably, less perfect, such as the phase boundaries [22]. Once the pitting starts the anodic (metal dissolution) and the cathodic (e.g. oxygen reduction) electrochemical reactions separate spatially. The local pit environment depleted of the cathodic reactant (e.g., oxygen) and enriched in metal cations shifts the cathodic reaction to the exposed surface and absorbs anionic species such as chloride ions, auto-catalyzing the pitting process. The acidic pH in the pit, due to cation hydrolysis and the absence of a local cathodic reaction helps to propagate the pit growth [19].

There is a general agreement that iron-rich IM particles are deleterious to the alloy's corrosion resistance [4, 16, 17, 23-25]. These particles are nobler with respect to the aluminum matrix and exhibit enhanced cathodic kinetics. Apart from the galvanic influence, it has been suggested that the alkaline dissolution of the matrix at the particle/ aluminum interface where the pH of the solution is increased due to the cathodic reaction on the particle surface can be the reason of pit nucleation [19]. Furthermore, on the alloy surface, the oxide is not continuous (from the IM particles to the aluminum matrix), leading to a significant defect site [18].

For cathodic particles (such as iron-rich IMs), circumferential pits appear as trenches around the intact particle and the corrosion attack is mainly in the matrix phase [18].

Silicon is also cathodic with respect to the aluminum matrix but its galvanic effect is minimal due to the low current density, promoted on the silicon surface, as a result of the high polarization of silicon particles [4]. However, the effect of silicon on the corrosion resistance of aluminum is not clear yet [16, 26]. For instance, Rehim et al [26, 27] showed that the rate of pit nucleation, in chloride containing environment, decreases by increasing the silicon content from 0 to 6 and 18%. According to their kinetic study, this trend does not change by the variation in halide ion (chloride) concentration, temperature or applied potential. However, no clear explanation is provided for this behavior.

Silicon also increases the corrosion potential of the aluminum solid solution, decreasing its potential difference with the secondary phases [28, 29].

Moreover, the 3D corrosion study by Mingo et al. [24] showed that in the rheocast aluminum alloy (A356), iron-rich IM particles are the preferential corrosion sites rather than the eutectic silicon phase. A recent study by Qi et al. [25, 30] on the effect of Rheo-HPDC process on the corrosion resistance of Al-8 Si-Fe alloy shows improved corrosion resistance of the alloy as a result of the semi-solid process and correlates it to the lower volume fraction of β-Al_5FeSi particles.

The morphology of iron-rich IM particles can be modified with the addition of Mn, resulting in the formation of Al-Fe-Si-Mn compounds with a reduced cathodic effect [16]. Magnesium has a similar effect on reducing the cathodic effect and Al–Fe–Si–Mg compounds are the least detrimental in comparison to Al–Fe, Al–Fe–Si and Al–Fe–Si–Mn phases [4].

As mentioned before, Al-Si alloys mainly suffer from the preferential corrosion at α-Al dendrites inside the Al–Si eutectic region [31]. Therefore, the corrosion behavior of these alloys depends on the volume fraction, the morphology and the distribution of α-Al particles, the eutectic silicon phase and iron-rich IMs, such as β-AlFeSi and π-AlFeSiMg [4].

Since the subject of this thesis is semi-solid cast Al-Si alloys, more information regarding their corrosion behavior is presented in the following sections.

2.2. Rheo-high pressure die cast process

2.2.1. Principles

High pressure die cast (HPDC) is widely used as the manufacturing process of the majority of light alloy components [32, 33]. In this technology liquid metal, maintained in a holding furnace at the desired temperature, is ladled into a shot sleeve and injected into the oil-cooled die where it rapidly solidifies under pressure [32, 34].

Advantages of this process include high productivity, possibility of manufacturing parts with complex geometry, dimensional accuracy, reduced need for finishing operations and producing a component with fine grain microstructure and good mechanical properties [35, 36]. While the formation of internal defects during the high-speed mold filling can be a problem in the conventional HPDC process [32, 37]. In addition, there is a tendency for hot tearing during HPDC due to a relatively wide freezing range and a low solidus temperature [38].

Semi-solid metal (SSM) processing integrated with HPDC (SSM-HPDC) is a promising casting technology to produce high-quality components with sound microstructure. The higher viscosity of semi-solid slurries in this process reduces air entrapment and the consequent porosity in the component. Moreover, it allows fabrication of parts with low thicknesses, which is not possible to achieve with the standard/conventional HPDC processes. Such a technology introduces a new opportunity to enhance the castability of a component, which is impossible to achieve by traditional manufacturing methods [33, 35, 39, 40].

Based on slurry production technology, there are two kinds of semi-solid processes: “rheocasting” and “thixocasting”. In 1976, Flemings et al. [41] introduced rheocasting process as an alternative to other metal forming processes such as die casting and forging, which can be used to prepare high-quality parts. Rheocasting, the method which is used in the current research, involves the application of shearing force during solidification to produce a non-dendritic semi-solid slurry that can be transferred directly into a mold or die to give a final product [42].

Rheo-HPDC parts possess advantages such as low porosity, heat treatability and high performance [33, 39].

One of the newly developed methods of slurry preparation for Rheo-HPDC is RheoMetal™ process, also known as the rapid slurry formation (RSF) (Fig. 2.1) [43]. This process utilizes an enthalpy exchange material (EEM), a piece of metal, to convert the molten metal into the slurry. The EEM is cast onto a steel rod, then while stirring the rode is immersed into the melt. The melt is cooled down during the melting of the EEM, due to internal enthalpy exchange, and at the end, a homogeneous slurry is prepared. In RheoMetal™ process, no external heat exchange and subsequently no temperature control during the slurry formation are required [44-46]. This approach decreases the time for slurry formation.

The solid fraction in the slurry is controlled by the initial temperatures of the melt and the EEM and the EEM/melt ratio. The slurry requires 30-35% solid fraction to be pourable into the shot sleeve of HPDC machine [38].

Proper materials for Rheo-HPDC process are limited to those which have a good castability with HPDC process (considering mold filling limitations) and also a wide solidification interval and therefore a low sensitivity of the solid fraction to variations of temperature, which helps to stabilize the solid fraction [47].

Rheo-HPDC increases the inhomogeneity of the microstructure in the final component, in comparison to the conventional HPDC process [37].

Specifically for aluminum (-silicon) alloys, this phenomenon arises from the fact that the formation of primary α-Al phase during the slurry preparation, characterized with low solubility of alloying elements, increases the amount of these elements in the remnant liquid phase [48]. Therefore, the final semi-solid microstructure consists of the primary globular α-Al phase (α_1-Al) and the secondary higher alloyed α-Al phase (α_2-Al) together with the eutectic phase and some intermetallic particles [49].

In addition, during the filling process both separation of the solid and liquid phase in the gating system (longitudinal macrosegregation) and the tendency of solid particles to migrate to the core of the component (transverse macrosegregation) increase the microstructure inhomogeneity of the final component.

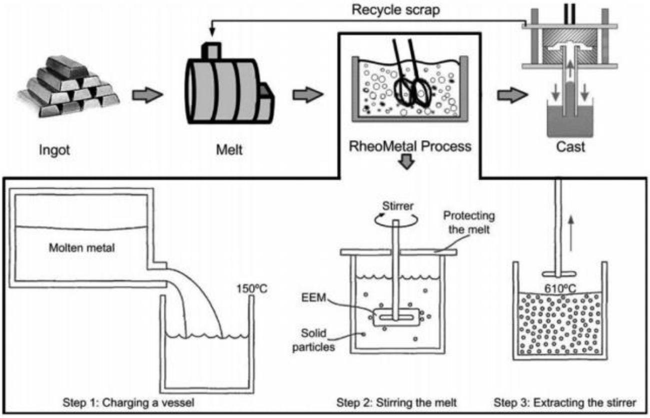

Fig. 2.1. Schematic illustration of RheoMetal^{TM} and Rheo-HPDC process [38].

This leads to variations of properties in different locations of the component either in microscopic or macroscopic scale [50-52].

The surface liquid segregated (SLS) layer observed in different SSM-HPDC aluminum alloys, mostly consisting of the eutectic phase in comparison to the bulk of the cast material, may have significantly different properties [53].

The furthest parts of the mold, particularly in thin geometries, will be filled mostly with liquid, while the solid fraction will concentrate in the core. This is due to the higher viscosity of the slurry compared to the liquid molten metal [54].

Due to the higher cooling rate and also the effect of stirring, semi-solid process slightly modifies the distribution and morphology of the β-AlFeSi IM particles. Therefore, semi-solid Al-Si alloys possess not only refined eutectic silicon but also smaller iron-rich IM particles.

2.2.2. Effect on the corrosion properties of Al-Si alloys

Studies on the corrosion behavior of semi-solid Al-Si alloys such as A356 and A357 include those performed by Yu et al. [55], Park et al.[56], Tahamtan et al. [57, 58], Masuku et al. [53], Qi et al. [25] and Arrabal et al. [4, 24]. These researchers have mostly emphasized on the localized corrosion inside the eutectic regions, at the interface of the eutectic silicon and iron-rich intermetallic particles with the α-Al phase.

Although both of the eutectic silicon phase and iron-rich IMs contribute in the localized corrosion, as mentioned before, some authors considered the contribution of IM particles to be more important [4, 25].

It is shown that the semi-solid casting process, such as thixoforming, can effectively change the morphology of the eutectic silicon in 357 alloy, resulting in an improved corrosion resistance [55]. The acicular eutectic silicon phase in the conventional cast 357 alloy has more contact area with the aluminum matrix in comparison to that of the globular eutectic silicon in the thixoformed alloy, which encourages the galvanic corrosion in the former alloy [55].

Rheocast process can increase the concentration of silicon in α-Al particles in A356 aluminum alloy. This leads to the smaller potential differences between this phase and the eutectic silicon phase or β-AlFeSi IM particles, which result in a higher resistance to pitting corrosion [4].

The effect of semi-solid process on the corrosion of aluminum alloys is still controversial. As for example Masuku et al. [53] indicated that the higher amount of eutectic phase on the surface as a result of surface liquid segregation in SSM-HPDC aluminum alloys can increase the pitting susceptibility.

2.3. Corrosion protection

General approaches to the corrosion protection of aluminum alloys include the deposition or growth of a manufactured oxide via electrochemical (anodizing) or chemical (conversion coating) means and the use of an organic coating (barrier and inhibitor combinations), normally including a primer and a top-coat. Beside corrosion protection, the oxide layers provide better adhesion for the organic exterior paints.

Anodic oxide layers possess a bilayered structure composed of a thin nonporous barrier layer under a thick porous layer, both formed from the anhydrous γ-Al_2O_3. These layers are electrochemically grown from the solutions of chromic, sulfuric, sulfuric-boric, sulfuric-tataric or phosphoric acid [18, 59].

Amongst the conversion coatings, chromate conversion coating (CrCC) provides outstanding corrosion resistance, excellent paint adhesion, ease of application and self-healing properties [60].

However, chromate (VI) is carcinogenic and ought to be eventually phased out. Replacements for CrCC include molybdate, permanganate, refractory metal oxyfluorides (mainly Ti/Zr, but also Hf, Nb and Ta), phosphates, silanes, sol–gels, self-assembling monolayers, conductive polymers, cobalt-based coatings, hydrotalcites and rare earth elements [18, 59-61].

The focus of this thesis is on one of the rare earth elements (cerium) and one of the conductive polymers (polypyrrole).

2.4. Cerium based conversion coatings

2.4.1. Research background

Conversion coatings are oxide-based coatings which have been utilized to replace the native oxide film on a metal surface such as aluminum, zinc, or magnesium to provide a higher corrosion resistance [62]. For many decades, CrCC has been used due to its extensive corrosion protection, especially for aluminum alloys. However, concerns and new restrictions on the environmental hazards of chromium compounds [63] have led to the intensive efforts to develop alternative pretreatments [59].

Anti-corrosion conversion coatings based on lanthanide salts have been studied as the environmentally friendly replacement for CrCC since the 1980s [64-66]. These coatings are both effective and non-toxic [66]. Studies like the one of Olivier et al. [67] have shown that cerium-based conversion coatings (CeCC) can be the most effective ones compared to the other lanthanide-based layers, such as yttrium and lanthanum. The deposition and corrosion properties of CeCC have been studied not only on aluminum alloys but also on other metals such as magnesium alloys [68-71] and steel [72-75]. Most of the researches on CeCC on aluminum alloys have been widely focused on the protection of the high strength alloys with aerospace applications such as AA2024 [76-95] and AA7075 [83, 96-103]. Other studies include those on AA5083 [75, 104-106], AA6061 [107-109], AA6063 [110, 111] and AA6082 [112]. Only a few works have been performed and published on Al-Si alloys such as those done by Pardo et al. [113, 114].

There are mainly three methods for applying CeCC including electrolytic deposition, spraying and immersion [60]. One of the challenges in the immersion method, which is the most frequently used method, is reducing the required immersion time. To speed up the process, researches have been mainly focused on the addition of hydrogen peroxide (H_2O_2) [78, 115-117] and/or chloride ions [91, 100, 117] and thermal activation [115]. Other process parameters including the concentration [118] and the type of cerium salt (nitrate or chloride) [106, 107, 112], the immersion time [106, 107, 111, 112], pH [106, 107, 112], oxidizing ability of the solution [67] and the temperature [106] have been investigated by different authors.

Pioneer studies on the corrosion inhibition effect of rare earth metal salts on aluminum alloys, such as AA7075, address the influence of cerium concentration and the immersion time on the thickness of conversion layer and the corrosion rate [119]. According to these preliminary results, addition of only 50 to 200 ppm cerium chloride to a sodium chloride solution of 0.1 M reduces the corrosion rate of AA7075 by a factor of 50. It was noted that a minimum cerium chloride concentration of 50 ppm is required to slow the corrosion process. A higher cerium concentration leads to a lower corrosion rate. In addition, longer immersion times result in the conversion layers with higher thicknesses containing a higher percentage of cerium oxide compared to the aluminum oxide [119]. It is worth mentioning that in this study the immersion time changed from 16 hours to 20 days. More recent studies on the other aluminum alloys such as AA2024 [120], AA6063 [111], AA5083 [106] and A361 [114] confirm the effect of increasing the immersion time and the cerium concentration on CeCC deposition. Hughes et al. [77] monitored the growth of the oxide layer on AA2024 during immersion in a cerium-based conversion solution. According to their study, the deposition of CeCC occurs in two different phases including an induction step and a ceria deposition step. The induction period includes activation of the surface, aluminum oxide growth and the deposition of cerium oxide on the IM particles. While the deposition phase includes the deposition of cerium oxide all over the surface, which increases linearly with the immersion time.

In some studies, the optimum amount for the cerium concentration [107] and/or the immersion time [114] was found. It was shown that a very high cerium concentration and/or a very long immersion time will result in cracked and spalled coatings which do not possess an improved corrosion resistance [111, 114, 120].

Many studies on the deposition of CeCC on different aluminum alloys benefit from the accelerating effect of addition of hydrogen peroxide (with the concentration from 0.02 to 1 M [100, 107, 120]), and/or sodium chloride (with the concentration from 0.05 to 0.3 M [87, 93]) to the conversion solution. In these studies, the concentration of cerium nitrate/chloride salt usually ranged from 0.005 to 0.1 M [67, 85, 109, 112, 120, 121] for different aluminum alloys. The immersion time differed from 12 to 24 hours for the non-accelerated deposition process [91, 93], while it was reduced to 2 minutes to 2 hours using an accelerated deposition process (in some cases the accelerated deposition process was performed at temperatures higher than 50 ºC) [106, 107, 109, 111, 114].

Pretreatment is another important factor, which significantly affects CeCC deposition, thickness, morphology, and corrosion protection. Especially alkaline and acid activation of the surface has been the subject of some studies [83, 101, 103, 122]. It is stated that CeCC layer will generally not deposit on an as-received surface. Physical abrasion, degreasing, alkaline and/or acid activations are the main proposed steps for the pretreatment [60]. Sodium hydroxide solution is one of the most frequently used solutions for the alkaline activation step [79, 83, 91, 92, 106]. This pretreatment has been shown to promote rapid CeCC deposition on AA7075 [101]. While for AA2024 an extra acid activation step, for instance in a sulfuric acid solution, is required for more rapid deposition [122]. In this alloy, the acid activation decreases the thickness of the oxide layer and the concentration of magnesium on the surface. It also increases the concentration of copper on the surface, likely due to the exposure of copper-rich IM particles. Exposure of more cathodic sites during the immersion increases the rate of coating deposition. For cast Al-Si alloys scientific support for the pretreatment procedure and its effect on CeCC deposition is almost unavailable.

2.4.2. Deposition and protection mechanism

Deposition and protection effect of CeCC is mainly due to the heterogeneous microstructure of aluminum alloys, especially with different IM particles. The potential difference between different microstructure components and the aluminum matrix introduces micro galvanic cells in which the aluminum matrix is often the anode and the IM particle is the cathode. Reduction of oxygen on the cathodic sites (e.g. IM particles) leads to the localized increment of pH, which results in cerium hydroxide/oxide deposition:

$$Al \rightarrow Al^{3+}+3e^- \qquad \text{Eq. 2.1}$$

$$O_2+2H_2O+2e^- \rightarrow H_2O_2+2OH^- \qquad \text{Eq. 2.2}$$

$$O_2+2H_2O+4e^- \rightarrow 4OH^- \qquad \text{Eq. 2.3}$$

$$2Ce^{3+}+6OH^- \rightarrow 2Ce(OH)_3 \rightarrow Ce_2O_3+3H_2O \qquad \text{Eq. 2.4}$$

$$2Ce^{3+}+H_2O_2+2OH^- \rightarrow 2Ce(OH)_2^{2+} \qquad \text{Eq. 2.5}$$

$$4Ce^{3+}+O_2+4OH^-+2H_2O \rightarrow 4Ce(OH)_2^{2+} \qquad \text{Eq. 2.6}$$

$$Ce(OH)_2^{2+}+2OH^- \rightarrow Ce(OH)_4 \rightarrow CeO_2+2H_2O \qquad \text{Eq. 2.7}$$

Therefore a physical barrier consisting of cerium compounds deposits on the IM particles increasing the resistance of aluminum alloy to the localized corrosion [85, 91]. These islands will grow further to cover the entire surface. This mechanism is known as the island growth [65, 123]. However, obviously, and to our favor, a higher deposition occurs on the cathodic sites

[91], which is attributed to the higher pH over these particles, due to oxygen reduction [124]. The pH drops off away from the IM particles, partly also due to the acidic pH due to the hydrolysis of dissolved aluminum ions [121, 125].

$$pAl^{3+}+qH_2O\rightarrow[Al_p(OH)_q]^{(3p-q)+}+qH^+ \qquad \text{Eq. 2.8}$$

Studies have shown the effect of different types of IM particles and the heterogeneous microstructure, especially in AA2024, on the deposition mechanism of cerium conversion layers. Many of IMs are cathodic with respect to the aluminum matrix (e.g. AlFeMnCu). However anodic particles such as Al_2CuMg (S-phase) also participate in the deposition mechanism by dealloying. Since after dealloying (selective dissolution of magnesium and aluminum) these IMs become nobler compared to the aluminum matrix and act as cathodic sites [85, 93]. Paussa et al. [93] elaborated this model to state that only a small dissolution of magnesium and intense hydrogen evolution, which happens locally and very close to the IM particle can increase the pH high enough for cerium hydroxide/oxide precipitation. Therefore, the precipitation of cerium compounds on the anodic IM particles can happen even before they become cathodic to the aluminum matrix.

Lau et al. [85] focused on the role of copper dissolution from S-phase during the deposition of the conversion coating. According to their model, further cathodic reduction of copper ions on the matrix results in the formation of copper islands which promote more dissolution of the surrounding aluminum matrix leading to areas of major oxide growth. In this case, the composition of cerium-based layer differs from CeO_2 on the more active IMs to $Ce(O_2)(OH)_2$ over the aluminum matrix [85].

As was mentioned before, studies on the formation and characterization of CeCC on cast Al-Si alloys are rare.

2.5. Conductive polymers

2.5.1. Polypyrrole

Conductive polymers including polythiophene, polyaniline and polypyrrole are able to conduct electricity thanks to the existence of conjugated bonds. As the carbon atoms are sp^2p_z hybridized and overlap along the polymer chain, they induce electron delocalization in the chain resulting in a polymer with conductive or semi-conductive nature [126].
These polymers have numerous electrochemical applications such as batteries, supercapacitors, electrochromic devices, fuel cells, light emitting cells, to name a few. Among other conductive polymers, polypyrrole has been the subject of many studies due to its ease of preparation, high electrical conductivity and good redox properties [127]. In fact, in a certain potential range (the so-called stability window), polypyrrole redox properties are reversible. Therefore, it can be cycled repeatedly without any degradation [128].
Polypyrrole is a conductive polymer based on the monomer with the formula of C_4H_4NH. It can be electrochemically polymerized on a conductive electrode immersing in a solution of the monomer. The electrode needs to be anodically polarized. The dispersed monomers lose an electron to the electrode, making radical cations. Dimerization of these radical cations leads to the formation of a polypyrrole film (Fig. 2.2) [128-130].
During the oxidation of conductive polymers, electrons are removed from the valence band and charges are generated in the conductive band. These resulting positive charges will be compensated with the counter-anions (p-type doping). On the other hand, the reduction of conductive polymers injects electrons into the conductive band. The resulting negative charges will be neutralized with the doped cations (n-type doping). Subsequently, the extent of oxidation/reduction in the polymer chain changes its conductivity [130, 131].

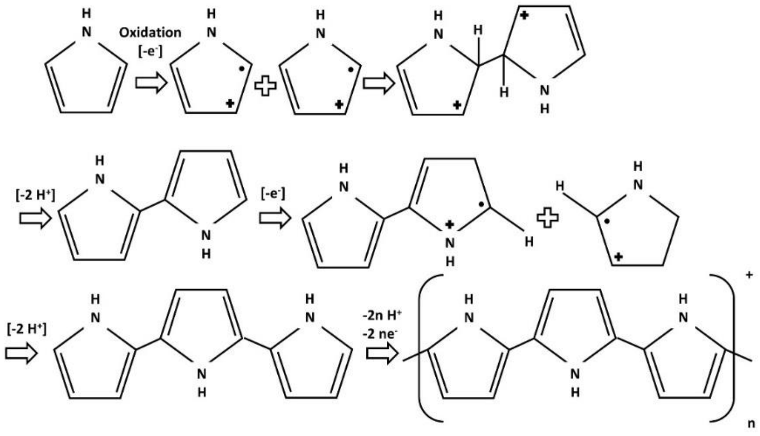

Fig. 2.2 Electropolymerization of polypyrrole.

2.5.2. *Application in corrosion protection*

Application of organic coatings for corrosion protection of various metals is mainly based on their barrier properties. Nevertheless, any prolonged exposure to the corrosive environments can lead to failure [132, 133].

Conductive polymers introduce a new category of organic coatings, that can maintain the surface potential noble and protect it from corrosion even when the corrosive species have reached the surface [134]. In fact, the barrier properties of conductive polymer coatings are not the best [134] and their redox activity leads to anion exchange with the electrolyte [135].

However, their galvanic interaction with the substrate results in the "passivation protection mechanism". According to this mechanism a conductive polymer, which is applied on the metal surface in its oxidized state, can undergo the redox reaction and act as an oxidizer, producing a protective oxide layer at the polymer/metal interface [133, 136]. As it was mentioned before, the passivation protection mechanism is influenced by the galvanic interaction between the substrate and the conductive polymer, which, in its turn, is affected by the quality of the coating and its electrical contact and interface with the substrate [137].

An alternative protection mechanism includes the role of conductive polymer in shifting the oxygen reduction site from the metal/polymer interface to the polymer/electrolyte interface. This will reduce the concentration of aggressive radicals formed during oxygen reduction at the metal/polymer interface, preventing or slowing down the coating detachment [133, 136, 138].

David W. DeBerry suggested the application of conductive polymers for corrosion protection for the first time in 1985 [139]. He deposited polyaniline coating on stainless steel and showed its ability to keep the substrate passivated in acidic solutions. Since then conductive polymers, especially polypyrrole and polyaniline, have been repeatedly used for corrosion protection purposes on aluminum alloys [135, 137, 138, 140-150] and steel [151-156].

Studies on the electrodeposition of polypyrrole on aluminum alloys include those on AA2024 [135, 138, 142, 145-147, 157, 158], AA6061 [143], AA6082 [146, 147] and AA7075 [159, 160]. Among these papers, few have discussed the effect of microstructural and compositional features of the substrate on the electrodeposition and the electrochemical properties of polypyrrole [135, 142, 143, 146]. As, apparently, the chemistry of the solution and the electropolymerization conditions are more effective variables [145, 158].

As an example, the catalytic effect of copper in AA2024 on the electrodeposition of polypyrrole is elaborated in the papers by Volpi et al. [135] and Rizzi et al. [146] and also briefly mentioned in the research performed by Arenas et al. [142]. In ref. [146], the effect of copper has been attributed to its migration from the alloy and then its interaction with the pyrrole ring through oxalate dopant ions (due to the application of oxalic acid in the solution). It is further shown that the presence of copper oxo-complexes in the polypyrrole film has a positive influence on its protection efficiency for the AA2024 substrate. This clearly connects the effect of compositional features to those of the solution chemistry.

Arenas et al. [142] have considered the influence of alloying elements, including copper, on the modification of aluminum oxide layer, which creates conductive pathways for the electrodeposition of polypyrrole.

Similarly, it has been shown that the presence of IM precipitates such as $Mg_3Si_6Al_8$ or Mg_2Si in AA6061 has a positive effect on promoting the electrodeposition of polypyrrole film. As they facilitate the electrical connection between the metal and the electrolyte [143].

The available researches show the potential of polypyrrole coating (without doped inhibitors) to protect aluminum alloys from corrosion [142, 143, 148]. However, the effective corrosion protection mechanism and the possible protection in chloride containing environment are still unclear and controversial. Some papers have cast doubt on the passivation mechanism in the presence of large defects [133, 144, 161]. Moreover, the galvanic interaction at the conductive polymer/metal interface has been considered as a serious obstacle in achieving the protection [162].

Electrochemical polymerization of polypyrrole provides the possibility to coat various metals. This process is advantageous in controlling the film thickness and its properties [128]. It also offers ways to improve the protection effect [128]. This includes controlling and altering the doped anions [145, 158, 163-171], the film conductivity and its thickness [128, 130] and the addition of desired fillers such as titania and graphene oxide [160, 172].

While doping voluminous anions into the polypyrrole film is one way to increase its ion-barrier properties, some researchers have introduced corrosion inhibitor anions to increase the protection influence. It is shown that large anion such as benzene sulfonate, dodecyl sulfate and p-toluene sulfonate will be trapped inside the polymer matrix and will not be interchanged with the aggressive anions such as chloride [164, 165, 171].

Whereas doped anions with corrosion inhibiting properties, such as molybdate and 8-hydroxyquinoline, get released during the reduction of the conductive polymer coating, migrate to the corroding defect and stabilize the passive film [163, 168-170].

Besides the advantages of the electrochemical polymerization, direct electrodeposition of a conductive polymer on some metals such as aluminum and magnesium is challenging. Since the concomitant anodic dissolution/oxidation of the substrate during the electrodeposition process hinders the formation of a homogenous coating. In the case of aluminum (alloys), the oxide layer insulates the charge transfer between the electrode and the electrolyte [173]. Therefore, care should be taken in selecting the supporting electrolyte and the electrodeposition conditions (applied voltage or current). The applied potential (or current) needs to be high enough to oxidize the monomer but low enough not to lead to the corrosion of electrode [173, 174].

In this case, application of electron transfer mediators such as 4,5-dihydroxy-1,3-benzenedisulfonic acid disodium salt (DHBDS, commercially known as Tiron) has been found helpful in reducing the required potential [173]. DHBDS can be doped into the polymer as well [157]. The applied conditions in the electrochemical process should not lead to the overoxidation of polypyrrole film which destroys its redox properties and its protective effect [141, 143].

The presence of some anions with passivating effect such as nitrate and molybdate has been shown to be beneficial in lessening the dissolution of the aluminum electrode during the anodic deposition [141, 175]. It is interesting to mention that doped anions, NO_3^- specifically, can alter the thickness and the morphology of polypyrrole coatings as well [145, 158, 176].

Chapter 3 Short review on the characterization techniques

This chapter describes the principles of main characterization techniques utilized in this thesis. However, at the beginning of chapters 4-6, separate “materials and methods” sections describe the detailed experimental procedures for each part.

3.1. Electrochemical measurements

3.1.1. Polarization measurements

Polarization measurement refers to the test where the potential of free corroding metal, open circuit potential (OCP), is changed in positive (anodic polarization) or negative (cathodic polarization) directions versus the OCP and the resulting current is measured.

In the current work, the polarization measurements were performed far away from the corrosion potential (>100 mV). This test provides information including the pitting, passivation and repassivation potentials [177].

The cell used for electrochemical measurements is schematically shown in Fig. 3.1. It includes the sample with an exposed area of 1 cm^2 as the working electrode, a standard Ag/AgCl (3 M KCl) (0.210 V vs NHE) reference electrode and a platinum counter electrode.

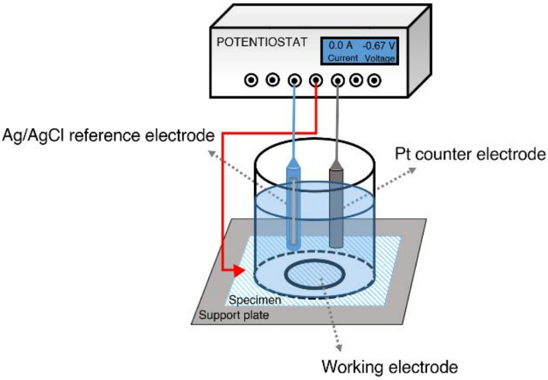

Fig. 3.1. The electrochemical cell for corrosion tests.

3.1.2. *Electrochemical impedance spectroscopy*

Electrochemical impedance spectroscopy (EIS) has been widely used in the current research to investigate the electrochemical behavior of coated and bare aluminum (alloy) samples immersed in different solutions as a matter of time.

Applying an electrical perturbation (e.g. potential) to an electrical circuit results in a response. EIS utilizes this principle to study various electrochemical systems. In this case, the perturbation imposed on the system is so low that the response is linear. A monochromatic signal ($v(t)=V_m \sin(\omega t)$) is applied to the electrochemical cell resulting in a steady state current ($i(t) = I_m \sin(\omega t+\theta)$). Theta ($\theta$) is the phase difference between the voltage and the current and it is zero for a purely resistive behavior.

The EIS spectra are presented as Bode or Nyquist plots. Bode plot represents the magnitude of impedance $|Z|$ ($z(\omega)= |Z| \exp(j\omega\theta)$) and the phase angle versus frequency. While Nyquist plot depicts the imaginary part of the impedance versus its real part ($|Z|^2=Z_{real}^2+Z_{img}^2$).

Impedance spectra provide information about the material itself such as conductivity, dielectric constant, the mobility of charges, etc. and about the material/electrolyte interface and the electrochemical reactions occurring there. This includes adsorption–reaction rate constants, the capacitance of the interface region, etc. Application of the equivalent electrical circuits and assigning physical models are required to consider these contributions to the EIS spectra [177-179].

For the EIS measurements, the same electrochemical cell (Fig. 3.1) was employed. The EIS responses were fitted using ZSimp Win 3.50 software.

3.1.3. Cyclic voltammetry

Cyclic voltammetry (CV) is a dynamic electrochemical test, where the potential of a sample is changed in a certain range (versus the reference electrode) with a constant rate and for a certain number of scans. In the current thesis, this method was used for the electropolymerization of polypyrrole coatings and later on for investigation of their redox properties. The electrochemical cell is presented in Fig. 3.2. In this cell, the sample to be coated is the working electrode and a graphite electrode is used as the counter electrode. A standard Ag/AgCl (3 M KCl) electrode is used as the reference electrode.

The 100 ml cell was placed on top of a magnetic stirrer that was set on 300 rpm (using a magnetic round bar of 20 mm length and 6 mm diameter).

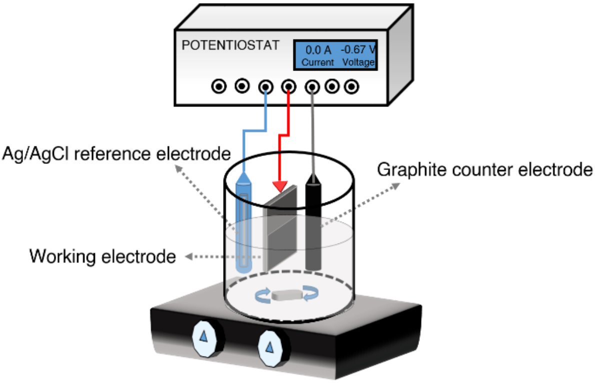

Fig. 3.2. The electrochemical cell for the electropolymerization process.

All the electrochemical measurements in this thesis were performed using a computer-controlled potentiostat (Metrohm Autolab PGSTAT302N).

3.2. Microscopy and spectroscopy techniques

3.2.1. Scanning electron microscopy

In this work, scanning electron microscopy (SEM (JSM-IT300)) has been widely used for the morphological and chemical examinations.

A focused beam of electrons produced by an electron gun (in the vacuum) is used in this technique. The interactions of electrons and atoms inside the specimen result in various signals which can be utilized for imaging and chemical analysis. Fig. 3.3 schematically depicts three subsequent signals resulting from these interactions.

Secondary electrons are the loosely bound electrons which emit from the surface when the primary beam strikes the sample. These electrons possess average energy of 3-5 eV and they come from a few nanometers beneath the surface providing topographic information.

The elastic interaction of the specimen atomic nucleus and the electrons bounces them back with 60–80% of their initial energy. These so-called backscattered electrons provide compositional contrast. As the elements with higher atomic numbers and therefore more positive charges on their nucleus bounce more electrons back appearing relatively lighter in the images.

When the primary beam displaces an inner shell electron, an outer shell electron may fall into the inner shell to return the atom from the ionized to the ground state. This incident occurs with the emission of an X-ray photon, which can be used for the chemical analysis which is called energy-dispersive X-ray spectroscopy (EDXS) [180].

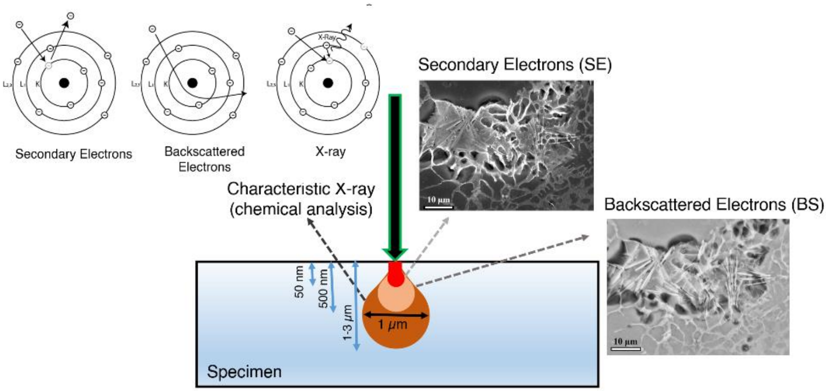

Fig. 3.3. Schematic interaction of an electron beam with a specimen (the SEM images are related to this work).

3.2.2. *Focused ion beam assisted SEM*

An SEM equipped with a Gallium ion (Ga^+) gun is called focused ion beam assisted SEM (FIB-SEM (LYRA3)). The sputtering action of Ga^+ ions can be used for precise micro-machining of the samples. In this thesis, this technique has been used to make microscopic cross-sections on the samples. Fig. 3.4 provides a schematic overview of FIB-SEM.

In the current work, this method has been used in studying the deposition mechanism of CeCCs and the protection mechanism of polypyrrole coatings.

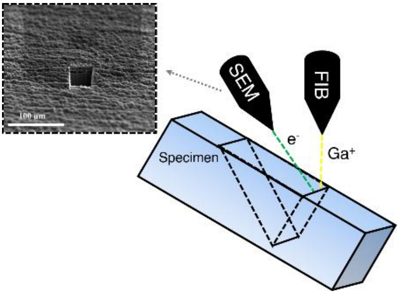

Fig. 3.4. Schematic illustration of FIB-SEM (the SEM image is related to this work).

3.2.3. *X-ray photoelectron spectroscopy*

The information regarding the chemical composition of coating surfaces (CeCC and polypyrrole) and their interfaces with the substrates is collected by X-ray photoelectron spectroscopy (XPS).

In this technique, the sample is irradiated by an X-ray (with hν energy) which ejects electrons from a core level (Fig. 3.5). The kinetic energy (E_k) and the number of electrons that emit from 0-10 nm depth of the surface are measured by the instrument. The binding energy of these electrons is calculated as follows:

$$E_B = h\nu - E_k - K \qquad \text{Eq. 3.1}$$

While K is the work function dependent on both the spectrometer and the material [181].

In this thesis, XPS has been used for the examination of cerium oxidation state in CeCCs, the composition of polypyrrole coatings and the state of their interface with the substrate. The analysis was carried out using an Axis DLD Ultra instrument.

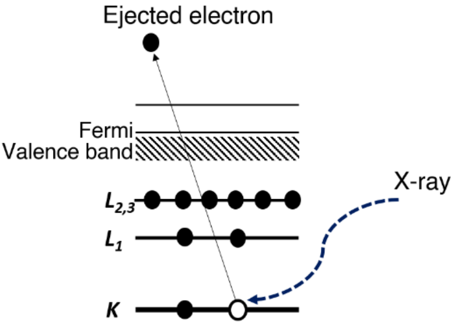

Fig. 3.5. Schematic illustration of XPS process.

Chapter 4 Microstructural and corrosion studies

This chapter presents and compares microstructural features and corrosion properties of the conventional HPDC and Rheo-HPDC Al-Si alloys in different solutions.
The results presented in this chapter have partially published, presented and are under submission in papers III, VII and XII, respectively.

4.1. Materials and methods

4.1.1. Sample preparation and microstructural studies

Cast samples were produced using a 400-ton HPDC machine equipped with an automated RheoMetal™ slurry generator. The RheoMetal™ utilized an EEM as an internal cooling agent to generate the slurry [182]. An experimental cavity filter (Fig. 4.1), demonstrator for telecom applications, was cast using both the conventional HPDC and Rheo-HPDC processes.

Measured compositions of the alloys are presented in Table. 4.1. The composition measurement was performed using optical emission spectrometry (OES) method.

The alloys cast by the conventional HPDC process are referred by the letter "L" and the alloys cast by Rheo-HPDC process are labeled by the letter "R" in their names.

The most important criterion in designing these alloys was to reduce the alloying elements without significantly compromising the castability and the mechanical properties. The alloys' composition was adjusted by adding pure silicon to a primary alloy in a resistance furnace.

In the casting process, the temperature of the fixed half of the die was set to 230-250 °C and the temperature of the moving half was set to 280-320 °C. The shot weight was approximately 5 kg and the holding furnace temperature was set at 675 °C. Ladling was done with a standard cast iron ladle to which the EEM was added (5-6 % of the shot weight) under stirring (900 rpm) to generate a slurry with a solid fraction of around 40 %. The final slurry temperature was 610 ± 1 °C. The die cavity fill-time was 31 ms with the first stage and the second stage piston speed set at 0.23 and 5.2 m/s, respectively. These conditions were similar to the standard settings for this type of component cast by the normal HPDC process.

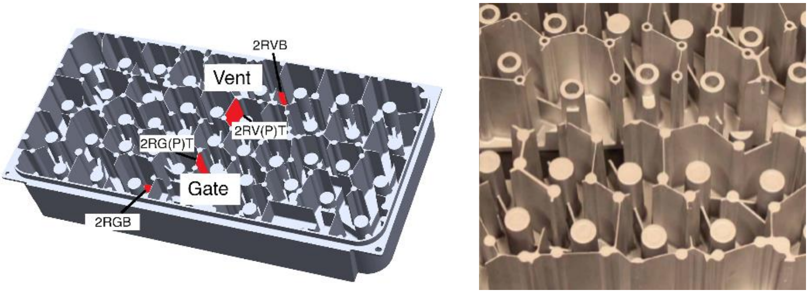

Fig. 4.1. The experimental cavity filter used for (Rheo)-HPDC process.

Table. 4.1. The measured composition (wt. %) of alloys

Name	Si	Fe	Cu	Mn	Mg	Zn	Al
Alloy 2R (L)	2.41	0.462	0.131	0.019	0.58	0.038	96.338
Alloy 4R (L)	4.50	0.481	0.137	0.019	0.58	0.035	94.223

*L: HPDC, R: Rheo-HPDC

For the microstructural studies, samples were taken from the thin walls (thickness ≈ 1.5 mm) or from the thick bottom plate (thickness ≈ 4 mm), underneath the component (Fig. 4.1).

To investigate the longitudinal segregation, both thin wall and thick bottom plate samples were taken from different locations: near the feeding gate (G) or near the die vent (V). The detailed designation symbols for different samples are presented in Table. 4.2 and shown in Fig. 4.1.

Table. 4.2. Designation of samples for the microstructural studies

	Section	Near the gate	Near the vent
Alloy 2R (L)	Thin wall	2R(L)GT	2R(L)VT
	Plate bulk	2R(L)GB	2R(L)VB
Alloy 4R (L)	Thin wall	4R(L)GT	4R(L)VT
	Plate bulk	4R(L)GB	4R(L)VB

* L: HPDC, R: Rheo-HPDC, G: Samples from near the gate, V: Samples from near the vent, T: Samples from thin walls, B: Samples from the thick bottom plate.

For the metallographic analyses, samples were wet ground through a successive grinding using silicon carbide abrasive papers from P600 to P4000, followed by the polishing using two diamond pastes (3 and 1 μm).
10 wt.% NaOH solution was used to clean the surface and to reveal the constituents of the microstructure. The microstructure of the surfaces and the bulk of components were studied using light optical microscope (LOM) and SEM. Energy/wave-dispersive X-ray spectroscopy (EDXS/WDS) was used to measure the composition of different phases.

4.1.2. Corrosion and electrochemical studies

4.1.2.1. Corrosion testing in the diluted Harrison solution

The aim of this section is to investigate the effect of segregation and surface condition on the corrosion resistance of Rheo-HPDC Al-Si alloys. Samples for corrosion testing were taken from the thin walls, in as-cast or ground condition, or from the thick bottom plate only in ground condition.
To investigate the longitudinal segregation, both kinds of samples were taken from different locations, as described in Table. 4.2.
To study the corrosion properties of alloys, the electrochemical measurements, including potentiodynamic polarization and EIS were performed. Due to the working environment of telecom components, the diluted Harrison solution (0.5 g/l NaCl and 3.5 g/l $(NH_4)_2SO_4$) was used to simulate the electrochemical behavior of alloys exposed to acid rain [183, 184].

Regarding the polarization test, for each sample, mainly the anodic branch was collected (as the cathodic branch did not exhibit any significant information). In order to highlight the effect of chloride ions, all the polarization experiments were also repeated using a solution of 3.5 g/l $(NH_4)_2SO_4$.

EIS measurements were conducted for the immersion time of 24 hours at the room temperature. In the EIS measurements, frequency range was 100 kHz to 10 mHz and the amplitude of the sinusoidal potential signal was 10 mV.

EIS measurements were conducted on as-cast and ground surfaces of the thin wall samples and also on ground surface of the thick bottom plate samples to investigate the effect of transverse macrosegregation and as-cast condition.

To distinguish the results of these different experiments, the letter “P” is added to the name of the thin wall samples, which were ground before the electrochemical test. These samples were wet ground by silicon carbide abrasive papers from P600 to P4000 to the extent that the skin layer was completely removed. In the case of bulk samples (of the thick bottom plate), the surfaces were ground until the middle of each sample was reached. In this way, the electrochemical behavior of the bulk of each alloy can be investigated. Repeatability of the results was tested by conducting each experiment on at least three specimens. After the corrosion tests, the corroded surfaces were examined using SEM/EDXS to study the morphology and composition of the corrosion products.

4.1.2.2. Corrosion testing in sodium chloride solutions

Enlightened by our studies in the sections 4.1.1 and 4.1.2.1, samples were selected based on not only the casting technology but also the thickness. The position of samples in the cavity is random. The details regarding the designation of samples are presented in Table. 4.3.

Each sample was cut from the main component (Fig. 4.1) and embedded in epoxy resin. Wet grinding was done using SiC abrasive papers of P600, P1200 and P4000, respectively. The polishing step included using diamond pastes of 3 and 1 μm.

The electrical connection to each sample was provided by attaching a copper wire to the sample using silver epoxy resin before embedding it inside the epoxy resin.

Table. 4.3. Designation of samples for the corrosion testing in NaCl solutions

Name of the sample	Casting technology	Thickness
2RB	Rheo-HPDC	≈ 4 mm
4RB	Rheo-HPDC	≈ 4 mm
4RT	Rheo-HPDC	≈ 1.5 mm
4LT	HPDC	≈ 1.5 mm

* L: HPDC, R: Rheo-HPDC, T: Samples from thin walls, B: Samples from the thick bottom plate. Samples positions are random.

The corrosion behavior of different samples was investigated and compared by means of EIS and potentiodynamic polarization test. The EIS tests were performed in sodium chloride solutions with different concentrations (0.01, 0.05, 0.1 and 0.6 M). The polarization tests were performed in 0.6 M NaCl solution. The details of both of the corrosion tests are similar to those described in section 4.1.2.1.

4.2. Results and discussion

4.2.1. Microstructural features

Generally, the microstructure of rheocast low silicon content aluminum alloys exhibits the presence of α-Al phase (primary and secondary) together with Al-Si eutectic phase and some intermetallic particles [185]. Based on the presence of iron in the composition of the two rheocast alloys (Table. 4.1), and since the solid solubility of iron in aluminum is very low [186], the presence of iron-rich intermetallic particles is expected. According to the composition of the initial melt, the sequence of phase formation (aluminum phase and the eutectic reaction) was calculated using ThermoCalc™ software [187, 188]. The results are shown in Fig. 4.2. As it is predicted by the thermodynamic model, the needle shape β-AlFeSi IM particle was the most favored intermetallic phase for precipitation in the two alloys and it is formed before the eutectic silicon phase.

The microstructural features of the polished surfaces of thin wall samples from different positions in the cavity, with different percentage of silicon, are illustrated in LOM images in Fig. 4.3. As it is expected, the usual dendritic structure is absent in the semi-solid materials [41, 189, 190].

From the images in Fig. 4.3, two different sizes of α-Al phase can be observed in all the samples: a coarse globular α-Al phase (α_1-Al) and a finer α-Al phase (α_2-Al). The formation of α_1 and α_2-Al particles is related to the two-step solidification in the semi-solid metal process. α_1-Al particles are nucleated during the slurry preparation outside the mold, at a higher temperature, while α_2-Al particles are formed during the secondary solidification stage inside the cavity, at a higher cooling rate and in the absence of shear force [49].

Regarding the effect of the position, the microstructure near the gate (Fig. 4.3 (a) and (c)) consists of a higher amount of α_1-Al particles in comparison to the sample taken from the region near to the vent (Fig. 4.3 (b) and (d)). However, this difference is less significant in the alloy 2R.

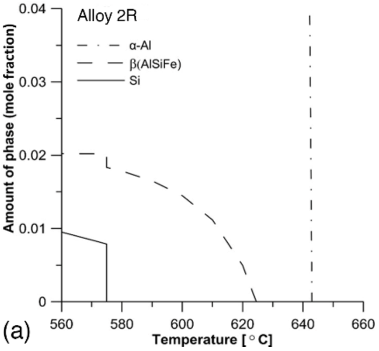

Fig. 4.2. Sequence of formation of different phases in the alloy (a) 2R and (b) 4R.

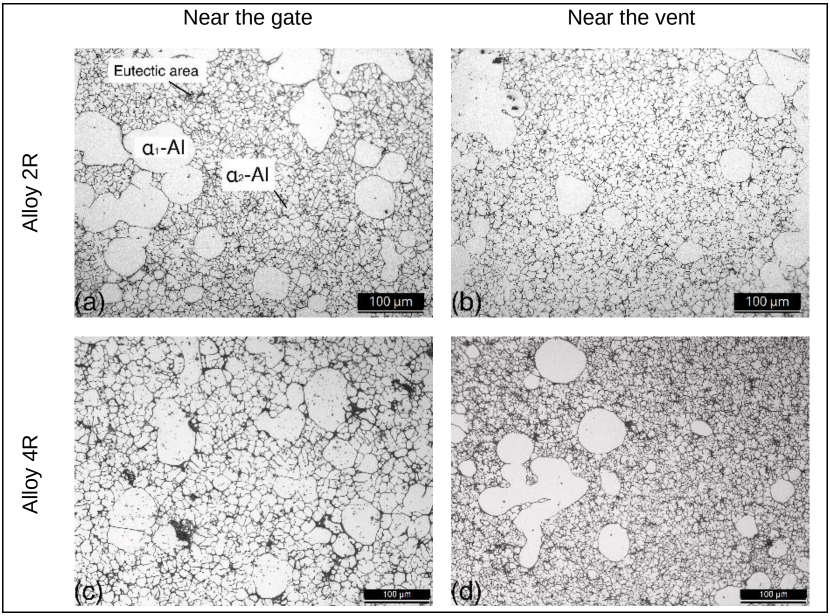

Fig. 4.3. LOM image of the sample (a) 2RGT, (b) 2RVT, (c) 4RGT and (d) 4RVT.

This inhomogeneity of the microstructure is attributed to the separation of liquid and solid portions of the slurry during the injection stage when the solute-enriched liquid portion of slurry squeezes out and leaves the solid part behind. During the later stages of injection, the portion of slurry that contains a larger fraction of α_1-Al particles together with some entrapped melt is pushed into the near-to-gate region. Easton et al. [191] showed this type of separation of the liquid and the solid portions of slurry in a SSM-HPDC component and explained it by a so-called “sponge effect”.

α_2-Al particles in the thin wall samples (of both alloys) are finer in the region near the vent in comparison to the region near the gate, due to the higher undercooling. This effect is more evident for the alloy 4R. It seems that by increasing the amount of silicon, the aluminum phase is refined, which can be due to more nucleation of the eutectic silicon [192].

LOM images of the samples 2RGB and 4RGB from the thick plate are presented in Fig. 4.4. In comparison to the microstructure of thin wall samples, the bulk microstructure contains more α_1-Al particles in both of the alloys, which is expected. In fact, due to the high viscosity of the semi-solid slurry, the thin walls are mostly filled by the liquid, while the relatively thicker parts are filled by the solid fraction of the slurry [54].

The cross-sectional LOM image of a thick plate sample of the alloy 2R in the region near the gate is reported in Fig. 4.5. According to this image, on the surface, segregation exists between the liquid phase and α_1-Al particles, which tend to aggregate in the center of the sample. This phenomenon is considered as the transverse macrosegregation. Three different phenomena lead to the transverse macrosegregation including the skin effect [50], migration of solid particle to the center [51] and shearing band in the form of porosity or positive macrosegregation (eutectic-rich band) [193].

Study of the transverse macrosegregation in different positions of the same Rheo-HPDC component performed by Payandeh et al. [194] showed that the thickness of the skin layer increases by increasing the liquid portion. Therefore, it is obvious that the thickness of this layer is larger for the samples taken from the region near the vent.

Govender et al. [195] also reported the existence of a surface layer consisting of mainly liquid or eutectic phase in SSM-HPDC A356 alloy.

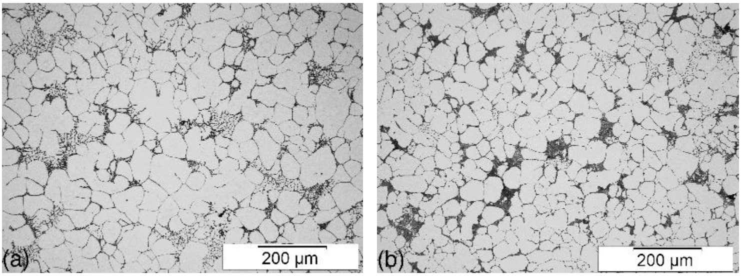

Fig. 4.4. LOM image of the sample (a) 2RGB and (b) 4RGB.

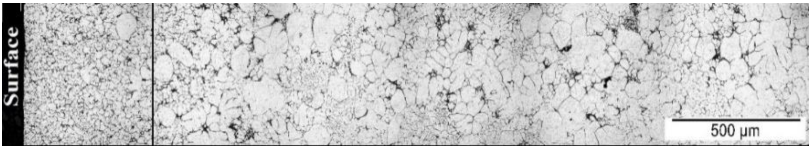

Fig. 4.5. Cross-sectional LOM image of the sample 2RGB.

Fig. 4.6 compares the SEM micrographs of as-cast and polished surfaces of the sample 2RGT. It is noticeable how the as-cast surface is enriched with the eutectic phase and IM particles. Moreover, localized defects such as porosities/voids among the grains and inclusions are visible.

SEM image of the sample 4RGT at higher magnification in Fig. 4.7 (a) depicts the microstructure of the eutectic phase and iron-rich IM particles. The eutectic silicon phase has a polygonal flake shape forming a continuous branched network [196]. This figure also shows that the location of the IM particles is inside the eutectic region.

According to the EDXS results in Fig. 4.7 (b), IM particles are rich in iron and as it is expected in hypoeutectic alloys the intermetallic particles are β-AlFeSi. These IM particles usually have a needle shape [4], and platelet morphology in 3D tomographic volume [24].

Fig. 4.8 represents the concentration of silicon at the center of α_1 and α_2-Al grains in the alloys 2R and 4R. α_2-Al particles, nucleated from the liquid portion of the slurry [197], have a higher amount of silicon which, according to the literature, leads to a smaller potential difference between them and the silicon eutectic phase/iron-rich IM particles and results in less severe corrosion [4].

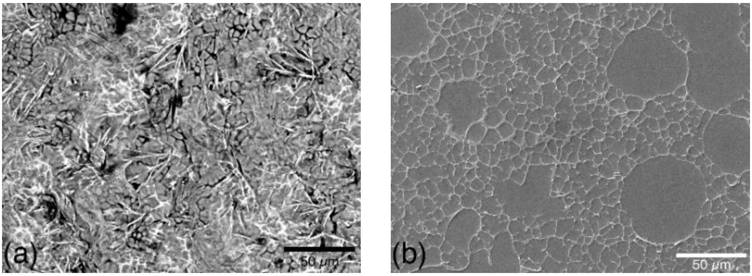

Fig. 4.6. SEM image of the sample 2RGT in (a) as-cast and (b) polished condition.

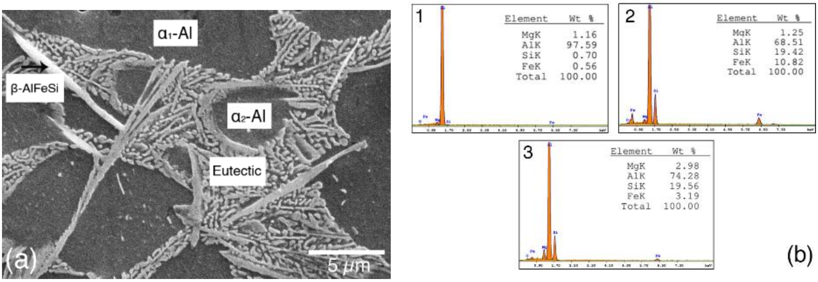

Fig. 4.7. SEM image (a) and spot EDS analysis (b) of polished surface of the sample 4RGT.

The microstructure of HPDC materials partially reveals a conventional dendritic structure (Fig. 4.9). In this case, heat transfer from the superheat melt to the metallic ladle or to the cold shot sleeve could start the solidification before the injection, leading to the formation of coarse dendrites or the so-called “externally solidified crystals (ESCs)” [51, 198].

In case of the alloy 2L (Fig. 4.9 (a) and (b)), the microstructure near the vent is finer compared to the microstructure near the gate.

As it was mentioned before, this can be due to the higher cooling rate in this region.

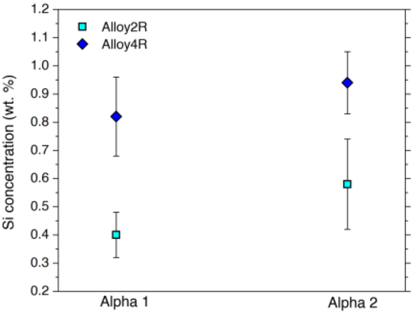

Fig. 4.8. Concentration of Si in α1 and α2-Al phases in the alloys 2R and 4R.

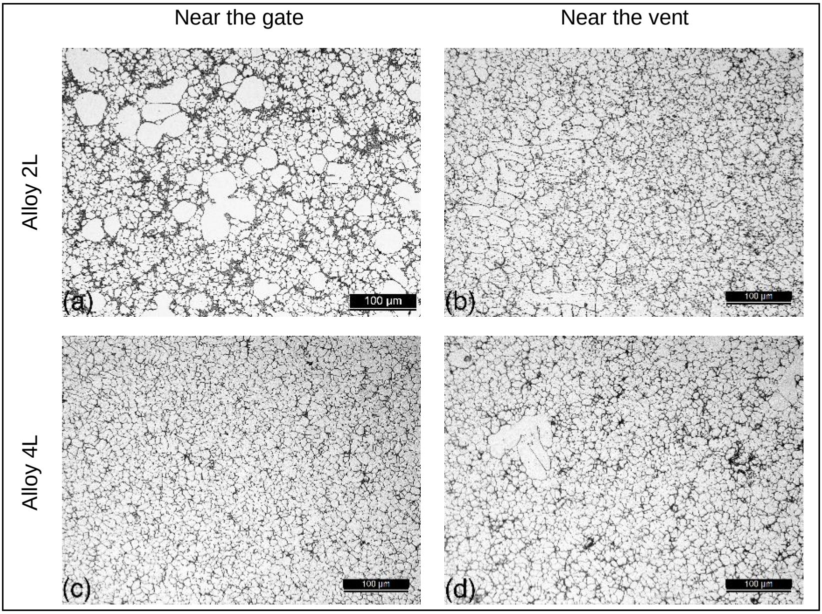

Fig. 4.9. LOM image of the sample (a) 2LGT, (b) 2LVT, (c) 4LGT and (d) 4LVT.

In general, the position does not seem to have a significant influence on the microstructure of the HPDC materials.

Concerning the effect of silicon content, regardless of the position (and the casting technology), a higher silicon content leads to the presence of more eutectic and a finer aluminum phase.

For the HPDC samples, the higher thickness of the bottom plate leads to a lower cooling rate [199] which causes coarser microstructure compared to the microstructure of thin wall samples (Fig. 4.10).

Fig. 4.11 compares SEM images of the samples 2LGT and 4LGT. Distribution of IM particles and the eutectic silicon phase seems to be similar in both conventional and Rheo-HPDC materials.

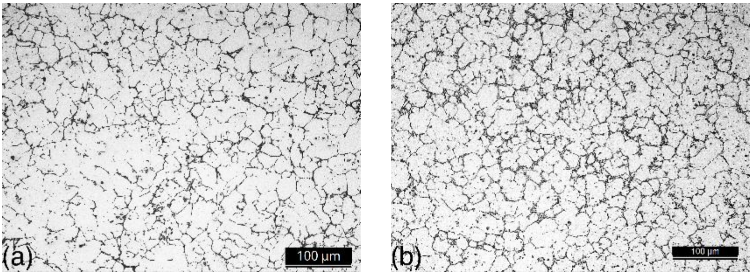

Fig. 4.10. LOM image of the sample (a) 2LGB and (b) 4LGB.

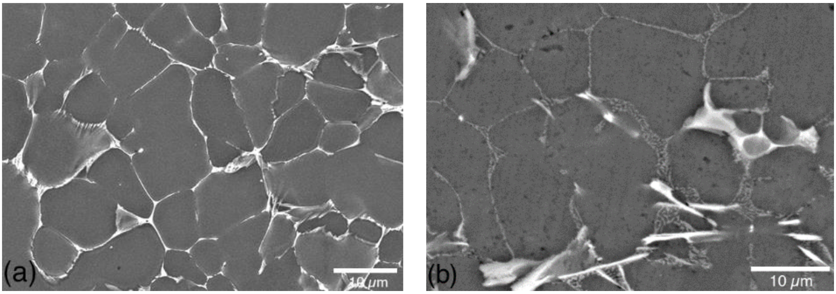

Fig. 4.11. SEM-BS image of the sample (a) 2LGT and (b) 4LGT.

4.2.2. Effect of segregation and surface condition (in Rheo-HPDC alloys)

Potentiodynamic polarization curves related to as-cast surfaces of the thin wall samples (2RGT, 2RVT, 4RGT and 4RVT) in the diluted Harrison solution and in 3.5 g/l $(NH_4)_2SO_4$ solution are reported in Fig. 4.12.

In both of the solutions values of the corrosion potential are similar for different samples regardless of the position and the silicon content. Regarding the effect of position, samples from near the gate (2RGT and 4RGT) possess higher pitting potentials (written in the graphs), in the solution of 3.5 g/l $(NH_4)_2SO_4$ (Fig. 4.12 (a)), compared to the samples taken from near the vent (2RVT and 4RVT). In the diluted Harrison solution, all of the samples (except for 4RVT) show the pitting from the OCP, which is due to the presence of chloride ions in the solution and the higher amount of iron-rich IM particles as well as the defective condition of the as-cast surfaces.

Considering the bulk microstructure, the results of potentiodynamic polarization test, in the diluted Harrison solution and in 3.5 g/l $(NH_4)_2SO_4$, solution related to the samples 2RGB and 4RGB are presented in Fig. 4.13. In both solutions, there is no significant difference in the corrosion potentials of the two samples.

The stability of the passive oxide layer is higher for the bulk samples in comparison to the as-cast surface of the thin wall samples, especially in the chloride-containing solution. This is due to the surface condition since the bulk samples have a higher α_1-Al and a less eutectic fraction and are ground while the thin wall samples are tested in as-cast condition.

SEM images of the corroded surfaces of the samples 2RGT and 4RGT after the polarization test are presented in Fig. 4.14. For both samples, in both solutions corrosion is localized and a galvanic coupling between the eutectic silicon phase or iron-rich IM particles and the aluminum matrix can be observed.

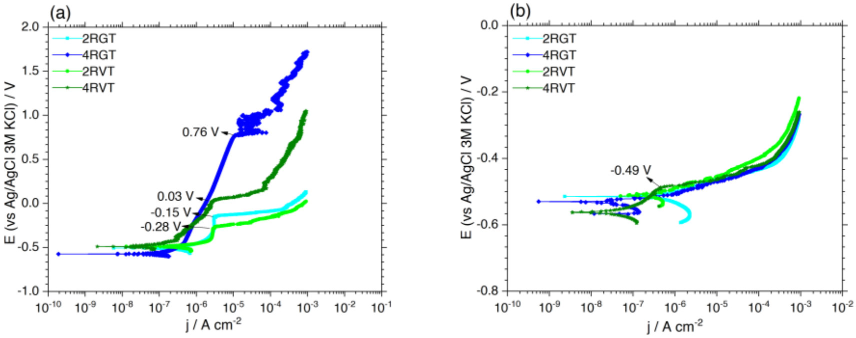

Fig. 4.12. Potentiodynamic polarization curves of the thin wall samples in (a) 3.5 g/l $(NH_4)_2SO_4$ and (b) the diluted Harrison solution.

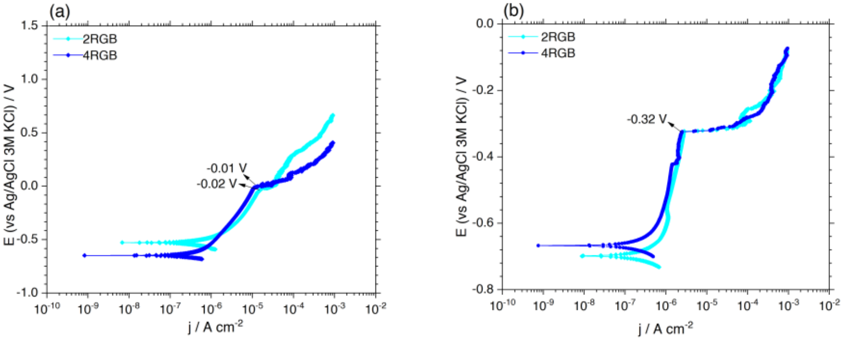

Fig. 4.13. Potentiodynamic polarization curves of the thick plate (bulk) samples in (a) 3.5 g/l $(NH_4)_2SO_4$ and (b) the diluted Harrison solution.

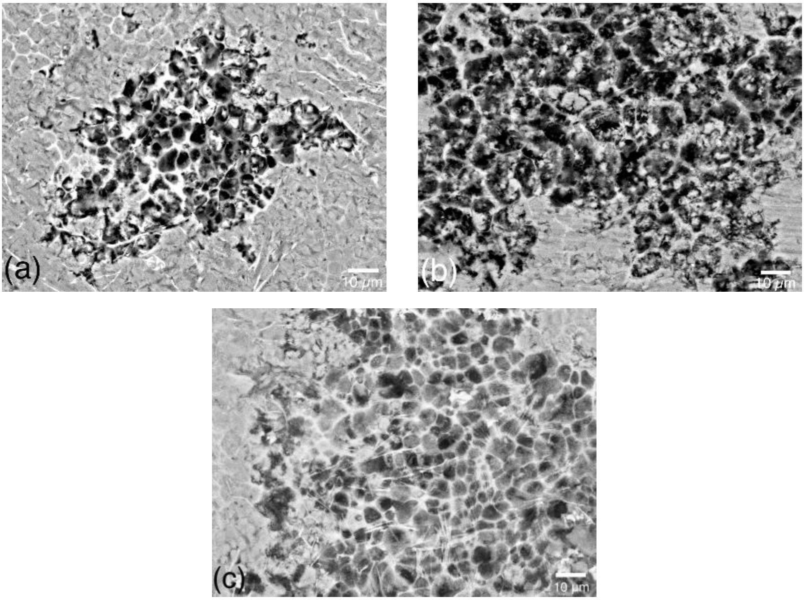

Fig. 4.14. Corroded surfaces of the sample (a) 2RGT, (b) 4RGT in the diluted Harrison solution and (c) 2RGT in 3.5 g/l $(NH_4)_2SO_4$ solution after the polarization test.

EIS spectra were obtained during 24 hours of immersion in the diluted Harrison solution. Bode plots of EIS spectra of the thin wall samples in as-cast condition are reported in Fig. 4.15. This figure also compares the effect of different positions in the cavity and the silicon content.

For all of the samples, the impedance values at the low frequencies decrease with the immersion time, which indicates the progressive corrosion process.

In addition, the phase angle maximum depresses through the immersion time, suggesting that the localized corrosion activity is increasing [200].

Regarding the effect of position, the samples taken from near the vent, almost always during the immersion show slightly higher impedance values at the low frequencies in comparison to the samples taken from near the gate, except at 24 hours when all the samples show the same values.

As it was discussed before, according to the LOM images in Fig. 4.3, the samples which are taken from near the vent, possess a higher fraction of α_2-

Al particles and they also have a finer microstructure compared to the samples which are taken from near the gate.

Concerning the effect of silicon, no noticeable difference is detectable. However, all the previous researches have indicated the positive effect of silicon on the pitting corrosion resistance of aluminum alloys [26, 201, 202]. Nevertheless, it is worth mentioning that these researches are focused on the silicon content higher than 6%, which is higher than the percentage of silicon in both of our alloys.

To remove the effect of as-cast surface quality, the thin wall samples were ground using SiC abrasive papers to the extent that the skin layer was totally removed. The samples were then monitored by EIS during 24 hours of immersion in the same solution. Bode presentations of EIS spectra of these samples are presented in Fig. 4.16.

According to these spectra, the ground thin wall samples show one order of magnitude higher impedance values at the low frequencies compared to the same samples in as-cast condition.

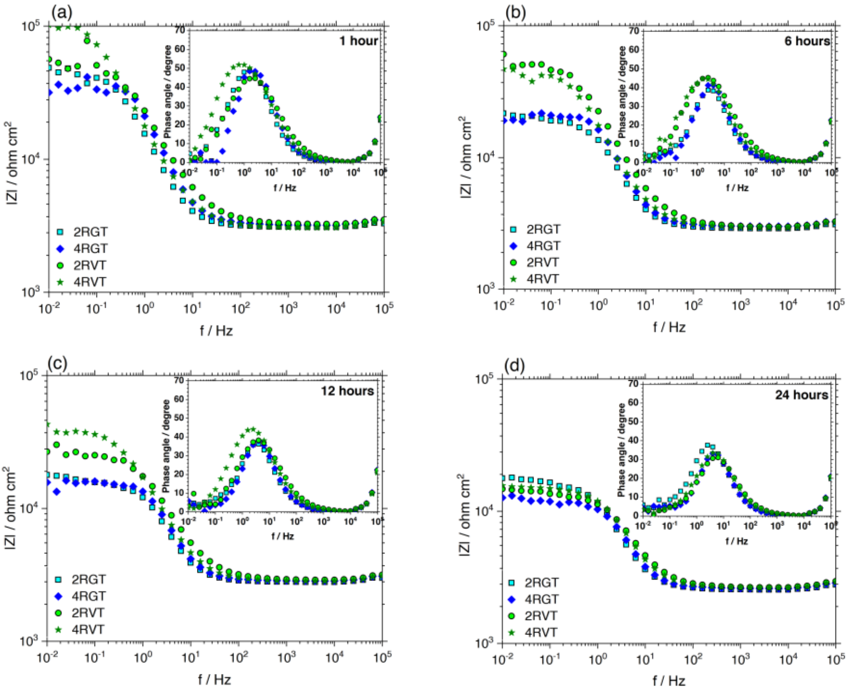

Fig. 4.15. EIS spectra of the samples 2RGT, 4RGT, 2RVT and 4RVT after (a) 1, (b) 6, (c) 12 and (d) 24 hours of immersion in the diluted Harrison solution.

In addition, the impendence values increased during 24 hours of immersion for all of these samples. This can be due to the presence of a protective oxide layer, which is more stable to the localized corrosion. This protective oxide layer is provided by better finishing quality on the ground surfaces. By grinding, the skin layer is removed and a surface containing more α_1-Al particles and fewer intermetallic particles (Fig. 4.6) is exposed to the corrosive solution.

The difference between corrosion performances of the samples from different positions is negligible in this condition. Impedance tends slightly to increase after 6 hours and no pits are developed after 24 hours. This proves that the poor behavior of as-cast surface is due to the poor surface quality and the higher amount of intermetallic particles.

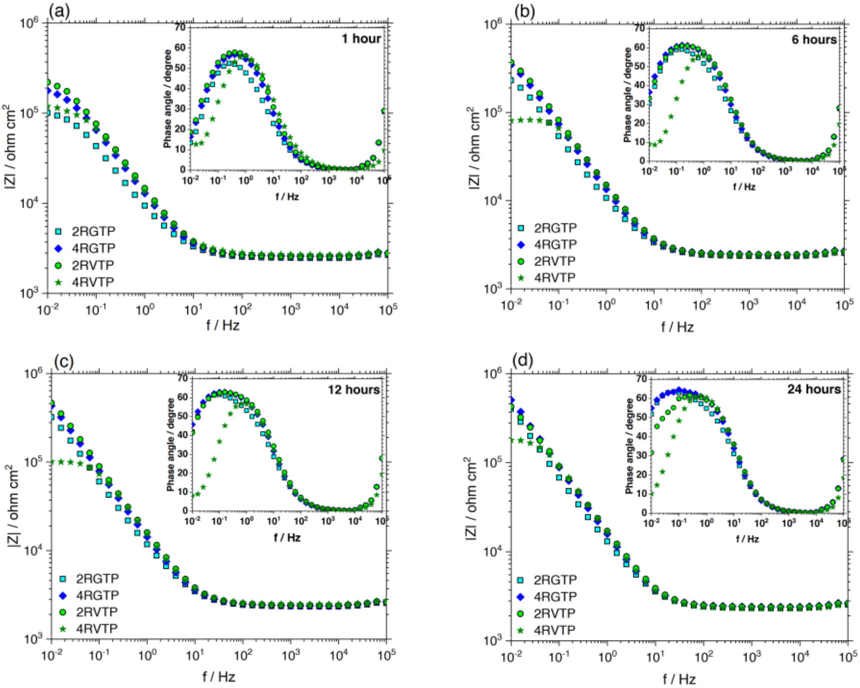

Fig. 4.16. EIS spectra of the samples 2RGTP, 4RGTP, 2RVTP and 4RVTP after (a) 1, (b) 6, (c) 12 and (d) 24 hours of immersion in the diluted Harrison solution.

EIS spectra of the samples taken from the thick plate, which are ground to the middle to expose the bulk microstructure, are reported in Fig. 4.17. These results indicate the growth of a protective oxide layer on the surface. The equivalent circuits used to describe the electrochemical responses of the samples 2RG(T/B)(P), 4RG(T/B)(P), 2RVT(P) and 4RVT(P) are shown in Fig. 4.18.

The electrochemical behavior of aluminum surface is affected by the presence of the passive oxide layer and the oxide layer/aluminum interface. The interface between the intermetallic particles/the eutectic silicon phase and the aluminum matrix influences the electrochemical response as well.

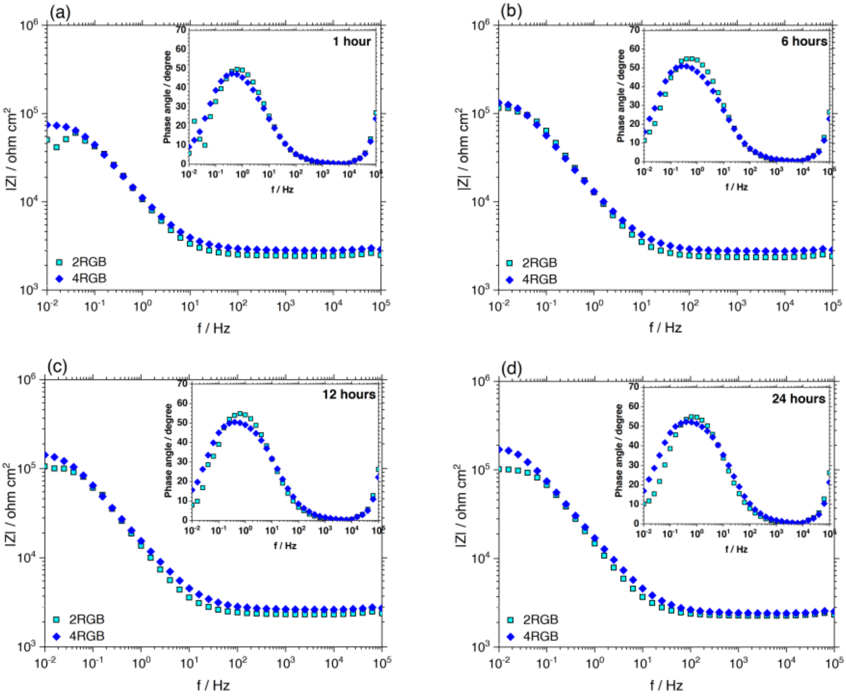

Fig. 4.17. EIS spectra of the samples 2RGB, 4RGB after (a) 1, (b) 6, (c) 12 and (d) 24 hours of immersion in the diluted Harrison solution.

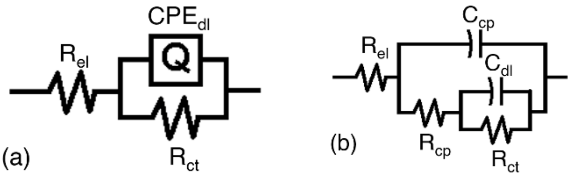

Fig. 4.18. Equivalent circuits for the studied alloys after (a) short time and (b) longer time of immersion in the diluted Harrison solution.

Although all these constituents are present, their time constants strongly overlap or one dominates. Therefore, only one phase angle maximum in the diagram can be observed for all of them.

The oxide layer is represented by a parallel circuit containing a resistor due to ionic conduction in the oxide, and a capacitor due to its dielectric properties [203]. The circuit in Fig. 4.18 (a) with one time constant has been used for the first 6 hours of immersion, for almost all the samples. While the circuit in Fig. 4.18 (b) has been used for the later hours of immersion when a second time constant was visible in the EIS spectrum. In the circuits depicted in Fig. 4.18 (a) and (b), R_{el} represents the resistance of the electrolyte.

Q_{dl} (or C_{dl}) and R_{ct} stand for capacitive behavior of the electrical double layer at the interface of the surface and the solution and for the resistance against the charge transfer (or polarization resistance), respectively.

The second time constant at longer immersion time shows the oxidation of aluminum and can represent the oxide layer (for the ground surface of the thin wall and the thick plate samples). It can also stand for the corrosion products formed due to the localized corrosion attack in case of the thin wall samples in as-cast condition. R_{cp} stands for the resistance behavior of oxide layer (or the corrosion products). C_{cp} is related to capacitive behavior of the oxide layer (or the corrosion products).

The fitting results of the two resistances (R_{ct} and R_{cp}) for the thin wall samples, ground and in as-cast condition, and the ground thick plate samples are presented in Fig. 4.19, Fig. 4.20 and Fig. 4.21, respectively.

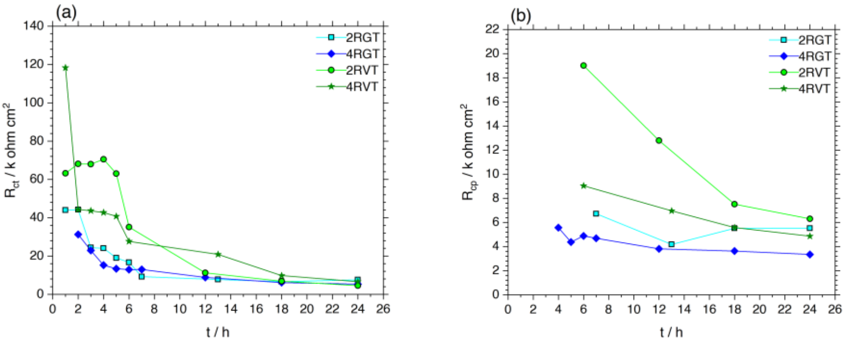

Fig. 4.19. Fitted EIS parameters of the as-cast thin wall samples: (a) R_{ct} and (b) R_{cp}.

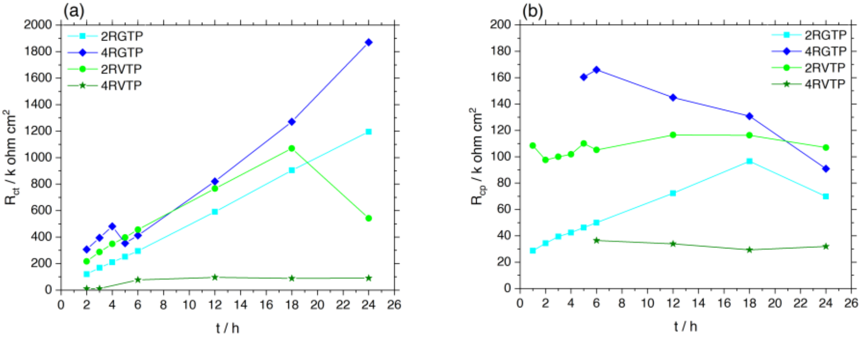

Fig. 4.20. Fitted EIS parameters of the ground thin wall samples: (a) R_{ct} and (b) R_{cp}.

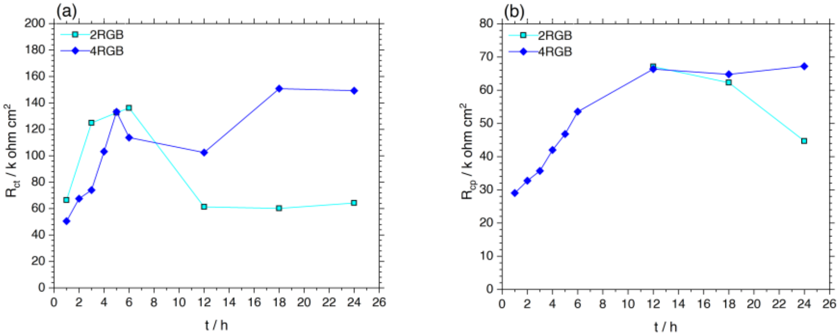

Fig. 4.21. Fitted EIS parameters of the ground thick plate (bulk) samples: (a) R_{ct} and (b) R_{cp}.

Values of R_{ct} of the thin wall samples in as-cast condition (Fig. 4.19 (a)) decrease with the immersion time for all the samples, which indicates an increase of the activity and a higher corrosion rate as localized attacks [204]. It should be noted that this decrease is immediate for the samples taken from near the gate, while for the samples taken from near the vent it starts after 5-6 hours of immersion. These values are higher for the samples taken from the region near the vent, in comparison to the samples taken from the region near the gate.

Regarding the effect of silicon content, the samples with a lower amount of silicon show slightly higher R_{ct} values at the very first hours of immersion.

The values of R_{cp} (Fig. 4.19 (b)), that for these samples represent the resistance of corrosion products in the pits, are very low and slightly decrease for all the samples due to the corrosion attacks.

Regarding the ground thin wall samples, R_{ct} values are generally one order of magnitude higher compared to the thin wall samples in as-cast condition. These values increase during the immersion time for all the samples (Fig. 4.20 (a)). This can be due to the growth of a protective and stable oxide layer on the ground surfaces. The values of R_{ct} for different samples, with regard to the position, and with different amounts of silicon are close to each other. In the case of these ground samples, values of R_{cp} represent the presence of a passive oxide layer. They remain almost constant for all of the samples and show a similar trend.

In case of the ground thick plate (bulk) samples, reported in Fig. 4.21, the behavior of 2RGB and 4RGB samples are very similar. After some initial fluctuation, values of R_{ct} remain almost constant for the two samples from 12 to 24 hours of immersion, but never reach the high resistance showed by the ground thin wall samples. R_{cp} values increase from the first hour of immersion for the sample 4.5 RGB.

SEM micrograph and the map analysis of a selected corroded surface are shown in Fig. 4.22.

As it is clearly visible in Fig. 4.22, corrosion is mainly localized in all the samples, and takes place especially in the eutectic region, at the interface of the eutectic silicon phase and aluminum and at the interface of aluminum grains and iron-rich intermetallic particles. These results are in accordance with the results of other researchers about the corrosion of Al-Si alloys in similar solutions [4, 57].

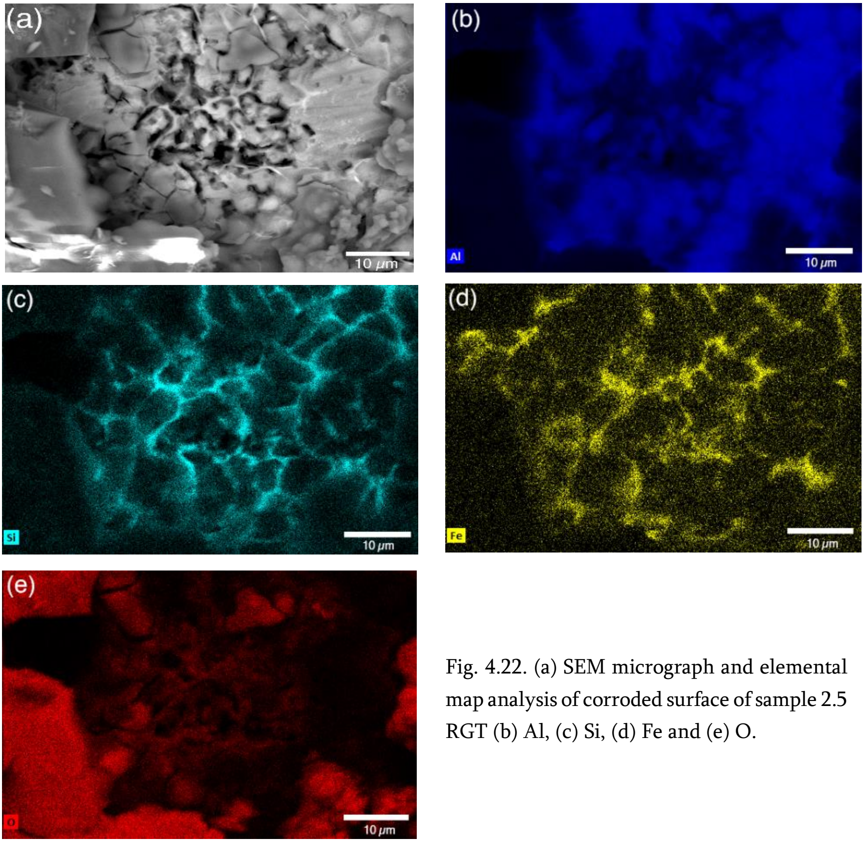

Fig. 4.22. (a) SEM micrograph and elemental map analysis of corroded surface of sample 2.5 RGT (b) Al, (c) Si, (d) Fe and (e) O.

4.2.3. Effect of casting technology and NaCl concentration

The results of 24 hours OCP monitoring for the samples 4RT, 4RB and 4LT in 0.01, 0.05, 0.1 and 0.6 M NaCl solutions are presented in Fig. 4.23. For the sample 2RB the monitoring has been done only in 0.6 M NaCl solution. In all the solutions and for all the samples, some fluctuations in the OCP values from the beginning of immersion until 4-5 hours can be observed. After these fluctuations, the OCP values increase and show relative stability until the end of the test.

The initial fluctuations can be related to the (metastable) localized corrosion activities [4].

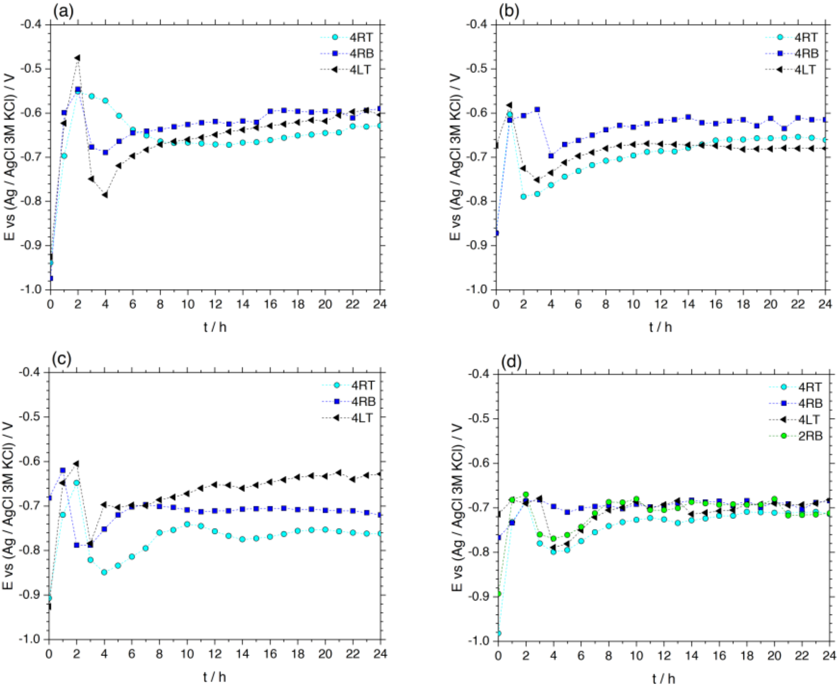

Fig. 4.23. OCP values of the samples 4RT,4RB, 4LT (and 2RB) versus time immersed in (a) 0.01, (b) 0.05, (c) 0.1 and (d) 0.6 M NaCl solution.

The sample 4RT shows the lowest OCP values in all concentrations. According to Fig. 4.3, this sample contains a higher fraction of the eutectic phase and α_2-Al particles, which makes it more (electrochemically) active. Since there are more possible sites for the galvanic coupling on the surface of this sample.

In 0.01 and 0.05 M NaCl solutions, the sample 4RB shows nobler OCP values compared to the samples 4RT and 4LT. While in 0.1 M NaCl solution the sample 4LT possesses higher OCP values and in 0.6 M NaCl solution all the samples, including the sample 2RB, present comparable OCP values.

It seems that in the less concentrated solutions (0.01 and 0.05 M), the sample with a higher fraction of α_1-Al particles (4RB) has the noblest corrosion potential.

Bode presentations of EIS spectra of the samples 4RT, 4RB and 4LT during 24 hours of immersion in the different NaCl solutions are presented in Fig. 4.24 and Fig. 4.25. For the sample 2RB, the EIS test was performed only in 0.6 M NaCl solution (Fig. 4.25 (b), (d) and (f)).

In 0.01 and 0.05 M NaCl solutions (Fig. 4.24), EIS responses of the three samples show minimum changes during 24 hours. The two samples 4RT and 4LT present similar impedance values, while the sample 4RB possesses relatively higher impedance values at the low frequency range, which can be attributed to higher corrosion resistance. According to the phase spectra in these two solutions, one time constant at the medium frequency range and one mass-transport-related constant or one time constant at the low frequency range are recorded for all the samples. However, due to the lack of experimental points and the occasional scattering of data at the low frequency range, it is difficult to distinguish if the last element is certainly a Warburg element or a RC constant.

The first time constant can be related to the charge transfer resistance (or the polarization resistance) and the capacitive behavior of the electrical double layer at the metal/electrolyte interface. The element(s) at the low frequency range is related to the localized corrosion phenomena [4]. If this element at the low frequency range is a Warburg element, it can be related to the diffusion of corrosion reactants through the corrosion products.

While if it is an RC constant it may present the behavior of IM particles/the eutectic silicon.

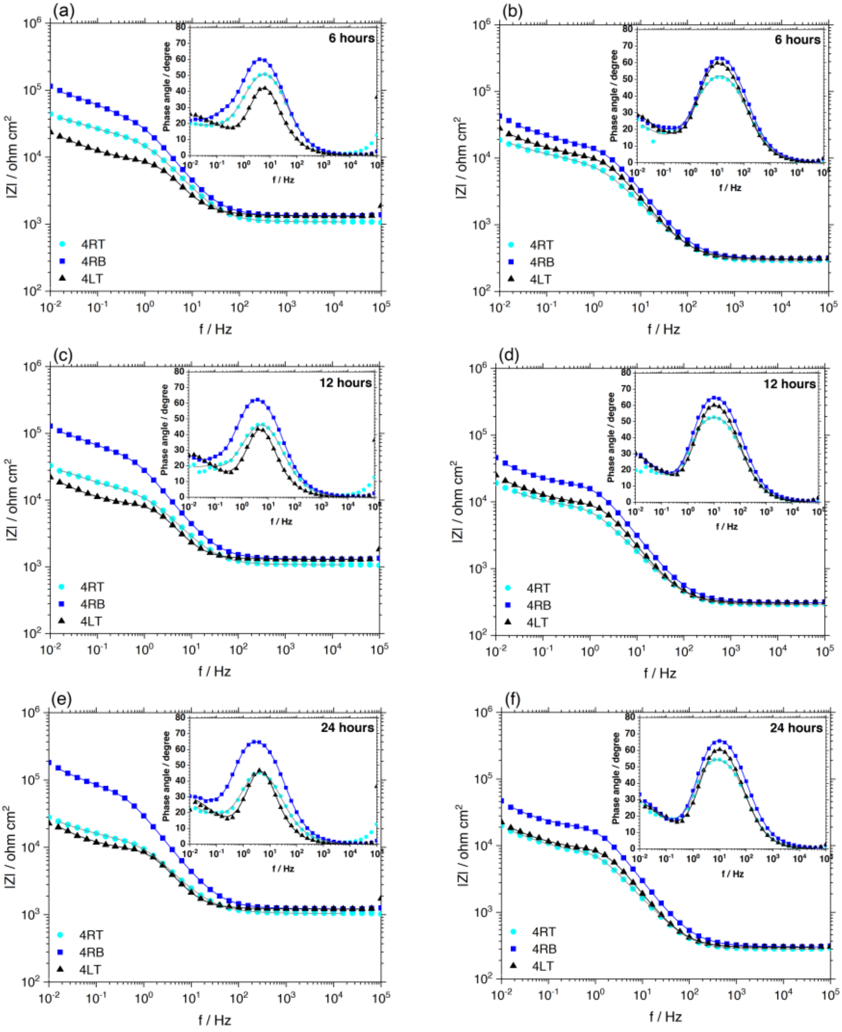

Fig. 4.24. EIS spectra of the samples 4RT, 4RB and 4LT after 6, 12 and 24 hours of immersion in (a), (c) and (e) 0.01 and (b), (d) and (f) 0.05 M NaCl solution (solid lines are the fitted data).

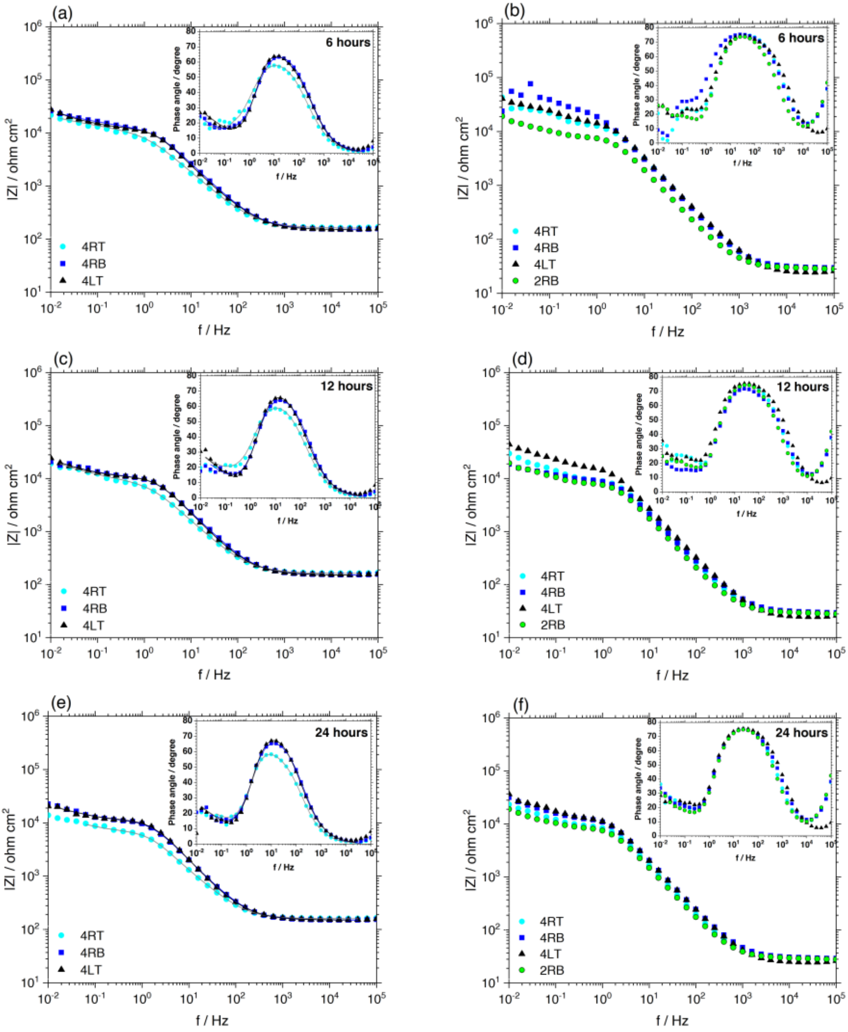

Fig. 4.25. EIS spectra of the samples 4RT, 4RB, 4LT and 2RB after 6, 12 and 24 hours of immersion in (a), (c) and (e) 0.1 and (b), (d) and (f) 0.6 M NaCl solution (solid lines are the fitted data).

The sample 4RT shows the highest degree of data scattering (noise) at the low frequency range (in both 0.01 and 0.05 M) indicating more localized corrosion activity on the surface. This noise is associated with the constant change of the active surface area [4].

The difference in total impedance values of various samples is not observed in the more concentrated solutions (0.1 and 0.6 M).

According to Fig. 4.25 (a), (c) and (e), values of total impedance for the three samples (4RT, 4RB and 4LT) during 24 hours of immersion in 0.1 M NaCl solution are similar and stable.

In 0.6 M NaCl solution, a slight decrease in the values of total impedance of the samples 4RT and 4RB can be observed. While these values are relatively stable for the samples 2RB and 4LT.

The EIS spectra of samples in 0.1 M NaCl solution are characterized by one time constant at the medium frequency range and one Warburg tail/RC constant at the low frequency range. This behavior is similar to those in the less concentrated solutions (Fig. 4.24).

According to Fig. 4.25 and Fig. 4.24, the scattering of data (noise) at the low frequency range for all samples increases by NaCl concentration.

According to these results, there is no significant difference between the corrosion mechanism of conventional HPDC and Rheo-HPDC Al-Si alloys. However, in the less concentrated solutions (0.01 and 0.05 M), the semi-solid sample from the thick plate (4RB) with a higher percentage of α_1-Al particles and a lower fraction of the eutectic phase show higher impedance values at the low frequency range.

According to the OCP (Fig. 4.23) and the EIS results (Fig. 4.24 and Fig. 4.25), the corrosion process of (Rheo)-HPDC Al-Si alloys possibly involves three steps:

(i) The metastable localized corrosion (due to micro galvanic coupling) from the beginning of immersion until ca. 4-5 hours, during which the OCP values fluctuate (Fig. 4.23) and the EIS response is noisy at the low frequency range (the EIS spectra are not presented here). Duration of this step seems to be unaffected by the concentration of NaCl.

(ii) Stable localized corrosion and extensive corrosion through the eutectic region. There is the possibility of an incubation period before this step.

(iii) At this step, the active corrosion sites are probably covered by the corrosion products and due to the presence of this diffusion barrier for corrosion reactants, other corrosion sites will possibly activate.

The equivalent circuit used to fit the EIS responses of the conventional and Rheo-HPDC Al-Si alloys (in 0.01, 0.05 and 0.1 M NaCl solutions) was suggested by Arrabal et al. [4] and is depicted in Fig. 4.26.

In this circuit, R_{ct} and C_{dl} correspond to the charge transfer resistance of the surface and the capacitive behavior of the electrical double layer at the aluminum/electrolyte interface. CPE_{pit} and R_{pit} are respectively the constant phase element and the resistance related to the localized corrosion areas (pits). W_{pit} is a finite length Warburg diffusion component.

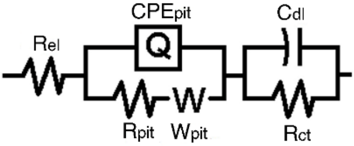

Fig. 4.26. Equivalent circuit for the EIS response of the Al-Si alloys in 0.01, 0.05 and 0.1 M NaCl solutions.

As the EIS responses in 0.6 M NaCl solution are highly noisy especially at the low frequency range, the fitting was carried out for the EIS responses in the other three solutions. A summary of the results is presented in Table. 4.4.

It is worth mentioning that the high degree of data scattering at the low frequency range introduces a significant error in calculating the values of R_{pit}.

The values of R_{ct} of all the samples, in all the solutions, increase by the immersion time, which can be attributed to the accumulation of corrosion products blocking the surface.

Table. 4.4. Summary of results derived from fitting the EIS responses of the Al-Si alloys in 0.01, 0.05 and 0.1 M NaCl solutions.

Parameter	R_{ct} (kΩ.cm^2)	Rel std erorr (%)	R_{pit} (kΩ.cm^2)	Rel std erorr (%)	χ^{2*}
4RT (0.01 M)					
6 h	3.9	17.7	20.9	1.4	1.1×10^{-4}
12 h	4.9	20.3	13.9	2.1	2.7×10^{-4}
24 h	4.0	17.6	8.8	9.4	2.9×10^{-4}
4RB (0.01 M)					
6 h	20.5	4.3	57.3	4.2	1.1×10^{-4}
12 h	30.0	3.1	56.8	5.7	5.9×10^{-5}
24 h	45.0	2.4	62.5	12.1	6.2×10^{-5}
4LT (0.01 M)					
6 h	6.1	1.5	42.2	38.9	1.5×10^{-4}
12 h	6.3	1.5	105.1	90.3	2.7×10^{-4}
24 h	7.2	1.6	85.2	67.9	3.0×10^{-4}
4RT (0.05 M)					
6 h	1.2	62.6	8.2	9.9	5.8×10^{-4}
12 h	5.4	5.6	2.1	20.6	3.1×10^{-4}
24 h	5.9	2.1	1.1	17.7	1.8×10^{-4}
4RB (0.05 M)					
6 h	10.4	3.8	10.9	15.4	2.6×10^{-4}
12 h	14.9	2.1	1.6	83.9	2.4×10^{-4}
24 h	16.2	1.8	2.0	151	1.9×10^{-4}
4LT (0.05 M)					
6 h	7.4	3.3	3.7	14.4	1.8×10^{-4}
12 h	7.9	0.9	0.5	54.2	1.7×10^{-4}
24 h	7.5	1.4	0.3	99.4	3.6×10^{-4}
4RT (0.1 M)					
6 h	2.7	23.9	10.2	7.6	6.3×10^{-4}
12 h	3.8	13.1	6.2	11.5	6.9×10^{-4}
24 h	5.3	1.2	0.5	18.6	1.7×10^{-4}
4RB (0.1 M)					
6 h	6.7	4.8	7.8	5.0	1.7×10^{-4}
12 h	8.3	5.0	2.0	37.8	2.7×10^{-4}
24 h	9.2	1.4	0.7	47.1	1.9×10^{-4}
4LT (0.1 M)					
6 h	9.9	0.9	0.5	27.8	2.4×10^{-4}
12 h	9.1	2.0	0.7	178	7.8×10^{-4}
24 h	9.8	1.9	0.2	141	6.1×10^{-4}

*Chi-squared: the sum of the squares of the residuals.

In 0.01 and 0.05 M solutions, these values are considerably higher for the sample 4RB compared to the other two samples. However, they are more comparable in 0.1 M solution.

Due to the significant difference between the active area related to R_{ct} and R_{pit}, the direct comparison of their values is not reasonable.

R_{pit} decreases by the immersion time which can be attributed to the fact that more localized sites are being actively corroded.

Comparing the R_{pit} values of the Rheo-HPDC (4RT and 4RB) and the conventional HPDC (4LT) samples shows that these values are higher for the semi-solid samples, which can be due to the lower number of the localized corrosion sites.

Fig. 4.27 depicts surface morphology of the sample 2RB after 12 (Fig. 4.27 (a)) and 24 hours (Fig. 4.27 (b), (c), (d) and (e)) of immersion in 0.6 M NaCl solution.

According to Fig. 4.27 (a), after 12 hours of immersion, the localized corrosion attacks (as trenching) in the eutectic regions (containing the iron-rich IM particles) can be observed. At this stage, no accumulation of corrosion product was detected on these active sites or any other place on the alloy's surface. However, after a longer immersion time (24 hours), the presence of a significant amount of corrosion products on the surface is noticeable.

Fig. 4.27 (b) depicts the later stage of deposition of corrosion products on a eutectic area which has been through trenching. Although the corrosion products initially dissolve in the solution, some of them deposit in longer immersion times. This may be due to the alkaline pH over the cathodic iron-rich IM particles/eutectic silicon that can reach as high as 9.5 [205] and it can dissolve any hydrated aluminum oxide product [23].

The results of EDXS analysis on two spots on the corrosion products in this figure are presented in Table. 4.5. In both spots the presence of chloride is detected. A low amount of magnesium is noticed in spot 2 which can be related to the selective dissolution of this element from an IM particle during the corrosion process.

The severe corrosion observed after 24 hours of immersion is probably due to the presence of the eutectic phase network all over the surface (Fig. 4.3 (a), (b) and Fig. 4.6).

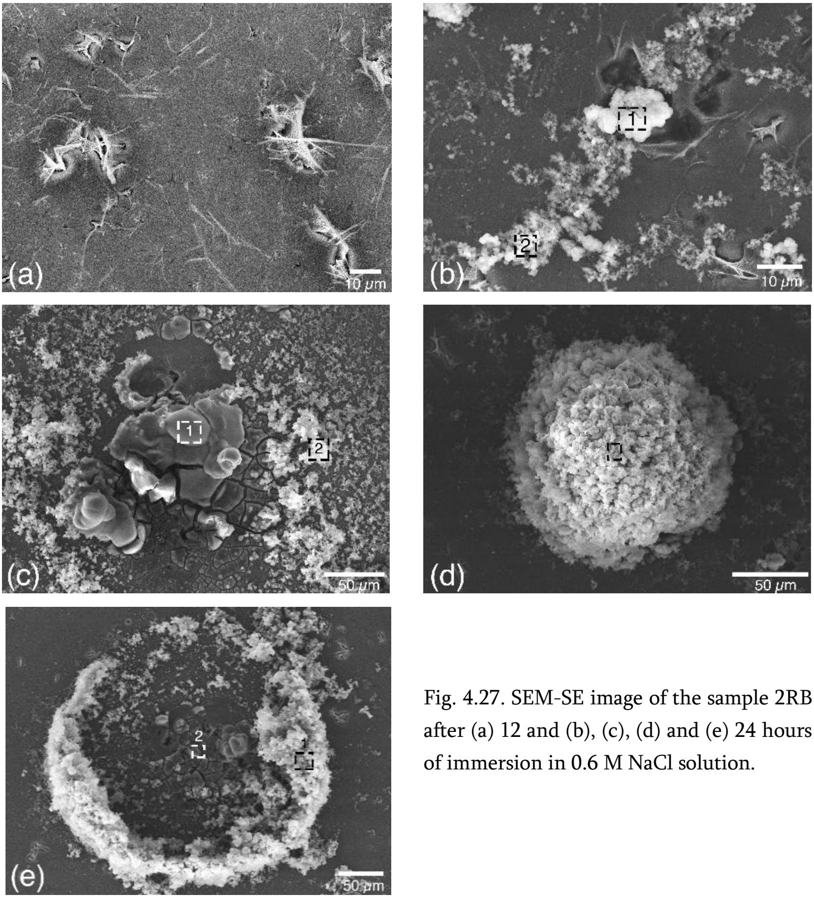

Fig. 4.27. SEM-SE image of the sample 2RB after (a) 12 and (b), (c), (d) and (e) 24 hours of immersion in 0.6 M NaCl solution.

In the case of other alloys such as AA2024, this type of corrosion event (so-called "co-operative corrosion") is attributed to the clustering of IM particles [206]. The typical co-operative corrosion sites create corrosion rings (e.g. Fig. 4.27 (c), (d) and (e)).

Table. 4.5. Results of EDXS analysis of the selected areas in Fig. 4.27

Area of analysis	Al (wt%)	Si (wt%)	Mg (wt%)	O (wt%)	Cl (wt%)
(b)-1	41.2	0.4	-	55.4	3.0
(b)-2	57.9	4.8	0.8	35.4	1.1
(c)-1	43.8	0.13	-	35.1	21
(c)-2	42.5	0.4	-	51.7	5.4
(d)	37.6	0.2	-	52.9	9.2
(e)-1	41.2	0.3	-	48.7	9.9
(e)-2	43.4	0.4	-	55.9	0.3

The morphology of corrosion products in the active rings on the surface of the alloy 2R (after 24 hours of immersion) shows two types:

(i) A domed cracked layer, which seems to be the first layer of the corrosion product (Fig. 4.27 (c) and (e))

(ii) A fine porous layer which apparently is placed on top of the domed layer (Fig. 4.27 (c), (d) and (e)).

According to Hughes et al. [206], domes of the corrosion products indicate the sites of H_2 evolution (Fig. 4.27 (c) and (e)). The cracked morphology of these corrosion products can be the result of dehydration of a gel [206].

The difference between the morphology of domes and fine corrosion products can be due to the fact that they have been formed under different solution conditions such as compositional or pH differences.

The EDXS results (Table. 4.5) indicate that both types of corrosion products contain chloride. While a low amount of silicon (and in one case magnesium) was detected in the composition of corrosion products, iron was always absent. Silicon oxide is soluble in the alkaline environment [207] caused by the intense localized cathodic activities.

It should be mentioned that the partial presence of some nodular oxide particles was observed in some places on the surface.

The alkaline pH due to the intense cathodic activity inside the corrosion rings results in the formation of a gel-like layer of corrosion products within them. Later on, this gel layer can be a diffusion barrier for the corrosion reactants. The anodic dissolution of the eutectic aluminum within the ring balances the mentioned cathodic activity.

One might think that the high pH value over the corrosion rings inhibits the precipitation of the other type of corrosion products (the fine porous layer). While the pH drops around the periphery of these active corrosion sites leading to the deposition of porous corrosion products.

With further growth, this porous corrosion layer will cover the gel layer (Fig. 4.27 (d) and (e)). However, the size of corrosion rings is more than 50 μm and Hughes et al. [206] mentioned that the maximum distance from a cathodic IM particle for the pH to drop (below 9) is 25 μm. Therefore, in a similar case, they have considered the possible effect of convection currents caused by H_2 evolution on the dispersion of anolyte solution into the bulk solution above the corrosion ring.

Although in the case of Al-Si alloy, the cathodic site is a eutectic region. Therefore, the mentioned distance (and subsequently the size of corrosion ring) can be more. The proposed growth pattern of corrosion products on the surface of Al-Si alloy is schematically depicted in Fig. 4.28.

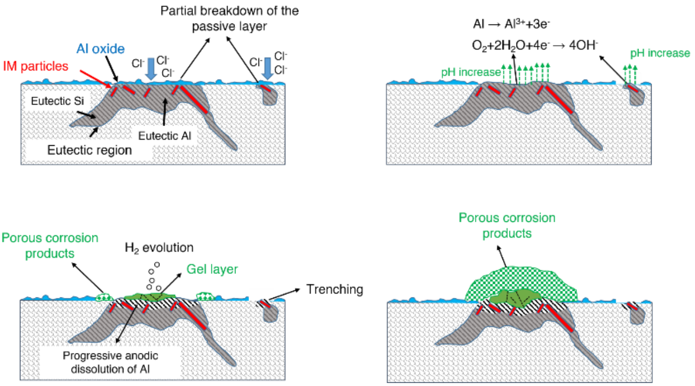

Fig. 4.28. The proposed growth pattern for corrosion products on Rheo-HPDC Al-Si alloys.

The SEM images of corroded surfaces of the samples 4RT, 4RB and 4LT after 24 hours of immersion in 0.6 M NaCl solution are presented in Fig. 4.29. Similar corrosion features to those of the sample 2RB including trenching around the eutectic silicon/iron-rich IM particles and severe corrosion rings are observed for these three samples.

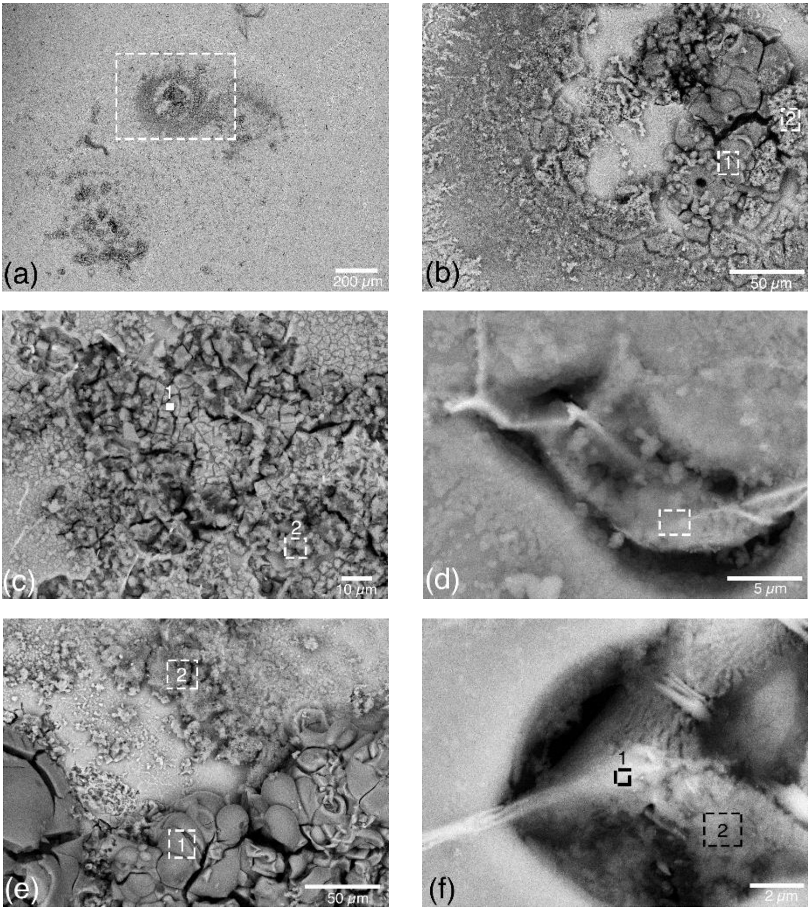

Fig. 4.29. SEM-BS image of the sample (a) and (b) 4RT, (c) and (d) 4RB and (e) and (f) 4LT after 24 hours of immersion in 0.6 M NaCl solution.

Fig. 4.29 (d) and (f) present the circumferential pits (as trenches) around two eutectic areas containing IM particles on the surface of the samples 4RT and 4LT. The EDXS analysis on the indicated spots in Fig. 4.29 (d) and (f)-spot 2 confirms the fact that these are eutectic regions (See Table. 4.6). According to these results, the concentration of alloying elements (Fe, Mg and Cu) in the eutectic area/on the IM particles (Fig. 4.29 (d) and (f)-spots 1 and 2) is significant.

Table. 4.6. Results of EDXS analysis of the selected areas in Fig. 4.29

Area of analysis	Al (wt%)	Si (wt%)	Fe (wt%)	Mg (wt%)	Cu (wt%)	O (wt%)	Cl (wt%)	Na (wt%)
(b)-1	30.9	0.45	-	-	-	45.6	23.0	-
(b)-2	28.1	0.5	-	-	-	39.3	26	6.2
(c)-1	69.0	1.2	-	0.5	-	25.8	3.3	0.11
(c)-2	35.2	0.43	-	-	-	54.7	9.3	0.47
(d)	27.6	16.8	7.1	1.2	4.0	21.1	6.3	15.9
(e)-1	36.7	0.2	-	-	-	48.7	14.4	-
(e)-2	38.7	1.7	-	-	-	43.3	15.8	0.6
(f)-1	45.5	31.6	4.2	3.5	2.8	10	0.14	2.4
(f)-2	52.5	24.8	1.7	1.9	-	15.9	0.18	2.9

No meaningful difference among the corrosion morphologies and compositions (in 0.6 M NaCl solution) were found for the samples of different alloys processed by the conventional HPDC and Rheo-HPDC techniques.

Fig. 4.30 compares the trenching sites on the surface of the samples 4RT and 4LT after 24 hours of immersion in 0.01 and 0.05 M NaCl solutions. For the semi-solid alloy, the pitting attack starts preferentially at the interface of α_2-Al particles with the eutectic phase (the liquid portion of the slurry). While α_1-Al particles seem to be more protected from the corrosion. However, some of these primary particles are corroded at their borders as well. This selective corrosion behavior is obviously absent in the conventional HPDC alloy.

Fig. 4.31 presents some examples of the corrosion rings on the surface of the samples 4RT and 4LT after 24 hours exposure to 0.01 and 0.05 M NaCl solutions. As it can be seen in this figure, in the less concentrated solutions the extent of stable corrosion rings is lower in comparison to those in 0.6 M NaCl solution. Fig. 4.31 (a) and (c) display the fact that a big corrosion ring might be the result of the combination of several active sites, which will be combined when the sample is immersed in a more concentrated solution (e.g. Fig. 4.31 (b) and (d)).

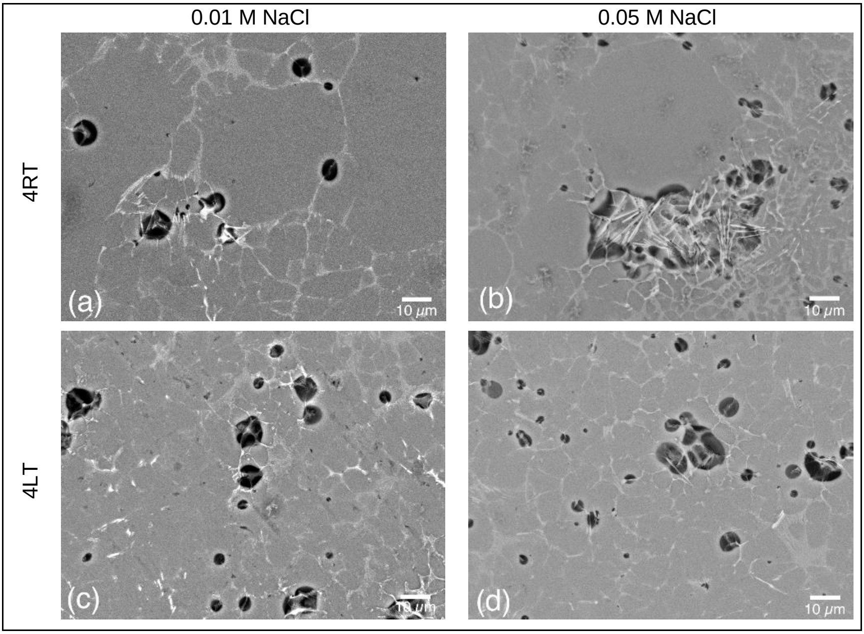

Fig. 4.30. SEM-BS image of trenching on surface of the sample (a) and (b) 4RT and (c) and (d) 4LT after 24 hours of immersion in 0.01 and 0.05 M NaCl solution, respectively.

At the center of a corrosion ring (Fig. 4.31 (b)) part of the gel layer is removed and the dissolution of the eutectic aluminum is evident. Fig. 4.32 provides SEM image at a higher magnification (of the same sample exposed to 0.01 M NaCl) to show the anodic dissolution of aluminum which occurs in the corrosion ring.

The presence of some porous corrosion products deposited far from the ring (or active sites) on the alloy matrix is observed in Fig. 4.31 (c) and (d).

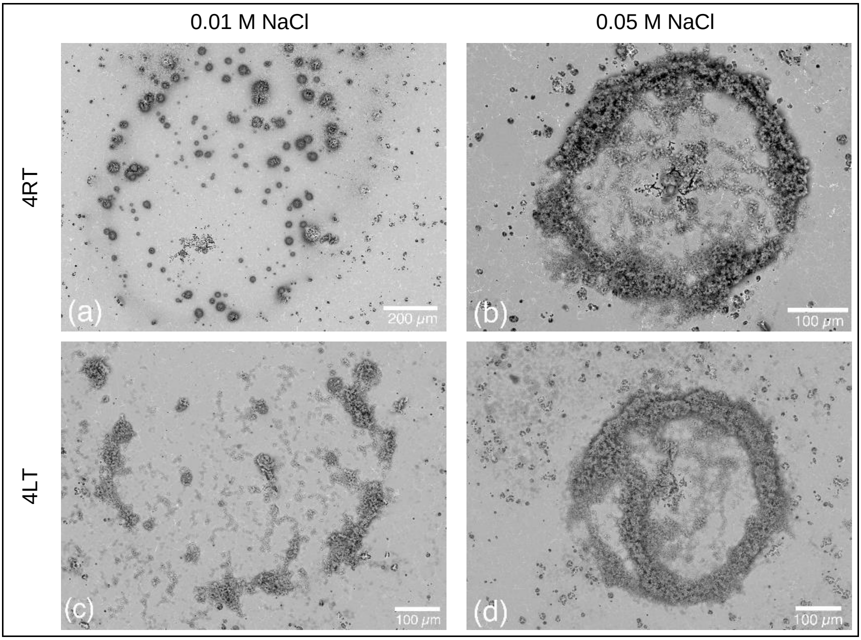

Fig. 4.31. SEM-BS image of co-operative corrosion on the sample (a) and (b) 4RT and (c) and (d) 4LT after 24 hours of immersion in 0.01 and 0.05 M NaCl solution, respectively.

As it was mentioned before, these products have probably been dragged away from the active corrosion site due to either a lower pH on the matrix or the convection currents by H_2 evolution.

On the surface of all samples (both the conventional HPDC and Rheo-HPDC materials and taken from different positions), some casting defects were present.

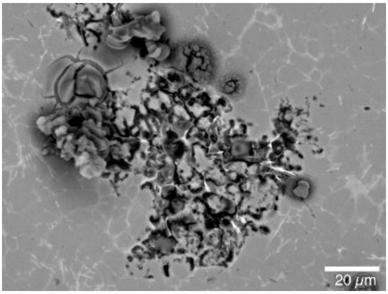

Fig. 4.32. SEM-BS image of a corrosion ring center on surface of the sample 4RT after 24 hours of immersion in 0.01 M NaCl solution.

It should be reminded that the OCP measurements (Fig. 4.23) and the EIS tests (Fig. 4.24 and Fig. 4.25) have been repeated at least three times for each sample to avoid the effect of inhomogeneity on the final judgment about the corrosion behavior.

While immersing in the NaCl solutions, these defects usually acted as the center of corrosion rings as shown in Fig. 4.33. It can be observed that the porous corrosion products are mostly deposited out of these flaws.

The results of anodic polarization tests for the samples 4RT, 4RB, 4LT and 2RB in 0.6 M NaCl solution are presented in Fig. 4.34.

Values of corrosion potentials decrease as following: 4LT>2RB>4RT=4RB.

For the Rheo-HPDC samples (2RB, 4RT and 4RB), the anodic polarization responses are characterized by a passive region, an active region, a re-passivation region and another active region.

According to these result, in a highly concentrated NaCl solution, the difference of corrosion behavior of the semi-solid samples taken from different positions in the cavity is negligible, which is in agreement with the EIS results (Fig. 4.25 (b), (d) and (f)). Therefore, the two samples of 4R alloy (4RT and 4RB) present similar behavior. However, their passive layer seems to be more stable and more resistant to pitting corrosion in comparison to the sample of 2R alloy (2RB). This is in accordance with the results reported by Rehim et al. [26, 27].

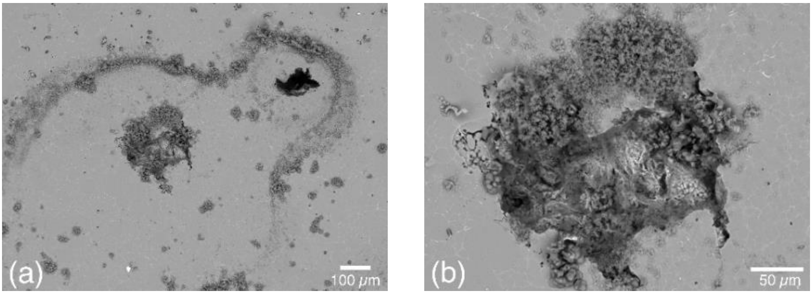

Fig. 4.33. (a) The appearance of two castings defects on the sample 4RT after 24 hours of immersion in 0.05 M NaCl solution and (b) the defect at higher magnification.

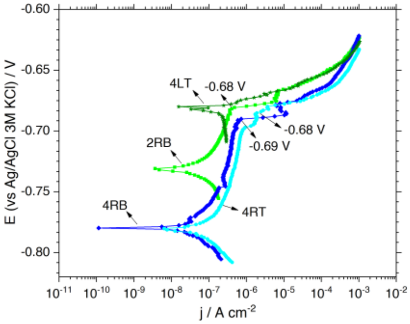

Fig. 4.34. Polarization curves of Al-Si samples in 0.6 M NaCl solution.

The incorporation of silicon oxide to the passive layer and its positive effect can be suggested. However, this needs further investigation, which is out of this thesis scope. Likewise, Pech-Canul et al. [208] have shown that for Al-12% Si, the presence of silicon oxide in the passive layer makes it more resistant to the pitting corrosion. Thanks to its electronic properties, silicon oxide has shown the ability to retard the adsorption of chloride ions. It can also block the entry sites and restrict the transport of chloride ions through the passive film [208].

The sample 2RB has a slightly higher pitting potential compared to the samples 4RT and 4RB. The sample 4LT shows pitting corrosion from the

OCP and no passive region is observed for this sample. The pitting potential decreased as following: 4LT>2RB>4RB>4RT.

Comparing the conventional HPDC and Rheo-HPDC materials, the semi-solid alloys seem to have a more resistant passive layer. However, the HPDC alloy showed more positive pitting potential. The reason behind this behavior is unclear to us.

4.3. Conclusions

Generally, the microstructure of Al-Si alloys contains α-Al particles, the eutectic phase and intermetallic particles. The semi-solid alloys include two types of α-Al particles: the primary α_1 and the secondary α_2-Al particles.

It was shown that the semi-solid samples taken from different positions and different parts with various thicknesses differ in the amount of α_1 and α_2-Al particles. These samples also show a transverse macrosegregation. α_1-Al particles which are the solid fraction of the slurry, tend to aggregate at the center of the samples while the surface is richer in α_2-Al particles. Longitudinal segregation induces the area near to the gate to have a higher fraction of α_1-Al particles and the one near to the vent a higher fraction of α_2-Al particles and the eutectic phase.

In the diluted Harrison solution, Rheo-HPDC Al-Si alloys are prone to the localized corrosion especially in the eutectic region and at the interface of iron-rich IM particles and the aluminum matrix. Segregation of phases due to the semi-solid process influences the corrosion behavior.

A big change in the corrosion resistance was shown by grinding the semi-solid samples. This is due to the presence of more intermetallic particles as well as more surface defects in as-cast surface condition. In as-cast surface condition, the samples with a higher amount of α_2-Al particles and a finer microstructure (taken from the region near the vent) show slightly higher corrosion resistance.

Both ground thin wall and thick plate samples possess a better corrosion resistance compared to the thin wall samples in as-cast condition. This improvement is due to the better surface condition. Nevertheless, the relatively thinner samples show a higher corrosion resistance compared to the thicker samples.

Surfaces of the rheocast component present a purely liquid microstructure due to the segregation, which makes them more resistant to corrosion when ground and therefore without the surface defects.

The corrosion resistance of the polished conventional HPDC and Rheo-HPDC Al-Si alloys was examined and compared in NaCl solutions of different concentrations.

In 0.01 and 0.05 M NaCl solutions, the semi-solid sample with a lower fraction of the liquid phase (4RB) possessed the noblest OCP values and the one with a higher fraction of the liquid phase (4RT) showed the lowest OCP.

Considering both the OCP and EIS results, in 0.1 and 0.6 M NaCl solutions, the corrosion responses of all samples were similar.

According to the EIS spectra in different NaCl solutions, the corrosion mechanism of the conventional and Rheo-HPDC alloys seemed similar.

In these solutions, both HPDC and Rheo-HPDC materials showed two major corrosion features including trenching around the eutectic regions (with IM particles) and severe corrosion rings.

At the center of corrosion rings, a gel-like layer of corrosion products was detected. It was observed that the rings are surrounded and in some cases covered by a fine porous corrosion product layer.

The casting defects on the surface of the alloys usually acted as active centers for the corrosion rings.

Polarization tests revealed the positive effect of silicon in stabilizing the passive layer in Rheo-HPDC alloys. In comparison to the conventional HPDC alloys, the semi-solid alloys presented a more resistant passive layer in 0.6 M NaCl solution.

Chapter 5 Cerium based conversion coatings

This chapter presents the study on the deposition and the electrochemical properties of cerium-based conversion coatings (CeCC) on the conventional HPDC and Rheo-HPDC Al-Si alloys. The main objectives of this study are optimization of the process parameters, unraveling the deposition mechanism and characterization of the corrosion properties. The results presented in this chapter were partially published and presented in papers I, II, V and VI, respectively.

5.1. Materials and methods

5.1.1. Substrate preparation

Samples of the alloys 2R(L) and 4R(L) (Table. 4.1) were used for this study. Samples were cut into pieces of 1cm × 1cm and ground using SiC abrasive papers of P1200 and P4000. They were then rinsed and ultrasonically cleaned in acetone for 10 minutes. The subsequent alkaline activation step included etching in 40 g/l NaOH solution for 15 seconds. Between each step, samples were rinsed with deionized water and then dried.

Samples were immersed in each conversion solution right after the final pretreatment step. After the immersion time was reached, the samples were dried and kept in a desiccator for further microstructural and electrochemical analyses.

5.1.2. Solution preparation and treatment conditions

The conversion solutions were prepared using hydrated cerium nitrate ($Ce(NO_3)_3.6H_2O$), sodium chloride (NaCl), hydrogen peroxide (H_2O_2) and deionized water.

Conditions of the conversion process are presented in Table. 5.1 and Table. 5.2.

Solutions were aged for at least 30 minutes prior to the coating process for cerium species to reach the equilibrium. To investigate the effect of each parameter (e.g. time and concentration), that parameter was varied while the others were kept constant. For example, constant $Ce(NO_3)_3$ concertation of 0.05 M was used to study the effect of NaCl concentration and addition of H_2O_2.

The effect of H_2O_2 addition was studied both in the presence and the absence of NaCl.

Table. 5.1. Details of the conversion process parameters (on the HPDC alloys)

Investigated parameter	Substrate	$Ce(NO_3)_3.6H_2O$ (M)	NaCl (M)	H_2O_2 (M)	Immersion time (min)
Concentration of $Ce(NO_3)_3$	2L	0.01*, 0.05**, 0.1***	0	0	1080 (18 h)
*pH= 4.98, **pH= 4.48, ***pH= 3.93					
Concentration of NaCl	2L, 4L	0.05	0.01, 0.05, 0.1	0	1080 (18 h)
Addition of H_2O_2/immersion time	2L, 4L	0.05	0	0.02	20, 60
pH=3.1					
Addition of H_2O_2 and NaCl /immersion time	2L	0.05	0.05	0.02	20, 60
pH=3.2					

Table. 5.2. Details of the conversion process parameters (on the Rheo-HPDC alloys)

Substrate	$Ce(NO_3)_3.6H_2O$ (M)	NaCl (M)	H_2O_2 (M)	Immersion time (h)
2R, 4R	0.01, 0.05, 0.1	0	0	1, 3, 6, 18, 24
2R, 4R	0.05	0.01, 0.05, 0.1	0	18
2R	0.05	0	0.02	0.3 (20 m),1
4R	0.05	0	0.01, 0.02	0.3 (20 m),1
2R	0.05	0.05	0.02	0.3 (20 m),1
4R	0.05	0.01, 0.05	0.02	0.3 (20 m),1

5.1.3. Layer characterization

Microstructural features of the cerium-based conversion coatings were examined by SEM, under high vacuum conditions with 20 kV beam energy. EDXS was exploited to measure the composition of the conversion layers and to collect the elemental maps. FIB-SEM was used for cross-sectioning and analysis of the treated surfaces. The FIB milling conditions were as follows: 30 kV, 5 nA for the rough milling and 1 nA for the final polishing. In this case, the beam energy of 15 kV was employed. For EDXS analysis 254 frames mapping and 50 μs dwell time were utilized.

The chemical state of the conversion treated samples were analyzed using XPS. Acquisitions were composed by wide scans on a binding energy range of 1250 – -5 eV using a 160 eV pass energy. High-resolution core line spectra were performed by setting the analyzer pass energy at 20 eV and the energy step at 0.05 eV. When necessary, charge compensation was utilized on the samples with scarce conductivity. Compensation was optimized by maximizing the peak intensity and minimizing the peak full width at half maximum (FWHM) of the main core line peaks. C 1s from contaminants at 285 eV was selected as a reference for energy scale alignment. The final energy resolution was ~ 0.35 eV. The analysis of the XPS spectra was performed using a home-made software based on the R platform. Care was taken when selecting the appropriate background subtraction and Gaussian components for peak fitting.

5.1.4. Electrochemical analysis

The electrochemical behavior and the corrosion resistance of CeCC treated Al-Si alloys were examined in a 0.05 M NaCl solution by potentiodynamic polarization and EIS tests.

A traditional three-electrode cell was exploited including the sample as the working electrode (with the exposure area of 1cm^2), a platinum electrode as the counter electrode and a silver/silver chloride electrode (Ag/AgCl (3 M KCl)) reference electrode (Fig. 3.1). In the polarization test, the sweep rate of 0.166 mV/s and the initial delay of 10 minutes were set. The cathodic and anodic branches were collected separately, starting from the OCP. The anodic and cathodic polarizations were stopped after the maximum current densities of 9×10^{-4} A/cm^2 and 4×10^{-5} A/cm^2 were reached, respectively. In the EIS tests, frequency ranged from 100 kHz to 10 mHz with 36 points and the amplitude of the sinusoidal potential signal was 10 mV. To guarantee the reliability of the data, the electrochemical tests were repeated at least three times. Moreover, to compare the results, all the electrochemical tests were also conducted on the bare alloys.

5.2. Results and discussion

5.2.1. Microstructural features

Fig. 5.1 shows the primary conversion coatings deposited from the solutions of different $Ce(NO_3)_3$ concentrations on the 2R alloy.

According to the images in Fig. 5.1, cerium hydroxide/oxide deposition (white islands in the backscattered SEM images) is or has been started locally. It can be observed that the amount of cerium-based precipitates is higher on the eutectic region or the iron-rich IM particles inside them. The deposition of the conversion layer increases with the concentration of $Ce(NO_3)_3$. It is noticeable that the background matrix of the conversion coating is less visible in case of the samples treated using the solutions of 0.01 and 0.05 M $Ce(NO_3)_3$, while for the sample immersed in the solution of 0.1 M $Ce(NO_3)_3$, the presence of a background matrix is easily detectable, especially due to its cracked microstructure.

According to the literature [65, 76], this means that the deposition of cerium hydroxide/oxide layer starts from the cathodic sites but it grows further to cover the entire surface [91]. In Fig. 5.1 (b), the SEM image from a cerium-based nucleus at higher magnification shows this lateral growth.

Higher $Ce(NO_3)_3$ concentration provides more cerium ions required for the precipitation since their numbers are reduced due to the formation of stable cerium nitrate complexes such as $Ce(NO_3)_5^{2-}$ and $Ce(NO_3)_6^{3-}$ [107]. These stable complexes result from the oxygen-donor ligand and cerium cation interactions [209].

In these series of treated substrates, no significant difference can be observed on the degree of cerium deposition over α_1 and α_2-Al particles. As expected, not all of the eutectic regions are covered by the CeCC and therefore not all of them were cathodically activated.

The effect of the addition of chloride ions and/or hydrogen peroxide on the morphology of the CeCC layers on the 2R alloy is presented in the SEM images of Fig. 5.2.

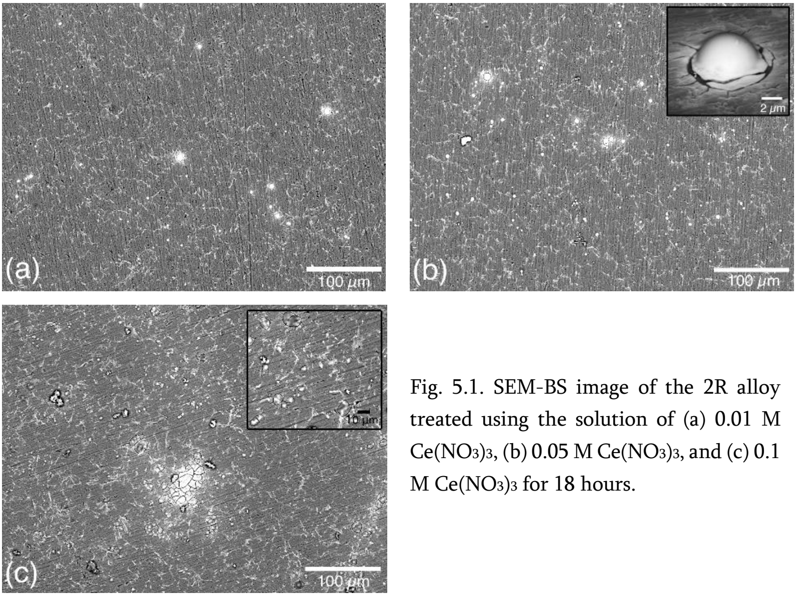

Fig. 5.1. SEM-BS image of the 2R alloy treated using the solution of (a) 0.01 M $Ce(NO_3)_3$, (b) 0.05 M $Ce(NO_3)_3$, and (c) 0.1 M $Ce(NO_3)_3$ for 18 hours.

Considering Fig. 5.2 (a), with 0.1 M NaCl in the solution a higher amount of cerium depositions is observed. This coating shows some differences in comparison to the coating deposited from the same solution without NaCl (Fig. 5.1 (b)). In the presence of NaCl, the primary α-Al particles (α_1-Al) show less coverage of CeCC (or a thinner layer) on their surfaces compared to α_2-Al particles or compared to the samples treated using the solutions without NaCl. SEM image of this coating at higher magnification and the results of EDXS analysis confirm this phenomenon (Fig. 5.3).

Chloride ions in the conversion solution have an accelerating effect on the precipitation of cerium hydroxide/oxide layer.

They can break the native aluminum oxide layer on the alloy surface and accelerate and activate the corrosion reactions (anodic and cathodic) on the micro-galvanic couples, formed in the eutectic regions [210].

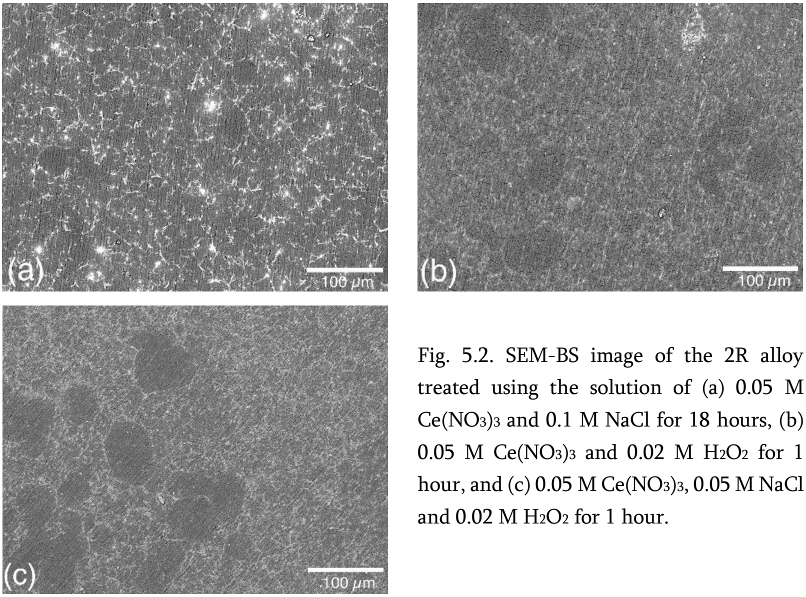

Fig. 5.2. SEM-BS image of the 2R alloy treated using the solution of (a) 0.05 M $Ce(NO_3)_3$ and 0.1 M NaCl for 18 hours, (b) 0.05 M $Ce(NO_3)_3$ and 0.02 M H_2O_2 for 1 hour, and (c) 0.05 M $Ce(NO_3)_3$, 0.05 M NaCl and 0.02 M H_2O_2 for 1 hour.

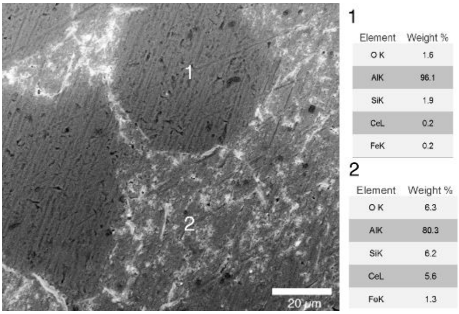

1

Element	Weight %
O K	1.6
AlK	96.1
SiK	1.9
CeL	0.2
FeK	0.2

2

Element	Weight %
O K	6.3
AlK	80.3
SiK	6.2
CeL	5.6
FeK	1.3

Fig. 5.3. SEM-BS image and results of EDXS analysis of the 2R alloy treated using the solution of 0.05 M $Ce(NO_3)_3$ and 0.1 M NaCl for 18 hours.

In fact, they are selectively adsorbed on the crystal lattice of the aluminum oxide film and make complexation with Al^{3+} hydrate ions. This reaction leads to surface activation, an unstable film, and formation of local defects [117]. Which result in a higher pH and therefore more cerium hydroxide deposition [100, 211]. Nitrate ions are not able to break down the aluminum oxide layer and they also passivate the surface of aluminum alloys by incorporating into the oxide [87, 212, 213]. Therefore, a faster deposition is expected in the presence of chloride ions compared to the plain cerium nitrate solution.

Moreover, the activating effect of chloride ions highlights the difference between the two different α-Al particles. α_1-Al particles are less covered compared to α_2-Al particles, resulting in a heterogeneous deposition of the conversion layer due to the different levels of cathodic activity. The results of WDS analysis of these grains show that they differ in the silicon content in the solid solution of aluminum: α_2-Al grains contain higher silicon in comparison to α_1-Al ones (Fig. 4.8). The higher level of silicon in α_2-Al phase contributes to increasing its potential toward more cathodic values [4]. Moreover, the size of the grains makes α_2-Al grains closer and more interacting with the eutectic silicon phase and the iron-rich IM particles and therefore easier to be covered.

The presence of chloride ions in the conversion solution can also affect the valence state of cerium.

The equilibrium potential of the oxidation reaction of Ce (III) to Ce (IV) is sensitive to the anions present in the solution:

$$Ce^{3+}+2H_2O \leftrightarrow Ce(OH)_2^{2+}+2H^++e^- \qquad \text{Eq. 5.1}$$

The chloride ions decrease the equilibrium potential by 400 mV, allowing the oxidation reaction to take place more easily [209].

Hydrogen peroxide can be added to the conversion solution to act as an oxidizing agent and therefore to have a more homogenous deposit. The presence of hydrogen peroxide, either alone or together with chloride ions increases the deposition rate and the thickness of the conversion layer, resulting in the formation of a conversion layer with cracked-mud structure (Fig. 5.2 (b) and (c)). This feature is due to the stresses induced in the coating during the drying step [78]. By adding hydrogen peroxide, the entire surface is covered by the conversion layer. However, some heterogeneities are still visible on the coating surface in which α_1-Al particles are covered by a thinner deposit.

In the deposition of cerium-based conversion layer, hydrogen peroxide acts as a complexing agent, an oxidant, a crystallization inhibitor, and a source of OH^- ions [116]. Reduction of hydrogen peroxide on the cathodic areas provides a source of hydroxyl ions. Hydrogen peroxide also oxidizes Ce^{3+} ions to Ce^{4+} [108, 116]:

$$2Ce^{3+} + H_2O_2 + 2OH^- \leftrightarrow 2Ce(OH)_2^{2+} \qquad \text{Eq. 5.2}$$

The literature reports that these conditions lead to the formation of a cerium hydroxide/oxide coating containing mainly Ce (IV) species [108, 116].

Fig. 5.4 summarizes surface morphologies of the cerium-based conversion coatings on the 2L alloy, deposited from the different conversion solutions. These images depict the effect of the addition of NaCl and H_2O_2 on the morphology of the conversion coatings. Similar features to those of CeCC on the semi-solid alloy can be observed on the conventional HPDC alloy.

According to Fig. 5.4, on all of the surfaces, some relatively large pits are visible. According to the appearance of the samples after the alkaline activation step, this is partially due to the alkaline cleaning which removes a number of IM particles [82, 91].

However, localized attack on the surface seems to occur also during the formation of cerium-based conversion layers. For the sample treated using the plain solution which only contained $Ce(NO_3)_3$ (Fig. 5.4 (a)), localized cerium hydroxide/oxide deposition is detectable as white islands in the backscattered SEM image.

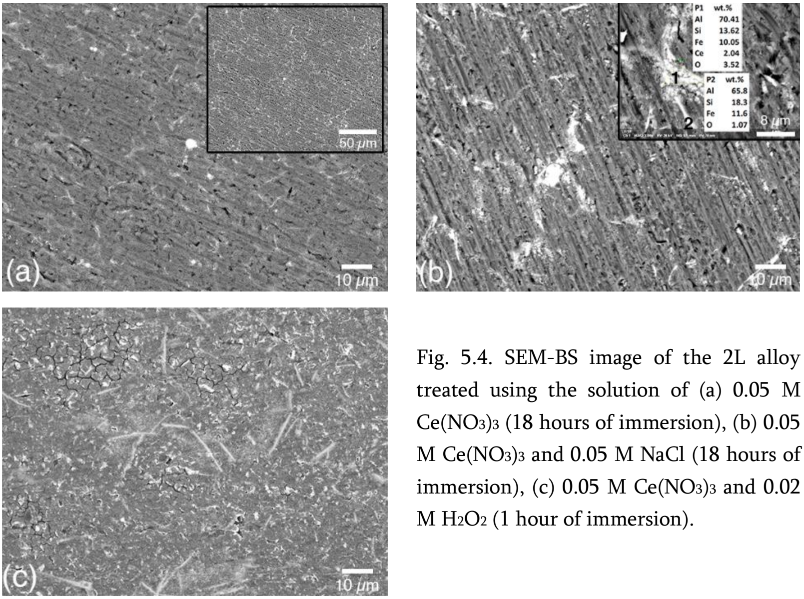

Fig. 5.4. SEM-BS image of the 2L alloy treated using the solution of (a) 0.05 M $Ce(NO_3)_3$ (18 hours of immersion), (b) 0.05 M $Ce(NO_3)_3$ and 0.05 M NaCl (18 hours of immersion), (c) 0.05 M $Ce(NO_3)_3$ and 0.02 M H_2O_2 (1 hour of immersion).

Both of the eutectic silicon phase and β-AlFeSi particles, in the alloy microstructure, are cathodic with respect to the α-Al phase [113]. Therefore, as mentioned before, they are proper sites for the cathodic reactions (e.g. oxygen reduction) and the local increase of pH which leads to the deposition of the conversion coating. It is then reasonable to expect the presence of a deposited layer with a higher thickness on these phases [109]. It should be noted that the coating growth starts from the cathodic sites, but it continues to cover the whole surface [93]. This fact is depicted in the elemental map of Ce related to this sample which is shown in Fig. 5.5 (e). In the case of the sample in Fig. 5.4 (a), the exact sites of localized deposition are not quite clear to be either the eutectic silicon phase or iron-rich IM particles.

The situation gets clearer by adding 0.05 M NaCl to the conversion solution (Fig. 5.4 (b)). According to Fig. 5.4 (b) and the EDXS analysis, in this condition, deposition of the conversion layer is still mainly localized.

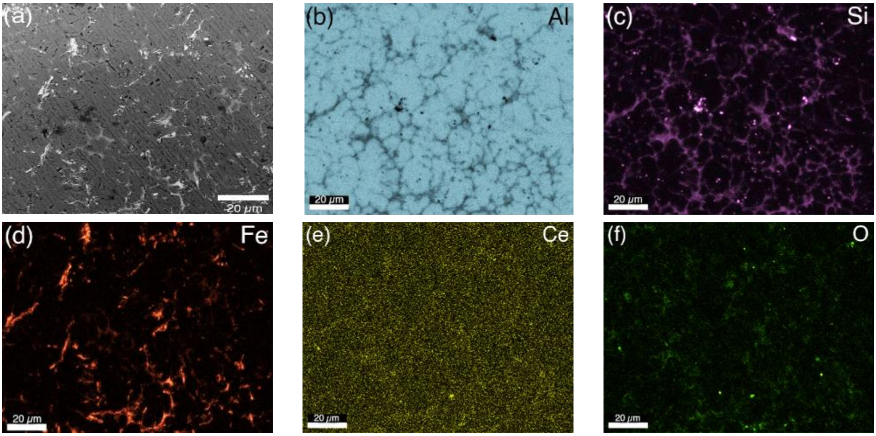

Fig. 5.5. (a) SEM-BS image of the 2L alloy treated using the solution of 0.05 M $Ce(NO_3)_3$ for 18 hours and the elemental map of (b) Al, (c) Si, (d) Fe, (e) Ce, and (f) O.

However, a bigger fraction of the cathodic sites is covered by the cerium-based layer. In this case, it seems that the coating has started to cover the whole surface. According to Fig. 5.4 (b), more pits are visible on the surface which can be attributed to the corrosion and breakdown of the aluminum oxide layer in the presence of chloride ions [117]:

$$Al^{3+}+4Cl^{-} \rightarrow AlCl_4^{-} \qquad \text{Eq. 5.3}$$

It is worth mentioning that, $AlCl^{-}_4$ is easily hydrolyzed according to the following reaction. The remained chloride ions continue to react with the aluminum surface:

$$AlCl_4^{-}+2H_2O \rightarrow Al(OH)_2Cl+2H^{+}+3Cl^{-} \qquad \text{Eq. 5.4}$$

The breakdown of the oxide layer takes place especially at the interface of α-Al phase and the eutectic silicon and/or iron-rich IM particles [210]. This phenomenon can be controversial, since it may also result in the formation of subsurface crevices [87]. However, the formation of subsurface crevices usually happens with a combination of NaCl and H_2O_2 in the solution [74]. Results of the EDXS analysis in the eutectic region which contains some iron-rich IM particles are presented in Fig. 5.4 (b). Presence of cerium on the eutectic region (point number 1) is evident. Point number 2 is an iron-rich IM particle on which the analysis does not show any cerium content. It seems that the deposition has started from a eutectic area containing iron-rich IM particles.

By adding H_2O_2 to the solution, the coating morphology changes and it forms a continuous layer with a mud-crack structure in some regions, covering all the surface (Fig. 5.4 (c)).

Results of XPS analysis of the 2R alloy treated using three different solutions (including the solution of 0.05 M $Ce(NO_3)_3$, the solution of 0.05 M $Ce(NO_3)_3$ and 0.1 M NaCl, and the solution of 0.05 M $Ce(NO_3)_3$ and 0.02 M H_2O_2) are illustrated in Fig. 5.6 (a), (b) and (c), respectively.

In each of the XPS spectrum, a peak of carbon is also noticeable. This peak is attributed to the accumulation of contaminants on the surface due to exposure to air, which has also been observed and reported before by other researchers [95]. It can also be due to the die releasing agent which is entrapped in the very first solidification layer of the aluminum alloy surface during casting. This was proved by XPS analysis of the bare aluminum alloys in which carbon peak was present in all the specimens (The results are not reported here).

The analyzed cerium-based conversion coatings presented a mixture of Ce (III) and Ce (IV) compounds. The interpretation of the Ce 3d core line was made a long time ago by Burroughs et al. [214]. In this case, the more recent work of Romeo et al. [215] can be also referred. Ce (IV) and Ce (III) in their ground state possess a $4f^0$ and $4f^1$ orbital, respectively.

When an X photon creates a hole in the 3d level a rearrangement of the cerium electronic structure in the valence band occurs. In particular, the 4f orbital is pulled away from the Fermi into the valence band to screen the 3d hole. This in the presence of Ce (IV) or Ce (III) oxides or hydroxides leads to a strong hybridization of the cerium ground state $4f^0$ with the 2p oxygen orbital.

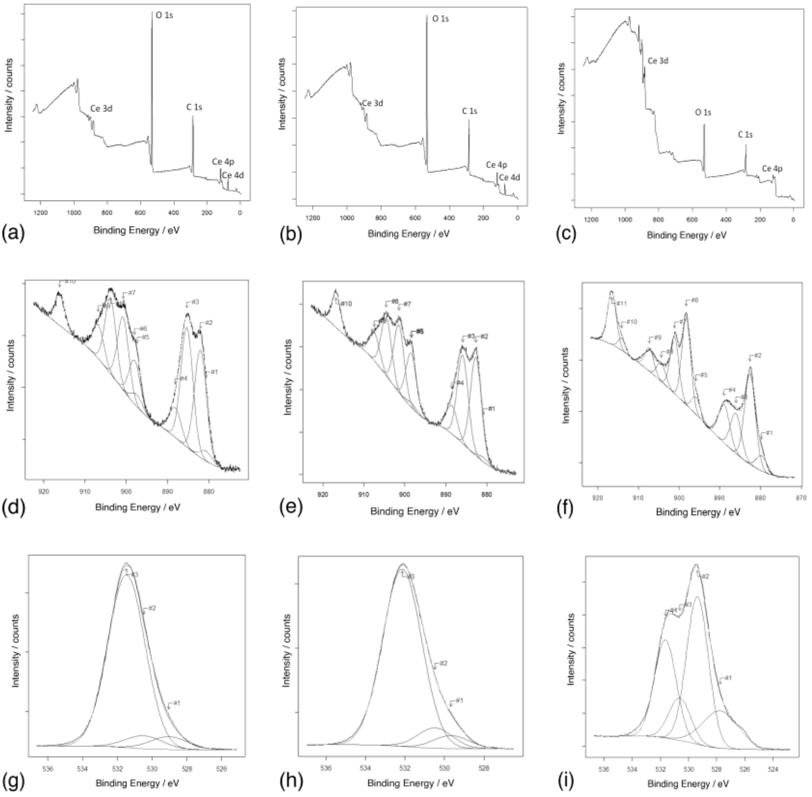

Fig. 5.6. XPS analysis of the 2R alloy treated using the solution of (a), (d), (g) 0.05 M $Ce(NO_3)_3$ for 18 hours; (b), (e), (h) 0.05 M $Ce(NO_3)_3$ and 0.1 M NaCl for 18 hours; (c), (f), (i) 0.05 M $Ce(NO_3)_3$ and 0.02 M H_2O_2 for 1 hour. (a), (b), (c) survey spectra; (d), (e), (f) Ce 3d core line, (g), (h), (i) O 1s core line.

Concerning the analysis, the Ce 3d core line appears as doublets in the XPS spectra due to the spin orbit splitting. The energy of the photo-emitted 3d electron will depend on the coupling between the initial 3d and 4f hybridized orbital. The result of this coupling is that in the case of Ce (IV) the $3d_{5/2}$ level will show three components while the same orbital in Ce (III) will be composed of two features. Then the description of the Ce 3d core line in presence of both the Ce (III) and Ce (IV) will need a total of 10 fitting components.

Here the component assignment and nomenclature is done in agreement with the work of Burroughs et al. [214]: v, v'' and v''' are associated with Ce (IV). The first two derived from a mixture of $(5d\ 6s)^0\ 4f^2\ O\ 2p^4$ and $(5s\ 6d)'\ 4f^1\ O\ 2p^5$ orbitals, while v''' is associated to $(5d\ 6s)^0\ 4f^0\ O\ 2p^6$ [215]. Features derived from Ce (III) are indicated with v_0 and v' and are generated by mixing $(5d\ 6s)^0\ 4f^2\ O2p^4$ and $(5d\ 6s)^0\ 4f^1\ O2p^5$ orbitals.

A list of correspondent components is presented for the $3d_{3/2}$ using the letter u and the same indexes. u and v components are separated by the spin orbit splitting energy which for cerium is ~18.3 eV. A summary of results for the coatings deposited from the different conversion solutions is presented in Table. 5.3.

The ratio of Ce (III)/Ce (IV) (in forms of oxide and/or hydroxide) is 0.86 for the conversion layer from the plain solution (with only 0.05 M $Ce(NO_3)_3$), 0.79 for the layer obtained from the solution with chloride ions, and 0.55 for the coating deposited from the solution containing hydrogen peroxide. As expected, the presence of chloride ions and hydrogen peroxide increases the fraction of Ce (IV) species in the coatings.

Hydrogen peroxide affects by oxidizing Ce^{3+} while chloride ions by decreasing the equilibrium potential of the oxidation reaction of Ce^{3+} to Ce^{4+}. Ce (III) species are shown to be concentrated in the inner layer of the conversion coating, while Ce (IV) species are mostly located in the outer layer of the coating [95, 109].

Considering oxygen peaks (high resolution peaks in Fig. 5.6 (g), (h) and (i)), the peaks centered at 531.49 eV, 532.14 eV, and 530.62 eV are ascribable to aluminum oxide (Al_2O_3) [109]. While the shoulders at 529.23 eV, 530.29 eV, 529.67 eV, 530.49 eV, 529.37 eV, and 530.62 eV can be attributed to the presence of CeO_2 and Ce_2O_3, respectively. Aluminum oxide (Al_2O_3) percentages vary from 16 % in the conversion coating from the plain solution to 16.5 % for the layer deposited from the solution with chloride ions and to 4 % for the coating deposited from the solution containing hydrogen peroxide.

Table. 5.3. Summary of results derived from XPS spectra of the cerium-based conversion layers on the 2R alloy

Conversion solution		Ce_2O_3	CeO_2	Ce_2O_3	CeO_2	CeO_2
0.05 M $Ce(NO_3)_3$	Ce3d5/2 BE	V_0	V	V’	V”	V”’
		880.6	882.0	885.3	888.1	897.4
	Ce3d3/2 BE	U_0	U	U’	U”	U”’
		899.0	900.7	903.8	906.8	916.1
0.05 M $Ce(NO_3)_3$, 0.1 M NaCl	Ce3d5/2 BE	V_0	V	V’	V”	V”’
		880.2	882.1	885.3	888.0	897.7
	Ce3d3/2 BE	U_0	U	U’	U”	U”’
		898.0	900.9	903.9	906.8	916.2
0.05 M $Ce(NO_3)_3$, 0.02 M H_2O_2	Ce3d5/2 BE	V_0	V	V’	V”	V”’
		879.7	882.6	886.1	888.9	895.9
	Ce3d3/2 BE	U_0	U	U’	U”	U”’
		898.2	901.1	904.4	907.3	916.5

The presence of hydrogen peroxide in the conversion solution also changes the oxidation state of aluminum, in which the sample treated using the solution of 0.05 M $Ce(NO_3)_3$ and 0.02 M H_2O_2 shows a significant difference in O 1s binding energy compared to the other two samples. In addition, in the oxygen peak in Fig. 5.6 (i), there is a component at the low binding energy whose essence is unclear to us.

Results of XPS analysis of samples of the 2L alloy treated using the solution of 0.05 M $Ce(NO_3)_3$ and the solution of 0.05 M $Ce(NO_3)_3$ and 0.02 M H_2O_2

are illustrated in Fig. 5.7. The results are similar to those on the 2R alloy. Based on these results, the Ce (III)/Ce (IV) ratio is 1.1 and 0.75 for the conversion coatings from the plain and hydrogen peroxide-containing conversion solutions, respectively. As expected, the addition of H_2O_2 to the conversion solution changes the valence state of cerium in the coating in favor of Ce (IV).

5.2.2. Effect of Si content

The conversion layers deposited on the 4R alloy from the solutions containing chloride ions (Fig. 5.8 (a)), hydrogen peroxide (Fig. 5.8 (b)), and chloride ions together with hydrogen peroxide (Fig. 5.8 (c)) have similar characteristics to those on the 2R alloy. The heterogeneity related to the thinner deposition over α_1-Al particles is detectable especially in the conversion coating deposited from the solution of 0.05 M $Ce(NO_3)_3$ and 0.1 M NaCl (Fig. 5.8 (a)).

The addition of hydrogen peroxide leads to the formation of a thick cracked coating all over the surface (Fig. 5.8 (b) and (c)). This coating is also heterogeneous in some parts as it can be seen in Fig. 5.8 (b).

Surface morphology of the cerium-based layer deposited from a combination of cerium ions, chloride ions, and hydrogen peroxide, contains cerium-rich nodules over the cracked background matrix.

Fig. 5.9 presents the coatings deposited from the same solution of those of Fig. 5.4 (a) and (b) (with the same and higher concentrations of NaCl) on the 4L alloy.

For the sample immersed in the solution containing only $Ce(NO_3)_3$, local deposition of the cerium compounds is similar to that on the alloy with a lower silicon content (the alloy 2L, Fig. 5.4). However, in this case, bigger and more deposition can be seen on the surface.

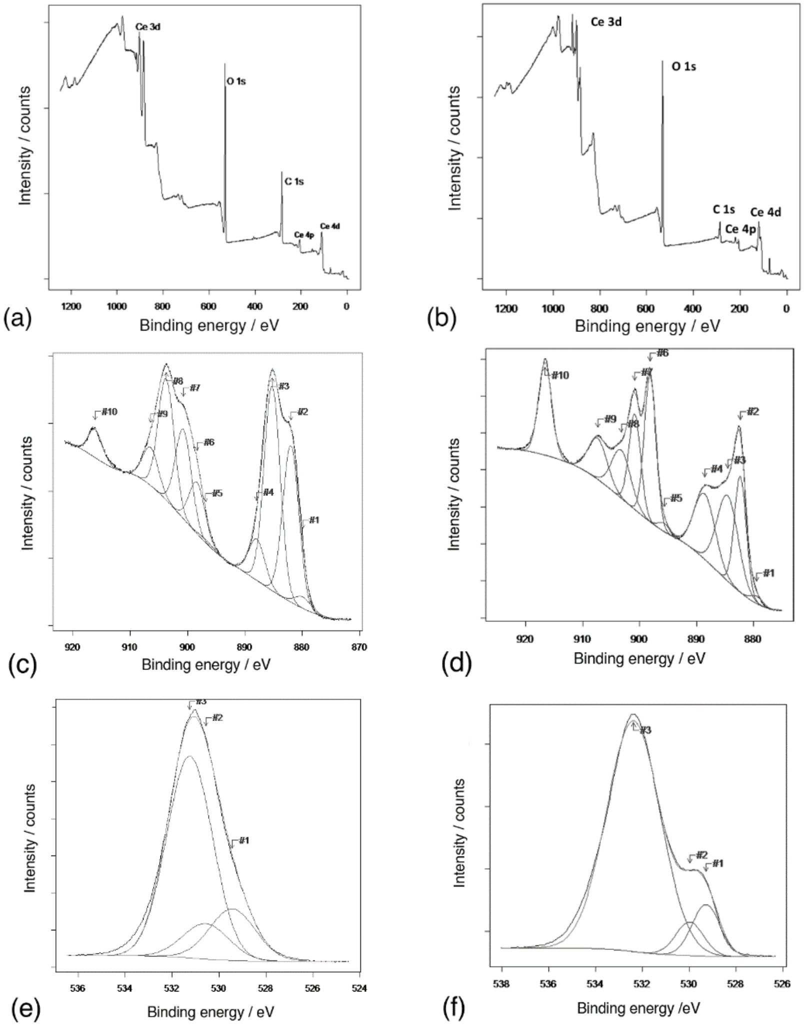

Fig. 5.7. XPS analysis of the 2L alloy treated using the solution of (a), (c), (e) 0.05 M Ce(NO_3)$_3$ for 18 hours; (b), (d), (f) 0.05 M Ce(NO_3)$_3$ and 0.02 M H_2O_2 for 1 hour. (a), (b) survey spectra; (c), (d) Ce 3d core line, (e), (f) O 1s core line.

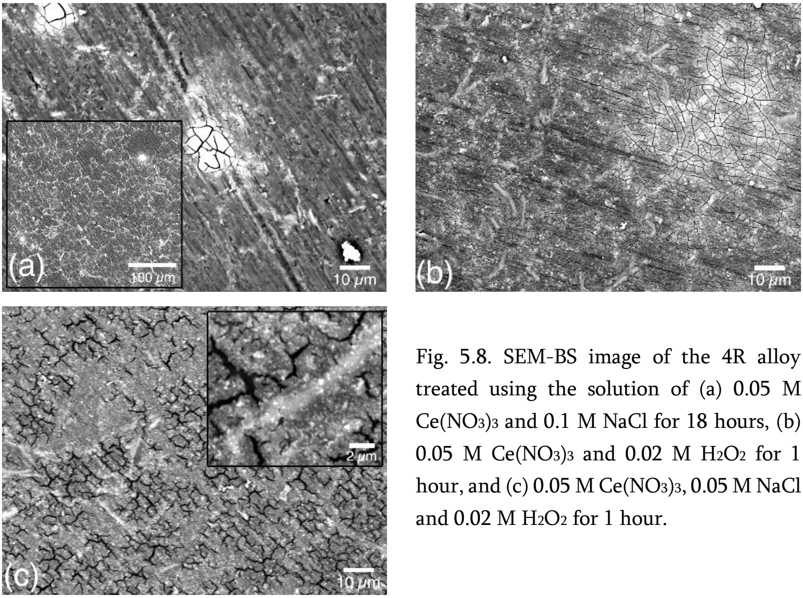

Fig. 5.8. SEM-BS image of the 4R alloy treated using the solution of (a) 0.05 M $Ce(NO_3)_3$ and 0.1 M NaCl for 18 hours, (b) 0.05 M $Ce(NO_3)_3$ and 0.02 M H_2O_2 for 1 hour, and (c) 0.05 M $Ce(NO_3)_3$, 0.05 M NaCl and 0.02 M H_2O_2 for 1 hour.

This is most probably attributed to the higher cathodic activity due to the presence of a bigger eutectic fraction. In the absence of chloride ions in the conversion solution, many of iron-rich IM particles remain uncovered (Fig. 5.9 (a)). By adding NaCl, more of the iron-rich IM particles are passivated by the cerium conversion layer and the coating morphology becomes more homogenous (Fig. 5.9 (b)). By increasing the concentration of NaCl, the coating thickness increases even more and it forms a cracked microstructure (Fig. 5.9 (c)).

Combining H_2O_2 and NaCl in the solution gives us a better insight into the preferential locations of cerium hydroxide/oxide deposition. Fig. 5.10 presents the coating deposited on a sample of the 4L alloy, using the solution of 0.05 M $Ce(NO_3)_3$, 0.05 M NaCl and 0.02 M H_2O_2. According to these figures, precipitation of cerium-based layer starts from iron-rich IM particles.

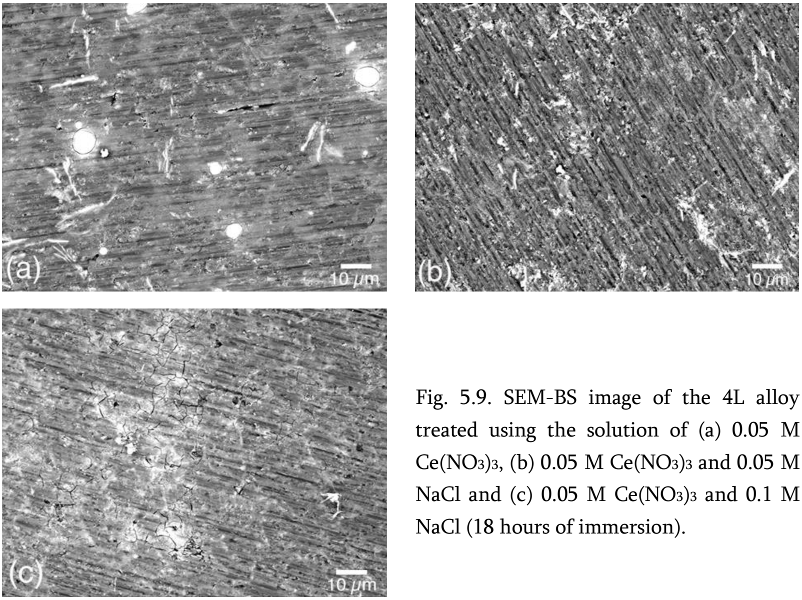

Fig. 5.9. SEM-BS image of the 4L alloy treated using the solution of (a) 0.05 M $Ce(NO_3)_3$, (b) 0.05 M $Ce(NO_3)_3$ and 0.05 M NaCl and (c) 0.05 M $Ce(NO_3)_3$ and 0.1 M NaCl (18 hours of immersion).

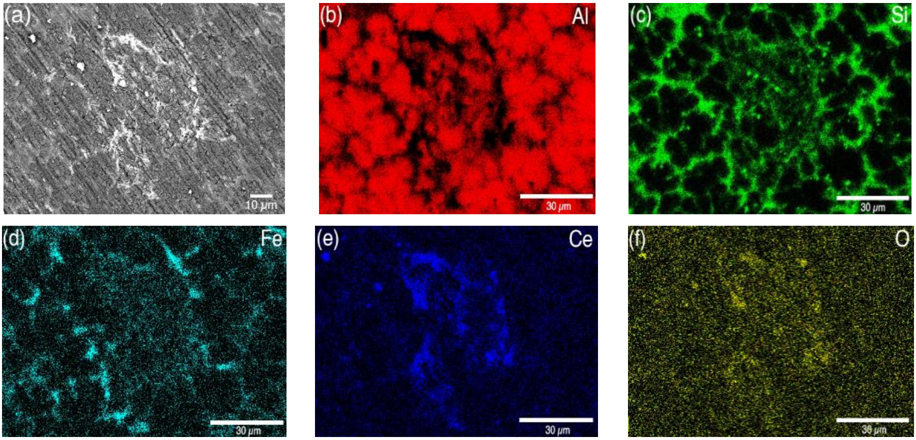

Fig. 5.10. SEM-BS image of the 4L alloy treated using the solution of 0.05 M $Ce(NO_3)_3$, 0.05 M NaCl and 0.02 M H_2O_2 (1 hour of immersion) and the elemental map of (b) Al, (c) Si, (d) Fe, (e) Ce, (f) O.

5.2.3. Deposition mechanism

Fig. 5.11 provides the cross-sectional view of the conversion coating on the 2L alloy, treated using the solution of 0.05 M $Ce(NO_3)_3$ and 0.1 M NaCl. The elemental maps of Al, Si, Fe, Ce and O are also provided in this figure.

Images in Fig. 5.11 show a localized deposition of cerium hydroxide/oxide, which apparently has started from an iron-rich IM particle.

As also obvious from SEM images of the alloy surface (Fig. 5.4 (b)), IM particles are located inside the eutectic area, which is detectable from the Si map (Fig. 5.11 (c)) as well. Therefore, we can assume that iron-rich IM particles are the primary locations for the deposition of cerium compounds. This cross-sectional view also confirms the lateral growth of cerium hydroxide/oxide nucleus, which finally covers the entire surface (Fig. 5.11 (a) and (e)).

No subsurface crevices are visible at the interface of the conversion coating and the aluminum alloy substrate. It seems that NaCl concentration of 0.1 M (in the conversion solution) is high enough to promote the conversion process and low enough not to cause any undesired pitting/crevice corrosion.

It is worth mentioning that our investigations show that the coating thickness is very different over the surface. This can be due to the high surface roughness and the presence of the different microstructural components. The thickness reaches the maximum of 5-8 μm over the localized depositions and it falls to 1-2 μm near to them and to 50-200 nm far from these precipitations. The coating is not detectable in some points on the surface.

Fig. 5.12 provides a cross-sectional SEM image of the conversion coating on the 2R alloy, immersed in the solution of 0.05 M $Ce(NO_3)_3$ for 18 hours. The elemental maps of Al, Si, Fe, Ce, and O are also provided in this figure. These images depict the presence of an iron-rich IM particle located inside the eutectic region, which is detectable through the elemental map of Si (Fig. 5.12 (c)).

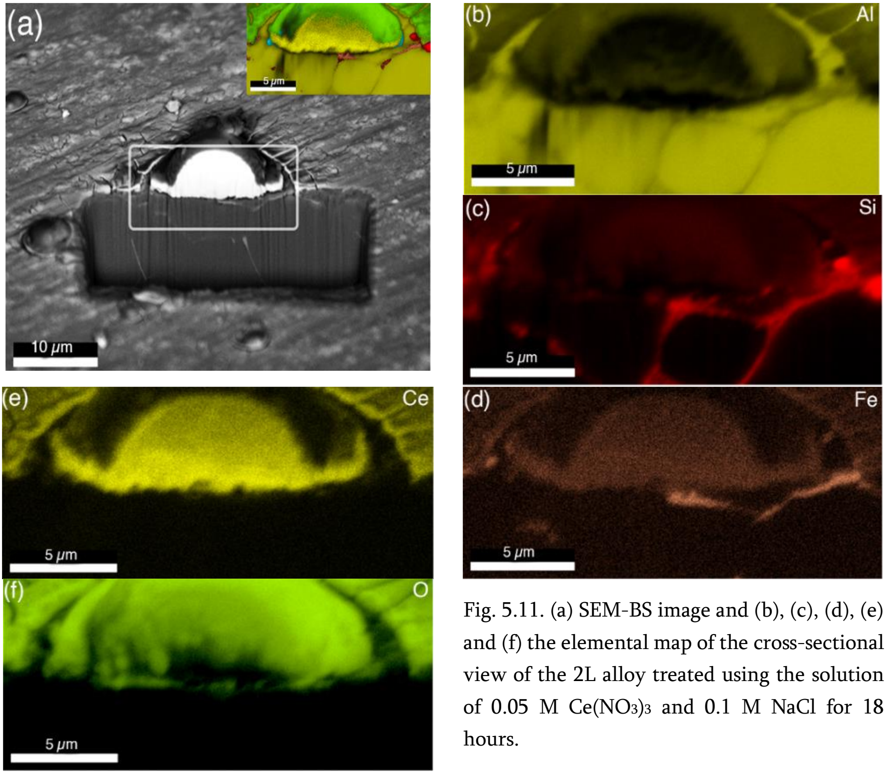

Fig. 5.11. (a) SEM-BS image and (b), (c), (d), (e) and (f) the elemental map of the cross-sectional view of the 2L alloy treated using the solution of 0.05 M $Ce(NO_3)_3$ and 0.1 M NaCl for 18 hours.

It can be observed that the formation of cerium-based layer started from the iron-rich IM particle. In addition, a cavity is visible under the cerium-based nucleus where the IM particle is located. The presence of this cavity is due to the corrosion process and is the result of the dissolution of aluminum phase in the eutectic region. It is worth mentioning that many cerium-based precipitates were checked and a cavity was always seen underneath each of them. According to the elemental map of O (Fig. 5.12 (f)), there is also oxide inside the cavity.

SEM image and the elemental maps from the cross-sectional view of a cerium-based nucleus on the 2R alloy treated in the solution of 0.05 M $Ce(NO_3)_3$ and 0.1 M NaCl for 18 hours are depicted in Fig. 5.13.

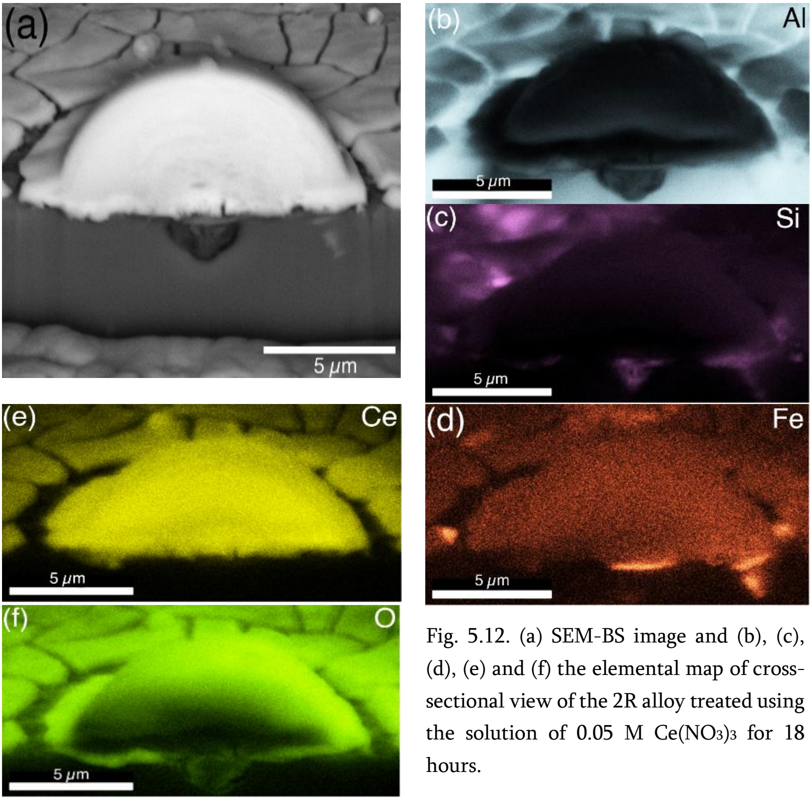

Fig. 5.12. (a) SEM-BS image and (b), (c), (d), (e) and (f) the elemental map of cross-sectional view of the 2R alloy treated using the solution of 0.05 M $Ce(NO_3)_3$ for 18 hours.

The interesting phenomenon captured in this image is the oxidation of the IM particle, which can be seen through the oxygen mapping in Fig. 5.13 (f). The oxide seems to fill the cavity that was formed in the previous step.

In the presence of chloride ions in the conversion solution, anodic and cathodic reactions are promoted and accelerated. After dissolution of aluminum from the aluminum phase, another process that can occur is the selective dissolution of aluminum from the IM particle that makes it richer in iron and silicon [216].

Considering the OCP of this system (~ -0.6 V), pH of the solution (4.4), and according to Pourbaix diagram of iron [217], oxidation of iron is not thermodynamically possible. However, cathodic reactions increase the pH locally high enough for the possible formation of iron oxide, when the entire aluminum phase has been dissolved.

Moreover, silicon does not seem to be participating in the oxidation process as no silicon is detected in the oxide.

The extension of iron oxidation is visible in the SEM image and the EDXS results taken after removing the conversion layer as shown in Fig. 5.14.

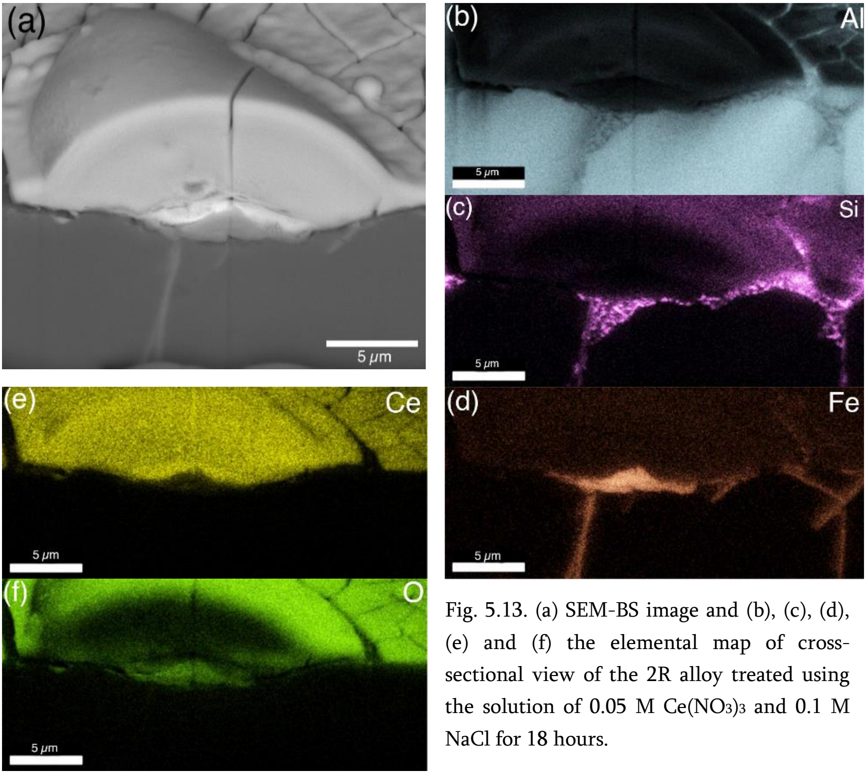

Fig. 5.13. (a) SEM-BS image and (b), (c), (d), (e) and (f) the elemental map of cross-sectional view of the 2R alloy treated using the solution of 0.05 M $Ce(NO_3)_3$ and 0.1 M NaCl for 18 hours.

Upon oxidation of iron, the particle becomes more cathodic [216], therefore, more suitable for the cathodic reactions.

The very first layer of the cerium-based nuclei seems to be richer in cerium compounds as it appears whiter in the backscattered image (Fig. 5.13 (a)). The rest of the coating can be assumed to be a mixture of cerium hydroxide/oxide and aluminum oxide.

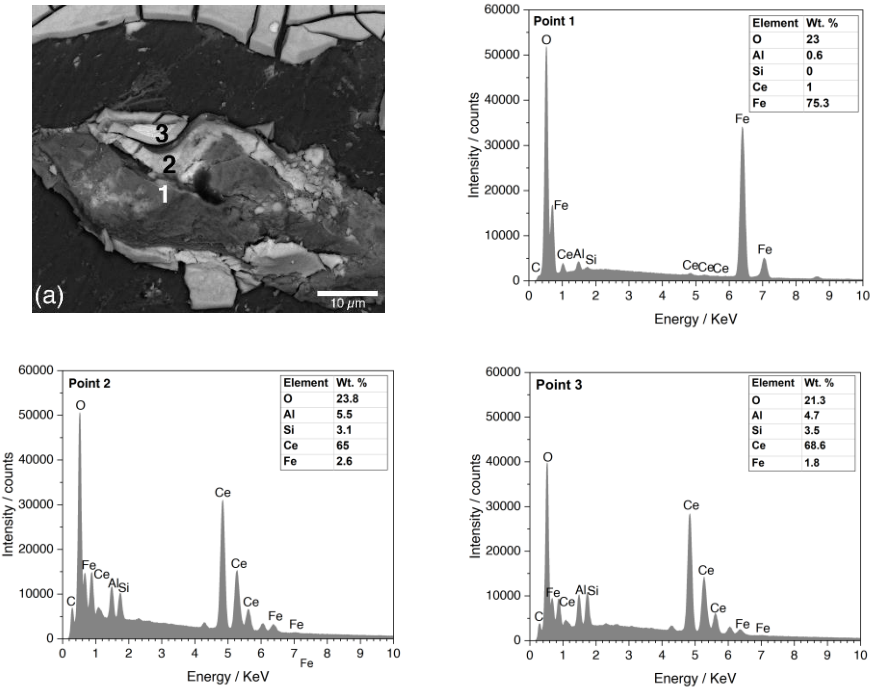

Point 1

Element	Wt. %
O	23
Al	0.6
Si	0
Ce	1
Fe	75.3

Point 2

Element	Wt. %
O	23.8
Al	5.5
Si	3.1
Ce	65
Fe	2.6

Point 3

Element	Wt. %
O	21.3
Al	4.7
Si	3.5
Ce	68.6
Fe	1.8

Fig. 5.14. (a) SEM-BS image of underneath a cerium-based nucleus (the sample treated using the solution of 0.05 M $Ce(NO_3)_3$ and 0.1 M NaCl for 18 hours), (b), (c), and (d) EDXS results from different points in the SEM image.

Fig. 5.15 presents the proposed formation mechanism of the cerium-based conversion layer. The presence of iron-rich IM particles is the main reason for the deposition of the conversion layer on the Al-Si alloy. According to our results, the formation mechanism can include three steps:

1. Dissolution of the aluminum phase next to an iron-rich IM particle until there is no connection between the IM particle and the aluminum matrix. The cathodic reactions are localized on the IM raising the pH and triggering the cerium hydroxide/oxide deposition.
2. Selective dissolution of aluminum from the IM particle and then oxidation of the remained iron. The dissolution of aluminum from the iron-rich IM particle can occur according to the following reaction [218]:

$$2Al+2OH^-+6H_2O \rightarrow 2Al(OH)_4^-+3H_2 \qquad \text{Eq. 5.5}$$

The iron oxide fills the cavity that was formed due to the dissolution of aluminum in the previous step. Cerium deposition continues during this step.

3. The growth of the existing cerium hydroxide/oxide nucleus and the start of lateral growth.

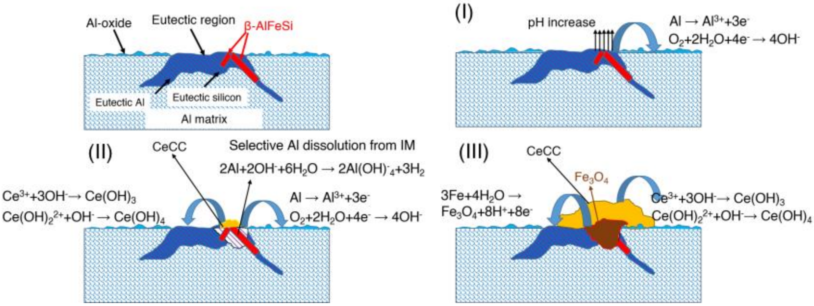

Fig. 5.15. Formation mechanism of the cerium-based conversion coating.

5.2.4. Electrochemical behavior (on Rheo-HPDC alloys)

Fig. 5.16 depicts the results of EIS test on samples of the 2R alloy treated using different conversion solutions. It presents the impedance and phase angle spectra after 6 and 24 hours of immersion in 0.05 M NaCl solution. The impedance values for all the samples are quite stable for 24 hours. Regarding the effect of $Ce(NO_3)_3$ concentration (Fig. 5.16 (a) and (d)), all the conversion layers possess higher impedance values at low frequencies compared to the bare aluminum alloy.

The low-frequency impedance modulus value, which is obtained at the frequency of 0.01 Hz ($|Z|_{0.01\ Hz}$) is an estimate of the total resistance of the system [67]. As it is obvious from Fig. 5.16 (a) and (d), these values are increased by more than one order of magnitude for the treated samples compared to the bare aluminum alloy. This improvement is due to the presence of cerium-based conversion layer, which especially passivates the iron-rich IM particles located inside the eutectic regions. Passivating these phases hinders the micro-galvanic coupling and therefore the corrosion process.

In general, in these set of results, the best corrosion performance is related to the conversion layer deposited from the solution of 0.05 M $Ce(NO_3)_3$. As the $Ce(NO_3)_3$ concentration increases so does the deposition extent and the thickness of the conversion layer. However, it seems that if the concentration of $Ce(NO_3)_3$ is too high (in this case 0.1 M) the deposited layer will develop cracks and therefore decrease its protection (Fig. 5.1(c)).

The addition of different concentrations of NaCl to the conversion solution also produces coatings with higher impedance values in comparison to the bare aluminum substrate.

However, according to the results shown in Fig. 5.16 (b) and (e), none of the conversion coatings deposited from NaCl containing solutions shows higher impedance values compared to those of the coating from the plain $Ce(NO_3)_3$ solution.

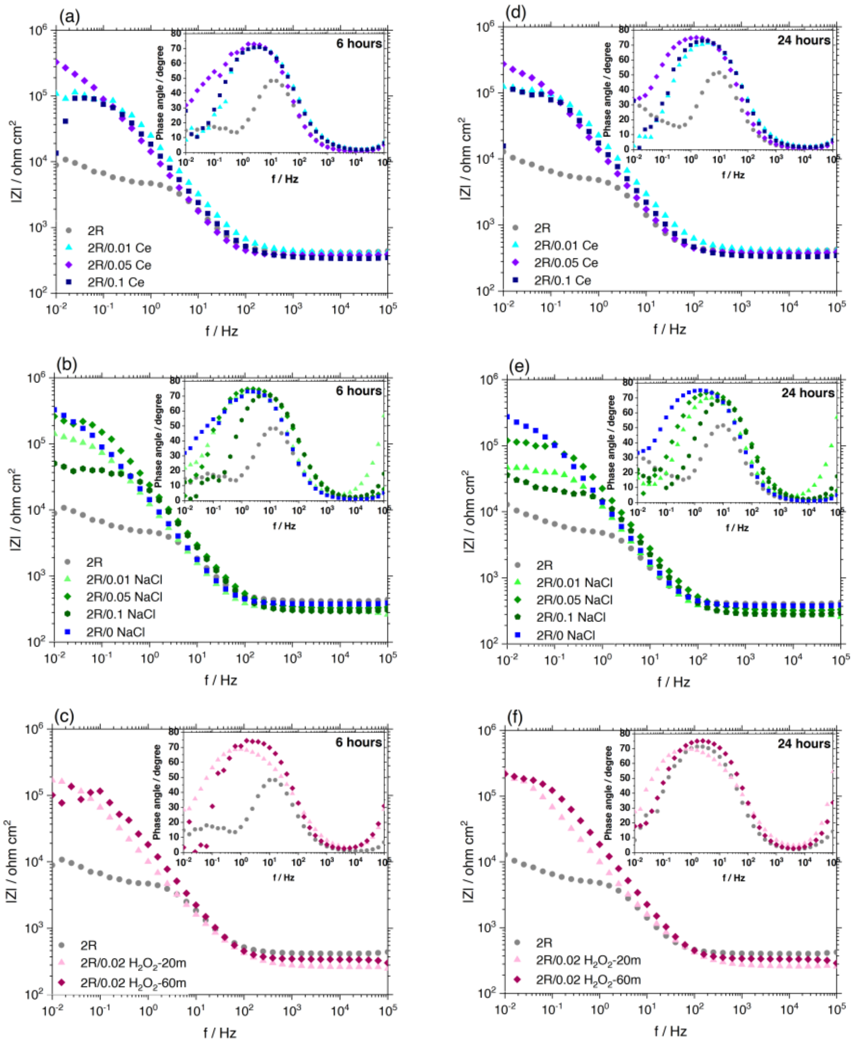

Fig. 5.16. EIS spectra of treated samples of the 2R alloy using the conversion solution of (a), (d) x M $Ce(NO_3)_3$ for 18 hours, (b), (e) 0.05 M $Ce(NO_3)_3$ and x M NaCl for 18 hours, (c), (f) 0.05 M $Ce(NO_3)_3$, 0.02 M H_2O_2 for 20 minutes and 1 hour.

For comparison, the results related to the coating deposited from the conversion solution of 0.05 M $Ce(NO_3)_3$ (the optimum concentration) are presented in these graphs as well (Fig. 5.16 (b) and (e)).

This can depict the detrimental effect of chloride ions, in the conversion solution, on the corrosion resistance of the aluminum substrate. In addition, a high concentration of NaCl (0.1 M) results in the deposition of a thicker conversion layer (Fig. 5.2 (a)) which suffers from the cracked morphology. According to these results, the optimum concentration of NaCl is 0.05 M.

By comparing the results related to the two optimum coatings (deposited from the solution of 0.05 M $Ce(NO_3)_3$ with and without 0.05 M NaCl) it can be seen that the conversion layer deposited from NaCl containing solution shows higher impedance values compared to the one deposited from the plain conversion solution after 6 hours of EIS test (Fig. 5.16 (b)). However, at the end of the 24-hour test (Fig. 5.16 (e)), the coating obtained from the chloride free conversion solution possesses higher impedance values at the low frequencies. The relatively lower corrosion resistance of the conversion layers deposited using NaCl containing solutions can be a result of heterogeneous deposition, in which α_1-Al particles are covered by a thinner conversion layer.

Hydrogen peroxide was added to the conversion solution (alone or together with NaCl) to shorten the required time for the conversion process and to obtain homogenously deposited coatings ((Fig. 5.16 (c) and (f) and Fig. 5.17).

Regarding the coatings deposited from the mix solution (Fig. 5.17), only 20 minutes of immersion is enough to achieve higher values of the total impedance, compared to the bare aluminum alloy, while 60 minutes of immersion deteriorates the corrosion properties. This is attributed to the fact that the combination of chloride ions and hydrogen peroxide can be very aggressive and cause subsurface crevices [100].

In addition, the coating deposited from this combination after longer immersion time is thicker and has a morphology full of cracks.

The conversion solution of 0.05 M $Ce(NO_3)_3$ and 0.02 M H_2O_2 produces a coating with improved corrosion resistance after both 20 and 60 minutes immersion (Fig. 5.16 (c) and (f)). This improvement is comparable to the conversion layer obtained from the solution of 0.05 M $Ce(NO_3)_3$, while the required process time has shortened from 18 hours to only 1 hour. However, it should be noted that the selectively deposited coating from the plain conversion solution (with the optimum concentration of $Ce(NO_3)_3$ still shows higher corrosion resistance.

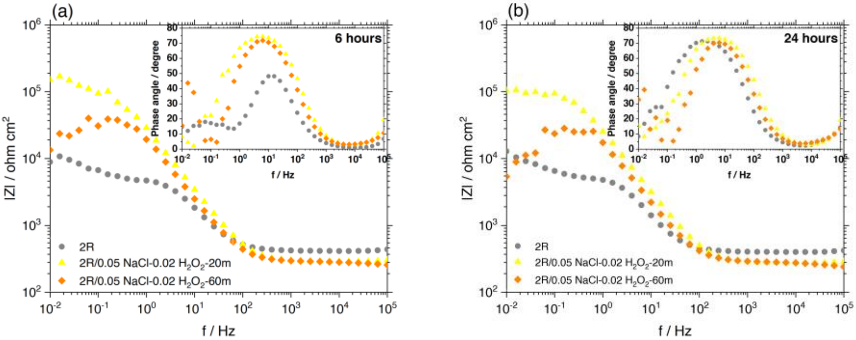

Fig. 5.17. EIS spectra of treated samples of the 2R alloy using the conversion solutions of 0.05 M $Ce(NO_3)_3$, 0.05 M NaCl and 0.02 M H_2O_2 for 20 minutes and 1 hour after (a) 6 and (b) 24 hours of EIS test.

By increasing the immersion time in the solution (with the optimum concentration of $Ce(NO_3)_3$), the total impedance values increase (Fig. 5.18). The highest impedance values are related to the coating deposited after 18 hours. By increasing the immersion time thicker cerium-based depositions cover the cathodic sites and the aluminum matrix, inhibiting the corrosion process. However, the thick and cracked coating deposited after 24 hours of immersion allows the corrosive solution to permeate into the surface and results in more corrosion [219]. Therefore, the optimum immersion time to deposit the adequate CeCC is 18 hours.

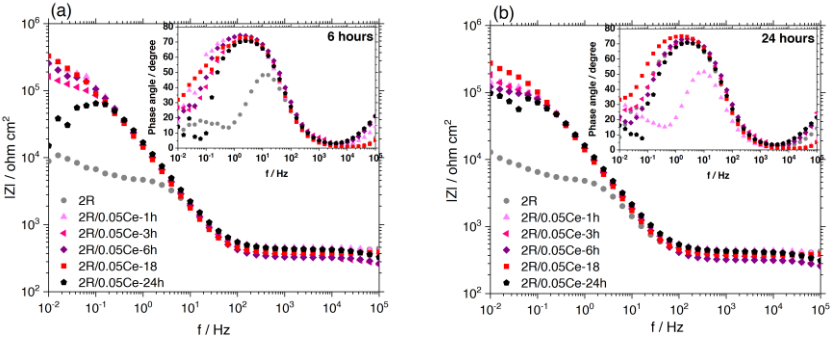

Fig. 5.18. EIS spectra of treated samples of the 2R alloy using the solution of 0.05 M $Ce(NO_3)_3$ for 1, 3, 6, 18 and 24 hours after (a) 6 and (b) 24 hours of EIS test.

The results of EIS measurements related to the treated samples of the 4R alloy are shown in Fig. 5.19 and Fig. 5.20. These samples were treated with the same conversion solutions presented in Fig. 5.16 and Fig. 5.17.

The samples were also treated using a solution with a lower concentration of sodium chloride mixed with hydrogen peroxide (0.05 M $Ce(NO_3)_3$, 0.01 M NaCl and 0.02 M H_2O_2) and also a solution with a lower concentration of hydrogen peroxide (0.05 M $Ce(NO_3)_3$ and 0.01 M H_2O_2).

First of all, the bare 4R alloy shows higher total impedance values compared to those of the 2R alloy. In fact, other researches on the corrosion behavior of Al-Si alloys have all indicated the positive effect of silicon on the corrosion resistance [24, 26, 196, 210, 220]. The higher corrosion resistance of the alloys with higher silicon content has been partly attributed to the incorporation of silicon atoms to the passive film, which repairs the film defects and renders it more stable [26, 201].

Regarding the treated samples using the plain $Ce(NO_3)_3$ solutions (Fig. 5.19 (a) and (d)), all the samples show almost the same extent of improvement in the total impedance values compared to the bare aluminum alloy substrate. It seems that surface of the 4R alloy (with 4.5 wt.% Si) has enough active cathodic sites for the oxygen reduction to occur (leading to the pH increase and the deposition of cerium hydroxide/oxide layers), even when it is immersed in the low concentrated solutions of $Ce(NO_3)_3$ [221, 222].

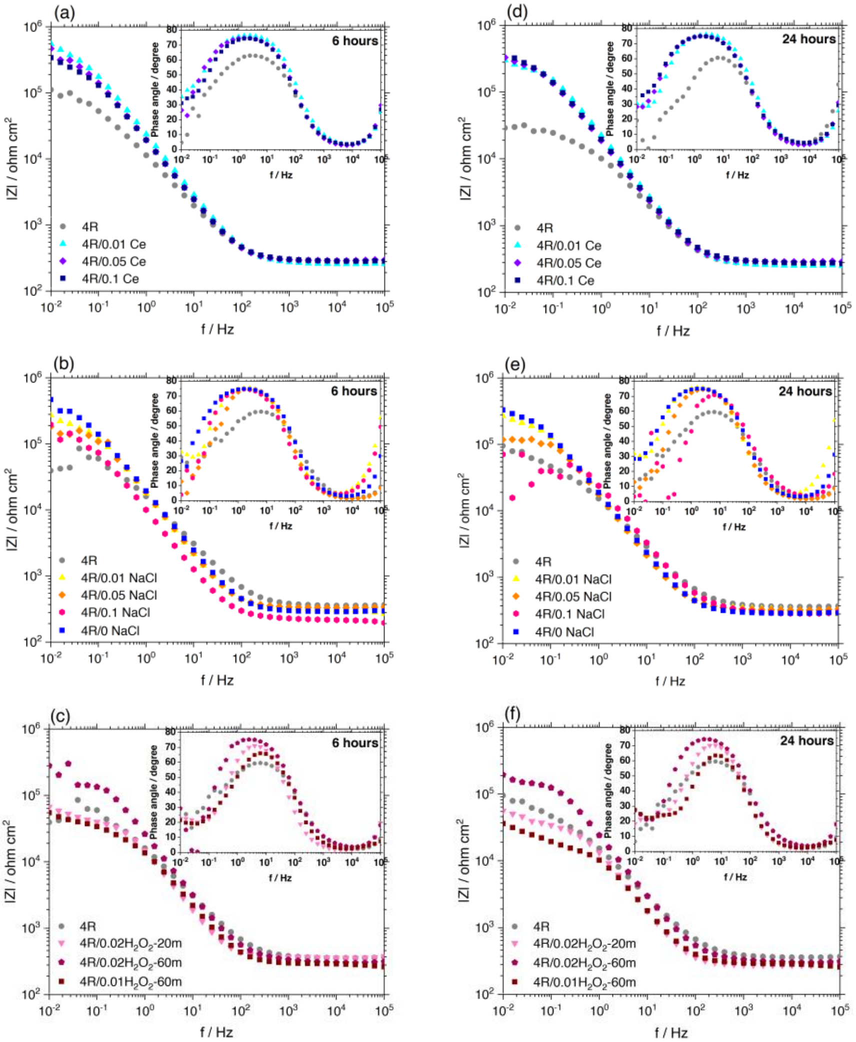

Fig. 5.19. EIS spectra of treated samples of the 4R alloy using the conversion solution of (a), (d) x M $Ce(NO_3)_3$, (b), (e) 0.05 M $Ce(NO_3)_3$ and x M NaCl for 18 hours, (c), (f) 0.05 M $Ce(NO_3)_3$, 0.02 (0.01) M H_2O_2 for 20 minutes and 1 hour.

As it can be seen, the negative effect of high concentration of $Ce(NO_3)_3$ is negligible, unlike the similar 2R treated samples. A decrease in the values of |Z| at the low and medium frequencies can be observed for the untreated sample after 24 hours of the EIS test. However, values of total impedance of the treated substrates remain considerably high even after 24 hours of immersion.

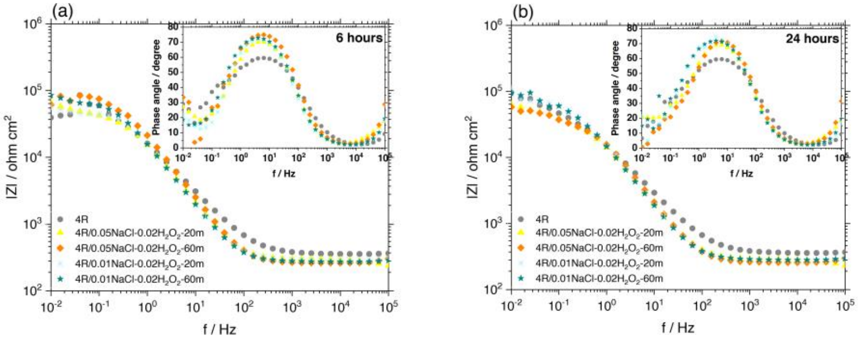

Fig. 5.20. EIS spectra of treated samples of the 4R alloy using the conversion solutions of 0.05 M Ce(NO$_3$)$_3$, 0.05 (0.01) M NaCl and 0.02 Ml H$_2$O$_2$ for 20 minutes and 1 hour after (a) 6 and (b) 24 hours of EIS test.

By adding the proper concentration of chloride ions to the conversion solution, cerium-based layers with improved total impedance values are achieved. According to Fig. 5.19 (b) and (e), the highest total impedance values among the coatings obtained from chloride ions containing solutions belong to the coating deposited from the solution containing 0.01 M NaCl. This shows that the surface of Al-Si alloy with a higher silicon content needs lower concentrations of chloride ions for its cathodic sites to get activated. The values of total impedance of this coating are similar to the ones from NaCl free solution, especially after 24 hours of EIS test. In this case, the higher concentration of NaCl in the conversion solution (0.05 and 0.1 M) results in poor corrosion resistance.

Results regarding the 4R alloy samples treated using more oxidizing solutions (solutions containing hydrogen peroxide and the mix solutions) are presented in Fig. 5.19 (c) and (f) and Fig. 5.20. According to these curves, almost all the solutions are too aggressive for the samples of 4R alloy. They produce thick and cracked conversion layers without a significant improvement in the corrosion resistance.

In the mix solution (Fig. 5.20), sodium chloride concentration was reduced to the optimum concentration of 0.01 M and in the solution of $Ce(NO_3)_3$ and H_2O_2, the concentration of hydrogen peroxide was reduced to 0.01 M. However, the only treated sample which showed improved corrosion resistance was the one immersed in the solution of 0.05 M $Ce(NO_3)_3$ and 0.02 M H_2O_2 for 1 hour. All the other samples of these two sets showed weaker or equal corrosion resistance to that of the bare aluminum alloy.

Fig. 5.21 depicts SEM image of the corroded surface of one of the mentioned set of conversion treated substrates. According to this image, the corrosive solution has permeated through the cracked coating resulting in intense corrosion. Here we can again conclude that the selectively deposited coatings from the plain conversion solutions possess higher corrosion resistance compared to that of the thick, cracked, and homogenously deposited coatings.

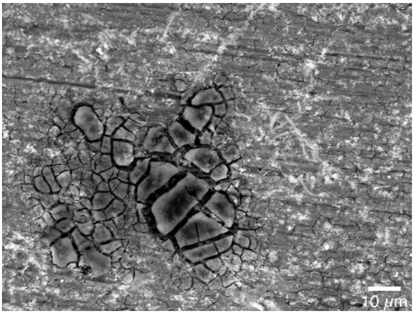

Fig. 5.21. SEM-BS image of corroded surface of the treated 4R alloy using the conversion solution of 0.05 M $Ce(NO_3)_3$, 0.01 M NaCl and 0.02 M H_2O_2 for 1 hour.

Results of the potentiodynamic polarization test in 0.05 M NaCl solution for samples of the 2R and 4R alloys treated under optimum conversion conditions are presented in Fig. 5.22. The results of the polarization test related to the bare 2R and 4R alloys are presented as well. The alloy with a higher silicon content shows a nobler corrosion potential and lower current densities in both anodic and cathodic branches.

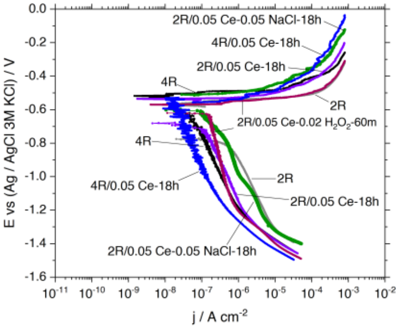

Fig. 5.22. Potentiodynamic polarization curves of CeCCs on 2R and 4R alloys in 0.05 M NaCl solution.

In case of the treated samples of 2R alloy, both samples (treated using the plain 0.05 M $Ce(NO_3)_3$ solution and hydrogen peroxide containing solution) show nobler corrosion potential in comparison to the bare 2R aluminum alloy. In the anodic branches, the sample treated using the plain solution (0.05 M $Ce(NO_3)_3$) shows lower current density compared to those of the conversion layer from the solution of 0.05 M $Ce(NO_3)_3$ and 0.02 M H_2O_2 and the bare 2R alloy. This is probably attributed to the cracked morphology of the conversion coating deposited from hydrogen peroxide containing solution that lets permeation of the corrosive solution to the surface resulting in the higher corrosion rates. Regarding the cathodic branches, both conversion layers show lower current densities compared to the untreated 2R aluminum alloy. This is attributed to the decreased oxygen reduction rate [67], which obviously shows the efficiency in passivating and blocking the cathodic sites. Similar results can be observed for the treated 4R alloy.

5.2.5. Electrochemical behavior (on HPDC alloys)

The effect of $Ce(NO_3)_3$ concentration on the corrosion resistance of treated samples of 2L alloy is presented in Fig. 5.23. This figure shows the EIS spectra for the coatings deposited from the conversion solutions with different concentrations of cerium nitrate, after 6, 12 and 24 hours of immersion in 0.05 M NaCl solution. All the treated samples possess higher impedance values compared to the untreated substrate. $|Z|_{0.01\ Hz}$ values are increased by more than one order of magnitude for the conversion treated samples, compared to the bare aluminum alloy.

In the absence of any accelerator (NaCl or H_2O_2), the impedance values increase by increasing the cerium nitrate concentration. The values of total impedance decrease through 24 hours of immersion in NaCl solution for both treated and the bare aluminum samples, indicating the progressive corrosion process. However, the corrosion resistance remains quite high for the conversion treated samples even after 24 hours.

The effect of the addition of NaCl in different concentrations to the conversion solution on the electrochemical response of CeCC on both 2L and 4L alloys are depicted in Fig. 5.24 (a) and (b).

For the conversion coatings on the 2L alloy, the highest $|Z|_{0.01\ Hz}$ value is reached using the solution containing 0.1 M NaCl. This indicates the effective role of NaCl in activating the corrosion processes near the cathodic sites in the alloy microstructure, which led to the deposition of a thicker layer over these cathodic areas.

However, for the 4L alloy (Fig. 5.24 (b)), due to the presence of more cathodic phases, the highest value of $|Z|_{0.01\ Hz}$ can be achieved even in the absence of NaCl.

By adding 0.05 M NaCl to the conversion solution, the results of the impedance value do not change and adding a higher amount of NaCl (0.1 M) reduces the total impedance of the system. This is obviously due to more corrosion in the presence of NaCl in the conversion solution for the 4L alloy.

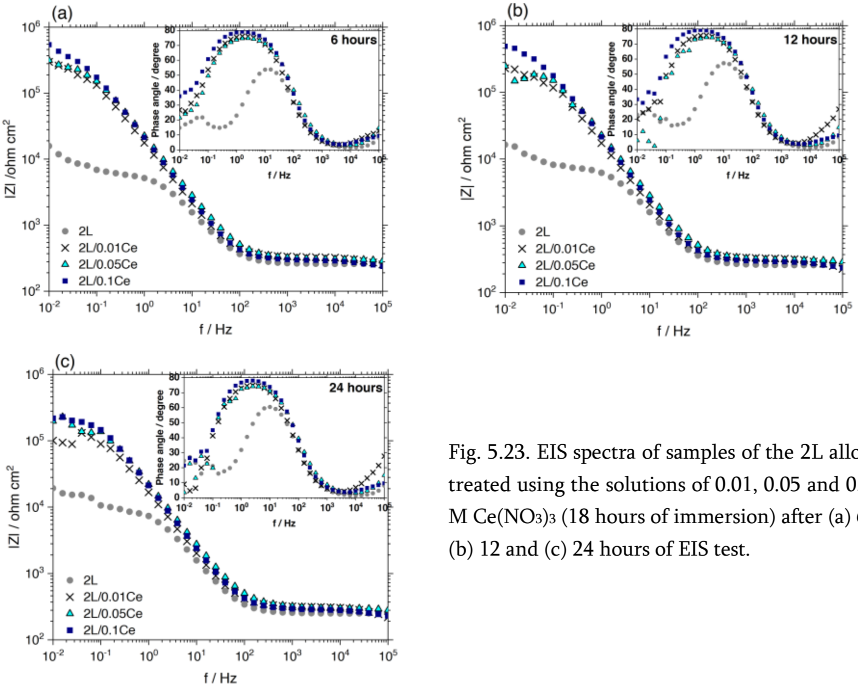

Fig. 5.23. EIS spectra of samples of the 2L alloy treated using the solutions of 0.01, 0.05 and 0.1 M $Ce(NO_3)_3$ (18 hours of immersion) after (a) 6, (b) 12 and (c) 24 hours of EIS test.

Regarding the effect of H_2O_2 in the conversion solution (Fig. 5.24 (c)), the conversion coating deposited from the solution of 0.02 M H_2O_2 with the immersion time of 1 hour shows improvement in total impedance values in comparison to the bare 2L alloy and to the coating deposited from the same solution with the immersion time of 20 minutes.

According to these results, 20 minutes is not enough time to form an adequate coating. By combining NaCl and H_2O_2, the required immersion time to achieve the same impedance values of the coating obtained from the solution of 0.05 M $Ce(NO_3)_3$ and 0.1 M NaCl reduces from 18 hours to 20 minutes. When using the solution containing both NaCl and H_2O_2, a longer immersion time reduces the corrosion resistance. Clearly, in this case, the solution is too aggressive and the formation of a thick cracked layer from this solution in longer immersion times results in the permeation of NaCl into the surface during the EIS test (Fig. 5.25).

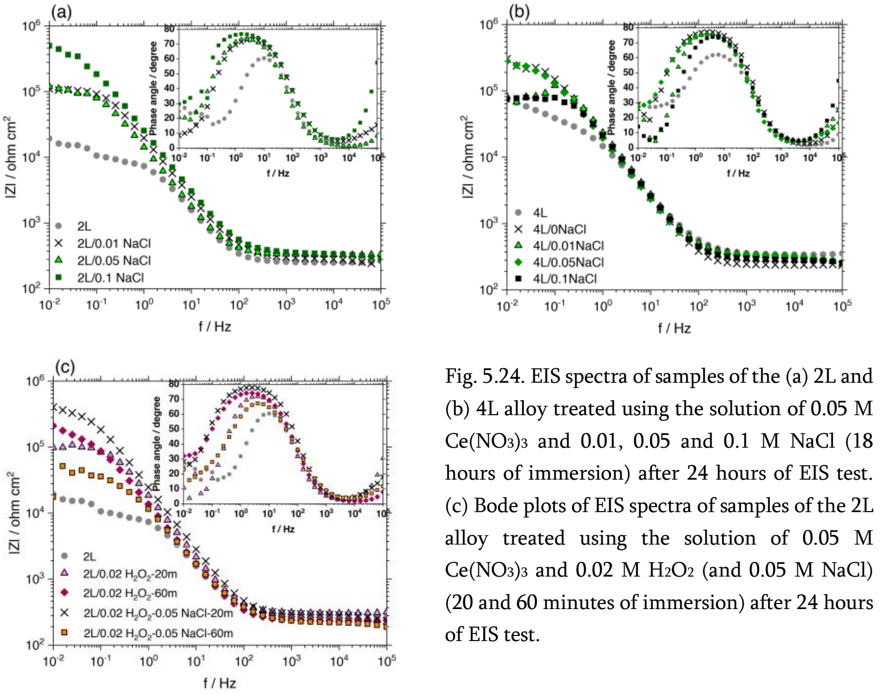

Fig. 5.24. EIS spectra of samples of the (a) 2L and (b) 4L alloy treated using the solution of 0.05 M $Ce(NO_3)_3$ and 0.01, 0.05 and 0.1 M NaCl (18 hours of immersion) after 24 hours of EIS test. (c) Bode plots of EIS spectra of samples of the 2L alloy treated using the solution of 0.05 M $Ce(NO_3)_3$ and 0.02 M H_2O_2 (and 0.05 M NaCl) (20 and 60 minutes of immersion) after 24 hours of EIS test.

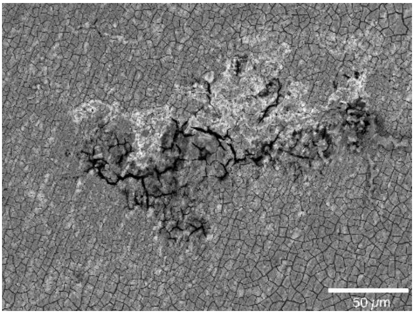

Fig. 5.25. SEM-BS image of corroded CeCC on the 2L alloy deposited from the solution of 0.05 M $Ce(NO_3)_3$, 0.05 M NaCl and 0.02 M H_2O_2 (1 hour of immersion).

Treating samples of the 4L alloy using the mixed solution of $Ce(NO_3)_3$, NaCl and H_2O_2 with the immersion time of 20 and 60 minutes does not result in the corrosion resistance improvement as it is obvious in the EIS results in Fig. 5.26.

Obviously, this solution is too aggressive for samples of the 4L alloy. Since there are more eutectic regions on the alloy surface due to the higher silicon content, more active sites for the anodic and cathodic reactions are available. This produces thick and cracked conversion layers without a significant improvement in the corrosion resistance.

Results of polarization tests on conversion treated samples of the 2L alloy, in 0.05 M NaCl solution are presented in Fig. 5.27. According to this figure, both anodic and cathodic branches are influenced by the presence of cerium-based conversion coatings on the alloy surface. Regarding the anodic branches, all the coatings show a decrease in the anodic current density, compared to the untreated sample. The best performances are related to the coatings deposited from the solutions of 0.05 M $Ce(NO_3)_3$ with and without 0.1 M NaCl. However, the coatings deposited from the solutions containing H_2O_2 show less improvement.

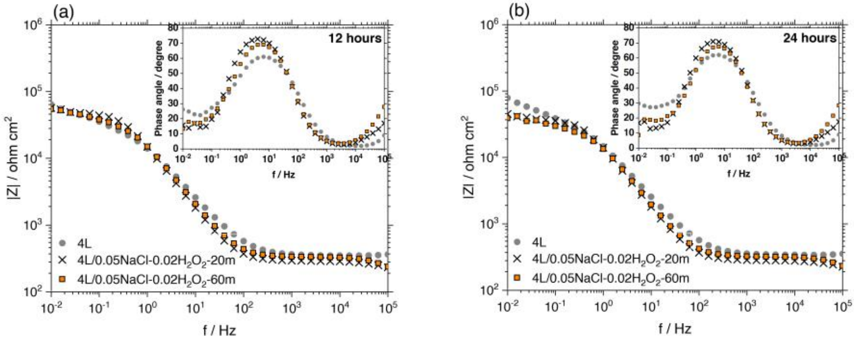

Fig. 5.26. EIS spectra of samples of the 4L alloy treated using the solution of 0.05 M $Ce(NO_3)_3$, 0.05 M NaCl and 0.02 M H_2O_2 for 20 and 60 minutes after (a) 12 and (b) 24 hours of EIS test.

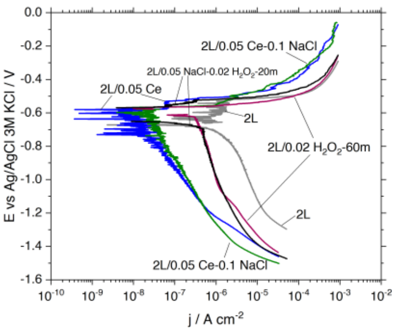

Fig. 5.27. Potentiodynamic polarization curves of the different conversion treated 2L samples in 0.05 M NaCl solution.

This is probably attributed to the cracked morphology of coatings from hydrogen peroxide containing solutions, which lets permeation of the corrosive solution to the metal surface and results in the higher corrosion rates. Concerning the cathodic branches, the cathodic current density decreases for all the cerium-based conversion coatings in comparison to the bare aluminum alloy. This is attributed to the lower oxygen reduction rate [67], which shows that cathodic sites have been blocked by cerium oxide/hydroxide deposition. In alignment with the previous results, the coatings formed from H_2O_2-containing solutions present less improvement in the cathodic branches. For all the coatings except for the one deposited from the solution of 0.05 M $Ce(NO_3)_3$, 0.05 M NaCl and 0.02 M H_2O_2, two reduction peaks are detectable, which can be attributed to the two steps in oxygen reduction [67] (Eq. 2.2 and Eq. 2.3).

Considering the results from both EIS and polarization tests, it can be concluded that the coatings from the conversion solutions without H_2O_2 possess a higher corrosion resistance. This can be attributed not only to the almost crack-less structure of these coatings but also to the higher amount of Ce (III) in these coatings, which oxidizes to Ce (IV) and acts as an anti-corrosion mechanism.

5.3. Discussion (comparison between the conventional HPDC and Rheo-HPDC Al-Si alloys)

Based on the results presented in sections 5.2.4 and 5.2.5, the cerium conversion treatment on the conventional and Rheo-HPDC Al-Si alloys is similar with a few differences.

Rheo-HPDC Al-Si alloys display different degrees of cerium deposition over α_1 and α_2-Al particles, especially when NaCl is present in the conversion solution. Since this is a semi-solid microstructural effect, it is not observed in the conventional HPDC alloys.

By comparing the chemistry of the solutions used to deposit the optimum coatings, it seems that the semi-solid alloys possess more electrochemically active surfaces. For instance, the optimum concentration of $Ce(NO_3)_3$ is 0.05 M for the alloy 2R and 0.1 M for the alloy 2L. The optimum concentration of NaCl (in a 0.05 M $Ce(NO_3)_3$ solution) is 0.05 M for the alloy 2R and 0.1 for the alloy 2L.

In addition, the selective dissolution of aluminum from the IM particles and the subsequent oxidation of the remained iron, which was explained in the deposition mechanism (Fig. 5.15), was only observed for the Rheo-HPDC alloys and not for the conventional HPDC ones. However, for both kind of alloys, IM particles were the initial nucleation sites for CeCC.

The corrosion resistance of the conversion treated samples of both kinds of alloys seems comparable.

5.4. Conclusions

Cerium based conversion coatings were successfully deposited on two conventional and Rheo-HPDC Al-Si alloys.

The effect of different deposition parameters including the immersion time, $Ce(NO_3)_3$ and NaCl concentrations and H_2O_2 addition on the microstructure and the corrosion resistance of the coatings was examined.

According to the results, the chemistry of the conversion solution changes the coating morphology from the locally and selectively deposited coating to a thick and cracked coating using the plain $Ce(NO_3)_3$ solution and NaCl and H_2O_2 containing solutions, respectively.

The presence of NaCl, in the conversion solution, promotes micro-galvanic coupling and accelerates the corrosion reactions and therefore the coating precipitation.

The coatings deposited from hydrogen peroxide free solutions possessed a higher amount of Ce (III) compared to the coatings deposited form the solutions with hydrogen peroxide, which showed a higher percentage of Ce (IV).

The deposition of the conversion layer starts from iron-rich IM particles located inside the eutectic region. The formation mechanism of the coating includes dissolution of the aluminum matrix and deposition of cerium hydroxide/oxide layer. When the process is very fast and aggressive, even selective dissolution of aluminum from the iron-rich IM particles and oxidation of iron on the surface of these particles are observed.

The aluminum alloy with the higher amount of silicon shows more active surface during the conversion process which reduces the required concentration of $Ce(NO_3)_3$ but also makes it difficult to work with more aggressive solutions.

Finally, the conversion treatment significantly increases the corrosion resistance of the aluminum alloys in which the selectively deposited coating shows more improvement compared to the cracked, thick, and homogenously deposited coating.

Chapter 6 **Polypyrrole coatings**

This chapter presents the experimental work and the results and discussion on electropolymerization and electrochemical characterization of polypyrrole coatings on pure aluminum (AA1050) and Rheo-HPDC Al-Si alloys for corrosion protection purpose. Due to the complexity of the electrodeposition process on aluminum alloys, the process was first carried out and optimized on pure aluminum substrates and then reproduced on the Rheo-HPDC Al-Si alloys.

Some parts of the results presented in this chapter have been presented and are under submission in papers IV, VIII, IX, X and XI, respectively.

6.1. Materials and methods

6.1.1. Substrate preparation

Samples of AA 1050, with minimum 99.5 % aluminum, and samples of the Rheo-HPDC Al-Si alloys (2R and 4R) were used. AA1050 was chosen as a simple electrode to optimize the electrodeposition process and to study the influence of process parameters, without the influence of the substrate.

Samples were cut in squares of 2 cm × 2 cm from the main sheet of 1 mm thickness. In the case of the Rheo-HPDC Al-Si alloys, as it was mentioned in Chapter 4, the cast component was a full-size telecom cavity filter. Due to the inevitable presence of casting defects, samples were primarily chosen carefully to be defect-free to see the effect of alloy composition and the semi-solid microstructure. However later on samples with casting defects were studied to examine the interaction of polypyrrole coating with these defects. These samples were cut in squares of 2 cm × 2 cm from the main component.

Prior to the electropolymerization, samples (both AA1050 and Al-Si alloys) were wet-abraded using SiC abrasive paper of P1200. Subsequently, they were ultrasonically cleaned in acetone for 10 minutes and then rinsed with deionized water. As the final pretreatment step, each sample was etched for 15 seconds in a solution of 40 g/l NaOH, at the room temperature.

6.1.2. Electropolymerization

Cyclic voltammetry (CV) was used to deposit polypyrrole coatings on the aluminum substrates, in a three-electrode 100 ml electrochemical cell (Fig. 3.2). The applied potential ranged from 0 to 0.7, 0 to 0.8 and 0 to 0.9 V versus Ag/AgCl (3 M KCl) as the reference electrode, while a graphite rode was used as the counter electrode. The cell was placed on top of a magnetic stirrer that was set on 300 rpm (a magnetic round bar of 20 mm length and 6 mm diameter was used). The scan rate was 10 mV/s and 20 scans were applied to form each coating.

The main reagents in each electrolyte were the pyrrole monomer (Py), sodium dodecyl sulfate (SDS) and DHBDS (Tiron). Citric acid ($C_6H_8O_7$) and sodium nitrate ($NaNO_3$) were added to the main solution to investigate the effect of electrolyte and the presence of different anions on the electrodeposition, the electrochemical and anti-corrosive properties of the polypyrrole coating. The details of the electropolymerization process are summarized in Table. 6.1.

6.1.3. Coating characterization

Morphological features of the bare and polypyrrole coated samples were examined using SEM, FIB-SEM and EDXS. The FIB milling conditions were as follows: 30kV, 5nA for rough milling and 1 nA for final polishing.

XPS analysis was performed to examine the composition of polypyrrole coatings.

Table. 6.1 Details of electrodeposition conditions

Substrate/Coating	Voltage range	Solution
Al/X	0-0.9 V	0.1 M Py, 0.05 M DHBDS, 0.005 M SDS*
Al/X-Cit	0-0.9 V	0.1 M Py, 0.05 M DHBDS, 0.005 M SDS, 0.05 M $C_6H_8O_7$**
Al/X-Nit	0-0.9 V	0.1 M Py, 0.05 M DHBDS, 0.005 M SDS, 0.05 M $NaNO_3$***
2R/X	0-0.9 V	0.1 M Py, 0.05 M DHBDS, 0.005 M SDS
4R/X	0-0.9 V	0.1 M Py, 0.05 M DHBDS, 0.005 M SDS
2R/2X	0-0.9 V	0.1 M Py, 0.1 M DHBDS, 0.005 M SDS
2R/X-Nit	0-0.9 V	0.1 M Py, 0.05 M DHBDS, 0.005 M SDS, 0.05 M $NaNO_3$
4R/X-Nit	0-0.9 V	0.1 M Py, 0.05 M DHBDS, 0.005 M SDS, 0.05 M $NaNO_3$
2R/X-2Nit	0-0.9 V	0.1 M Py, 0.05 M DHBDS, 0.005 M SDS, 0.1 M $NaNO_3$
2R/2X (0.7)	0-0.7 V	0.1 M Py, 0.1 M DHBDS, 0.005 M SDS
2R/2X (0.8)	0-0.8 V	0.1 M Py, 0.1 M DHBDS, 0.005 M SDS
2R/2X-Nit (0.7)	0-0.7 V	0.1 M Py, 0.1 M DHBDS, 0.005 M SDS, 0.05 M $NaNO_3$
2R/2X-Nit (0.8)	0-0.8 V	0.1 M Py, 0.1 M DHBDS, 0.005 M SDS, 0.05 M $NaNO_3$

*pH=5.84, **pH=2.47, ***pH=5.48

These measurements consisted of the acquisition of a wide spectrum at a pass energy of 160 eV. Higher energy resolution was obtained by analyzing the core lines of interest at a pass energy of 20 eV, which led to an energy resolution of ~ 0.3 eV. The thick coatings needed charge compensation which was performed by adjusting the flood gun working conditions to minimize the peak FWHM (full width at half maximum) while maximizing its intensity.

XPS analysis was carried out on the surface of each coating as well as at the polypyrrole/aluminum interface. To analyze the interface, coatings were sputtered using an Ar^+ ion gun operated at 3800 V and 20 mA current that applied a raster of 3 mm × 3 mm.

To reduce the sputtering time thinner coatings (deposited by applying six (X) and four (X-Cit and X-Nit) scans in the CV process) were used for this analysis. The coatings thicknesses were as follows: X: 1.2 ± 0.2 μm, X-Cit: 2.6 ± 0.4 μm and X-Nit: 5.1 ± 0.6 μm.

Since sputtering is an energetic process and could induce a change in the chemical state of the elements, the obtained results were confirmed by repeating the same analysis on the surface of unsputtered thin coatings. In this case, coatings with a thickness lower than the XPS sampling depth were deposited by applying two scans in the CV process.

The coatings thicknesses were measured using cross-sectional SEM images. At least five images were taken of each sample. The Java-based image processing program (ImageJ) was employed for the measurement.

6.1.4. Electrochemical analysis

The corrosion resistance and the electrochemical stability of polypyrrole coatings on AA1050 and Al-Si alloys were investigated in 0.1 and 0.6 M NaCl solutions by means of EIS and OCP monitoring for immersion times of 24 and 168 hours (7 days). In the EIS measurements, the frequency range was from 100 kHz to 10 mHz (36 points) and the amplitude of the sinusoidal potential signal was 10 mV.

The redox properties of polypyrrole films were examined using CV in 0.1 and 0.6 M NaCl solutions. In this case, the scanning range was between -1 and 1 V and the sweep rate was 10 mV/s.

All the electrochemical measurements were carried out in a traditional three-electrode cell (Fig. 3.1), containing the sample (with the exposure area of 1 cm^2) as the working electrode, Ag/AgCl 3 M KCl reference electrode and a platinum counter electrode.

After exposure to the NaCl solutions, surfaces of the coated and bare samples were examined by means of SEM, EDXS and FIB-SEM analysis.

6.2. Results and discussion I (Polypyrrole coatings on AA1050)

6.2.1. Effect of solution chemistry

CV curves (the first and last scans) related to the electropolymerization of the three different polypyrrole coatings (X, X-Cit and X-Nit) are depicted in Fig. 6.1. According to these curves, in the first scan, oxidation of pyrrole and the formation of polypyrrole film on the aluminum electrode start at a voltage between 0.62-0.66 V (vs Ag/AgCl). Similar oxidation voltages for pyrrole have been reported by other researchers [140, 176]. According to Fig. 6.1, the oxidation voltage is almost independent of pH of the electropolymerization solution (Table. 6.1). The current density increases sharply at this point and it reaches its highest value at the upper limit of the scanning range. For next CV scans, the inflection potential decreases to 0.55-0.59 V demonstrating the easier formation of the polymeric film after the first cycle.

For the X-Nit coating, during polymerization, the current density in the upper anodic region is higher than the other two coatings. During twenty scans, the changes in the current density for the three solutions are negligible.

It is interesting to mention that the color of the electrolyte containing $NaNO_3$ changes from colorless to dark blue at the end of the deposition process. This can be attributed to the presence of undeposited polymerized polypyrrole globules suspended in the solution. These colloid nanospheres are black and change the color of the solution [223]. The color change is not noticed in the other two solutions, as probably the amounts of the colloid nanospheres are less.

To see the effect of the supporting electrolyte on the electrochemical behavior of aluminum substrate, two successive CV scans were performed in the same solutions without the pyrrole monomer (Fig. 6.2).

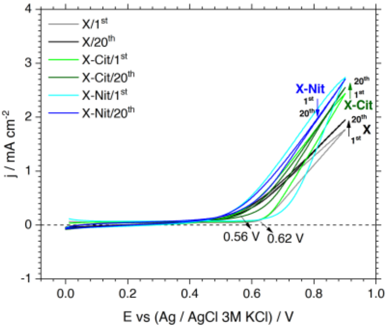

Fig. 6.1. CV curves of electropolymerization of polypyrrole coatings on AA1050 substrates from the solutions X, X-Cit and X-Nit (1st and 20th scans) (scanning rate = 10 mV/s).

According to Fig. 6.2, following the first forward scan a decrease in the anodic current density can be observed, which is probably due to the passivation of the electrode. Afterward, a wide passive region is recorded. The initial decrease in the current could be due to the fact that the voltage range is behind the active/passive potential for the substrate. According to this graph, the values of current densities are substantially lower in comparison to the condition when the monomer is present in the solution.

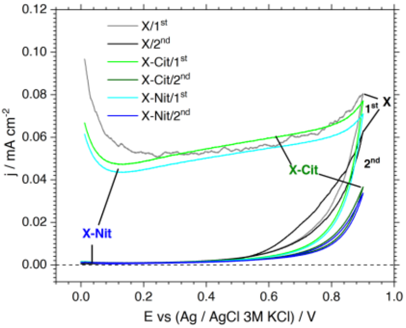

Fig. 6.2. Two successive scans in the solutions X, X-Cit and X-Nit without the pyrrole monomer (scanning rate = 10 mV/s).

As it is obvious, the oxidation of pyrrole has a higher contribution to the increase in the current density, observed in Fig. 6.1 in the high anodic region, compared to the oxidation/dissolution of the aluminum substrate. Fig. 6.2 shows that the solutions containing $C_6H_8O_7$ and $NaNO_3$ yield lower current densities in both forward and reverse scans. During the second scan, a significant decrease in the current density is observed for these two solutions compared to the X solution.

In fact, citric acid is a corrosion inhibitor for aluminum as citrate anions are able to be adsorbed on the surface and make different complexes with Al^{3+} cations [224]. The formation of these surface compounds can inhibit the dissolution of aluminum without preventing the electropolymerization process. Nitrate anions, on the other hand, form resistive transitory compounds such as $Al(NO_3)_3$, which contribute to the inhibition of the anodic dissolution of aluminum electrode [213].

Surface morphologies of polypyrrole coatings are shown in Fig. 6.3. Three coatings show the so-called cauliflower morphology, which is the characteristic morphology of a coating that grows from initial globules on the surface, forming island and later on grows laterally to cover the surface. All the coatings are homogenous and no specific difference in the size or the shape of polypyrrole globules can be observed.

As Nam et al. [223] showed, the morphology of a polypyrrole film is dependent on the reactivity of pyrrole radical cations which is comparable in the three electropolymerization solutions we used in this work. Coatings display a compact structure.

Cross-sectional images in Fig. 6.4 exhibit the presence of dense, homogenous coatings.

The thickness of the three coatings was measured as follows: X, 7.1 ± 0.7 μm; X-Cit, 10.4 ± 1.0 μm and X-Nit, 11.9 ± 1.1 μm. This trend is in agreement with the observations extracted from the polypyrrole formation CV curves in Fig. 6.1.

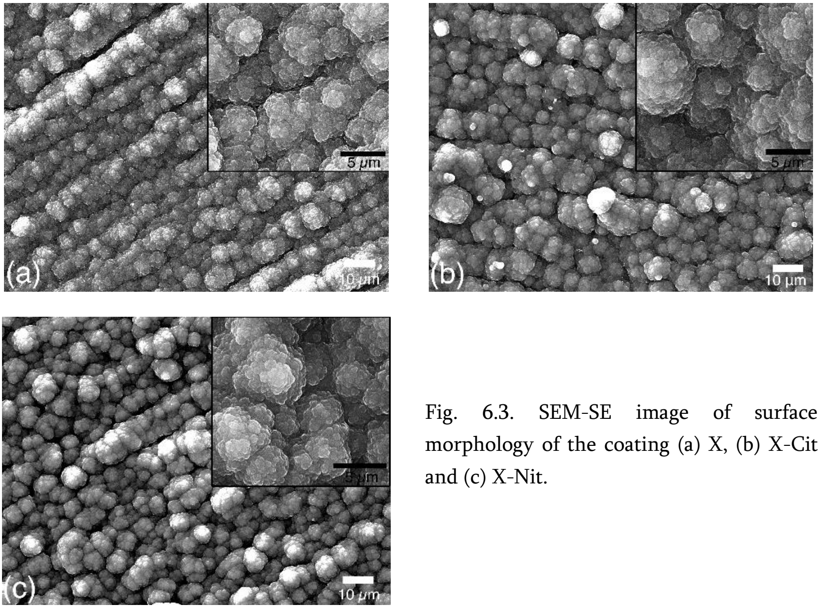

Fig. 6.3. SEM-SE image of surface morphology of the coating (a) X, (b) X-Cit and (c) X-Nit.

XPS analysis was employed to study surface chemical composition of the three polypyrrole coatings and also the composition state of polypyrrole/aluminum interface. Fig. 6.5 depicts the high-resolution XPS spectra (C 1s, S 2p and N 1s) for the three coatings.

The three coatings present similar spectra. As an example, the details of peak assignment for the X coating are summarized in Table. 6.2.

The C 1s peak was fitted using six different Gaussian components to account for the aromatic ring and the CN bond of pyrrole, the CH_x bonds and the different carbon-oxygen bonds formed during the electropolymerization process.

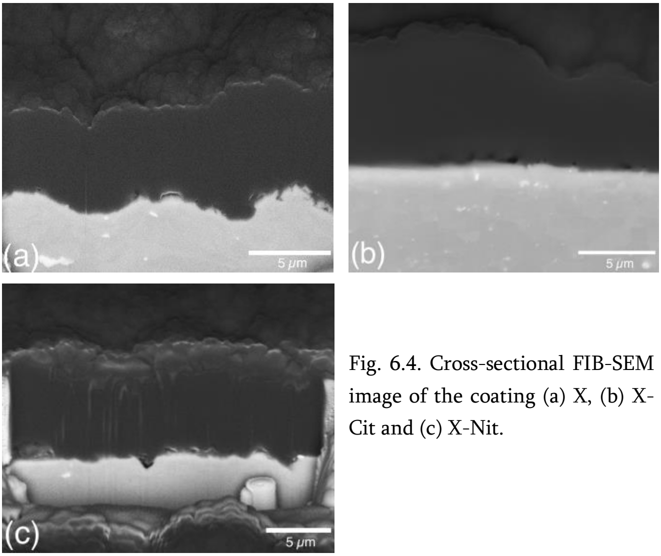

Fig. 6.4. Cross-sectional FIB-SEM image of the coating (a) X, (b) X-Cit and (c) X-Nit.

Similarly, the N 1s peak is described by nitrogen in an aromatic ring similar to pyridine. Nitrogen in the pyrrole ring can be in neutral, ionized form and the NO_3 bond. This last component is present in all three coatings, although very weak, which indicates that its presence in the coating is not necessarily related to the presence of $NaNO_3$ in one solution.

Finally, the S 2p core line in the three coatings is mainly located at the low binding energies. The two deconvoluted peaks at ~ 169 eV are assigned to $NaSO_4$. A small variation in the intensity of the S 2p core lines appears at ~164 eV, which can be assigned to the 1/2 – 3/2 spin orbit components of sulfur in Na_2SO_4.

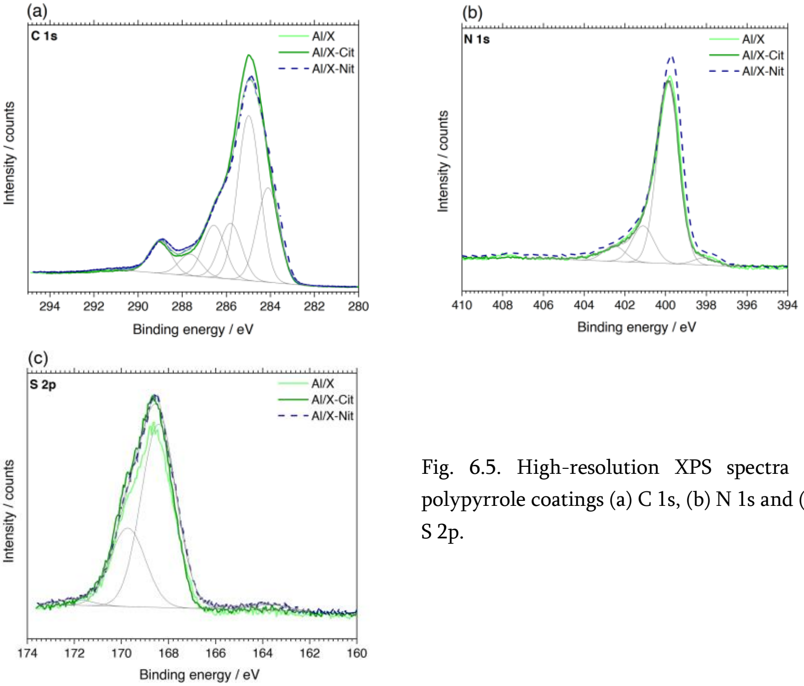

Fig. 6.5. High-resolution XPS spectra of polypyrrole coatings (a) C 1s, (b) N 1s and (c) S 2p.

The XPS results suggest incorporation of DHBDS (Tiron) and SDS into the polymer. However, no strong proof was found for the incorporation of citrate and nitrate anions into the X-Cit and X-Nit coatings, respectively.

The difference between the X-Nit coating and the other two coatings becomes more evident when analyzing the polypyrrole/aluminum interface. Fig. 6.6 compares the Al 2p core lines after sputtering the polypyrrole coatings.

Table. 6.2. Details of XPS analysis for the X coating

Signal	Binding energy (eV)	Assignment
C 1s	285.050	
	284.24	aromatic ring
	285.12	CH_x
	285.94	-CN-
	286.70	C-OH
	287.78	-C=O, -O-C-O-
	289.14	-O-(C=O)
O 1s	532.150	
	530.98	SO_3
	532.01	C=O
	533.59	C-OH
	535.36	H_2O
N 1s	399.950	
	398.03	-CN as in pyridine
	399.94	-CNH of pyrrole
	401.16	$-CNH^+$
	402.52	Not assigned
	408.00	$-NO_3$
S 2p	168.600	
	168.45	Na_2SO_4-3/2
	169.76	Na_2SO_4-1/2
	171.46	$Na+SO_3$-1/2
Na 1s	1071.700	
	1071.70	$NaSO_4$
	1073.24	Na(OH)

The spectra are noisy since as soon as the Al 2p peak appeared sputtering was switched off to preserve the interface and its chemistry. Therefore, the aluminum substrate is partially masked by the residual polypyrrole coating. The aluminum spectrum was described utilizing two Gaussian components. The prominent shoulder at the high binding energy corresponds to the aluminum oxide (Al_{ox}), while the sharper peak at lower energy corresponds to the crystalline bulk aluminum (Al^0).

As it appears from Fig. 6.6, the intensity of the non-oxidized metallic peak on the X and X-Cit substrates is higher with respect to the oxidized one, while the two components are similar in the case of the X-Nit substrate. Table. 6.3 summarizes the contribution of the Al^0 and Al_{ox} components (in percent) for the different coatings.

Based on these results, the ratio of the aluminum oxide to the metallic aluminum is higher at polypyrrole/substrate interface of the X-Nit sample compared to the other two samples.

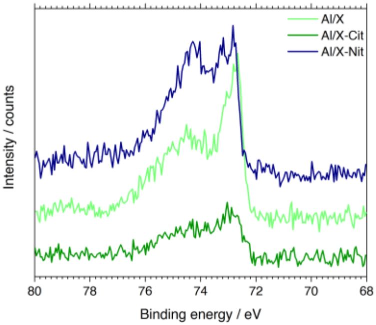

Fig. 6.6. Aluminum core line at the interface of polypyrrole/aluminum.

Table. 6.3 contribution of the metallic and oxidized components to the total spectral power of the Al 2p spectrum

Sputtered coatings	Al^0 (%)	Al_{ox} (%)
X	27.9	72.1
X-Cit	26.7	73.3
X-Nit	14.5	85.5

This suggests the passivating effect of nitrate anions on the aluminum surface during the electropolymerization process. While according to Fig. 6.2, both nitrate and citrate anions should provide this effect, based on the XPS results nitrate anions are passivating the substrate more efficiently.

One could argue that sputtering may modify the oxidation state of aluminum. However, these results were confirmed by the XPS spectra acquired on the unsputtered thin films where the modulation of the oxidized and bulk aluminum intensities shows similar behavior in the three samples.

In order to understand the oxidation reactions at the aluminum/electrolyte interface during the electropolymerization, an XPS survey was carried out on samples listed in Table. 6.4. Samples were treated in the listed solutions for two CV scans in the voltage range of 0-0.9 V by the scanning rate of 10 mV/s. The bare sample was pretreated as described in the experimental section.

Table. 6.4. Details of electrodeposition conditions for XPS survey of the oxidation reactions (CV (2 scans): voltage range = 0-0.9 V, scanning rate = 10 mV/s)

Sample's name	Electrolyte
Al	-
AlPy	0.1 M Py
AlPyTi	0.1 M Py, 0.05 M DHBDS
AlPyS	0.1 M Py, 0.005 M SDS
AlTiS	0.05 M DHBDS, 0.005 M SDS
AlPyTiS (X)	0.1 M Py, 0.05 M DHBDS, 0.005 M SDS
AlNPy	0.1 M Py, 0.05 M $NaNO_3$
AlNPyTi	0.1 M Py, 0.05 M $NaNO_3$, 0.05 M DHBDS
AlNPyS	0.1 M Py, 0.05 M $NaNO_3$, 0.005 M SDS
AlNTiS	0.05 M DHBDS, 0.005 M SDS, 0.05 M $NaNO_3$
AlNPyTiS (X-Nit)	0.1 M Py, 0.05 M DHBDS, 0.005 M SDS, 0.05 M $NaNO_3$
AlCiTiS	0.05 M DHBDS, 0.005 M SDS, 0.05 M $C_6H_8O_7$
AlCiPyTiS (X-Cit)	0.1 M Py, 0.05 M DHBDS, 0.005 M SDS, 0.05 M $C_6H_8O_7$

The CV curves related to the samples treated in the electrolytes with and without $NaNO_3$ (AlNPy, AlNPyTi, AlNPyS, AlPyTi and AlPyS) are presented in Fig. 6.7.

In an electrolyte containing only the pyrrole monomer and $NaNO_3$ (Fig. 6.7 (a), grey and black curves), the current density decreases from the first to the second scan. As the decrease in the current due to passivation of the electrode dominates the increase of current due to the polymerization.

Addition of DHBDS (Tiron) or SDS facilitates the electropolymerization of polypyrrole on the aluminum substrate and significantly increases the current density (Fig. 6.7 (a), green and blue curves).

In the absence of $NaNO_3$ (Fig. 6.7 (b)), no passivation is observed and the current density increases from the first to the second scan. According to Fig. 6.7 (b), the effect of SDS on catalyzing the electropolymerization process is not comparable to that of DHBDS (blue curves). While the mixture of $NaNO_3$ and SDS has a comparable effect on increasing the current density to that of DHBDS (Fig. 6.7 (a), green curves).
The results related to the ratio of aluminum oxide to the metallic form for the different samples of Table. 6.4 is presented in Fig. 6.8.

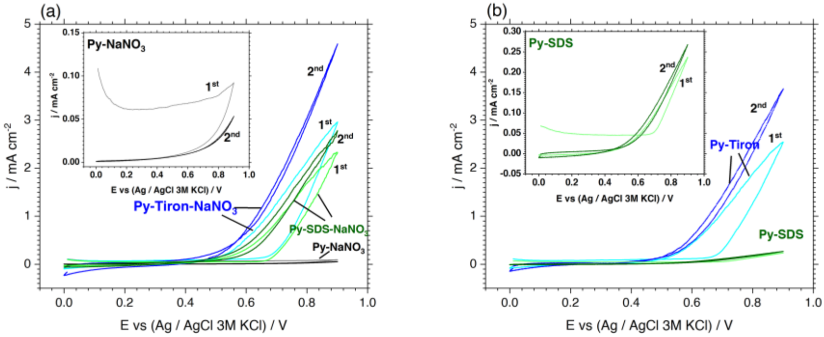

Fig. 6.7. CV curves of the aluminum samples treated in the solutions (a) with $NaNO_3$ and (b) without $NaNO_3$ (scanning rate = 10 mV/s).

The presence of passivating anions increases the Al_2O_3/Al ratio on the substrate. However, based on the graph shown in Fig. 6.8 (b), in the absence of other chemical reagents in the solution, including the Py monomer, DHBDS and SDS, nitrate and citrate anions do not show a significant difference in their passivating effect on the aluminum substrate. This behavior is expected from the CV curves depicted in Fig. 6.2.
By separately adding the different chemicals, it seems that the Py monomer is the key chemical component which leads to more oxidation of the aluminum electrode.

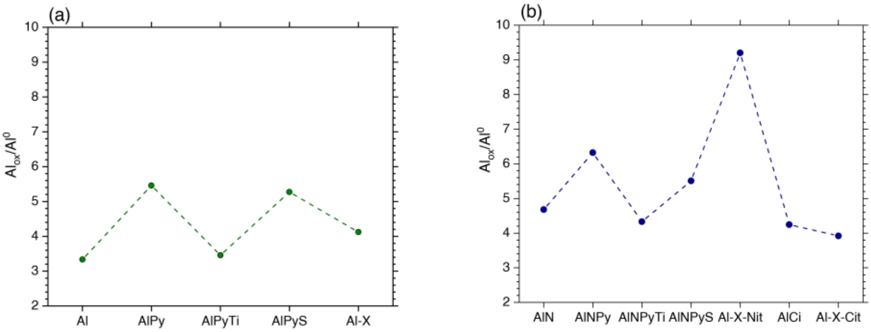

Fig. 6.8. Al_2O_3/Al ratio for samples treated in electrolytes (a) without the passivating anions (b) with passivating anions (nitrate and citrate).

Addition of DHBDS to both kind of electrolytes (with and without the passivating anions), decreases the oxidation of aluminum. While in this sense, SDS seems to have a negligible effect. The X-Nit solution leads to the highest level of oxidation.

6.2.2. Effect of NaCl concentration

The redox responses of the three different polypyrrole coatings (X, X-Cit and X-Nit) were investigated in 0.1 M NaCl solution. These coatings were subjected to potential cycling between -1 and 1 V (vs Ag/AgCl (3 M KCl)) at a scanning rate of 10 mV/s for five successive scans (Fig. 6.9). The cyclic voltammograms are quite similar to those reported in the literature [225].
According to Fig. 6.9, all the coatings are electrochemically active and were not overoxidized during the electropolymerization step. One oxidation and one reduction peak can be seen in the related curves in this figure. The oxidation peak is around 0.05-0.15 V and it can be related to the oxidation of polypyrrole.
The X-Nit coating yields the most positive oxidation voltage. All the coatings reveal a negative shift in the oxidation peak from the first to the fifth cycle.

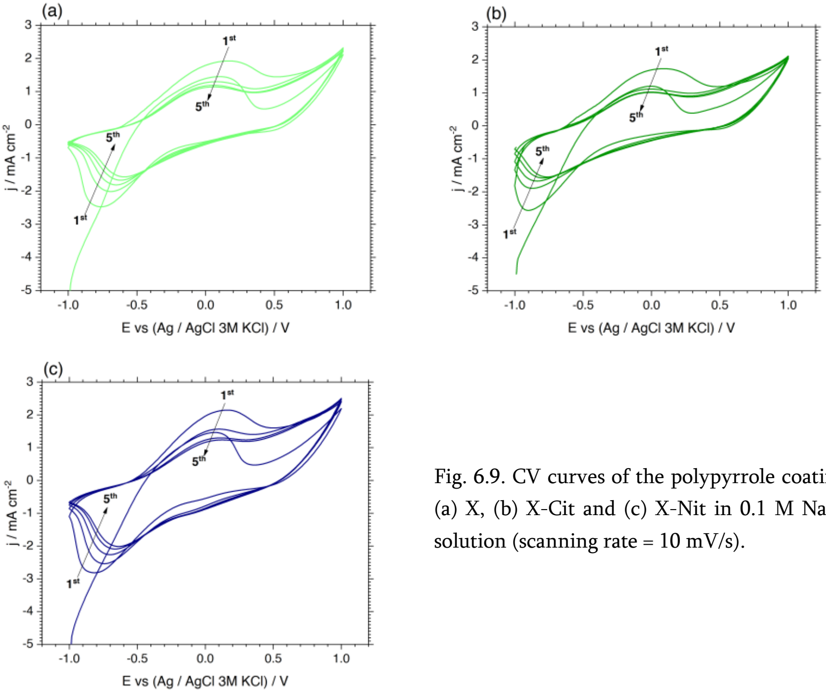

Fig. 6.9. CV curves of the polypyrrole coating (a) X, (b) X-Cit and (c) X-Nit in 0.1 M NaCl solution (scanning rate = 10 mV/s).

Oxidation peaks of the coatings X and X-Cit are similar, while the coating X-Nit shows slightly higher currents.

The reduction peak is around -0.8 - -0.9 V and it can be related to the reduction of the polypyrrole film. The potential of this peak is very similar for all three coatings. A positive shift in this reduction peak from the first to the last scan can be observed. Evidently, the coatings lose their redox capability as the test proceeds from the first to the last scan. This can be easily observed by checking the values of current densities that decrease by increasing the number of voltammetric cycles. This shows the main drawback of polypyrrole coatings which is irreversible degradation under anodic potentials [225].

Values of current density are maximum for the coating X-Nit among the three coatings, which can be related to the presence of more material, as this coating has the highest thickness.

EIS responses of the three coatings were measured to investigate the electrochemical degradation of the coatings and to monitor their electrochemical interaction with the aluminum substrate.

Two concentrations of 0.1 and 0.6 M NaCl were chosen to investigate the effect of chloride ion concentration on the coatings' behavior and stability. OCP was also monitored during immersion in both NaCl solutions (Fig. 6.10). The coated samples were kept immersed in the more concentrated solution for longer times (up to 7 days) to assess the failure time (Fig. 6.10 (c)).

Bode presentations of EIS spectra for the bare and coated aluminum samples during 24 hours of immersion in 0.1 and 0.6 M NaCl solutions are depicted in Fig. 6.11 and Fig. 6.12, respectively.

The OCP value of a polypyrrole coated aluminum sample is an average of the electrochemical reactions taking place in the system, including the reduction of the polypyrrole film and the corrosion of aluminum. Due to the large potential difference between these reactions, OCP monitoring provides information about the dominant electrochemical process [226]. At a high OCP value, the potential is dominated by the polypyrrole reduction, while at the low OCP values the corrosive dissolution of aluminium prevails. Therefore, a noble OCP is indicative of a protected substrate, while an active potential indicates that the substrate is actively corroding.

According to Fig. 6.10, OCP values of all coated samples in both solutions are considerably nobler in comparison to the bare sample. The average difference is around 0.8 V, which is quite significant. OCP values recorded in 0.1 M NaCl solution (Fig. 6.10 (a)) are comparable for the three polypyrrole coatings up to 10 hours of immersion. However, at the longer times, OCP decreases for the X and X-Cit coatings, while it remains quite stable for the X-Nit coating.

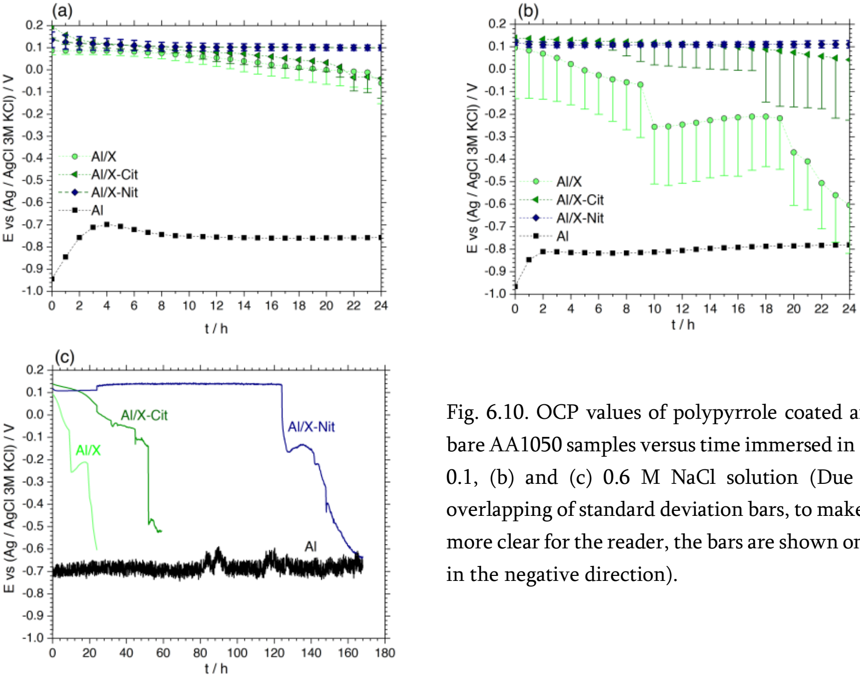

Fig. 6.10. OCP values of polypyrrole coated and bare AA1050 samples versus time immersed in (a) 0.1, (b) and (c) 0.6 M NaCl solution (Due to overlapping of standard deviation bars, to make it more clear for the reader, the bars are shown only in the negative direction).

It can also be seen that the OCP values for the X-Nit coating show smaller standard deviation indicating better reproducibility of the measurements performed on this coating.

The difference between OCP values of the three polypyrrole coatings is more distinct in 0.6 M NaCl solution. As it can be observed from Fig. 6.10 (b), OCP initially decreases linearly for the X coating, suddenly dropping after 8 hours and remaining constant up to 18 hours, when again drops and continues to decrease.

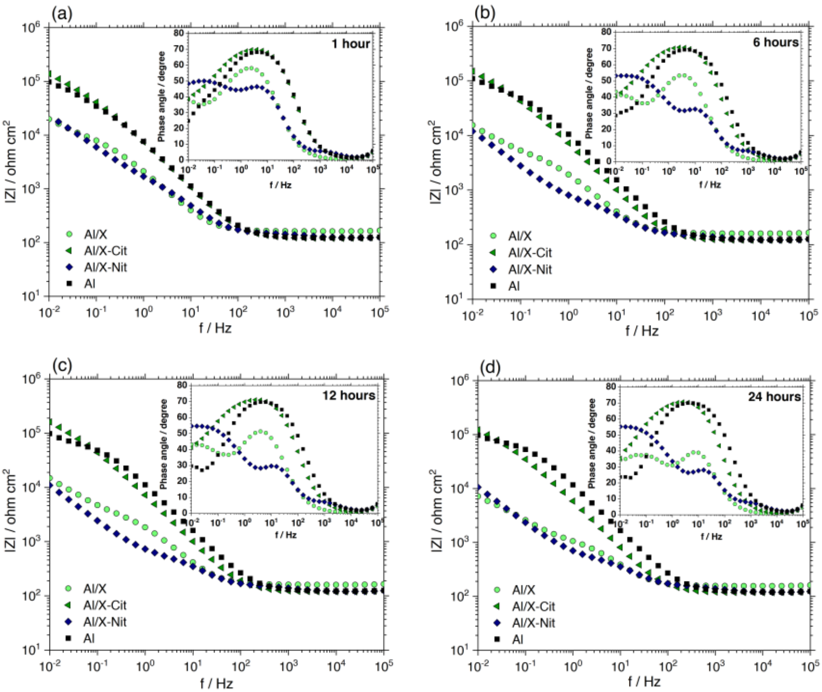

Fig. 6.11. EIS spectra of the polypyrrole coated and bare AA1050 after (a) 1, (b) 6, (c) 12 and (d) 24 hours of immersion in 0.1 M NaCl solution.

The two sudden drops indicate the breakdown of the coating with partial repair after the first breakdown and continuous deterioration after the second breakdown.

The X-Cit coating appears to be more stable, starting to deteriorate after ca. 18 hours of immersion. As evidenced in Fig. 6.10 (c), the final failure for these two coatings occurs after 18 hours (coating X) and 48 hours (coating X-Cit).

The coating X-Nit, however, retains its OCP value constant for 120 hours (5 days), after which it first breaks down and partially re-heals, and then again breaks down to yield the OCP similar to that of the unprotected surface after 7 days of immersion.

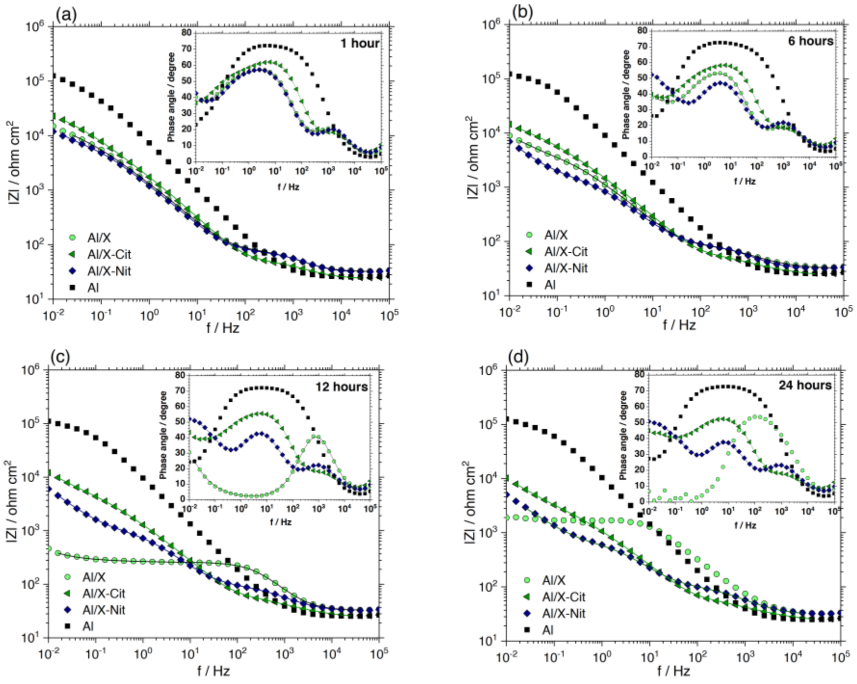

Fig. 6.12. EIS spectra of the polypyrrole coated and bare AA1050 after (a) 1, (b) 6, (c) 12 and (d) 24 hours of immersion in 0.6 M NaCl solution (solid lines are the fitted data).

Considering the results in Fig. 6.10, the protective performance of the coatings can be ranked as follows: X-Nit >> X-Cit > X.

Regarding the EIS results (Fig. 6.11), for the bare aluminum substrate in 0.1 M NaCl solution, one time constant at the medium frequency range and a hint of a Warburg tail at the low frequency range, after ca. 12 hours of immersion, are recorded.

The coating X starts with one time constant (RC constant) at the medium and one Warburg tail at the low frequency ranges, both descending and shifting toward higher frequencies in the phase spectra over the immersion time. The mass-transport-related constant (Warburg element) is converted to a separate RC constant at the end of 24 hours.

For the X-Nit coating, in addition to the Warburg element/time constant at the low and one RC constant at the medium frequency ranges, an extra time constant at the high frequency range is present from the first hour of immersion. The EIS response of this coating does not change much over the immersion time.

The EIS spectra of the coating X-Cit is different in comparison to those of the other two coatings. The behavior of this coating is characterized by only one time constant. For this coating, the total impedance values are similar to those of the bare sample. However, the total impedance values of the other two polypyrrole coatings are lower compared to aluminum. These results do not stand for worse corrosion performances of the polymer coatings but represent the (semi) conductive nature of the polypyrrole film. Other researchers have reported similar results [143, 227]. Based on these observations, the conductivity of the three polypyrrole coatings in 0.1 M NaCl solution can be ranked as follow: X-Nit > X > X-Cit.

Initially, impedance responses of the three polypyrrole coatings in 0.6 M NaCl solution depict the presence of two time constants, at the high and medium frequencies. A mass-transport-related constant appears at the low frequency range and converts to a time constant at longer times (Fig. 6.12). The EIS response of the bare aluminum is similar in both solutions.

The coating X is the first coating to fail in this solution as evidenced by the results in Fig. 6.10 (b). Unlike the phase spectra of this coating recorded in 0.1 M NaCl solution (Fig. 6.11), the first phase angle maximum recorded at the high frequencies is quite obvious from the first hour (Fig. 6.12 (a)). The coating breaks down after 10 hours of immersion and its total impedance drops abruptly, which is in agreement with the OCP behavior in Fig. 6.10 (b).

The EIS spectra after the coating breakdown are first characterized by one time constant and one Warburg response (12 hours) and then only by one-time constant (24 hours). Clearly, as the corrosive solution reaches the surface, the EIS spectra alter from presenting the coating behavior to showing the substrate response.

The EIS spectrum of the X-Nit coating commences with a response characterized by two time constants. However, after ca. 6 hours of immersion, a Warburg tail starts appearing, which further develops into a separate time constant thus yielding a spectrum that is characterized by three time constants after 24 hours of immersion (Fig. 6.12 (c)). This behavior is similar to that of the same coating in 0.1 M NaCl (Fig. 6.11 (c)). Unlike in 0.1 M NaCl solution, from the first immersion hour the X-Cit coating presents the first phase angle maximum at the high frequency range together with the second one at the medium frequency. The development of EIS response of this coating in 0.6 M NaCl solution is similar to that of the X-Nit coating. However, the conversion of Warburg tail to a separate time constant is slower.

The difference of total impedance responses of the three polypyrrole coatings is less significant in the more concentrated NaCl solution while it increases over time (after ca. 12 hours). However, the three coatings keep the same trend in conductivity at both NaCl concentrations.

To interpret the EIS results (performed in 0.6 M NaCl solution), these impedance responses were modeled using an equivalent electrical circuit (Fig. 6.13) and the fitting parameters were analyzed as a function of time.

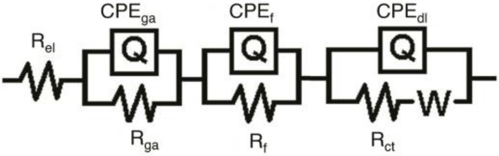

Fig. 6.13. Equivalent circuit to fit the EIS responses of the polypyrrole coatings.

The corresponding circuits employed to fit the EIS responses of polypyrrole/metal systems (aluminum and steel) are commonly based on the interpretation of a time constant (RC constant) at medium/high and a Warburg tail at low frequency ranges [152, 155, 156, 228]. Which are typically attributed to the coating (pore) resistance, charge transfer resistance of the redox reaction of the polymer and diffusional process through the film, respectively [156, 229, 230]. Some have also considered the contribution of passive oxide layer [152, 230, 231].

The equivalent circuit (Fig. 6.13) was selected by comparing the present EIS spectra with the EIS spectra of polypyrrole coated platinum substrate (Fig. I/appendix). However, interpretation of the EIS results is complicated and different explanations might be valid.

The time constant at the high frequency range can probably be attributed to the (localized) galvanic interaction of polypyrrole film and the aluminum substrate. A resistance (R_{ga}) and a constant phase element (CPE_{ga}) represent this contribution. The time constant at the medium frequency range can be related to the polypyrrole film that is modeled by a resistance (R_f) and another constant phase element (CPE_f).

As it was mentioned before, at the low frequency range there is an exchange process between a mass-transport-related constant (Warburg element) and a separate time constant (presented by CPE_{dl} (none ideal double layer capacitance of the metal/solution interface) and R_{ct} (charge transfer resistance). This transfer shows that as the solution penetrates into the coating the response at the low frequency range changes from a diffusion-controlled to a charge-controlled behavior.

Modeling the EIS results, with the lowest error values, was not possible in the absence of any of these two elements. Which can be due to the fact that even though from time to time the presence of one of them is dominated by the other they probably always contribute to the spectra.

An alternative interpretation of the time constant at the low frequency range can be related to the reduction of oxygen at the polypyrrole/electrolyte interface [138].

Comparing the EIS spectra of the three coatings, the time constant related to the galvanic interaction is missing in the case of X and X-Cit coating, immersed in 0.1 M NaCl solution, however, it appears in 0.6 M NaCl solution. In addition, the Warburg element at the low frequency range is almost absent for the X-Cit coating at both chloride concentrations. Which may reflect a less extent of diffusion into this coating compared to the coatings X and X-Nit. In addition, it seems that the galvanic interaction of polypyrrole coating and the aluminum substrate is affected not only by the presence of electrolyte (and possibly chloride concentration) at the polypyrrole/aluminum interface but also by the conductivity of the coating. The results of data fitting for 24-hour immersion test of the three polypyrrole coatings in 0.6 M NaCl solution are presented in Table. 6.5. In addition, the fitted spectra are presented as solid lines in Fig. 6.12.

Table. 6.5. Summary of results derived from fitting the EIS responses of the polypyrrole coatings in 0.6 M NaCl solution

Parameter	R_{ga} ($\Omega.cm^2$)	R_f ($\Omega.cm^2$)	R_{ct} ($\Omega.cm^2$)	W ($S. Sec^{0.5}.cm^{-2}$)	χ^{2*}
Coating X					
1 h	40.53	488	7163	3.31×10^{-4}	1.76×10^{-4}
6 h	53.69	1372	159	5.06×10^{-4}	3.91×10^{-4}
12 h	-	2457	224	2.71×10^{-2}	2.66×10^{-4}
24 h	-	-	-	-	-
Coating X-Cit					
1 h	32.82	1938	28170	2.51×10^{-4}	1.12×10^{-4}
6 h	57.12	18250	16040	1.81×10^{-4}	1.33×10^{-4}
12 h	59.36	11190	4485	2.13×10^{-4}	1.25×10^{-4}
24 h	62.95	7099	1832	1.8×10^{-4}	1.16×10^{-4}
Coating X-Nit					
1 h	37.94	1957	1419	3.25×10^{-4}	1.72×10^{-4}
6 h	46.2	29090	1254	2.46×10^{-3}	1.13×10^{-4}
12 h	53.72	45760	725	5.70×10^{-3}	1.11×10^{-4}
24 h	66.05	426	1047	3.94×10^{-4}	9.74×10^{-5}

*Chi-squared: the sum of the squares of the residuals.

For all of the coatings, values of R_{ga} increase by the immersion time, which may imply that the galvanic interaction is slowed down/decreased due to the decrease in the coating conductivity. The film resistance (R_f) increases by the immersion time until its value drops (for the coatings X-Cit and X-Nit). The increase in R_f can be related to the decreasing conductivity of the film due to polymer reduction [232, 233]. While its increase after 24 hours of immersion in the case of the X-Cit and X-Nit coatings can be related to the gradual exposure of the metal surface to NaCl solution disturbing the trend and making the equivalent circuit unreliable.

The coating X breaks after 10 hours which alters the behavior and of course the equivalent circuit (not shown here). Due to huge scattering of the spectra, fitting has not been performed for this sample after 24 hours.

The charge transfer resistance decreases through the immersion time which shows easier charge transfer, hence faster corrosion and eventually failure. If the charge transfer resistance is considered for the oxygen reduction its decrease by the immersion time shows a faster reaction on the polymer surface.

The longer protection provided by the coating X-Nit in the more concentrated solution may be attributed to the better quality of the polypyrrole/aluminum interface due to the passivating effect of nitrate ions, which leads to a better galvanic interaction (anodic protection). The higher conductivity of X-Nit coating compared to the X and X-Cit coatings may affect the (anodic) protection as well [138]. The lower conductivity of X-Cit coating can be due to the overoxidation of polymer in citric acid solution [234].

To clarify the electrochemical behavior, we examined the coating surfaces and their cross-sectional view after the immersion tests in NaCl solutions. These observations provide a better insight regarding the electrochemical reactions at the polypyrrole/aluminum interface and facilitate understanding of the protection effect. The related images are presented in Fig. 6.14, Fig. 6.15, Fig. 6.16 and Fig. 6.17.

Fig. 6.14 depict the surfaces of the three polypyrrole coatings after 24 hours of immersion in 0.1 M NaCl solution. On all of the surfaces, the presence of some blisters is evident. The size of these blisters varies in the same order as the performances of the coatings (with respect to the OCP results in 6.10 (a)). Therefore, the coating X-Nit exhibits the smallest and the coating X the biggest blisters.

Cross-sectioning these blisters using FIB elucidates corrosion/oxidation reactions occurring at the polypyrrole/aluminum interface. SEM (BS) images of the polypyrrole/aluminum interfaces inside the blisters after 1-day immersion in 0.1 M NaCl solution are shown in Fig. 6.15. With some variations, the presence of three distinct layers including the aluminum substrate, an oxide layer and the polypyrrole film is noticeable at all cross-sections. This observation shows the inevitable galvanic interaction of polypyrrole coating with the aluminum substrate [162]. Which can keep the surface passivated but locally causes serve oxidation and forms blisters. The polypyrrole/aluminum interface outside the blister was unchanged.

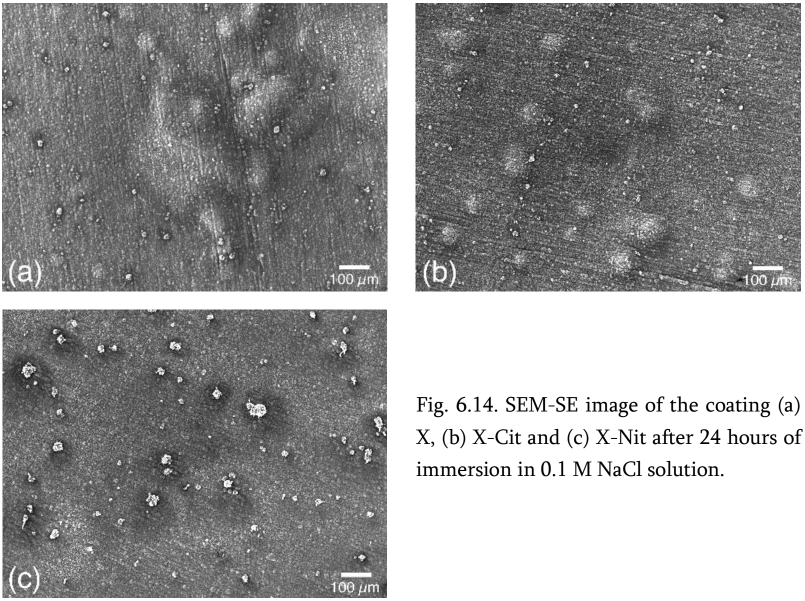

Fig. 6.14. SEM-SE image of the coating (a) X, (b) X-Cit and (c) X-Nit after 24 hours of immersion in 0.1 M NaCl solution.

The X-Nit coating was examined after 24 and 168 hours of immersion (after failure) in 0.6 M NaCl solution (Fig. 6.16). SEM image of the corroded aluminum substrate after 168 hours of exposure to 0.6 M NaCl solution is provided for comparison. The bare substrate is severely corroded and heavily covered by porous corrosion products in the absence of any protective coating (Fig. 6.16 (c)).

The blisters have significantly spread on the coating surface after 24 hours (Fig. 6.16 (a)) and finally caused failure after 5 days.

A FIB-SEM image taken after cross-sectioning a blister, shown in Fig. 6.16 (a), displays the presence of a dense aluminum oxide layer at the interface of the polypyrrole coating with the aluminum substrate (Fig. 6.17 (a)). The composition of these three layers (the polymer coating, the aluminum oxide layer and the aluminum substrate) is confirmed using EDXS and map analysis of carbon, oxygen and aluminum (Fig. 6.17 (b)). For this analysis, the sample has been rotated to the optimum measurement position of the instrument.

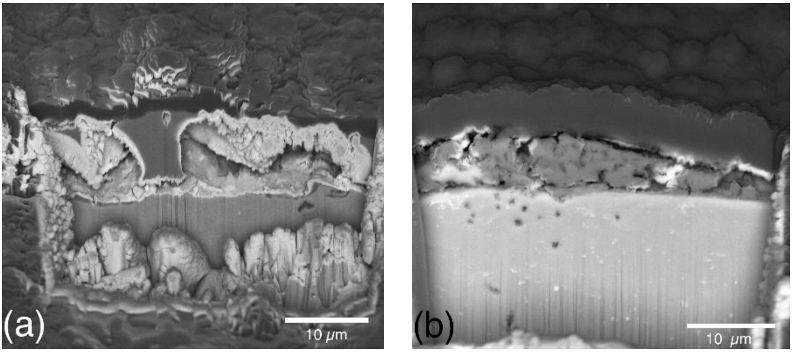

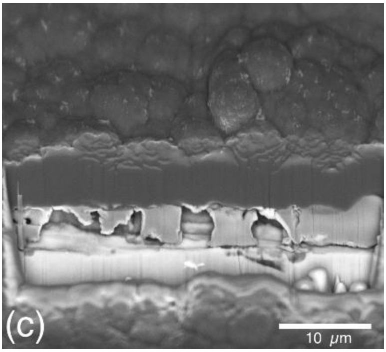

Fig. 6.15. Cross-sectional FIB-SEM (BS) image of the coating (a) X, (b) X-Cit and (c) X-Nit after 24 hours of immersion in 0.1 M NaCl solution.

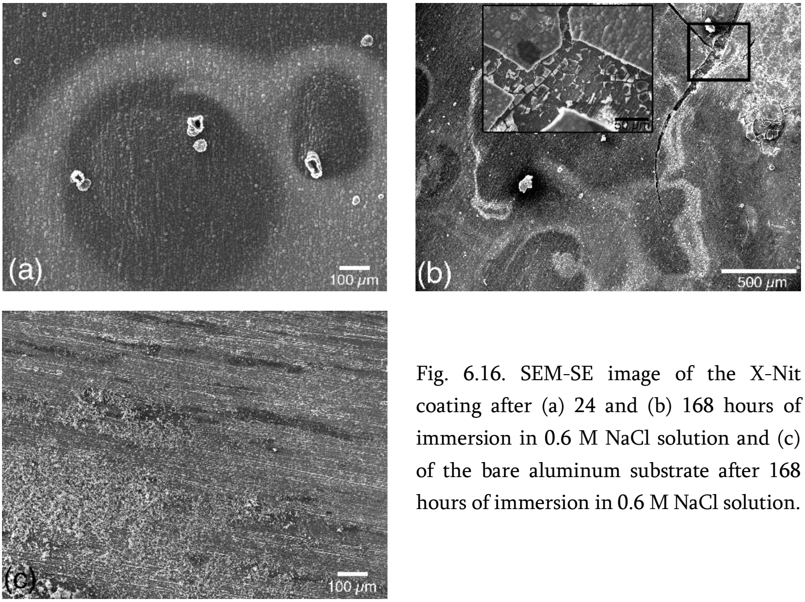

Fig. 6.16. SEM-SE image of the X-Nit coating after (a) 24 and (b) 168 hours of immersion in 0.6 M NaCl solution and (c) of the bare aluminum substrate after 168 hours of immersion in 0.6 M NaCl solution.

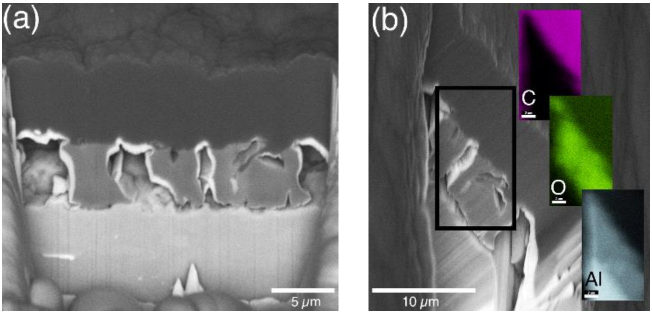

Fig. 6.17. (a) Cross-sectional FIB-SEM (BS) image of the X-Nit coating after 24 hours of immersion in 0.6 M NaCl solution (b) results of map analysis of this cross-section.

Formation of blister at both chloride concentrations for all the coatings is inevitable, however, their formation is significantly limited on the X-Nit coating in 0.1 M NaCl solution compared to the other two coatings. In this solution, the chloride ions are present at the interface, but the X-Nit coating keeps the surface passivated and protected.

In other words, the addition of $NaNO_3$ to the electropolymerization solution results in the formation of the coating with a reduced number of blisters (after immersion) and longer protection provided in more concentrated NaCl solutions.

6.2.3. Conclusions I

Polypyrrole coatings were successfully electropolymerized on substrates of AA1050 using cyclic voltammetry. Different electropolymerization solutions containing Py, SDS, DHBDS, $C_6H_8O_7$ and $NaNO_3$ were used. Solutions containing citrate or nitrate anions led to thicker coatings. The coatings' morphologies were unaffected by the solution chemistry. The presence of nitrate anions led to the passivation of the aluminum electrode during the electropolymerization step and to the deposition of a more conductive/electrochemically active polymer layer. These facts resulted in better and longer corrosion protection in 0.1 and 0.6 M NaCl solutions. However, the difference among the corrosion protection properties of the three polypyrrole coatings was more obvious in 0.6 M NaCl solution. In the presence of chloride ions, all coatings suffered from the formation of blisters as a result of severe (localized) galvanic interaction of polypyrrole coating with aluminum. This may question the application of polypyrrole coating in concentrated NaCl solutions. However, it is shown the protection efficiency can be improved by altering the solution chemistry which affects the polymer/metal interface and the conductivity of the coating. Therefore, the application of polypyrrole in corrosion protection is not totally ruled out but needs specific considerations.

Based on the results of this section, the solution X and X-Nit were selected to be used for the electropolymerization of polypyrrole coatings on Rheo-HPDC Al-Si alloys.

6.3. Results and discussion II (Polypyrrole coatings on Al-Si alloys)

6.3.1. Effect of solution chemistry

Fig. 6.18 (a) presents the effect of increasing the concentration of DHBDS (the electron transfer mediator) and addition and increasing the concentration of $NaNO_3$ on electrodeposition. Both of these chemicals have an increasing effect on the deposition current density. However, their action mechanism is quite different.

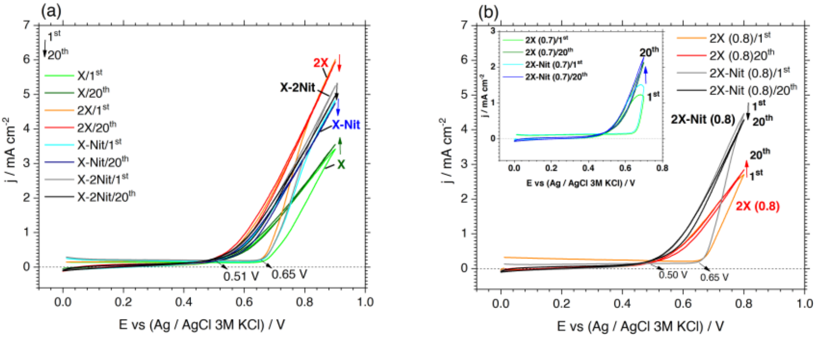

Fig. 6.18. CV curves (1st and 20th scans) of electropolymerization of the polypyrrole coating on Al-Si substrate (2R) at (a) 0-0.9 V and (b) 0-0.7 and 0-0.8 V (scanning rate=10 mV/s).

In all the solutions, changes in the values of current density during twenty scans are negligible. The oxidation voltage of pyrrole (indicated in the graphs) is fairly similar in different solutions.

As it was explained in section 6.2, the mechanism through which the nitrate (NO_3^-) anions increase the growth of polypyrrole film is passivation of the aluminum electrode. As in their presence, the dissolution of the substrate is alleviated, therefore, thicker coating will be electrodeposited on the surface [141, 175, 213, 235].

The mechanism of catalytic action of DHBDS (Tiron) is schematically presented in Fig. 6.19. According to this figure, since DHBDS provides extra electrons for the oxidation reaction, it can be utilized to decrease the required over-potential for the electrodeposition of the coating [157, 173, 236].

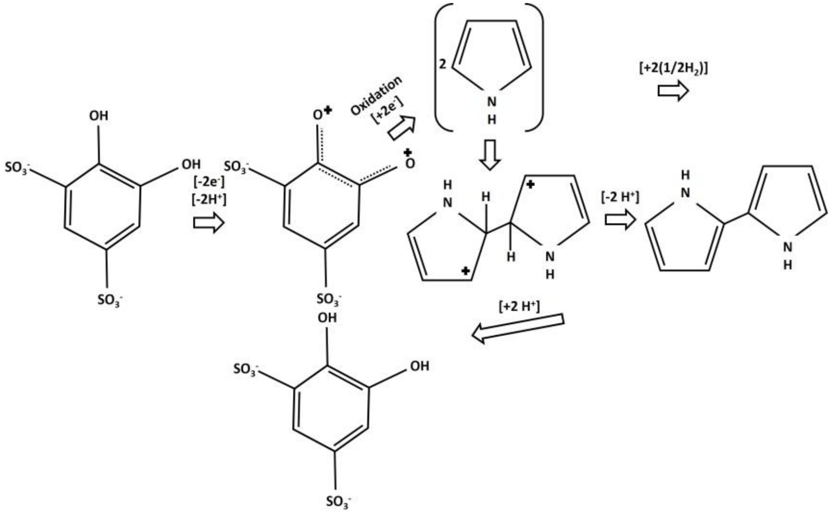

Fig. 6.19. Schematic presentation of the catalytic effect of DHBDS (Tiron) on the electropolymerization of polypyrrole.

The increase in the curve's slope in case of the solution 2X in comparison to the solution X (Fig. 6.18 (a)), confirms this catalytic mechanism. In other words, by doubling the concentration of DHBDS the growth rate of polypyrrole is increased. The same change is not seen in the case of the solution X-2Nit compared to the solution X-Nit.

SEM images of the substrate surfaces underneath the coatings 2X and X-2Nit are presented in Fig. 6.20. In the case of the coating 2X (Fig. 6.20 (a)), the surface underneath the coating is not much different compared to the untreated sample (Fig. 6.20 (c)). However partial anodic dissolution of the surface is obvious, especially at the interface of aluminum with the eutectic silicon phase and/or iron-rich intermetallic particles, making these two phases appear more prominent in Fig. 6.20 (a).

According to Fig. 6.20 (b), the substrate underneath the coating X-2Nit has been oxidized. As it can be observed the oxidation is not homogenous and some areas are covered by a thicker oxide layer. The results of EDXS analysis related to one of these areas (shown in a box in Fig. 6.20 (b)), is provided in Table. 6.6.

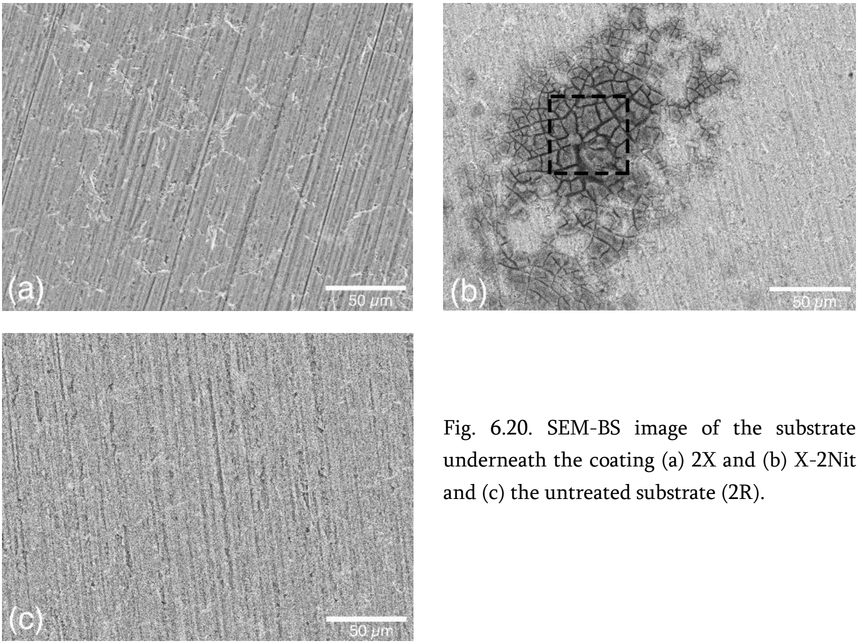

Fig. 6.20. SEM-BS image of the substrate underneath the coating (a) 2X and (b) X-2Nit and (c) the untreated substrate (2R).

Table. 6.6. Result of EDXS analysis on oxidized area shown in Fig. 6.20(b)

Element	Mass percentage
O	59.6
Al	29.3
Fe	0.2
Si	0.5
N	3.4
C	6.3

Fig. 6.21 illustrates the granular cauliflower morphology of the coatings X, X-Nit and X-2Nit on the 2R alloy.

Anion doping as an essential process in the electropolymerization of polypyrrole has a significant influence on the polymer morphology [237].

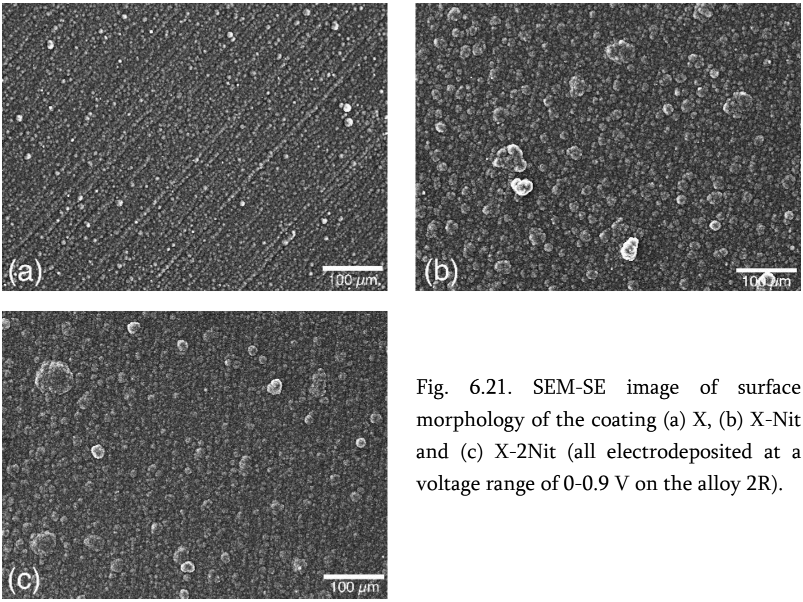

Fig. 6.21. SEM-SE image of surface morphology of the coating (a) X, (b) X-Nit and (c) X-2Nit (all electrodeposited at a voltage range of 0-0.9 V on the alloy 2R).

Considering the solutions we have used two organic anions, dodecyl sulfate (DS^-) and $DHBDS^{2-}$, and one inorganic anion (NO_3^-) can be doped into the polypyrrole coating.

Based on Fig. 6.21 (b) and (c), introducing NO_3^- into the coating increases its grain size and inhomogeneity. According to Singh et al. [238], the presence of inorganic doping anions such as NO_3^- can alter the growth behavior of polypyrrole coating from a laminar-type (in the presence of organic doping anions) to a fractal-type. Indeed, the presence of a rougher surface (hills and downs) (Fig. 6.21 (b) and (c)) indicates a more complicated 3D growth pattern.

To reduce the anodic dissolution of the substrate, electropolymerization of polypyrrole coating (2X) was performed at the smaller voltage ranges, by decreasing the upper voltage limit from 0.9 to 0.8 and 0.7 V. 0.05 M $NaNO_3$ was added to the solution as well. Fig. 6.18 (b) presents the CV curves for these samples.

The effect of upper voltage shows itself in the considerably decreased current densities for the samples treated in the smaller voltage ranges compared to those previously shown in Fig. 6.18 (a). However, as expected, the oxidation voltage of pyrrole during the first scan and the next ones are quite alike for all the samples. The lower current density is firstly due to the lower overpotential and therefore lower driving force for the electropolymerization. In addition, lower anodic dissolution of the aluminum substrate is expected in this condition.

In the 2X solution, the growth rate is higher at the smaller potential range, while in the 2X-Nit solution the growth rate is similar at both potential ranges. This is due to the fact that the anodic dissolution of the substrate has a more prominent effect in a solution without any passivating anion.

Surface morphologies of the related coatings in Fig. 6.18 are presented in Fig. 6.22. According to this figure, the upper voltage limit has no noticeable influence on the growth pattern and therefore the morphology. However, it slightly increases the size of the polypyrrole globules, as seen and reported by other researchers before [143].

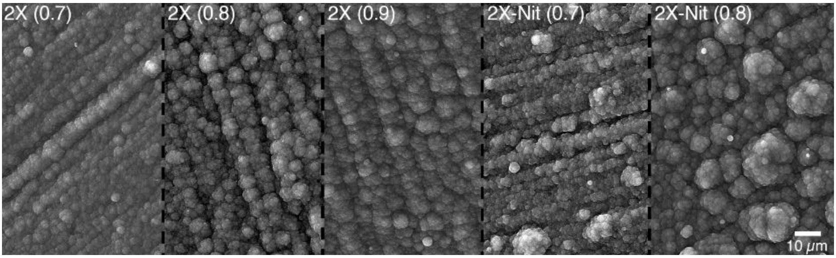

Fig. 6.22. SEM-SE image of surface morphology of the polypyrrole coatings electrodeposited at the different voltage ranges and from the two solutions 2X and 2X-Nit (on the alloy 2R).

Measured thicknesses of the different polypyrrole coatings are summarized in Fig. 6.23. As it is expected from the CV curves (Fig. 6.18), the thickness of the polypyrrole film increases by increasing the concentration of DHBDS, addition and increasing the concentration of $NaNO_3$ and increasing the upper limit of the voltage range.

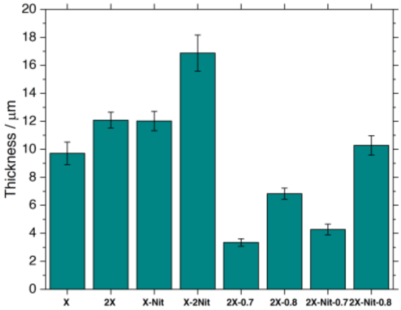

Fig. 6.23. Thickness of the different polypyrrole coatings on the 2R alloy.

6.3.2. Effect of silicon content

Fig. 6.24 compares the first and the last CV scans in two different solutions (with and without $NaNO_3$) for the alloys and pure aluminum.

Following the first forward scan, for all the samples the current density increases at the voltage of ca. 0.66 V. This increase coincides with the formation of a black polypyrrole film on the surface indicating that this is the oxidation voltage of the pyrrole monomer. Oxidation of the polymer film occurs almost at the same voltage on the three different substrates. No major cathodic peak can be observed for any of the samples and values of current density remain unchanged during the twenty scans. The polymer oxidation voltage decreases to ca. 0.55 V after the first scan.

However, negative current densities are recorded for all of the coatings at the voltage range between 0-0.2 V, during both forward and reverse scans. This implies that the coatings are being reduced to some level.

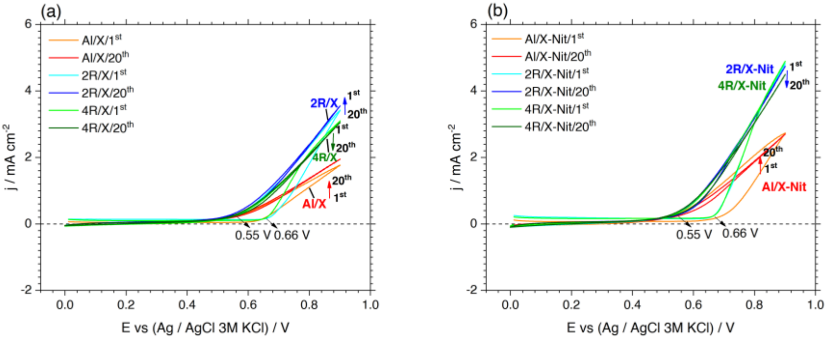

Fig. 6.24. CV curves of electropolymerization of polypyrrole coating on the Al-Si alloys and AA1050 in the solution (a) X, (b) X-Nit (scanning rate = 10 mV/s).

However absolute values of the negative current densities are as low as 0.03-0.3 mA/cm^2.

The electrodeposition is faster on the alloy samples compared to the pure aluminum, which is evident by significantly higher current densities and curve slopes.

Similar to the results presented in sections 6.2.1 and 6.3.1, the addition of $NaNO_3$ increases the deposition current density for all the samples.

Before further discussion about the effect of $NaNO_3$, the different behavior of Al-Si alloys and pure aluminum will be argued.

Fig. 6.25 presents the SEM images and the results of mapping analysis of the alloy 2R treated for a single cycle in the two solutions, X and X-Nit. After the treatment samples were partially covered by a thin polypyrrole film.

According to the results presented in chapter 4, the microstructure of Rheo-HPDC Al-Si alloys includes α-aluminum particles in two different sizes (primary α_1-Al and secondary α_2-Al), Al-Si eutectic dual phase region, and iron-rich intermetallic particles (β-AlFeSi) located inside the eutectic phase.

Based on the elemental maps in Fig. 6.25 and considering the size of particles, the uncovered areas in both samples are primary α_1-Al particles. Following the elemental map analysis of silicon and iron, the adjacent areas are shown to be α_2-Al particles and the eutectic phase containing iron-rich intermetallic particles.

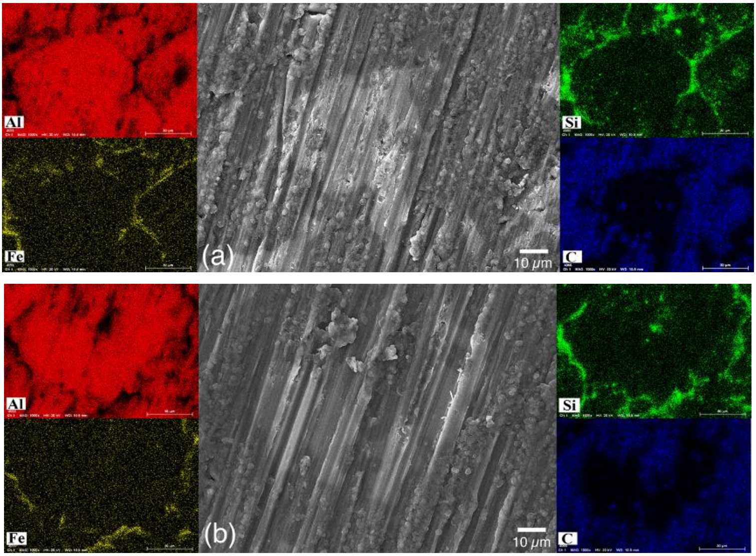

Fig. 6.25. SEM-SE image and map analysis of surface morphology of the coating (a) X and (b) X-Nit on the alloy 2R after one CV scan.

Based on these results and the fact that alloy samples present higher current densities and steeper curves during the electrodeposition (compared to the pure aluminum) (Fig. 6.24), the catalytic effect of the eutectic silicon phase and/or iron-rich intermetallic particles on the electropolymerization of polypyrrole coatings can be suggested.

These results are similar to those reported by Martins et al. [143] about the effect of intermetallic compounds (such as $Mg_3Si_6Al_8$ or Mg_2Si) in AA6061 on promoting the electropolymerization of polypyrrole.

Oxidation/dissolution of the eutectic silicon phase and intermetallic particles is less probable compared to the aluminum phase. Therefore, these phases can be the preferential electrodeposition sites.

To compare the passivating effect of NO_3^- anions on different Al-Si samples, two CV scans in each of the two electrolytes, without the pyrrole monomer, were applied. The results are presented in Fig. 6.26.

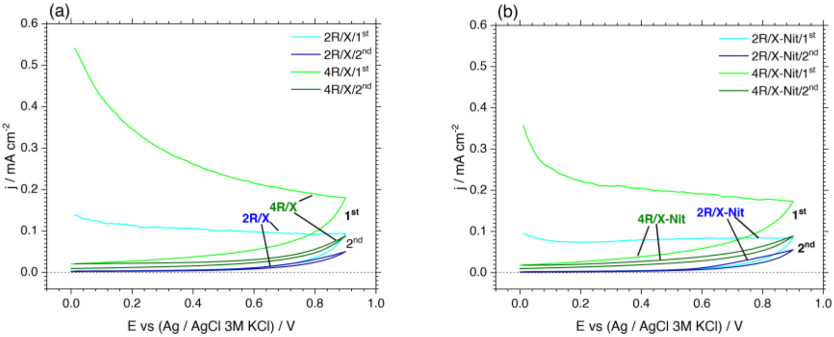

Fig. 6.26. CV curve in the solution (a) X and (b) X-Nit without the pyrrole monomer on the alloys 2R and 4R.

For the alloy 2R, the first scan in both X and X-Nit solutions starts with decreasing the current density and continues with a wide passive range. The values of current density are lower when the sample is treated in the X-Nit solution which shows a lower rate of anodic dissolution. The second scan displays significantly lower current densities in both cases, indicating that the anodic dissolution is reduced due to the presence of a passive aluminum oxide layer.

The same trends can be observed for the alloy 4R. Starting from the first scan, current densities in both solutions are considerably higher for the alloy 4R in comparison to the alloy 2R. Previous studies on these alloys (presented in chapter 5) have revealed that the alloy with the higher amount of silicon possesses a surface that is more electrochemically active. This fact justifies the higher values of current density.

The lower anodic dissolution of the alloy 2R compared to the alloy 4R yields to the higher deposition current density during the electropolymerization process (in the absence of passivating anions) (Fig. 6.24 (a)).

Fig. 6.27 compares the thickness of the coatings X and X-Nit on the alloys 2R and 4R and on the pure aluminum. As it is expected from the CV curves in Fig. 6.24, the coating X-Nit, on both alloys, possesses higher thickness.

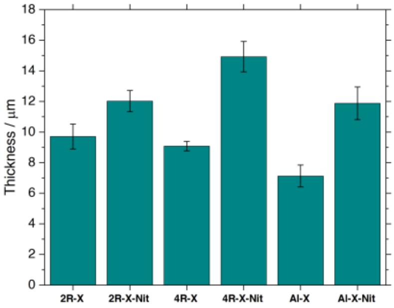

Fig. 6.27. Thickness of the polypyrrole coatings on different aluminum substrates.

Fig. 6.28 compares surface morphology of the coatings X and X-Nit on the alloy 4R and the pure aluminum substrates. The cauliflower morphology can be seen for all the coatings. Similar to the results depicted in Fig. 6.21, the coating X-Nit on the alloy 4R shows coarser, rougher and less homogenous morphology compared to the X coating. This difference in the morphology is less significant and can be ignored for the coatings on the pure aluminum substrates (Fig. 6.28 (c) and (d)).

This phenomenon can suggest that the electrochemical activity of surface and its oxidation/passivation behavior promote or impede the effect of NO_3^- anions.

The chemical composition of the two polypyrrole coatings, X and X-Nit, electrodeposited on the alloy 2R, examined by XPS, is presented in Fig. 6.29.

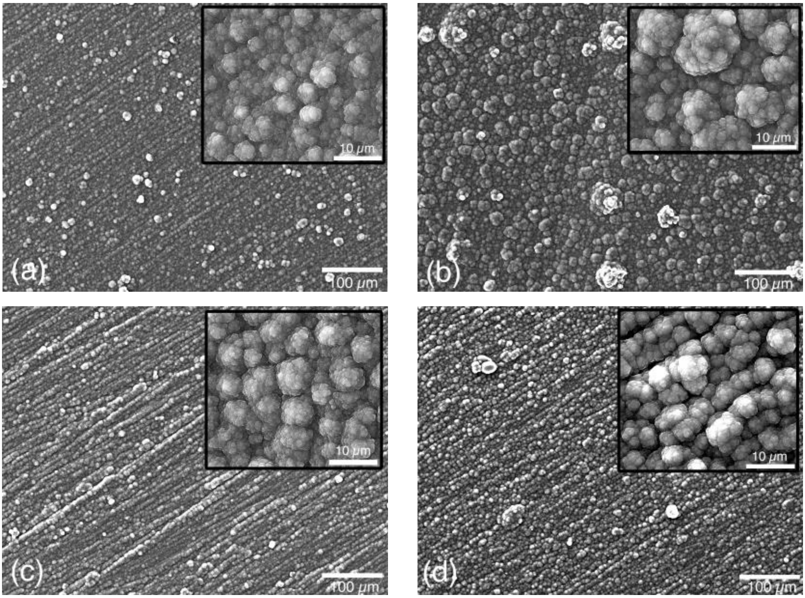

Fig. 6.28. SEM-SE image of surface morphology of the coating X on (a) alloy 4R and (c) AA1050 and the coating X-Nit on (b) alloy 4R and (d) AA1050.

This figure depicts the high-resolution spectra of carbon, nitrogen and sulfur. The two coatings seem similar in composition, however, a small variation in the nitrogen peak (Fig. 6.29 (b)), in terms of intensity, at the high binding energy can be observed for the coating X-Nit, which may be related to the incorporation of NO_3^- anions.

The component at the low binding energy can be assigned to C=NH, while the components at ~ 401 and ~ 402 eV can be assigned to $C-N^+$ and $C=N^+$, respectively [239, 240].

It should be reminded that, unlike the alloy samples, the results of XPS analysis on the polypyrrole coating on the pure aluminum showed no strong proof for the incorporation of nitrate anions (Fig. 6.5).

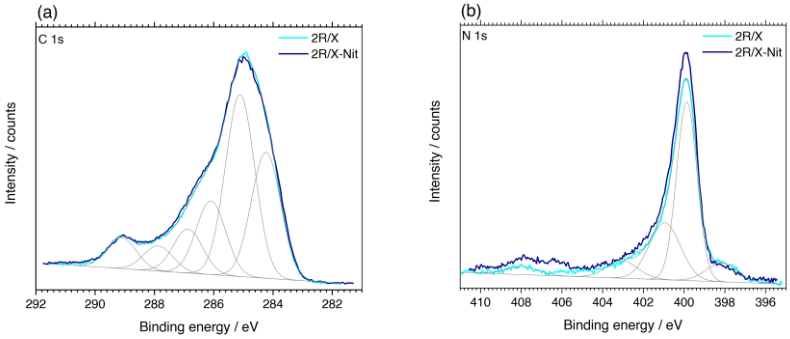

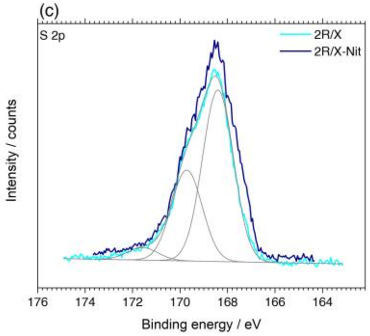

Fig. 6.29. High-resolution XPS spectra of the polypyrrole coatings on the alloy 2R (a) C 1s, (b) N 1s and (c) S 2p.

This can be attributed to the higher thickness of the coating on the alloy substrate compared to that on the pure aluminum. Similar results have been reported by Idla et al. [241] on the effect of thickness on the anion incorporation.

While examining the surface morphology of the polypyrrole coatings on Al-Si alloys, some abnormalities/defects were found on some of the samples. Fig. 6.30 (a) displays one of them. The cross-sectional view (Fig. 6.30 (b)) suggests that these abnormalities are due to the presence of casting defects on the substrates.

Fig. 6.31 (a) depicts the SEM image of a casting defect on the bare Al-Si substrate. Due to the presence of the eutectic silicon phase and/or iron-rich intermetallic particles, the casting defect starts to get covered by the polypyrrole deposition from the first scan, as it is shown in Fig. 6.31 (b).

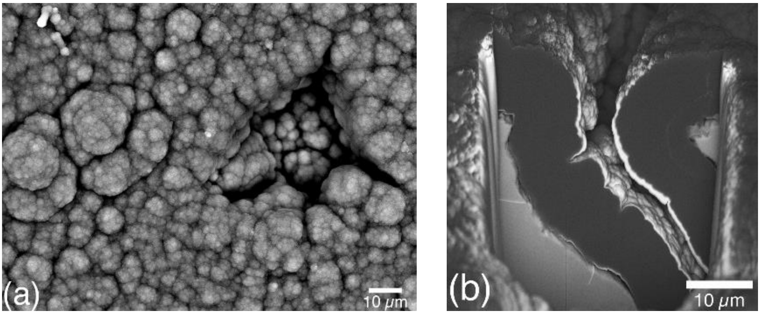

Fig. 6.30. (a) SEM-SE image of the defected coating X (on 2R alloy) and (b) cross-sectional SEM-FIB (BS) of a defect.

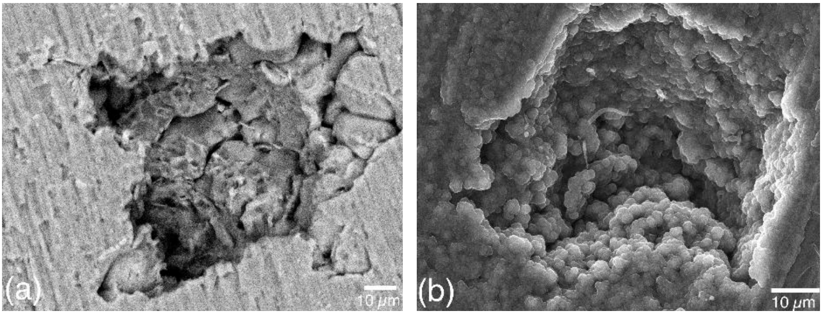

Fig. 6.31. SEM-BS of the alloy 2R with a casting defect (a) before and (b) after the first CV scan.

6.3.3. Electrochemical examination and protection/failure mechanism (part I)

OCP values of the polypyrrole coated and bare samples of the 2R and 4R alloys during 24 hours of immersion in 0.6 M NaCl solution are depicted in Fig. 6.32.

The polypyrrole coated samples of both alloys present nobler potential values in comparison to the bare substrates. The two different coatings, X and X-Nit, show different degrees of stability on the two alloys. For the coating X, when electrodeposited on the alloy 4R, OCP values decrease during 24 hours leading to a partial breakdown after ca. 12 hours.

This coating displays more stable values of OCP on the alloy 2R. Which can be attributed to the fact that the alloy with lower silicon percentage is less prone to localized corrosion due to less available spots for the possible galvanic coupling [220].

The coating X-Nit, on both alloys, presents nobler and more stable OCP values. In addition, this coating shows lower values of standard deviation in comparison to the coating X, indicating better reproducibility of the measurements.

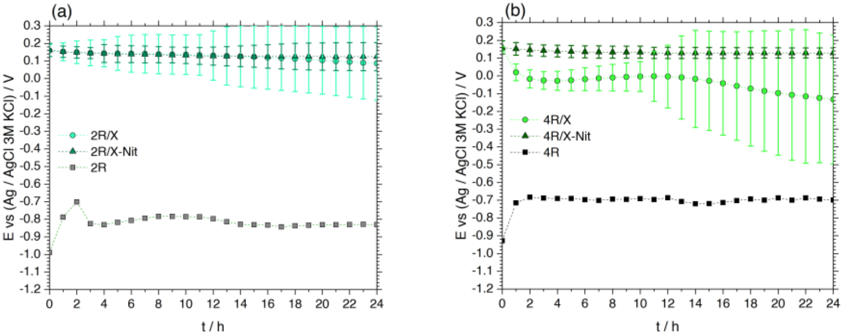

Fig. 6.32. OCP values of the bare and polypyrrole coated samples of (a) 2R and (b) 4R alloy versus time, immersed for 24 hours in 0.6 M NaCl solution.

Bode presentations of EIS spectra of the bare and polypyrrole coated (X and X-Nit) samples of 2R and 4R alloys during 24 hours of immersion in 0.6 M NaCl solution are depicted in Fig. 6.33 and Fig. 6.34, respectively.

According to these figures, the total impedance values of the two polypyrrole coatings are lower compared to the Al-Si alloys, which, as stated before, is normal for this kind of coatings.

It should be mentioned that the EIS spectra presented in Fig. 6.33 and Fig. 6.34 are related to the defect-free coatings. The samples have been selected by double checking the substrates before the electropolymerization. In other words, the following discussion is on the corrosion protection effect of polypyrrole coatings on Rheo-HPDC Al-Si alloys in the absence of any casting defects.

The EIS responses related to the coating X (on the alloy 2R) are characterized by two time constants at the high and the medium frequency ranges, together with a Warburg response at the low frequency range, converting to a separate time constant during 24 hours (Fig. 6.33). For the coating X-Nit (on the alloy 2R) a similar response is recorded.

EIS spectra of the coating X (on the alloy 4R) start with the two time constants at the high and medium and a hint of Warburg element at the low frequency ranges (Fig. 6.34). The Warburg tail gets more distinct after 6 hours of immersion. The coating partially breaks down after 24 hours of immersion. At this time, the RC constant at the medium frequency range is significantly depressed in the EIS spectrum. The coating X-Nit presents similar EIS responses on both alloys.

To examine the protection effect of this coating in the long term, its electrochemical behavior in 0.6 M NaCl solution was monitored for 7 days (168 hours). The results are presented in Fig. 6.35 and Fig. 6.36.

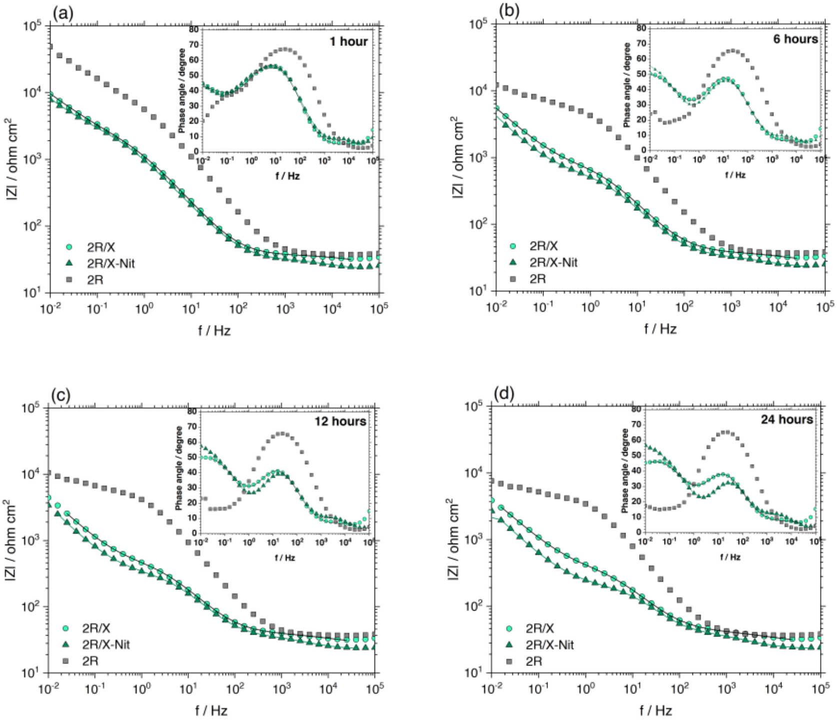

Fig. 6.33. EIS spectra of the bare and polypyrrole coated 2R samples after (a) 1, (b) 6, (c) 12 and (d) 24 hours of immersion in 0.6 M NaCl solution (solid lines are the fitted data).

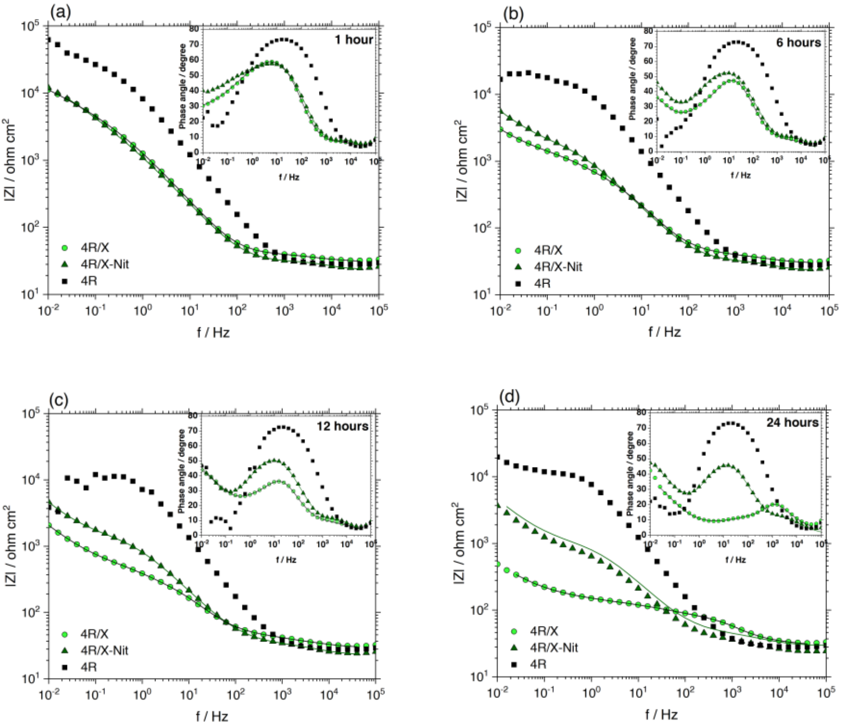

Fig. 6.34. EIS spectra of the bare and polypyrrole coated 4R samples after (a) 1, (b) 6, (c) 12 and (d) 24 hours of immersion in 0.6 M NaCl solution (solid lines are the fitted data).

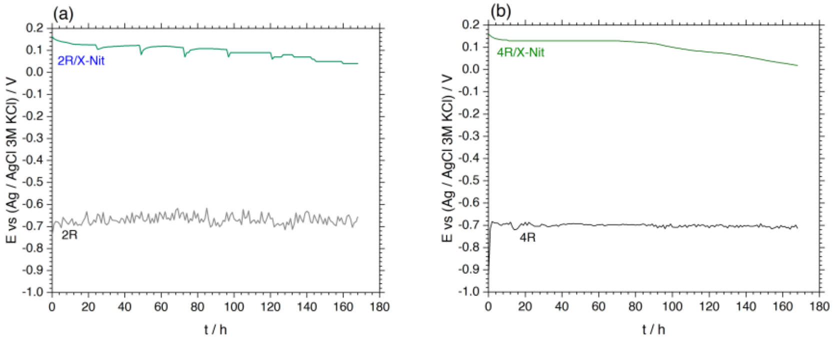

Fig. 6.35. OCP values of the bare and polypyrrole coated samples of (a) 2R and (b) 4R alloy versus time, immersed for 168 hours in 0.6 M NaCl solution.

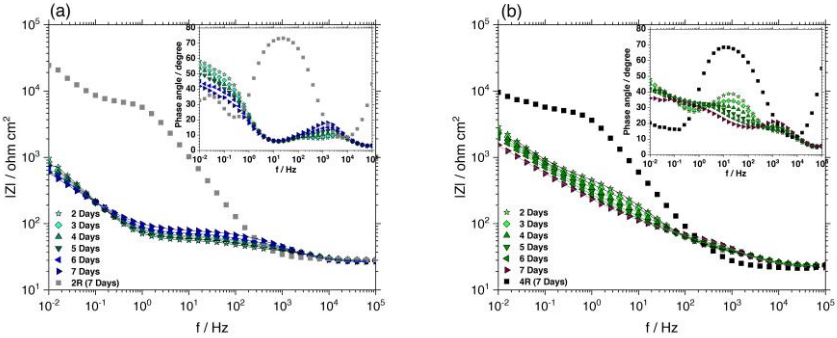

Fig. 6.36. EIS spectra of the coating X-Nit on the alloy (a) 2R and (b) 4R after 168 hours of immersion in 0.6 M NaCl solution (solid lines are the fitted data).

According to Fig. 6.35, despite the decreasing trend in the OCP values, the coating X-Nit is able to keep the surface potential of both the alloys quite noble for at least 7 days. The potential values are comparable for both alloys. However, the EIS responses of this coating on the alloys 2R and 4R during 7 days of immersion are different (Fig. 6.36).

On the alloy 2R (Fig. 6.36 (a)), from the second to the seventh day, the EIS response presents three time constants at the high, medium and low frequency range and one Warburg element. The RC constants at the medium and high frequency ranges are close and overlapping.

On the alloy 4R (Fig. 6.36 (b)), the coating displays the time constants for seven days of immersion. The second time constant (at the medium range) depresses through time.

The impedance responses were fitted using the equivalent electrical circuits (Fig. 6.37) and the fitting parameters were analyzed as a function of time.

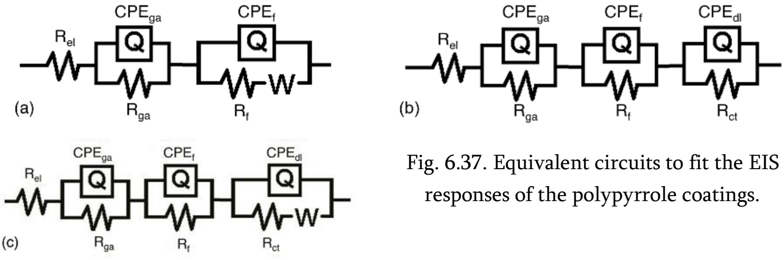

Fig. 6.37. Equivalent circuits to fit the EIS responses of the polypyrrole coatings.

The first Voigt element including CPE_{ga} and R_{ga} is considered for the galvanic interaction at the polypyrrole/aluminum interface. This contribution is observed as a phase angle maximum at the high frequency range.

The second Voigt element (CPE_f and R_f) is related to the coating characteristics, probably the reduction properties, appearing as a phase angle maximum at the medium frequency range.

The mass-transport-related constant (Warburg element) converting to a time constant (CPE_{dl} (none ideal double layer capacitance of the metal/solution interface) and R_{ct} (charge transfer resistance)) shows the change from a diffusion-controlled to a charge-controlled behavior.

As it was mentioned before the last time constant can be also related to the oxygen reduction on the polypyrrole surface.

For a better fitting, the Warburg element is replaced with a constant phase element (CPE). CPE describes a non-ideal capacitive behavior due to different factors such as surface roughness and heterogeneities, electrode porosity, the variation of the coating composition, slow adsorption reactions or a non-uniform potential and current distribution. The impedance of a CPE is given by the following equation:

$$Z_{CPE} = Q^{-1}(j\omega)^{-n} \text{ with } -1 \leq n \leq 1 \qquad \text{Eq. 6.1}$$

In this equation Q is the CPE constant ($\Omega^{-1}cm^{-2}s^{n}$), j is the imaginary number $j = (-1)^{0.5}$, ω is the angular frequency (ω=2πf, f being the frequency) and n is a dimensionless constant in the range of $-1 \leq n \leq 1$.

An ideal capacitor behavior yields n=1, a resistor yields n=0 and an inductor yields n=-1, while n=0.5 represents the response of mass-transport processes.

A summary of the fitting results is presented in Table. 6.7.

Based on the results presented in Table. 6.7, the coating X shows comparable results on both alloys.

R_{ga} is the resistance of the galvanic coupling between the substrate and the polymer film, promoted by the reduction of polypyrrole film [138, 233]:

$$[PPy^{m+}(mA^{-})] \rightarrow PPy^{0} + A^{-} \qquad \text{Eq. 6.2}$$

For all coatings, R_{ga} increases with the immersion time as probably the galvanic interaction is slowed down/decreased with time.

If we consider that R_f is related to the reduction of the polypyrrole (Eq. 6.2), its decrease during the test shows faster reaction. The reduction of the polypyrrole film is accompanied by the release of the dopant anions (e.g. NO_3^- and DS^-) while its re-oxidation is accompanied by the uptake of anions such as chloride to maintain the polymer electroneutrality [242]. If we consider that R_f is related to the coating resistance, its decrease displays easier ion mobility through the coating with the immersion time. The entry of electrolyte during the immersion can also decrease the coating resistance [242].

R_{ct}, the charge transfer resistance at the aluminum/electrolyte interface. Its values do not follow a distinct trend for all the samples.

According to the EIS results, the galvanic interaction of the polypyrrole film and aluminum substrate is inevitable, passivating the surface and keeping the potential noble. However, irreversible and fast consumption of the charge stored in the conductive polymer limits the protection provided.

A significant decrease in the values of R_f after ca. 2 days of immersion for the coatings shows this drawback.

Table. 6.7. Summary of results derived from fitting the EIS responses of the polypyrrole coatings in 0.6 M NaCl solution

Parameter	R_{ga} ($\Omega.cm^2$)	R_f ($\Omega.cm^2$)	R_{ct} ($\Omega.cm^2$)	n (in Q asW)	χ^{2*}
2R-X					
1 h	7.4	2320	-	0.55	4.74×10^{-4}
6 h	7.5	528	118800	-	3.05×10^{-4}
12 h	10.3	340	34480	-	1.28×10^{-4}
24 h	12.8	269	16390	-	1.2×10^{-4}
2R-X-Nit					
1 h	7.1	3075	-	0.60	5.92×10^{-4}
6 h	9.7	637	-	0.71	1.67×10^{-4}
12 h	10.6	318.5	-	0.71	4.19×10^{-5}
24 h	14.7	175.6	-	0.69	1.04×10^{-4}
2 days	14.2	13.3	112	0.78	1.55×10^{-4}
3 days	15.5	16.2	452	0.67	6.80×10^{-5}
4 days	18.8	15.7	446	0.67	8.44×10^{-5}
5 days	20.9	17.3	271	0.61	4.89×10^{-5}
6 days	25.5	18.5	224	0.53	3.85×10^{-5}
7days	51.6	-	392	0.60	3.15×10^{-4}
4R-X					
1 h	3.5	31.48	-	0.83	1.19×10^{-4}
6 h	11.2	361	-	0.60	2.24×10^{-4}
12 h	11.04	441	-	0.59	3.62×10^{-4}
24 h	95.4	20.8	-	0.57	1.24×10^{-4}
4R-X-Nit					
1 h	6.03	624	-	0.38	3.17×10^{-4}
6 h	6.3	2168	-	0.65	5.89×10^{-4}
12 h	9.06	1614	-	0.68	3.83×10^{-4}
24 h	11.2	889	-	0.66	1.44×10^{-4}
2 days	12.4	507	-	0.62	8.49×10^{-5}
3 days	11.5	500	-	0.59	2.13×10^{-4}
4 days	10.5	-	669	0.56	1.21×10^{-4}
5 days	12.1	-	2292	0.73	8.65×10^{-5}
6 days	21.03	-	3424	0.71	5.31×10^{-5}
7days	21.2	-	252	0.52	1.86×10^{-4}

*Chi-squared: the sum of the squares of the residuals.

Based on the n values in Table. 6.7, assigning a physical meaning to the last CPE is impossible, while its presence is necessary for the fitting quality.

Fig. 6.38 depicts surfaces of the polypyrrole coatings, X and X-Nit on the alloys 2R and 4R, after 24-hour immersion test in 0.6 M NaCl solution. Fig.

6.39 presents the surface of the coating X-Nit on the alloys 2R and 4R after 7 days (168 hours) of exposure to the NaCl solution.

According to Fig. 6.38, on all the coatings, the presence of some blisters is evident. The coating X on the alloy 4R (Fig. 6.38 (c)) is failed at some points, on which the porous powdery corrosion products can be observed (shown in the boxes). The blisters spread during 7 days of exposure to 0.6 M NaCl solution (Fig. 6.39).

The cross-sectional FIB-SEM image of a blister on the coating X (on the alloy 2R) after 24 hours of immersion in 0.6 M NaCl solution is shown in Fig. 6.40.

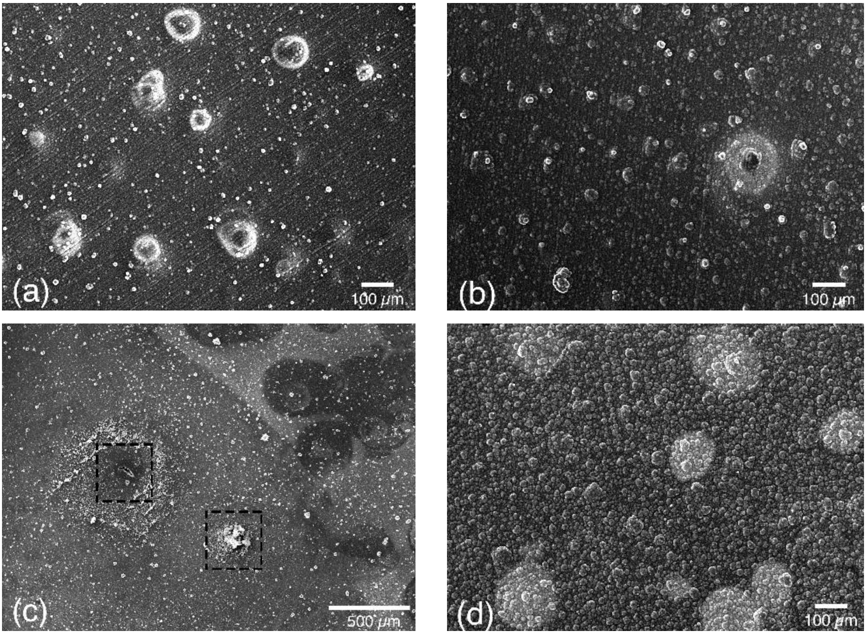

Fig. 6.38. SEM-SE image of surface morphology of the coating X on the alloy (a) 2R and (c) 4R and the coating X-Nit on alloy (b) 2R and (d) 4R after 24 hours of immersion in 0.6 M NaCl solution.

A relatively dense aluminum oxide layer is present at the polypyrrole/Al-Si interface. No visible pitting or localized attack (at the aluminum/eutectic silicon/intermetallic interfaces) is observed at this interface or toward the substrate. Therefore, the oxide can be considered as protective, however, it’s fast ceaseless growth leads to degradation (complete reduction) of the polymer and breakdown of the coating.

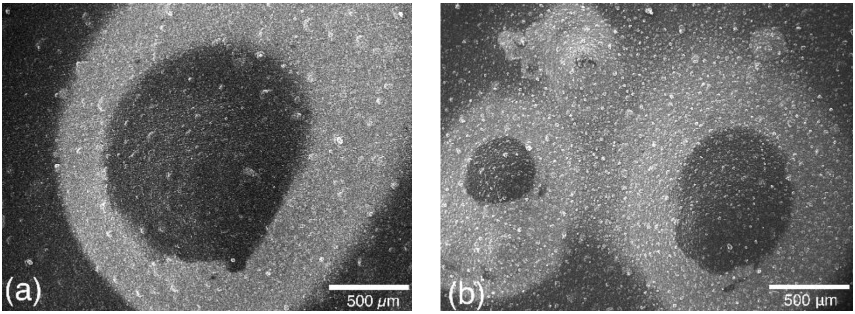

Fig. 6.39. SEM (SE) image of surface morphology of the coating X-Nit on the alloy (a) 2R and (b) 4R after 168 hours of immersion in 0.6 M NaCl solution.

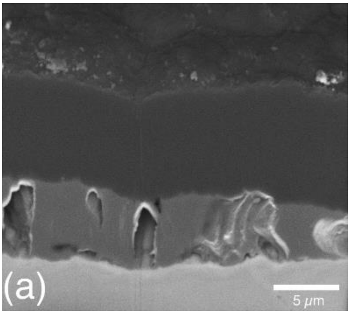

Fig. 6.40. Cross-sectional FIB-SEM of a blister on the coating X on the alloy 2R after 24 hours exposure to 0.6 M NaCl solution.

The polypyrrole coating is able to relatively decrease the corrosion rate of the Al-Si alloys. The galvanic interaction at the polypyrrole/aluminum interface passivates the surface. However, in the presence of chloride ions, the polypyrrole coatings are prone to the formation of blisters as a result of drastic localized galvanic interaction with aluminum. Based on OCP values and EIS results, the X-Nit coating seems to be the coating with a higher corrosion protection efficiency. Therefore, by changing the solution chemistry which influences the polymer/metal interface and the conductivity of the coating the protection efficiency can be improved. These results are in agreement with the earlier results on the protection effect of the same coatings on pure aluminum.

The X-Nit coating presents an improved performance on the 4R alloy. According to the EIS results (Table. 6.7), the degradation of the coating is slower and smaller and fewer number of blisters (Fig. 6.39 (b)) are observed after long-term immersion. This can be attributed to the easier formation of the coating due to higher silicon content. Which can suggest that the polypyrrole coating may work better on the alloys with higher silicon content.

6.3.4. Effect of casting defects

Fig. 6.41 depicts the surface and the cross-sectional view of the X coating with one (relatively) big casting related defect after 24 hours of immersion in 0.6 M NaCl solution, which has led to its failure. As it is obvious from Fig. 6.41, the casting defect has been fully covered by the polypyrrole coating. However, probably due to the imperfect interface adhesion and subsequently the inferior electrical contact between the polymer film and the substrate in this area, the coating is not able to passivate the defect. In this condition an accelerated corrosion attack results in the formation of porous corrosion products. These corrosion products can be seen especially on top of the defect. Considering the size of the defects, these results can be in agreement with those of Rohwerder et al. [133], which state that the polypyrrole coating is not able to passivate the relatively large defects. In this condition, the breakdown of the whole coating will occur due to the fast reduction.

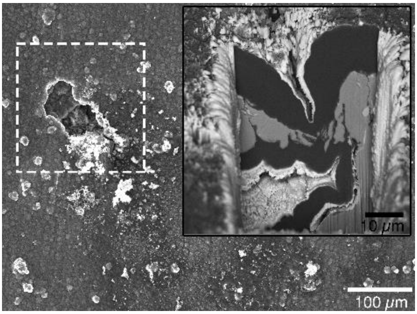

Fig. 6.41. (FIB)-SEM image of the coating X with casting related defect failed during the 24-hour immersion test in 0.6 M NaCl.

6.3.5. Electrochemical examination and protection/failure mechanism (part II)

As an example, the redox responses of the two polypyrrole coatings electrodeposited from the solutions with extreme chemistries (2X and X-2Nit) on the alloy 2R, at the potential range of 0-0.9 V, were evaluated and compared in 0.6 M NaCl solution. The related results are presented in Fig. 6.42.

The coatings are electrochemically active and while scanning from -1 to 1 V one anodic and one cathodic peak are recorded for both of them. The oxidation peaks are quite similar for both of the coatings (around 0.19 V). While the reduction voltage is more positive for the coating 2X (-0.43 V) compared to the coating X-2Nit (-0.63 V). In general, the electrochemical activities of the two coatings are comparable.

OCP was recorded for these two coatings and the coatings electropolymerized at different potential ranges (Fig. 6.18 (b)), during 24 hours of immersion in 0.6 M NaCl solution. The results are presented in Fig. 6.43 (a) and (b).

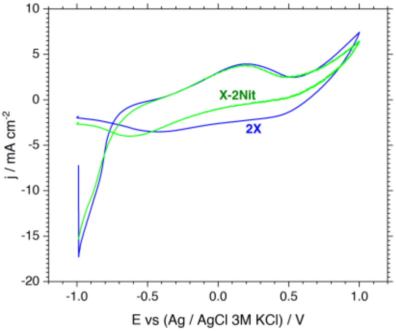

Fig. 6.42. Redox behavior of the coatings 2X and X-2Nit (deposited on the alloy 2R) in 0.6 M NaCl (scanning range = 10 mV).

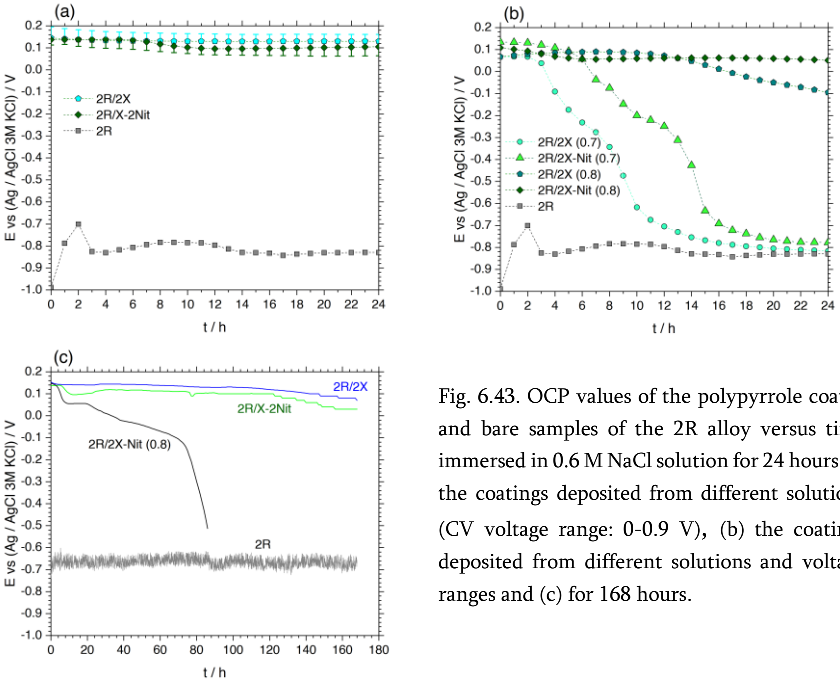

Fig. 6.43. OCP values of the polypyrrole coated and bare samples of the 2R alloy versus time immersed in 0.6 M NaCl solution for 24 hours (a) the coatings deposited from different solutions (CV voltage range: 0-0.9 V), (b) the coatings deposited from different solutions and voltage ranges and (c) for 168 hours.

According to Fig. 6.43 (a), OCP values of the two coatings, 2X and X-2Nit are considerably nobler compared to the bare substrate and these coatings are able to keep the surface potential noble for at least 24 hours. The corrosion protection effect of these two coatings seems comparable.

The results presented in section 6.3.3 showed that addition of $NaNO_3$ to the solution X improves the corrosion protection performance of the polypyrrole coating. Nitrate anions affect the polymer/metal interface (by passivating the electrode) and the conductivity of the coating (increasing it) resulting in an improved protection efficiency. The present results show that doubling the concentration of DHBDS has almost the same effect (at least for 24 hours of immersion). While increasing the concentration of $NaNO_3$ does not result in a coating with significantly improved corrosion protection.

Most of the coatings electrodeposited at the smaller potential ranges (0-0.7 and 0-0.8 V) are not able to protect the surface for 24 hours and fail before the end of the test (Fig. 6.43 (b)). In this set of coatings, the only coating with a comparable corrosion protection effect to those of the 2X and X-2Nit coatings is the coating 2X-Nit (0.8).

According to these results and based on the results of thickness measurement (Fig. 6.23), the minimum thickness for the polypyrrole coating to be protective is around 9-10 μm.

Fig. 6.43 (c) shows the protection effect of the three coatings, 2X, X-2Nit and 2X-Nit (0.8), in long-term (168 hours). The surface potential of the first two coatings is considerably noble even after 7 days of immersion. The EIS spectra of these two coating after 1, 6, 12, 24 and 168 hours of immersion are shown in Fig. 6.44.

During the first 6 hours of immersion, the EIS spectrum of the coating 2X is characterized by three time constant at the high, medium and low frequency ranges. The RC constant at the medium frequency range fades after 6 hours and the electrochemical response turns into showing two time constants from 12 to 168 hours of immersion. The coating X-2Nit presents the three time constants for 24 hours. The RC constant at the medium frequency range is absent after 168 hours. For both coatings, the phase angle maximum at the high frequency has increased at the end of the test (Fig. 6.44 (e)).

Comparing the EIS spectra in Fig. 6.44, from the beginning of the test for the coating 2X the second time constant is not distinct (and later on is absent), while the same is not seen for the coating X-2Nit. Earlier this time constant was attributed to the coating properties and R_f was attributed to the reduction of the polymer. This can suggest a lower rate of reduction for the coating doped with a higher concentration of DHBDS, a voluminous anion with lower mobility. Evidenced by the presence of the time constant at the high frequency range, the anodic protection mechanism is effective for both coatings. However, due to the lower redox activity of the 2X coating (during the immersion test) its protection performance can be influenced.

Fig. 6.45 depicts the coatings, 2X and X-2Nit, after 24 and 168 hours of immersion test. After 24 hours (Fig. 6.45 (a) and (b)), the presence of some blisters is evident on of both coatings. These blisters are considerably bigger on the X-2Nit coating compared to the 2X coating.

After 168 hours, these blisters spread. As it is obvious from Fig. 6.45 (c) and (d), the coating X-2Nit is cracked on top of a blister, while the coating 2X is still quite adhesive to the substrate.

This coating (X-2Nit) was totally peeled off and the substrate underneath was examined by SEM (Fig. 6.45 (e) and (f)). A considerable fraction of the surface is protected from any corrosion (including the localized corrosion (e.g. pitting and trenching), showing the barrier properties of the coating, while some thick oxide layers are present underneath a few blisters, which indicate the localized corrosion of the substrate as a result of drastic galvanic interaction at polypyrrole/aluminum interface. The ceaseless growth of these oxide layers leads to the formation of blisters and eventually failure. The exposed surface of the bare Al-Si alloy after 24 and 168 hours is presented in Fig. 6.45 (g) and (h) for comparison. In the absence of any coating, the surface suffers from localized corrosion attacks at the interface of the aluminum matrix with the eutectic silicon and intermetallic particles (Fig. 6.45 (g)). It is heavily covered by the porous corrosion products at the end of the 168-hour immersion test (Fig. 6.45 (h)).

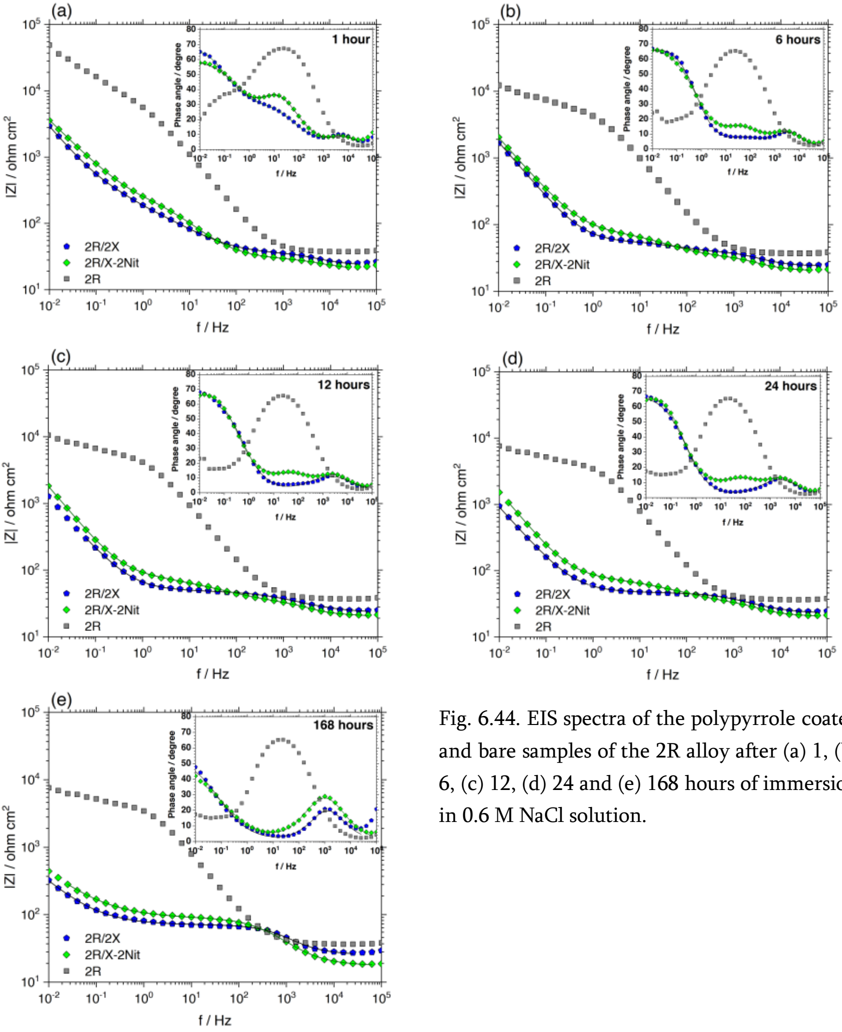

Fig. 6.44. EIS spectra of the polypyrrole coated and bare samples of the 2R alloy after (a) 1, (b) 6, (c) 12, (d) 24 and (e) 168 hours of immersion in 0.6 M NaCl solution.

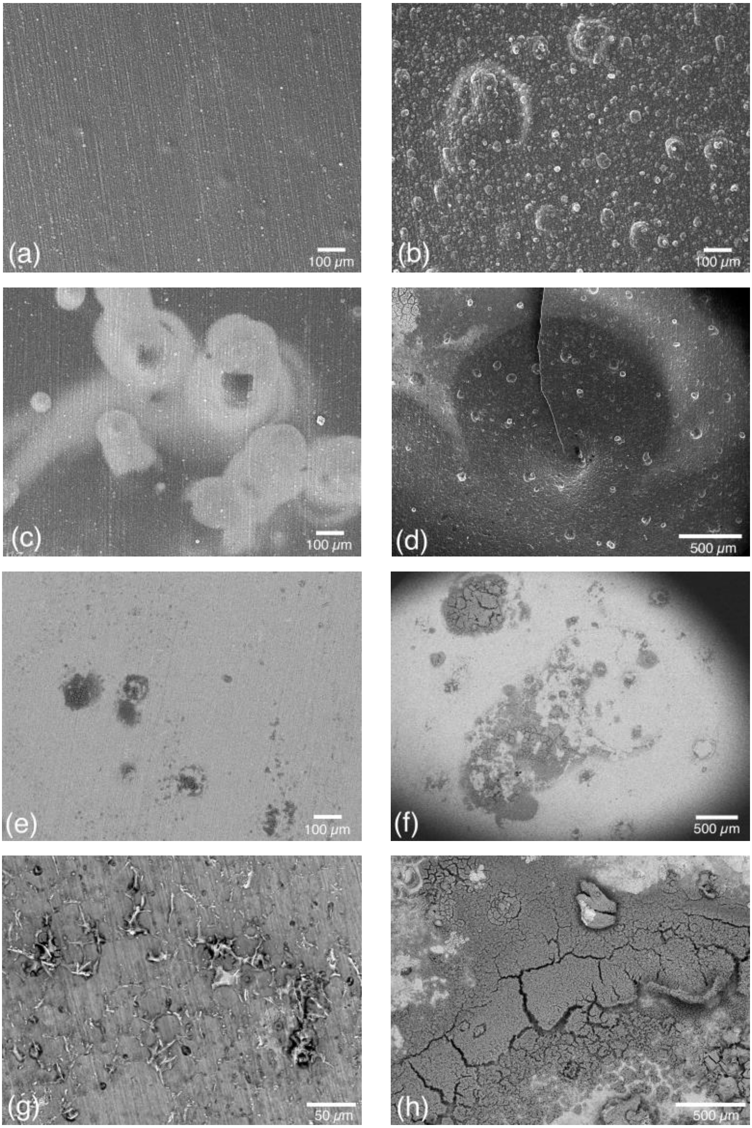

Fig. 6.45. SEM-SE(BS) image of the polypyrrole coating (a) and (c) 2X; (b) and (d) X-2Nit after 24 and 168 hours of immersion in 0.6 M NaCl solution, respectively; (e) and (f) substrate underneath the coating X-2Nit (after 168 hours); (g) and (h) the bare substrate (the alloy 2R) after 24 and 168 hours of immersion in 0.6 M NaCl solution, respectively.

According to the present results, the coating 2X offers a longer/more efficient corrosion protection effect in comparison to the coating X-2Nit. This improvement in protection effect is a result of reduced/controlled redox activity (during the immersion test), which decreases the severe localized galvanic interaction at the polypyrrole/aluminum interface.

Increasing the concentration of $NaNO_3$ does not result in a coating with significantly improved corrosion protection properties. While doubling the concentration of DHBDS (Tiron) results in a polypyrrole coating with better corrosion protection properties. This can be related to the incorporation of large DHBDS anions into the polymer chain which also impedes the entrance of chloride ions.

6.3.1. Conclusions II

Electropolymerization of polypyrrole coatings was studied on two Al-Si alloys with 2.5 and 4.5 wt% silicon. It was shown that electrodeposition of the polymer film is promoted on the alloy surface compared to the pure aluminum, probably due to the presence of eutectic silicon phase or intermetallic particles. Therefore, the coatings on the alloys possess higher thicknesses.

Increasing the concentration of $NaNO_3$ and DHBDS increases the coating thickness. $NaNO_3$ passivates the electrode during the electrodeposition, alleviating the anodic dissolution problem, while DHBDS has a catalytic effect. Introducing NO_3^- also increases the grain size and the inhomogeneity of the coating and probably alters the growth pattern from a laminar-type to a fractal-type. Increasing the upper voltage range increases the coating thickness and it slightly increases the grain size.

Coated samples show nobler surface potential in 0.6 M NaCl solution compared to the bare sample. This noble potential can be attributed to the anodic protection provided by the polypyrrole reduction. However, the galvanic interaction at the polypyrrole/aluminum interface is locally severe resulting in the formation of blisters, fast reduction (degradation) of the polymer and finally failure.

The protection efficiency can be influenced by the electrolyte chemistry and substrate characteristics. In this sense, the presence of $NaNO_3$ and a higher silicon content have positive effects on the coating performance.

A higher concentration of DHBDS in the electrolyte results in the polypyrrole coating with improved protection efficiency. It seems that the incorporation of a higher fraction of voluminous anions controls the entrance of chloride ions and the redox activity of the coating during the immersion test, leading to the formation of fewer blisters.

The polypyrrole coating provides relative corrosion protection for Al-Si alloys, however, its application needs consideration regarding blistering. Moreover, it is shown that the large casting related defects in the coatings can interfere with the protection effect either due to the inferior adhesion/connection with the conductive polymer or the fast reduction of the whole coating.

6.4. Discussion and conclusions (comparison between parts I and II)

Electrodeposition of polypyrrole coatings on the pure aluminum (AA1050) and Rheo-HPDC Al-Si alloys for corrosion protection purposes was investigated in the sections 6.2 and 6.3, respectively.

During the CV, the two types of electrodes present comparable behavior and the oxidation voltage of pyrrole is similar in both cases. However, the presence of eutectic silicon phase or intermetallic particles facilitates the electrodeposition process. Therefore, higher values of current density are recorded for the alloy samples in comparison to the pure aluminum. It was shown that the eutectic phase region is the primary location for the film deposition.

The polypyrrole coatings are able to fairly reduce the corrosion rate of both pure aluminum and aluminum-silicon alloys in NaCl solution and the protection effect seems comparable on both of them.

However, for the cast alloy samples, the presence of casting related defects in the coating results in the early failure, which was never observed for the coatings on pure aluminum substrates.

Chapter 7 Conclusions and future perspectives

This thesis contributes to the development of the knowledge on electrochemical/corrosion behavior and surface treatments of rheo-high pressure die cast (Rheo-HPDC) aluminum-silicon alloys. The focus was on two newly designed low silicon content aluminum alloys. The samples were taken from the prototype of a real component used in telecom base stations connecting the acquired scientific knowledge to a real application.

Due to the Rheo-HPDC process, the alloy develops a new microstructure which is heterogeneous along the component. This semi-solid process mainly shows its effect by the presence of different aluminum grains varying in the concentration of alloying elements and various macro-segregations depending on the sample's thickness and location with respect to the feeding gate (Section 4.2.1).

Moreover, during the semi-solid casting process a surface liquid segregation layer is formed. By considering the surface condition in the real application, this thesis has tested the as-cast surfaces differently from most of the results in the literature (Section 4.2.2).

In addition, the corrosion behavior of the semi-solid low silicon aluminum alloys was compared to that of the conventional HPDC alloys.

It is shown that, regardless of the casting technology or the silicon content, all the Al-Si alloys mainly suffer from the localized corrosion attacks in the eutectic region due to the micro-galvanic coupling between the aluminum and the eutectic silicon or iron-rich intermetallic phases (Sections 4.2.2 and 4.2.3).

However, this corrosion behavior is also a function of the macrosegregation (especially the surface liquid segregation), surface condition and silicon content.

Irrespective of the chloride concentration, the corrosion mechanism and the growth pattern of corrosion products seem comparable for both the conventional and Rheo-HPDC alloys. However, for the semi-solid alloys the passive layer is more resistance to pitting.

One approach to stop this type of corrosion is using cerium-based conversion coatings that selectively deposit on the cathodic phases. The approach that, despite its effectiveness, has been rarely studied on cast Al-Si alloys. In this thesis, this treatment was studied on both types of Al-Si alloys. The study focused on understanding the deposition mechanism and it exploited FIB-SEM method for the examination.

The iron-rich intermetallic particles were shown to be the primary deposition sites for both the conventional and Rheo-HPDC Al-Si alloys. However, it was observed that for the semi-solid alloys, under accelerated conditions, intermetallic particles play a more complex role in the deposition mechanism (Section 5.2.3).

Different from the conventional HPDC alloy or other wrought aluminum-silicon alloys, for the Rheo-HPDC Al-Si alloys it was proven that, probably due to the presence of more reactive sites, the iron-rich intermetallic particles can be oxidized during the cerium deposition.

Besides the influence of the treatment parameters, the semi-solid microstructure and the silicon content can affect the deposition as well.

In this research, the application of a conductive polymer coating (polypyrrole) for the corrosion protection of semi-solid Al-Si alloys was proposed and studied.

This study focused on the effect of substrate composition and the solution chemistry, especially the presence of different passivating and doping anions (e.g. nitrate, citrate, etc.), on the electropolymerization (electrodeposition) of the polypyrrole coatings.

It was shown that both factors can be mainly effective on the thickness of the coating.

The results revealed that, regardless of the composition of the substrate (either pure Al or Al-Si), the polypyrrole coating can offer corrosion protection depending on the condition under which it has been deposited (Sections 6.2.2, 6.3.3 and 6.3.5).

This thesis contributes to understanding the controversial corrosion protection effect of conductive polymers based on not only OCP monitoring but also EIS analysis. The protection mechanism seems to be a combination of the barrier effect and the anodic protection induced by the reduction of the conductive polymer. It is shown that the severe localized galvanic coupling between the polypyrrole coating and the aluminum substrate is inevitable and leads to the coating failure due to the formation of blisters. However, the possible protection effect of the resulting oxide layer requires more investigations.

By considering the effect of casting defects on the performance of the polypyrrole coating, this study tries to link theoretical science to a real application.

In conclusion, the semi-solid casting process not only affects the microstructure and the corrosion properties of the Al-Si alloys but also partially influences certain surface treatments.

Moreover, the effect of macrosegregation should be considered while using the Rheo-HPDC Al-Si components in the applications where they are exposed to corrosive environments.

Based on the results presented in this thesis, the future development of this work could consider the following points in the corrosion studies and the proposed surface treatments:

(i) More examination on the passive layer of the Rheo-HPDC Al-Si alloy and comparing it to that on the conventional HPDC alloy can reveal the reason behind its higher pitting resistance. Moreover, deeper analysis of the effect of silicon on the corrosion resistance of the passive layer can be useful as well.

(ii) More investigation on the possible influence of Ce (III)/Ce (IV) ratio on the electrochemical properties of cerium-based conversion coatings on aluminum can be considered.

(iii) The future work on polypyrrole coating on aluminum could consider a conversion pretreatment step to increase the protection efficiency. Moreover, incorporation of corrosion inhibitor anions to the coating can be considered as a possible strategy to enhance the protection properties of the oxide layer induced by the reduction of polypyrrole. In addition, due to the complexity and limitation of EIS measurement, future studies need to use complementary techniques.

Appendix

To eliminate the effect of aluminum interface and to distinguish the electrochemical behavior of the polymer coatings, the same polypyrrole films (X, X-Cit and X-Nit) were electropolymerized on the platinum substrates. These coating were further examined using EIS test in 0.6 M NaCl solution for 24 hours. The impedance responses of these coatings are summarized in Fig. I.

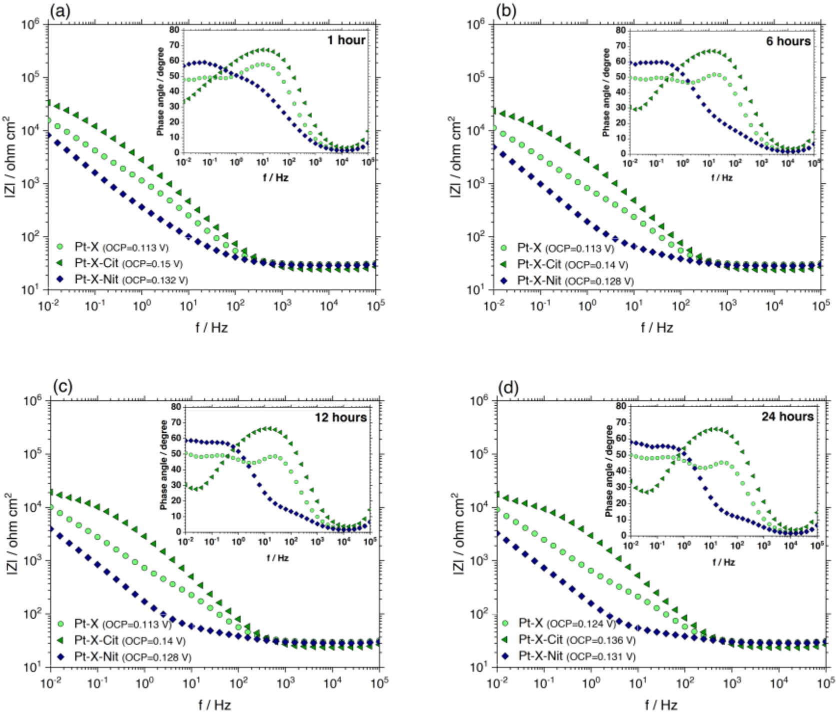

Fig. I. EIS spectra of the polypyrrole coated platinum after (a) 1, (b) 6, (c) 12 and (d) 24 hours of immersion in 0.6 M NaCl solution.

All the three coatings lack the time constant at the high frequency range, which was attributed to the galvanic interaction at the polypyrrole/aluminum interface.

The coating X-Cit presents a response characterized by one time constant at the medium and one Warburg tail at the low frequency ranges. During the first 6 hours of immersion, the other two coatings, X and X-Nit, present two time constants at the medium and the low frequency ranges. After 12 hours, a hint of a Warburg response is observed for these two coatings.

Bibliography

[1] V.S. Zolotorevsky, N.A. Belov, M.V. Glazoff, Casting aluminum alloys, Elsevier Amsterdam, 2007.

[2] M. Faraji, L. Katgerman, Distribution of trace elements in a modified and grain refined aluminium–silicon hypoeutectic alloy, Micron, 41 (2010) 554-559.

[3] M. Warmuzek, Aluminum-Silicon Casting Alloys Atlas of Microfractographs, ASM International, 2004.

[4] R. Arrabal, B. Mingo, A. Pardo, M. Mohedano, E. Matykina, I. Rodríguez, Pitting corrosion of rheocast A356 aluminium alloy in 3.5 wt.% NaCl solution, Corros. Sci., 73 (2013) 342–355.

[5] S.G. Shabestari, The effect of iron and manganese on the formation of intermetallic compounds in aluminum–silicon alloys, Mater. Sci. Eng., A, 383 (2004) 289–298.

[6] A. Pacz, in: U. Patent (Ed.), 1921.

[7] S. Haro-Rodríguez, R.E. Goytia-Reyes, D.K. Dwivedi, V.H. Baltazar-Hernández, H. Flores-Zúñiga, M.J. Pérez-López, On influence of Ti and Sr on microstructure, mechanical properties and quality index of cast eutectic Al–Si–Mg alloy, Mater. Des., 32 (2011) 1865-1871.

[8] S.D. McDonald, K. Nogita, A.K. Dahle, Eutectic nucleation in Al–Si alloys, Acta Mater., 52 (2004) 4273-4280.

[9] M. Timpel, N. Wanderka, R. Schlesiger, T. Yamamoto, N. Lazarev, D. Isheim, G. Schmitz, S. Matsumura, J. Banhart, The role of strontium in modifying aluminium–silicon alloys, Acta Mater., 60 (2012) 3920-3928.

[10] G. Heiberg, L. Arnberg, Investigation of the microstructure of the Al–Si eutectic in binary aluminium–7 wt% silicon alloys by electron backscatter diffraction (EBSD), J. Light Met., 1 (2001) 43-49.

[11] A. Mahato, S. Xia, T. Perry, A. Sachdev, S.K. Biswas, Role of silicon in resisting subsurface plastic deformation in tribology of aluminium–silicon alloys, Tribol. Int., 43 (2010) 381-387.

[12] M. Harun, I.A. Talib, A.R. Daud, Effect of element additions on wear property of eutectic aluminium-silicon alloys, Wear, 194 (1996) 54-59.

[13] J.-S. Shin, S.-H. Ko, K.-T. Kim, Development and characterization of low-silicon cast aluminum alloys for thermal dissipation, J. Alloys Compd., 644 (2015) 673-686.

[14] J. Shin, S. Ko, K. Kim, Development of low-si aluminum casting alloys with an improved thermal conductivity, Mater. Technnol., 48 (2014) 195–202.

[15] N. Birbilis, B. Hinton, Corrosion and corrosion protection of aluminium, in: R.N. Lumley (Ed.), Woodhead Publishing Limited, 2011.

[16] K. Nisancioglu, Electrochemical Behaviorof Aluminum-Base Intermetallics Containing Iron, J. Electrochem. Soc., 137 (1990) 69-77.

[17] N. Birbilis, R.G. Buchheit, Electrochemical Characteristics of Intermetallic Phases in Aluminum Alloys, J. Etectrochem. Soc., 152 (2005) B140-B151.

[18] A.E. Hughes, N. Birbilis, J.M. Mol, S.J. Garcia, X. Zhou, G.E. Thompson, High strength Al-alloys: microstructure, corrosion and principles of protection, in: Recent Trends in Processing and Degradation of Aluminium Alloys, InTech, 2011.

[19] G.S. Frankel, Pitting Corrosion of Metals, J. Electrochem. Soc., 145 (1998) 2186-2198.

[20] Z.A. Foroulis, M.J. Thubrikar, On the Kinetics of the Breakdown of Passivity of Preanodized Aluminum by Chloride Ions, J. Electrochem. Soc., 122 (1975) 1296-1301.

[21] R.T. Foley, T.H. Nguyen, The Chemical Nature of Aluminum Corrosion, J. Electrochem. Soc., 129 (1982) 464-467.

[22] T.P. Hoar, The production and breakdown of the passivity of metals, Corros. Sci., 7 (1967) 341-355.

[23] A. Boag, A.E. Hughes, A.M. Glenn, T.H. Muster, D. McCulloch, Corrosion of AA2024-T3 Part I: Localised corrosion of isolated IM particles, Corros. Sci., 53 (2011) 17-26.

[24] B. Mingo, R. Arrabal, A. Pardo, E. Matykina, P. Skeldon, 3D study of intermetallics and their effect on the corrosion morphology of rheocast aluminium alloy, Mater. Charact., 112 (2016) 122–128.

[25] M. Qi, Y. Kang, W. Tang, Q. Qiu, B. Li, Microstructure, mechanical properties and corrosion behavior of Rheo-HPDC a novel Al-8Si-Fe alloy, Mater. Lett., 213 (2018) 378-382.

[26] S.S.A. Rehim, H.H. Hassan, M.A. Amin, Chronoamperometric studies of pitting corrosion of Al and (Al–Si) alloys by halide ions in neutral sulphate solutions, Corros. Sci., 46 (2004) 1921–1938.

[27] S.S.A. Rehim, H.H. Hassan, M.A. Amin, Corrosion and corrosion inhibition of Al and some alloys in sulphate solutions containing halide ions investigated by an impedance technique, Appl. Surf. Sci., 187 (2002) 279–290.

[28] W.J. Liang, P.A. Rometsch, L.F. Cao, N. Birbilis, General aspects related to the corrosion of 6xxx series aluminium alloys: Exploring the influence of Mg/Si ratio and Cu, Corros. Sci., 76 (2013) 119-128.

[29] S.K. Kairy, P.A. Rometsch, K. Diao, J.F. Nie, C.H.J. Davies, N. Birbilis, Exploring the electrochemistry of 6xxx series aluminium alloys as a function of Si to Mg ratio, Cu content, ageing conditions and microstructure, Electrochim. Acta, 190 (2016) 92-103.

[30] M. Qi, Y. Kang, Q. Qiu, W. Tang, J. Li, B. Li, Microstructures, mechanical properties, and corrosion behavior of novel high-thermal-conductivity hypoeutectic Al-Si alloys prepared by rheological high pressure die-casting and high pressure die-casting, J. Alloys Compd., 749 (2018) 487-502.

[31] M. Qian, D. Li, S.B. Liu, S.L. Gong, Corrosion performance of laser-remelted Al–Si coating on magnesium alloy AZ91D, Corros. Sci., 52 (2010) 3554-3560.

[32] F. Bonollo, N. Gramegna, G. Timelli, High-Pressure Die-Casting: Contradictions and Challenges, JOM, 67 (2015) 901-908.

[33] M. Qi, Y. Kang, B. Zhou, W. Liao, G. Zhu, Y. Li, W. Li, A forced convection stirring process for Rheo-HPDC aluminum and magnesium alloys, J. Mater. Process. Technol., 234 (2016) 353-367.

[34] M.S. Dargusch, G. Dour, N. Schauer, C.M. Dinnis, G. Savage, The influence of pressure during solidification of high pressure die cast aluminium telecommunications components, J. Mater. Process. Technol., 180 (2006) 37-43.

[35] S. Ji, Z. Zhen, Z. Fan, Effects of rheo-die casting process on the microstructure and mechanical properties of AM50 magnesium alloy, J. Mater. Sci. Technol., 21 (2005) 1019-1024.

[36] S. Ji, Y. Wang, D. Watson, Z. Fan, Microstructural Evolution and Solidification Behavior of Al-Mg-Si Alloy in High-Pressure Die Casting, Metall. Mater. Trans. A, 44 (2013) 3185-3197.

[37] C.K. Jin, C.H. Jang, C.G. Kang, Die design method for thin plates by indirect rheo-casting process and effect of die cavity friction and punch speed on microstructures and mechanical properties, J. Mater. Process. Technol., 224 (2015) 156-168.

[38] M. Esmaily, N. Mortazavi, J.E. Svensson, M. Halvarsson, D.B. Blucher, A.E.W. Jarfors, M. Wessen, L.G. Johansson, Atmospheric Corrosion of Mg Alloy AZ91D Fabricated by a Semi-Solid Casting Technique: The Influence of Microstructure, J. Electrochem. Soc., 162 (2015) C311-C321.

[39] Z. Fan, S. Ji, G. Liu, Development of the Rheo-Diecasting Process for Mg-Alloys, Mater. Sci. Forum, 488-489 (2005) 405-412.

[40] H. Moller, W.E. Stumpf, P.C. Pistorius, Influence of elevated Fe, Ni and Cr levels on tensile properties of SSM-HPDC Al-Si-Mg alloy F357, Trans. Nonferrous Met. Soc. China, 20 (2010) s842-s846.

[41] M.C. Flemings, R.G. Riek, K.P. Young, Rheocasting, Mater. Sci. Eng., 25 (1976) 103-117.

[42] Z. Fan, Semisolid metal processing, Int. Mater. Rev., 47 (2002) 49-85.

[43] M. Östklint, M. Wessén, A.E.W. Jarfors, Microstructure and material soundness in liquid and rheocast AZ91: effect of section thickness, Int. J. Cast Metal. Res, 28 (2015) 65-71.

[44] M. Östklint, M. Wessén, A. Jarfors, Microstructure and material soundness in liquid and rheocast AM50 and effect of section thickness, Int. J. Cast Metal. Res, 27 (2014) 235-241.

[45] M. Payandeh, A.E.W. Jarfors, M. Wessén, Effect of superheat on melting rate of EEM of Al alloys during stirring using the RheoMetal process, in: Solid State Phenom., 2013, pp. 392-397.

[46] M. Payandeh, Rheocasting of Aluminium Alloys: Process and Components Characteristics, in, Jönköping University, 2016.

[47] H.V. Atkinson, Alloys for Semi-Solid Processing, Solid State Phenom., 192-193 (2013) 16-27.

[48] M. Payandeh, Rheocasting of Aluminium Alloys: Slurry Formation, Microstructure, and Properties, in: Department of Materials and Manufacturing, Jönköping University, 2015.

[49] M. Payandeh, A.E.W. Jarfors, M. Wessén, Solidification Sequence and Evolution of Microstructure During Rheocasting of Four Al-Si-Mg-Fe Alloys with Low Si Content, Metall. Mater. Trans. A, 47A (2016) 1215-1228.

[50] Z.W. Chen, Skin solidification during high pressure die casting of Al–11Si–2Cu–1Fe alloy, Mater. Sci. Eng., A, 348 (2003) 145-153.

[51] H.I. Laukli, C.M. Gourlay, A.K. Dahle, Migration of crystals during the filling of semi-solid castings, Metall. Mater. Trans. A, 36 (2005) 805-818.

[52] H. Kaufmann, W. Fragner, U. Galovsky, P.J. Uggowitzer, Fluctuations of alloy composition and their influence on sponge effect and fluidity of A356-NRC, in: H. Kaufmann (Ed.) The 2nd International Light Metals Technology Conference, LKR-Verlag, St. Wolfgang, Austria, 2005.

[53] E.P. Masuku, H. Moller, U.A. Curle, P.C. Pistorius, W. Li, Influence of surface liquid segregation on corrosion behavior of semi-solid metal high pressure die cast aluminium alloys, Trans. Nonferrous Met. Soc. China, 20 (2010) s837-s841.

[54] S. Zabler, A. Ershov, A. Rack, F. Garcia-Moreno, T. Baumbach, J. Banhart, Particle and liquid motion in semi-solid aluminium alloys: A quantitative in situ microradioscopy study, Acta Mater., 61 (2013) 1244-1253.

[55] Y. Yu, S. Kim, Y. Lee, J. lee, Phenomenological Observations on Mechanical and Corrosion Properties of Thixoformed 357 Alloys: A Comparison with Permanent Mold Cast 357 Alloys, Metall. Mater. Trans. A, 33 A (2002) 1399-1412.

[56] C. Park, S. Kim, Y. Kwon, Y. Lee, J. Lee, Mechanical and corrosion properties of rheocast and low-pressure cast A356-T6 alloy, Mater. Sci. Eng., A, 391 (2005) 86–94.

[57] S. Tahamtan, A.F. Boostani, Quantitative analysis of pitting corrosion behavior of thixoformed A356 alloy in chloride medium using electrochemical techniques, Mater. Des., 30 (2009) 2483–2489.

[58] S. Tahamtan, A.F. Boostani, Evaluation of pitting corrosion of thixoformed A356 alloy using a simulation model, Trans. Nonferrous Met. Soc. China, 20 (2010) 1702-1606.

[59] S.M. Cohen, Review: Replacements for Chromium Pretreatments on Aluminum, CORROSION, 51 (1995) 71-78.

[60] T.G. Harvey, Cerium-based conversion coatings on aluminium alloys: a process review, Corr. Eng. Sci. Technol, 48 (2013) 248-269.

[61] M.W. Kendig, R.G. Buchheit, Corrosion Inhibition of Aluminum and Aluminum Alloys by Soluble Chromates, Chromate Coatings, and Chromate-Free Coatings, CORROSION, 59 (2003).

[62] A.E. Hughes, J.D. Gorman, P.J.K. Paterson, The characterisation of Ce-Mo-based conversion coatings on Al-alloys: Part I, Corros. Sci., 38 (1996) 1957-1976.

[63] G. HJ, L. PS, P. PF, R. BC, Lung cancer among workers in chromium chemical production., Am. J. Ind. Med., 38 (2000) 115-126.

[64] B. Hinton, D. Arnott, N. Ryan, The inhibition of aluminium alloy corrosion by cerous cations, in: Met. Forum, Pergamon Press, 1984, pp. 211-217.

[65] B. Hinton, D. Arnott, N. Ryan, Cerium conversion coatings for the corrosion protection of aluminum, in: Mater. Forum, 1986, pp. 162-173.

[66] B.R.W. Hinton, Corrosion inhibition with rare earth metal salts, J. Alloys Compd., 180 (1992) 15-25.

[67] M. Olivier, A. Lanzutti, C. Motte, L. Fedrizzi, Influence of oxidizing ability of the medium on the growth of lanthanide layers on galvanized steel, Corros. Sci., 52 (2010) 1428-1439.

[68] C.S. Linz, S.K. Fang, Formation of Cerium Conversion Coatings on AZ31 Magnesium Alloys, J. Electrochem. Soc., 152 (2005) B54-B59

[69] C. Wang, S. Zhu, F. Jiang, F. Wang, Cerium conversion coatings for AZ91D magnesium alloy in ethanol solution and its corrosion resistance, Corros. Sci., 51 (2009) 2916-2923.

[70] Y.L. Lee, F.J. Chen, C.S. Lin, Corrosion Resistance Studies of Cerium Conversion Coating with a Fluoride-Free Pretreatment on AZ91D Magnesium Alloy, J. Electrochem. Soc., 160 (2013) C28-C35

[71] K. Brunelli, M. Dabalà, I. Calliari, M. Magrini, Effect of HCl pre-treatment on corrosion resistance of cerium-based conversion coatings on magnesium and magnesium alloys, Corros. Sci., 47 (2005) 989-1000.

[72] Y. Kobayashi, Y. Fujiwara, Effect of SO42– on the corrosion behavior of cerium-based conversion coatings on galvanized steel, Electrochim. Acta, 51 (2006) 4236-4242.

[73] J. Creus, F. Brezault, C. Rebere, M. Gadouleau, Synthesis and characterisation of thin cerium oxide coatings elaborated by cathodic electrolytic deposition on steel substrate, Surf. Coat. Technol., 200 (2006) 4636-4645.

[74] E. Onofre-Bustamante, M.A. Domínguez-Crespo, A.M. Torres-Huerta, A. Olvera-Martínez, J. Genescá-Llongueras, F.J. Rodríguez-Gómez, Characterization of cerium-based conversion coatings for corrosion protection of AISI-1010 commercial carbon steel, J. Solid State Electrochem., 13 (2009) 1785-1799.

[75] M.A. Arenas, M. Bethencourt, F.J. Botana, J. de Damborenea, M. Marcos, Inhibition of 5083 aluminium alloy and galvanised steel by lanthanide salts, Corros. Sci., 43 (2001) 157-170.

[76] Y. Xingwen, C. Chunan, Y. Zhiming, Z. Derui, Y. Zhongda, Study of double layer rare earth metal conversion coating on aluminum alloy LY12, Corros. Sci., 43 (2001) 1283-1294.

[77] A.E. Hughes, J.D. Gorman, P.R. Miller, B.A. Sexton, P.J.K. Paterson, R.J. Taylor, Development of cerium-based conversion coatings on 2024-T3 Al alloy after rare-earth desmutting, Surf. Interface Anal., 36 (2004) 290-303.

[78] P. Campestrini, H. Terryn, A. Hovestad, J.H.W. de Wit, Formation of a cerium-based conversion coating on AA2024: relationship with the microstructure, Surf. Coat. Technol., 176 (2004) 365-381.

[79] C. Wang, F. Jiang, F. Wang, Cerium Chemical Conversion Coating for Aluminum Alloy 2024-T3 and Its Corrosion Resistance, CORROSION, 60 (2004) 237-243.

[80] N. Birbilis, R.G. Buchheit, D.L. Ho, M. Forsythb, Inhibition of AA2024-T3 on a Phase-by-Phase Basis Using an Environmentally Benign Inhibitor, Cerium Dibutyl Phosphate, Electrochem. Solid-State Lett., 8 (2005) C180-C183

[81] L.E.M. Palomino, I.V. Aoki, H.G. de Melo, Microstructural and electrochemical characterization of Ce conversion layers formed on Al alloy 2024-T3 covered with Cu-rich smut, Electrochim. Acta, 51 (2006) 5943-5953.

[82] C.M. Rangel, T.I. Paiva, P.P. da Luz, Conversion coating growth on 2024-T3 Al alloy. The effect of pre-treatments, Surf. Coat. Technol., 202 (2008) 3396-3402.

[83] A. de Frutos, M.A. Arenas, Y. Liu, P. Skeldon, G.E. Thompson, J. de Damborenea, A. Conde, Influence of pre-treatments in cerium conversion treatment of AA2024-T3 and 7075-T6 alloys, Surf. Coat. Technol., 202 (2008) 3797-3807.

[84] P.S. Jones, P. Yu, W.R. Pinc, M.J. O'Keefe, W.G. Fahrenholtz, T.J. O'Keefe, Spray Deposition of Cerium Oxide-Based Conversion Coatings on Al 2024-T3, Int. J. of Appl. Ceram. Technol., 5 (2008) 63-73.

[85] D. Lau, A.M. Glenn, A.E. Hughes, F.H. Scholes, T.H. Muster, S.G. Hardin, Factors influencing the deposition of Ce-based conversion coatings, Part II: The role of localised reactions, Surf. Coat. Technol., 203 (2009) 2937-2945.

[86] D.K. Heller, W.G. Fahrenholtz, M.J. O'Keefe, Effect of Phosphate Source on Post-Treatment of Cerium-Based Conversion Coatings on Al 2024-T3, J. Electrochem. Soc., 156 (2009) C400-C406

[87] W. Pinc, S. Maddela, M. O'Keefe, W. Fahrenholtz, Formation of subsurface crevices in aluminum alloy 2024-T3 during deposition of cerium-based conversion coatings, Surf. Coat. Technol., 204 (2010) 4095-4100.

[88] D.K. Heller, W.G. Fahrenholtz, M.J. O'Keefe, The effect of post-treatment time and temperature on cerium-based conversion coatings on Al 2024-T3, Corros. Sci., 52 (2010) 360-368.

[89] H. Shi, E.-H. Han, F. Liu, Corrosion protection of aluminium alloy 2024-T3 in 0.05 M NaCl by cerium cinnamate, Corros. Sci., 53 (2011) 2374-2384.

[90] D.K. Heller, W.G. Fahrenholtz, M.J. O'Keefe, Chemical and structural analyses of subsurface crevices formed during spontaneous deposition of cerium-based conversion coatings, Mater. Charact., 62 (2011) 1071-1075.

[91] F. Andreatta, M.E. Druart, A. Lanzutti, M. Lekka, D. Cossement, M.G. Olivier, L. Fedrizzi, Localized corrosion inhibition by cerium species on

clad AA2024 aluminium alloy investigated by means of electrochemical micro-cell, Corros. Sci., 65 (2012) 376-386.

[92] A.C. Balaskas, M. Curioni, G.E. Thompson, Evaluation of Inhibitor Performance by Electrochemical Methods: Comparative Study of Nitrate Salts on AA 2024-T3, J. Electrochem. Soc., 161 (2014) C389-C394.

[93] L. Paussa, F. Andreatta, D. De Felicis, E. Bemporad, L. Fedrizzi, Investigation of AA2024-T3 surfaces modified by cerium compounds: A localized approach, Corros. Sci., 78 (2014) 215-222.

[94] L. Paussa, F. Andreatta, N.C. Rosero Navarro, A. Durán, L. Fedrizzi, Study of the effect of cerium nitrate on AA2024-T3 by means of electrochemical micro-cell technique, Electrochim. Acta, 70 (2012) 25-33.

[95] X. Yu, G. Li, XPS study of cerium conversion coating on the anodized 2024 aluminum alloy, J. Alloys Compd., 364 (2004) 193-198.

[96] B.Y. Johnson, J. Edington, M.J. O’Keefe, Effect of coating parameters on the microstructure of cerium oxide conversion coatings, Mater. Sci. Eng., A, 361 (2003) 225-231.

[97] B.F. Rivera, B.Y. Johnson, M.J. O'Keefe, W.G. Fahrenholtz, Deposition and characterization of cerium oxide conversion coatings on aluminum alloy 7075-T6, Surf. Coat. Technol., 176 (2004) 349-356.

[98] B.Y. Johnson, J. Edington, A. Williams, M.J. O'Keefe, Microstructural characteristics of cerium oxide conversion coatings obtained by various aqueous deposition methods, Mater. Charact., 54 (2005) 41-48.

[99] S. Joshi, W.G. Fahrenholtz, M.J. O'Keefe, Effect of Humidity on Cerium-based Conversion Coatings on Al 7075-T6, ECS Trans., 28 (2010) 217-228.

[100] S. Joshi, B.L. Treu, M.J. O’Keefe, W.G. Fahrenholtz, Characterization of Cerium-Based Conversion Coatings on Al 7075-T6 Deposited from Chloride and Nitrate Salt Solutions, J. Electrochem. Soc., 158 (2011) C88-C93

[101] S. Joshi, W.G. Fahrenholtz, M.J. O'Keefe, Alkaline activation of Al 7075-T6 for deposition of cerium-based conversion coatings, Surf. Coat. Technol., 205 (2011) 4312-4319.

[102] W.G. Fahrenholtz, M.J. O'Keefe, H. Zhou, J.T. Grant, Characterization of cerium-based conversion coatings for corrosion protection of aluminum alloys, Surf. Coat. Technol., 155 (2002) 208-213.

[103] S. Joshi, W.G. Fahrenholtz, M.J. O’Keefe, Effect of alkaline cleaning and activation on aluminum alloy 7075-T6, Appl. Surf. Sci., 257 (2011) 1859-1863.

[104] M. Bethencourt, F.J. Botana, M.J. Cano, M. Marcos, High protective, environmental friendly and short-time developed conversion coatings for aluminium alloys, Appl. Surf. Sci., 189 (2002) 162-173.

[105] M. Bethencourt, F.J. Botana, M.J. Cano, M. Marcos, Advanced generation of green conversion coatings for aluminium alloys, Appl. Surf. Sci., 238 (2004) 278-281.

[106] M. Dabalà, E. Ramous, M. Magrini, Corrosion resistance of cerium-based chemical conversion coatings on AA5083 aluminium alloy, Mater. Corros., 55 (2004) 381-386.

[107] S. Kiyota, B. Valdez, M. Stoytcheva, R. Zlatev, J.M. Bastidas, Anticorrosion behavior of conversion coatings obtained from unbuffered cerium salts solutions on AA6061-T6, J. Rare Earths, 29 (2011) 961-968.

[108] B. Valdez, S. Kiyota, M. Stoytcheva, R. Zlatev, J.M. Bastidas, Cerium-based conversion coatings to improve the corrosion resistance of aluminium alloy 6061-T6, Corros. Sci., 87 (2014) 141-149.

[109] M. Dabalà, L. Armelao, A. Buchberger, I. Calliari, Cerium-based conversion layers on aluminum alloys, Appl. Surf. Sci., 172 (2001) 312-322.

[110] D.-c. Chen, W.-f. Li, W.-h. Gong, G.-x. Wu, J.-f. Wu, Microstructure and formation mechanism of Ce-based chemical conversion coating on 6063 Al alloy, Trans. Nonferrous Met. Soc. China, 19 (2009) 592-600.

[111] M. Kanani, I. Danaee, M.H. Maddahy, Microstructural characteristics and corrosion behavior of cerium oxide conversion coatings on AA6063, Mater. Corros., 65 (2014) 1073-1079.

[112] A. Decroly, J.-P. Petitjean, Study of the deposition of cerium oxide by conversion on to aluminium alloys, Surf. Coat. Technol., 194 (2005) 1-9.

[113] A. Pardo, M.C. Merino, R. Arrabal, F. Viejo, M. Carboneras, Improvement of Corrosion Behavior of A3xx.x/SiCp Composites in 3.5 wt % NaCl Solution by Ce Surface Coatings, J. Electrochem. Soc., 153 (2006) B52-B60.

[114] A. Pardo, M.C. Merino, R. Arrabal, F. Viejo, J.A. Muñoz, Ce conversion and electrolysis surface treatments applied to A3xx.x alloys and A3xx.x/SiCp composites, Appl. Surf. Sci., 253 (2007) 3334-3344.

[115] M. Bethencourt, F.J. Botana, M.J. Cano, R.M. Osuna, M. Marcos, Combination of thermal activation and addition of H2O2 to improve cerium-based immersion treatment of alloy AA5083, Mater. Corros., 54 (2003) 77-83.

[116] F.H. Scholes, C. Soste, A.E. Hughes, S.G. Hardin, P.R. Curtis, The role of hydrogen peroxide in the deposition of cerium-based conversion coatings, Appl. Surf. Sci., 253 (2006) 1770-1780.

[117] B.L. Treu, S. Joshi, W.R. Pinc, M.J. O'Keefe, W.G. Fahrenholtz, Characterization of localized surface states of Al 7075-T6 during deposition of cerium-based conversion coatings, J. Electrochem. Soc, 157 (2010) C282-C287.

[118] D. Zhao, J. Sun, L. Zhang, Y. Tan, J. Li, Corrosion behavior of rare earth cerium based conversion coating on aluminum alloy, J. Rare Earths, 28 (2010) 371-374.

[119] D.R. Arnott, N.E. Ryan, B.R.W. Hinton, B.A. Sexton, A.E. Hughes, Auger and XPS studies of cerium corrosion inhibition on 7075 aluminium alloy, Appl. Surf. Sci., 22/23 (1985) 236-251.

[120] S. Geng, P. Yu, M.J. O’Keefe, W.G. Fahrenholtz, T.J. O’Keefe, Screening study of spray solution parameters for depositing cerium-based conversion coatings on Al alloy 2024-T3, J. Appl. Electrochem., 40 (2010) 551-559.

[121] A.E. Hughes, F.H. Scholes, A.M. Glenn, D. Lau, T.H. Muster, S.G. Hardin, Factors influencing the deposition of Ce-based conversion coatings, part I: The role of Al3+ ions, Surf. Coat. Technol., 203 (2009) 2927-2936.

[122] W. Pinc, S. Geng, M. O'Keefe, W. Fahrenholtz, T. O'Keefe, Effects of acid and alkaline based surface preparations on spray deposited cerium based conversion coatings on Al 2024-T3, Appl. Surf. Sci., 255 (2009) 4061-4065.

[123] A.J. Aldykewicz, Jr., A.J. Davenport, The Investigation of Cerium as a Cathodic Inhibitor for Aluminum-Copper Alloys, J. Electrochem. Soc, 142 (1995) 3342-3350.

[124] J.O. Park, C.H. Paik, Y.H. Huang, R.C. Alkire, Influence of Fe-Rich Intermetallic Inclusions on Pit Initiation on Aluminum Alloys in Aerated NaCl, J. Electrochem. Soc., 146 (1999) 517-523.

[125] P.L. Brown, R.N. Sylva, The Hydrolysis of Metal Ions. Part 8. Aluminium (III), J. Chem. Soc. Dalton trans, (1985) 5/248.

[126] T.P. Kaloni, G. Schreckenbach, M.S. Freund, Band gap modulation in polythiophene and polypyrrolebased systems, Sci. Rep., 6 (2016) 36554

[127] Y. Huang, H. Li, Z. Wang, M. Zhu, Z. Pei, Q. Xue, Y. Huang, C. Zhi, Nanostructured Polypyrrole as a flexible electrode material of supercapacitor, Nano Energy, 22 (2016) 422-438.

[128] T.V. Vernitskaya, O.N. Efimov, Polypyrrole: a conducting polymer; its synthesis, properties and applications, Russ. Chem. Rev, 66 (1997) 443 – 457.

[129] T. Ohtsuka, Corrosion Protection of Steels by Conducting Polymer Coating, Int. J. Corr., 2012 (2012).

[130] P.P. Deshpande, D. Sazou, Corrosion Protection of Metals by Intrinsically Conducting Polymers, Taylor & Francis Group, 2016.

[131] G.M. Spinks, A.J. Dominis, G.G. Wallace, D.E. Tallman, Electroactive conducting polymers for corrosion control, J Solid State Electrochem., 6 (2002) 85-100.

[132] P. Zarras, J.D. Stenger-Smith, An Introduction to Corrosion Protection Using Electroactive Polymers, in: Electroactive Polymers for Corrosion Control, American Chemical Society, 2003, pp. 2-17.

[133] M. Rohwerder, A. Michalik, Conducting polymers for corrosion protection: What makes the difference between failure and success?, Electrochim. Acta, 53 (2007) 1300-1313.

[134] P.P. Deshpande, N.G. Jadhav, V.J. Gelling, D. Sazou, Conducting polymers for corrosion protection: a review, J. Coat. Technol. Res., 11 (2014) 473-494.

[135] E. Volpi, M. Trueba, S.P. Trasatti, Electrochemical investigation of conformational rearrangements of polypyrrole deposited on Al alloys, Prog. Org. Coat., 74 (2012) 376-384.

[136] A. Michalik, M. Rohwerder, Conducting Polymers for Corrosion Protection: A Critical View, zpch, 219 (2005) 1547–1559.

[137] M. Yan, D.E. Tallman, G.P. Bierwagen, Role of oxygen in the galvanic interaction between polypyrrole and aluminum alloy, Electrochim. Acta, 54 (2008) 220-227.

[138] J. He, D.E. Tallman, G.P. Bierwagen, Conjugated Polymers for Corrosion Control: Scanning Vibrating Electrode Studies of Polypyrrole-Aluminum Alloy Interactions, J. Electrochem. Soc., 151 (2004) B644-B651.

[139] D.W. DeBerry, Modification of the Electrochemical and Corrosion Behavior of Stainless Steels with an Electroactive Coating J. Electrochem. Soc, 132 (1985) 1022-1026.

[140] S.B. Saidman, J.B. Bessone, Electrochemical preparation and characterisation of polypyrrole on aluminium in aqueous solution, J. Electroanal. Chem., 521 (2002) 87-94.

[141] I.L. Lehr, S.B. Saidman, Characterisation and corrosion protection properties of polypyrrole electropolymerised onto aluminium in the presence of molybdate and nitrate, Electrochim. Acta, 51 (2006) 3249-3255.

[142] M.A. Arenas, L.G. Bajos, J.J. de Damborenea, P. Ocón, Synthesis and electrochemical evaluation of polypyrrole coatings electrodeposited onto AA-2024 alloy, Prog. Org. Coat., 62 (2008) 79-86.

[143] N.C.T. Martins, T. Moura e Silva, M.F. Montemor, J.C.S. Fernandes, M.G.S. Ferreira, Electrodeposition and characterization of polypyrrole films on aluminium alloy 6061-T6, Electrochim. Acta, 53 (2008) 4754-4763.

[144] M.C. Yan, D.E. Tallman, S.C. Rasmussen, G.P. Bierwagen, Corrosion Control Coatings for Aluminum Alloys Based on Neutral and n-Doped Conjugated Polymers, J. Electrochem. Soc., 156 (2009) C360-C366.

[145] A.C. Balaskas, I.A. Kartsonakis, G. Kordas, A.M. Cabral, P.J. Morais, Influence of the doping agent on the corrosion protection properties of polypyrrole grown on aluminium alloy 2024-T3, Prog. Org. Coat., 71 (2011) 181-187.

[146] M. Rizzi, M. Trueba, S.P. Trasatti, Polypyrrole films on Al alloys: The role of structural changes on protection performance, Synth. Met., 161 (2011) 23-31.

[147] E. Volpi, M. Trueba, S.P. Trasatti, S. Trasatti, Effect of polypyrrole conformational rearrangement on Al alloys corrosion protection, J. Electroanal. Chem., 688 (2013) 289-297.

[148] K.R.L. Castagno, V. Dalmoro, D.S. Azambuja, Characterization and corrosion of polypyrrole/sodium dodecylbenzene sulfonate electropolymerised on aluminum alloy 1100, Mater. Chem. Phys., 130 (2011) 721-726.

[149] M. Mrad, Y.B. Amor, L. Dhouibi, F. Montemor, Electrochemical study of polyaniline coating electropolymerized onto AA2024-T3 aluminium alloy: Physical properties and anticorrosion performance, Synth. Met., 234 (2017) 145-153.

[150] R.M. Bandeira, J. van Drunen, A.C. Garcia, G. Tremiliosi-Filho, Influence of the thickness and roughness of polyaniline coatings on corrosion protection of AA7075 aluminum alloy, Electrochim. Acta, 240 (2017) 215-224.

[151] J.O. Iroh, W. Su, Corrosion performance of polypyrrole coating applied to low carbon steel by an electrochemical process, Electrochim. Acta., 46 (2000) 15–24.

[152] L. Koene, W.J. Hamer, J.H.W. de Wit, Electrochemical behaviour of poly(pyrrole) coatings on steel, J. Appl. Electrochem., 36 (2006) 545-556.

[153] D. Sazou, M. Kourouzidou, E. Pavlidou, Potentiodynamic and potentiostatic deposition of polyaniline on stainless steel: Electrochemical and structural studies for a potential application to corrosion control, Electrochim. Acta, 52 (2007) 4385-4397.

[154] M.B. González, S.B. Saidman, Electrodeposition of polypyrrole on 316L stainless steel for corrosion prevention, Corros. Sci., 53 (2011) 276–282.

[155] M.B. González, S.B. Saidman, Corrosion protection properties of polypyrrole electropolymerized onto steel in the presence of salicylate, Prog. Org. Coat., 75 (2012) 178–183.

[156] A. El Jaouhari, M. Laabd, E.A. Bazzaoui, A. Albourine, J.I. Martins, R. Wang, G. Nagy, M. Bazzaoui, Electrochemical and spectroscopical studies of polypyrrole synthesized on carbon steel from aqueous medium, Synth. Met., 209 (2015) 11-18.

[157] D.E. Tallman, M.P. Dewald, C.K. Vang, G.G. Wallace, G.P. Bierwagen, Electrodeposition of conducting polymers on active metals by electron transfer mediation, Curr. Appl. Phys., 4 (2004) 137-140.

[158] H.S. Jung, K.S. Kim, M.K. Kwak, J.H. Ko, Effect of polystyrenesulphonate and electrolyte concentration for electrical properties of polypyrrole film on aluminium alloy using conductive AFM, Corr. Eng. Sci. Technol., 49 (2014) 608-613.

[159] B.D. Mert, R. Solmaz, G. Kardaş, B. Yazıcı, Copper/polypyrrole multilayer coating for 7075 aluminum alloy protection, Prog. Org. Coat., 72 (2011) 748-754.

[160] B. Doğru Mert, Corrosion protection of aluminum by electrochemically synthesized composite organic coating, Corros. Sci., 103 (2016) 88-94.

[161] X. Bai, T.H. Tran, D. Yu, A. Vimalanandan, X. Hu, M. Rohwerder, Novel conducting polymer based composite coatings for corrosion protection of zinc, Corros. Sci., 95 (2015) 110-116.

[162] M. Rohwerder, L.M. Duc, A. Michalik, In situ investigation of corrosion localised at the buried interface between metal and conducting polymer based composite coatings, Electrochim. Acta, 54 (2009) 6075-6081.

[163] G. Paliwoda-Porebska, M. Stratmann, M. Rohwerder, K. Potje-Kamloth, Y. Lu, A.Z. Pich, H.J. Adler, On the development of polypyrrole coatings with self-healing properties for iron corrosion protection, Corros. Sci., 47 (2005) 3216-3233.

[164] N.T.L. Hien, B. Garcia, A. Pailleret, C. Deslouis, Role of doping ions in the corrosion protection of iron by polypyrrole films, Electrochim. Acta, 50 (2005) 1747-1755.

[165] V. Branzoi, L. Pilan, F. Golgovici, F. Branzoi, Electrochemical Activity and Corrosion Protection Properties of Doped Polypyrrole Electrodeposited at Pure Aluminium Electrode, Mol. Cryst. Liq. Cryst., 446 (2006) 305–318.

[166] M. Atobe, H. Tsuji, R. Asami, T. Fuchigami, A study on doping–undoping properties of polypyrrole films electropolymerized under ultrasonication, J. Electrochem. Soc., 153 (2006) D10-D13.

[167] S. Zor, F. Kandemirli, E. Yakar, T. Arslan, Electrochemical synthesis of polypyrrole on aluminium in different anions and corrosion protection of aluminium, Prot. Met. Phys. Chem. Surf., 46 (2010) 110-116.

[168] D. Kowalski, M. Ueda, T. Ohtsuka, Self-healing ion-permselective conducting polymer coating, J. Mat. Chem., 20 (2010) 7630-7633.

[169] M. Mrad, L. Dhouibi, M.F. Montemor, E. Triki, Effect of doping by corrosion inhibitors on the morphological properties and the performance

against corrosion of polypyrrole electrodeposited on AA6061-T6, Prog. Org. Coat., 72 (2011) 511-516.

[170] H. Ryu, N. Sheng, T. Ohtsuka, S. Fujita, H. Kajiyama, Polypyrrole film on 55% Al–Zn-coated steel for corrosion prevention, Corros. Sci., 56 (2012) 67-77.

[171] R. Vera, R. Schrebler, P. Grez, H. Romero, The corrosion-inhibiting effect of polypyrrole films doped with p-toluene-sulfonate, benzene-sulfonate or dodecyl-sulfate anions, as coating on stainless steel in NaCl aqueous solutions, Prog. Org. Coat., 77 (2014) 853-858.

[172] M. Li, X. Ji, L. Cui, J. Liu, In situ preparation of graphene/polypyrrole nanocomposite via electrochemical co-deposition methodology for anti-corrosion application, J. Mat. Sci., 52 (2017) 12251-12265.

[173] D.E. Tallman, C. Vang, G.G. Wallace, G.P. Bierwagen, Direct Electrodeposition of Polypyrrole on Aluminum and Aluminum Alloy by Electron Transfer Mediation, J. Electrochem. Soc., 149 (2002) C173-C179.

[174] A. de Leon, R.C. Advincula, Chapter 11 - Conducting Polymers with Superhydrophobic Effects as Anticorrosion Coating, in: Intelligent Coatings for Corrosion Control, Butterworth-Heinemann, Boston, 2015, pp. 409-430.

[175] S.B. Saidman, O.V. Quinzani, Characterisation of polypyrrole electrosynthesised on aluminium, Electrochim. Acta, 50 (2004) 127-134.

[176] S.B. Saidman, The effect of pH on the electrochemical polymerisation of pyrrole on aluminium, J. Electroanal. Chem., 534 (2002) 39-45.

[177] F.B. Mansfeld, P. Marcus, Analytical methods in corrosion science and engineering, CRC press, 2005.

[178] Impedance Spectroscopy Theory, Experiment, and Applications, John Wiley & Sons, Inc., 2005.

[179] F. Scholz, Electroanalytical methods, Springer, 2010.

[180] W. Zhou, R. Apkarian, Z. Wang, Fundamentals of Scanning Electron Microscopy (SEM), Springer, 2007.

[181] J.F. Watts, o. Wolstenholme, An Introduction to Surface Analysis by XPS and AES, Wiley, 2003.

[182] M. Wessén, H. Cao, The RSF technology; A possible breakthrough for semi-solid casting processes, in: International Conference of High Tech Die Casting, Vicenza, Italy, 2006.

[183] E. Cano, D. Lafuente, D.M. Bastidas, Use of EIS for the evaluation of the protective properties of coatings for metallic cultural heritage: a review, J. Solid State Electrochem., 14 (2010) 381–391.

[184] P. Letardi, 7 - Electrochemical measurements in the conservation of metallic heritage artefacts: an overview A2 - Dillmann, P, in: D. Watkinson, E. Angelini, A. Adriaens (Eds.) Corrosion and Conservation of Cultural Heritage Metallic Artefacts, Woodhead Publishing, 2013, pp. 126-148.

[185] D.H. Kirkwood, M. Suery, P. Kapranos, H.V. Atkinson, K.P. Young, Semi-solid Processing of Alloys, Springer, New York, 2010.

[186] N.A. Belov, A.A. Aksenov, Iron in Aluminum Alloys: Impurity and Alloying Element, Taylor & Francis Inc, New York, 2002.

[187] B. Sundman, B. Jansson, J.-O. Andersson, The thermo-calc databank system, Calphad, 9 (1985) 153-190.

[188] J.-O. Andersson, T. Helander, L. Höglund, P. Shi, B. Sundman, Thermo-Calc & DICTRA, computational tools for materials science, Calphad, 26 (2002) 273-312.

[189] D.B. Spencer, R. Mehrabian, M.C. Flemings, Rheological behavior of Sn-15 pct Pb in the crystallization range, Metall. Trans., 3 1925-1932.

[190] M.C. Flemings, Behavior of metal alloys in the semisolid state, Metall. Trans. A, 22 (1991) 957-981.

[191] M. Easton, H. Kaufmann, W. Fragner, The effect of chemical grain refinement and low superheat pouring on the structure of NRC castings of aluminium alloy Al–7Si–0.4 Mg, Mater. Sci. Eng., A, 420 (2006) 135-143.

[192] B. Zhu, S. Seifeddine, P.O.Å. Persson, A.E.W. Jarfors, P. Leisner, C. Zanella, A study of formation and growth of the anodised surface layer on cast Al-Si alloys based on different analytical techniques, Mater. Des., 101 (2016) 254-262.

[193] C. Gourlay, A. Dahle, T. Nagira, N. Nakatsuka, K. Nogita, K. Uesugi, Granular deformation mechanisms in semi-solid alloys, Acta Mater., 59 (2011) 4933-4943.

[194] M. Payandeh, A.E.W. Jarfors, M. Wessén, Influence of Microstructural Inhomogeneity on Fracture Behaviour in SSM-HPDC Al-Si-Cu-Fe Component with Low Si Content, Solid State Phenom., 217-218 (2015) 67-74.

[195] G. Govender, H. Möller, Evaluation of Surface Chemical Segregation of Semi-Solid Cast Aluminium Alloy A356, Solid State Phenom., 141-143 (2008) 433-438.

[196] C.M. Dinnis, A.K. Dahle, J.A. Taylor, Three-dimensional analysis of eutectic grains in hypoeutectic Al–Si alloys, Mater. Sci. Eng., A, 392 (2005) 440-448.

[197] S. Ji, A. Das, Z. Fan, Solidification behavior of the remnant liquid in the sheared semisolid slurry of Sn–15 wt.%Pb alloy, Scripta Mater., 46 (2002) 205-210.

[198] S.L. dos Santos, R.A. Antunes, S.F. Santos, Influence of injection temperature and pressure on the microstructure, mechanical and corrosion properties of a AlSiCu alloy processed by HPDC, Mater. Des., 88 (2015) 1071-1081.

[199] J.G. Kaufman, E.L. Rooy, Aluminum Alloy Castings: Properties, Processes, and Applications, ASM International, Materials Park, 2004.

[200] X.-h. Wang, J.-h. Wang, C.-w. Fu, Characterization of pitting corrosion of 7A60 aluminum alloy by EN and EIS techniques, Trans. Nonferrous Met. Soc. China, 24 (2014) 3907–3916.

[201] M.A. Amin, Uniform and pitting corrosion events induced by SCN– anions on Al alloys surfaces and the effect of UV light, Electrochim. Acta, 56 (2011) 2518–2531.

[202] M.A. Amin, H.H. Hassan, O.A. Hazzazi, M.M. Qhatani, Role of alloyed silicon and some inorganic inhibitors in the inhibition of meta-stable and stable pitting of Al in perchlorate solutions, J. Appl. Electrochem., 38 (2008) 1589–1598.

[203] A. Despić, V.P. Parkhutik, Electrochemistry of Aluminum in Aqueous Solutions and Physics of Its Anodic Oxide, in: J.O.M. Bockris, R.E. White,

B.E. Conway (Eds.) Modern Aspects of Electrochemistry No. 20, Springer US, Boston, MA, 1989, pp. 401-503.

[204] J.A. Moreto, C.E.B. Marino, W.W.B. Filho, L.A. Rocha, J.C.S. Fernandes, SVET, SKP and EIS study of the corrosion behaviour of high strength Al and Al–Li alloys used in aircraft fabrication, Corros. Sci., 84 (2014) 30–41.

[205] O. Schneider, G. Ilevbare, J. Scully, R. Kelly, In situ confocal laser scanning microscopy of AA 2024-T3 corrosion metrology II. Trench formation around particles, J. Electrochem. Soc., 151 (2004) B465-B472.

[206] A.E. Hughes, A. Boag, A.M. Glenn, D. McCulloch, T.H. Muster, C. Ryan, C. Luo, X. Zhou, G.E. Thompson, Corrosion of AA2024-T3 Part II: Co-operative corrosion, Corros. Sci., 53 (2011) 27-39.

[207] E. Estragnat, G. Tang, H. Liang, S. Jahanmir, P. Pei, J.M. Martin, Experimental investigation on mechanisms of silicon chemical mechanical polishing, J. Electron. Mater., 33 (2004) 334-339.

[208] M.A. Pech-Canul, M.I. Pech-Canul, P. Bartolo-Pérez, M. Echeverría, The role of silicon alloying addition on the pitting corrosion resistance of an Al-12 wt.%Si alloy, Electrochim. Acta, 140 (2014) 258–265.

[209] P. Campestrini, Microstructure-related quality of conversion coatings on aluminium alloys, in: Applied Sciences, Delft University, 2002.

[210] M. Eslami, F. Deflorian, M. Payandeh, A.E.W. Jarfors, C. Zanella, Investigation of corrosion behavior of SSM-HPDC aluminum-silicon alloys, in: EuroCorr 2016, Montpellier, 2016.

[211] I. Aziz, Q. Zhang, M. Xiang, Using EIS to evaluate anti-corrosion properties of the SiCp/5A06 aluminium MMC treated by cerium conversion coatings, J. Rare Earths, 28 (2010) 109-116.

[212] W. Pinc, S. Maddela, W. Fahrenholtz, M. O'Keefe, Corrosion Protection of Cerium-based Conversion Coatings With Subsurface Crevices ECS Trans., 28 (2010) 187-201.

[213] S.-I. Pyun, S.-M. Moon, The inhibition mechanism of pitting corrosion of pure aluminum by nitrate and sulfate ions in neutral chloride solution, J. Solid State Electrochem., 3 (1999) 331-336.

[214] P. Burroughs, A.H. Anthony, F. Orchard, G. Thornton, Satellite structure in the X-ray photoelectron spectra of some binary and mixed oxides of lanthanum and cerium, J. Chem. Soc., Dalton Trans., (1976) 1686-1698.

[215] M. Romeo, K. Bak, J. El Fallah, F. Le Normand, L. Hilaire, XPS Study of the reduction of cerium dioxide, Surf. Interface Anal., 20 (1993) 508-512.

[216] K. Nis¸ancioğlu, Electrochemical Behaviorof Aluminum-Base Intermetallics Containing Iron, J. Electrochem. Soc., 137 (1990) 69-77.

[217] E. McCafferty, Introduction to Corrosion Science, Springer New York, 2010.

[218] D. Snihirova, S.V. Lamaka, M.F. Montemor, Smart composite coatings for corrosion protection of aluminium alloys in aerospace applications, in: M.F. Montemor (Ed.) Smart Composite Coatings and Membranes 2016.

[219] M. Eslami, F. Deflorian, M. Fedel, C. Zanella, Ce-based conversion coatings on Rheo-HPDC low Si content aluminium alloy, in: EUROCORR

2017 - The Annual Congress of the European Federation of Corrosion, 20th International Corrosion Congress and Process Safety Congress 2017, 2017.

[220] M. Eslami, M. Payandeh, F. Deflorian, A. Jarfors, C. Zanella, Effect of Segregation and Surface Condition on Corrosion of Rheo-HPDC Al–Si Alloys, Metals, 8 (2018) 209.

[221] M. Eslami, M. Fedel, G. Speranza, F. Deflorian, N.-E. Andersson, C. Zanella, Study of selective deposition mechanism of cerium-based conversion coating on Rheo-HPDC aluminium-silicon alloys, Electrochim. Acta., 255 (2017) 449-462.

[222] M. Eslami, M. Fedel, G. Speranza, F. Deflorian, C. Zanella, Deposition and Characterization of Cerium-Based Conversion Coating on HPDC Low Si Content Aluminum Alloy, J. Electrochem. Soc., 164 (2017) C581-C590.

[223] D.-H. Nam, M.-J. Kim, S.-J. Lim, I.-S. Song, H.-S. Kwon, Single-step synthesis of polypyrrole nanowires by cathodic electropolymerization, J. Mat. Chem. A, 1 (2013) 8061-8068.

[224] J. Wysocka, S. Krakowiak, J. Ryl, Evaluation of citric acid corrosion inhibition efficiency and passivation kinetics for aluminium alloys in alkaline media by means of dynamic impedance monitoring, Electrochim. Acta, 258 (2017) 1463-1475.

[225] L.F.Q.P. Marchesi, F.R. Simões, L.A. Pocrifka, E.C. Pereira, Investigation of Polypyrrole Degradation Using Electrochemical Impedance Spectroscopy, J. Phys. Chem. B, 115 (2011) 9570-9575.

[226] W. Hamer, Polypyrrole Electrochemistry, Environmentally friendly corrosion protection of steel: (im)possibilities, in, Technische Universiteit Delft, 2005

[227] M. Bazzaoui, J.I. Martins, S.C. Costa, E.A. Bazzaoui, T.C. Reis, L. Martins, Sweet aqueous solution for electrochemical synthesis of polypyrrole: Part 1-A. On non-ferrous metals, Electrochim. Acta., 51 (2006) 2417-2426.

[228] P. Hülser, F. Beck, Electrodeposition of polypyrrole layers on aluminium from aqueous electrolytes, J. Appl. Electrochem., 20 (1990) 596-605.

[229] A. El Jaouhari, A. El Asbahani, M. Bouabdallaoui, Z. Aouzal, D. Filotás, E.A. Bazzaoui, L. Nagy, G. Nagy, M. Bazzaoui, A. Albourine, D. Hartmann, Corrosion resistance and antibacterial activity of electrosynthesized polypyrrole, Synth. Met., 226 (2017) 15-24.

[230] N.Ö.i.e. Pekmez, K. Cınkıllı, B. Zeybek, The electrochemical copolymerization of pyrrole and bithiophene on stainless steel in the presence of SDS in aqueous medium and its anticorrosive performance, Prog. Org. Coat., 77 (2014) 1277–1287.

[231] L. Zhang, S. Liu, H. Han, Y. Zhou, S. Hu, C. He, Q. Yan, Studies on the formation process and anti-corrosion performance of polypyrrole film deposited on the surface of Q235 steel by an electrochemical method, Surf. Coat. Technol., 341 (2018) 95-102.

[232] H. Nguyen Thi Le, B. Garcia, C. Deslouis, Q. Le Xuan, Corrosion protection and conducting polymers: polypyrrole films on iron, Electrochim. Acta, 46 (2001) 4259-4272.

[233] M. Ascencio, M. Pekguleryuz, S. Omanovic, Corrosion behaviour of polypyrrole-coated WE43 Mg alloy in a modified simulated body fluid solution, Corros. Sci., 133 (2018) 261-275.

[234] A.S. Liua, M.A.S. Oliveira, Corrosion Control of Aluminum Surfaces by Polypyrrole Films: Influence of Electrolyte, Mater. Res., 10 (2007) 205-209.

[235] O. Grari, L. Dhouibi, F. Lallemand, S. Lallemand, E. Triki, Effects of nitrate ions on the electrochemical synthesis and behavior of polypyrrole films, Prog. Org. Coat., 77 (2014) 1867-1873.

[236] K. Levine, Nanocomposite PPy Coatings for Al Alloys Corrosion Protection, in: V. Mittal (Ed.) Polymer Nanocomposite Coatings, CRC Press, 2013.

[237] A. Eftekhari, M. Kazemzad, M. Keyanpour-Rad, Significant Effect of Dopant Size on Nanoscale Fractal Structure of Polypyrrole Film, Polym. J., 38 (2006) 781.

[238] S.R. K., K. Amit, A. Khushboo, K. Mahesh, S.H. K., S. Pankaj, S. Ramadhar, DC electrical conduction and morphological behavior of counter anion-governed genesis of electrochemically synthesized polypyrrole films, J. Polym. Sci., Part B: Polym. Phys., 50 (2012) 347-360.

[239] C. Malitesta, I. Losito, L. Sabbatini, P.G. Zambonin, New findings on polypyrrole chemical structure by XPS coupled to chemical derivatization labelling, J. Electron. Spectrosc. Relat. Phenom., 76 (1995) 629-634.

[240] J. Tabačiarová, M. Mičušík, P. Fedorko, M. Omastová, Study of polypyrrole aging by XPS, FTIR and conductivity measurements, Polym. Degrad. Stab., 120 (2015) 392-401.

[241] K. Idla, A. Talo, H.E.-M. Niemi, O. Forsén, S. Yläsaari, An XPS and AFM study of polypyrrole coating on mild steel, Surf. Interface Anal., 25 (1997) 837-854.

[242] M.G. Hosseini, M. Raghibi-Boroujeni, I. Ahadzadeh, R. Najjar, M.S. Seyed Dorraji, Effect of polypyrrole–montmorillonite nanocomposites powder addition on corrosion performance of epoxy coatings on Al 5000, Prog. Org. Coat., 66 (2009) 321-327.